
**An analytical and numerical analysis of fluid-filled crack
propagation in three dimensions**

Timothy Davis

June, 2021

Cumulative dissertation

to obtain the academic degree
"doctor rerum naturalium" (Dr. rer. nat.)
in the scientific discipline Geophysics

Submitted to the
Faculty of Mathematics and Natural Sciences
at the University of Potsdam, Germany

Place and date of the defence:

University of Potsdam, 28/May/2021

Principal supervisor: Prof. Torsten Dahm
Second supervisor: Prof. Eleonora Rivalta

Reviewers: Prof. Torsten Dahm
Dr. Valérie Cayol
Prof. David Pollard

Examining committee: Prof. Bodo Bookhagen
Prof. Torsten Dahm
Dr. Gerold Zeilinger
Prof. Gert Zöllner
Prof. Stephan Sobolev

Published online on the
Publication Server of the University of Potsdam:
<https://doi.org/10.25932/publishup-50960>
<https://nbn-resolving.org/urn:nbn:de:kobv:517-opus4-509609>

Statement of originality

I declare that the work presented in this thesis is, to the best of my knowledge and belief, original and my own work.

Timothy Davis

Potsdam, June, 2021

Abstract

Fluids in the Earth's crust can move by creating and flowing through fractures, in a process called 'hydraulic fracturing'. The tip-line of such fluid-filled fractures grows at locations where stress is larger than the strength of the rock. Where the tip stress vanishes, the fracture closes and the fluid-front retreats. If stress gradients exist on the fracture's walls, induced by fluid/rock density contrasts or topographic stresses, this results in an asymmetric shape and growth of the fracture, allowing for the contained batch of fluid to propagate through the crust.

The state-of-the-art analytical and numerical methods to simulate fluid-filled fracture propagation are two-dimensional (2D). In this work I extend these to three dimensions (3D). In my analytical method, I approximate the propagating 3D fracture as a penny-shaped crack that is influenced by both an internal pressure and stress gradients. In addition, I develop a numerical method to model propagation where curved fractures can be simulated as a mesh of triangular dislocations, with the displacement of faces computed using the displacement discontinuity method. I devise a rapid technique to approximate stress intensity and use this to calculate the advance of the tip-line. My 3D models can be applied to arbitrary stresses, topographic and crack shapes, whilst retaining short computation times.

I cross-validate my analytical and numerical methods and apply them to various natural and man-made settings, to gain additional insights into the movements of hydraulic fractures such as magmatic dikes and fluid injections in rock. In particular, I calculate the 'volumetric tipping point', which once exceeded allows a fluid-filled fracture to propagate in a 'self-sustaining' manner. I discuss implications this has for hydro-fracturing in industrial operations. I also present two studies combining physical models that define fluid-filled fracture trajectories and Bayesian statistical techniques. In these studies I show that the stress history of the volcanic edifice defines the location of eruptive vents at volcanoes. Retrieval of the ratio between topographic to remote stresses allows for forecasting of probable future vent locations. Finally, I address the mechanics of 3D propagating dykes and sills in volcanic regions. I focus on Sierra Negra volcano in the Galápagos islands, where in 2018, a large sill propagated with an extremely curved trajectory. Using a 3D analysis, I find that shallow horizontal intrusions are highly sensitive to topographic and buoyancy stress gradients, as well as the effects of the free surface.

Zusammenfassung

Flüssigkeiten und Gase (Fluide) können sich in der Erdkruste bewegen, indem sie Risse erzeugen und durch diese fließen. Die Mechanik dieses Problems wird im Forschungsbereich der Bruchmechanik beschrieben. Das Vorhandensein von Spannungsgradienten verursacht einen Rissausbreitungsvorgang durch die Erdkruste. Auf den Flächen dieser Rissufer können verschiedene Arten von Belastungen auftreten, welche definieren, wie sich die Rissfront vergrößert.

In dieser Arbeit adaptiere ich zuvor entwickelte zweidimensionale (2D) Modelle der flüssigkeitsgefüllten Bruchausbreitung für drei Dimensionen (3D). Anhand der dreidimensionalen Betrachtung können die Bewegungen dieser Frakturen detaillierter untersucht werden. Analoge und neotektonische Beobachtungen, die mit vorhandenen 2D-Techniken nicht beschreibbar waren, können mit der neuen Technik erklärt werden. Zusätzlich beschreibe ich, wie man mit einer 3D Randelementmethode (boundary element method) Spannungsintensitätsfaktoren berechnen und komplexe Rissgeometrien erfassen kann. Die Rechenzeiten sind vergleichbar mit 2D-Modellen. Ich stelle neue Analysetechniken bereit, mit denen diese Probleme schnell, aber kohärent quantifiziert werden können.

Ich verwende diese 3D-Techniken, um eine Reihe von Fallstudien zu untersuchen, wobei ich mich zunächst auf den Wendepunkt konzentriere, ab dem sich der mit Fluiden gefüllte Riss autark bewegt. Ich habe herausgefunden, dass dies durch das in der Fraktur enthaltene Volumen beschrieben werden kann, was Auswirkungen auf den industriellen Betrieb hat. Anschließend präsentiere ich zwei Studien, die physikalische Rissausbreitungsmodelle und Bayes'sche statistische Techniken kombinieren. Ich zeige, dass die Spannungshistorie den Ort eruptiver Entlüftungsöffnungen definiert und dass die Einbeziehung der topografischen und tektonischen Spannungsverhältnisse mit diesem Schema die Vorhersage wahrscheinlicher zukünftiger Entlüftungsstellen ermöglicht. Mit der 3D Randelementmethode befasse ich mich mit der Ausbreitung von Gängen und Lavagängen in vulkanischen Regionen. Ich konzentriere mich auf eine Fallstudie vom Vulkan Sierra Negra auf den Galapagos-Inseln, auf der eine große Lavagängen beobachtet wurden, die sich mit einer stark gekrümmten Kurve ausbreitet. Ich habe herausgefunden, dass die Bewegung von Lavagängen in solchen Systemen aus einer Wechselwirkung von topografischen- und Auftriebs-Spannungsgradienten sowie den Auswirkungen von Halbraumeffekten resultieren.

Acknowledgements

DFG/ICDP: This work was funded by the Deutsche Forschungsgemeinschaft(DFG)-International Continental Scientific Drilling Program(ICDP) grant number. RI 2782/3-1, and hosted in the Deutsche GeoForschungsZentrum and the University of Potsdam. I am extremely grateful to these bodies in providing the opportunity for me to perform this research

Eleonora Rivalta: Eleonora has been a truly inspirational supervisor throughout this process, managing to guide the science, encourage ideas and promote discussion. She has truly been a joy to work with and has provided me with a wealth of opportunities I did not foresee in advance. Her focus on both the development and application of highly theoretical physical concepts has motivated the research direction within this thesis.

Torsten Dahm: Torsten's guidance at key points in this process was helpful to catch mistakes and shape the research questions. The work environment he has created is relaxed, allowing for ideas to flourish and truly collaborative exchange from which this research has benefited.

David Healy: Dave helped me realise my Masters research and worked on Chapter 2 of this thesis, his excitement is infectious and his knowledge crossover between theoretical rock physics and field geology is inspirational.

Susanne Köster: I am indebted to Susanne for help with numerous tasks both when arriving and during my stay in Germany. All of the travel arrangements and admin tasks related to this research have benefited tremendously from Susanne, I cannot thank her enough.

Caitlin Jukes: Caitlin has helped immensely with this thesis, reading multiple drafts of the manuscripts and forcing me to take well needed breaks from the research.

Berlin friends: I would like to thank all my friends in Berlin, specifically I would like to mention Xenia Müller, Thomas Pearson and Hannah Ferchland who have all been extremely welcoming, and great friends since my arrival. Also thanks to my Krefelder Straße flat mates Francesco and Jose who showed me how excellent a WG can be, along with the dangers of Kniffel.

Section 2.1: To all my colleagues in the section, it's truly been a joy to work here. I feel privileged to have worked with you all, in such a supportive environment. Special thanks to Francesco Maccaferri, Luigi Passarelli and Mehdi Nikkhoo for the sound scientific advice, all the coffee and for each individually inspiring me to work on the simulation fluid-filled fractures in 3D. Additionally Gesa Petersen and Peter Niemz get a special thanks for distracting me from work with stimulating lake-side conversations and long distance bike trips around Berlin.

Family: Lastly, I would like to thank my family, who have been very supportive during this whole process and an excellent sounding board for communicating my research clearly.

Contents

Abbreviations & Notation	1
1 Introduction	2
1.1 Motivation	2
1.1.1 An introduction to fluid-filled fractures	2
1.1.2 Fluid-filled fractures in 3D	7
1.2 Objectives	10
1.2.1 Research goals	10
1.2.2 Thesis outline	11
1.3 Publications and authors contribution	12
1.3.1 Published articles	12
1.3.2 Submitted/in revision articles	13
1.3.3 Published code	13
1.4 Theory	14
1.4.1 General linear elasticity	14
1.4.2 Linear Elastic Fracture Mechanics	15
1.4.3 Analytical and numerical solutions to LEFM problems	18
2 Friction on wavy faults	21
2.1 Introduction	22
2.1.1 Fault slip profiles	22
2.1.2 Motivation: non-planar faults	23
2.1.3 Previous numerical work	24
2.2 Background	25
2.2.1 Theoretical background and terminology	25
2.2.2 Motivation	27
2.3 Displacement discontinuity method with friction	28
2.3.1 3D DDM formulation: equations, elements and convention	28
2.3.2 Aims of the DDM solution	30
2.3.3 DDM formulation with friction	30
2.3.4 Aims of the frictional DDM solution	32
2.4 Benchmarking and model setup	34

Contents

2.4.1	Boundary conditions and shear profile of the crack	34
2.4.2	Stress intensity approximation	40
2.5	Model results	42
2.5.1	Effect of corrugation amplitude and wavelength: comparison to 2D results	42
2.5.2	Effect of corrugation orientation in 3D	45
2.5.3	Stress intensity factors	49
2.5.4	Effect of waveform on opening aperture	49
2.6	Discussion	50
2.6.1	Relationships in slip reduction	50
2.6.2	Additional complexity	52
2.6.3	Fluid flow	55
2.7	Conclusions	55
	Acknowledgements and funding	56
3	Critical fluid injection volumes	57
3.1	Introduction	58
3.1.1	Hydrofracturing and stress gradients	59
3.1.2	Analytical formulation	59
3.1.3	Numerical model	61
3.2	Applications	63
3.2.1	Analog gelatine experiments	63
3.2.2	Magmatic dykes	65
3.2.3	Water injection into stiff rock	65
3.3	Discussion and conclusions	66
	Acknowledgements and funding	68
4	Forecasting magma pathways	69
4.1	Introduction	69
4.2	Model and inversion scheme	72
4.2.1	Concept of the vent forecast scheme	72
4.2.2	Parametric volcano stress model	73
4.2.3	Location of dike nucleation	76
4.2.4	Probabilistic scheme and inversion procedure	77
4.2.5	Explanatory models and forecasts	78
4.3	Results and discussion	78
4.3.1	Application to Campi Flegrei caldera	78
4.3.2	Forward explanatory model for Campi Flegrei	80
4.3.3	Discussion on model assumptions	83
4.3.4	Forecast for Campi Flegrei	84
4.3.5	Explaining non-axisymmetric volcanism	87

Contents

4.3.6	Forecast potential for other calderas	88
4.4	Conclusions	90
	Acknowledgements and funding	91
5	Analog stress inversion	92
5.1	Introduction	93
5.2	Methods	94
5.2.1	Experimental Setup	94
5.2.2	Scaling	97
5.2.3	Numerical Modelling	98
5.2.4	MCMC Scheme	99
5.2.5	Forecasting Approach	99
5.3	Results	101
5.3.1	Experimental Results and Numerical Modelling	101
5.3.2	Parameters sampling	102
5.3.3	Forecasts	102
5.4	Discussion	104
5.5	Conclusions	106
	Acknowledgements and funding	106
6	Unstable sill trajectories	107
6.1	Introduction	107
6.2	Parameters and numerical result	110
6.3	Effects defining the sill's path	111
6.4	Full 3D propagation model	113
6.5	Conclusions	116
6.6	Methods	117
6.6.1	GPS data	117
6.6.2	Definition of K	117
6.6.3	InSAR processing and additional observations	118
6.6.4	InSAR inversions along track	118
6.6.5	Choosing physical parameters	119
6.6.6	Comparison of different effects on stress intensity factors	119
	Acknowledgements and funding	119
7	Summary and discussion	121
7.1	Summary	121
7.2	Discussion	122
7.2.1	Assumptions	123
7.2.2	Comparison to other work	127
7.3	Outlook	129

Supplementary information	130
SI for Chapter 2: Friction on wavy faults	130
SI for Chapter 3: Critical fluid injection volumes	137
SI for Chapter 4: Forecasting magma pathways	139
SI for Chapter 5: Analog stress inversion	147
SI for Chapter 6: Unstable sill trajectories	156
Bibliography	169

List of Figures

1.1	Schematic diagram of fracture features	3
1.2	2D fluid-filled crack shape changes	4
1.3	Effects on dyke paths 2D	6
1.4	Air-filled crack ascent in gelatin	7
1.5	Model of non-planar fracture growth	8
1.6	Fracture growth methods	9
1.7	2D fracture geometries	16
1.8	The stress intensity approximation	17
2.1	Boundary conditions on 2D and 3D shear cracks	27
2.2	Displacement discontinuity convention	29
2.3	3D friction cone approximation	33
2.4	3D displacement discontinuity slip profile	36
2.5	Boundary conditions used for this study	37
2.6	3D planar and wavy fault slip distributions	39
2.7	Shear crack stress intensity factors	41
2.8	2D vs 3D fault slip reduction due waveform	43
2.9	Corrugation orientation effects on the shearing of a fractures walls	44
2.10	Corrugation orientation effect on the volume of slip	46
2.11	Out of plane stress effect on the volume of slip	47
2.12	2D vs 3D reductions in stress intensity factors due to waveform	48
2.13	Waveform and associated lenticular opening apertures on the fault surface	51
2.14	Comparison of slip on an undulating fault to that of a real fault surface	54

List of Figures

3.1	3D stress gradient boundary conditions	60
3.2	Numerical simulation of crack propagation	62
3.3	Comparing critical volumes to analog experiments	64
3.4	Processes that can hinder fracture ascent	67
4.1	Principal stressseses and resulting magma trajectories	75
4.2	Eruptive history of the Campi Flegrei caldera during the last 15 ka	79
4.3	Forward model	82
4.4	Vent forecasts	85
4.5	Explaining asymmetric volcanism	87
4.6	Performance of the unloading model for notable worldwide calderas	89
5.1	Experimental and numerical setup	95
5.2	Summary of inversion and forecast results	103
6.1	Interferogram spanning the sill propagation phase of the 2018 eruption	109
6.2	Simulating the propagation direction of fracture at selected locations	112
6.3	Numerical simulation of the sill propagation	114
6.4	Effects of parameters on the simulated sill path	115
S1	Crack wall displacement comparison, K approximation	134
S2	3D displacement discontinuity stress intensity errors for different meshes	135
S3	Example of meshes used to compute stress intensity errors	136
S4	Numerical error in approximating K for an elliptical crack	138
S5	Probability distributions for model parameters of epoch 1	141
S6	Probability distributions for model parameters of epoch 2	142
S7	Probability distributions for model parameters of epoch 3	143
S8	Covariance distributions	144
S9	Impact of variability of starting depth	145
S10	Parameters projection for the time-varying stress forecast	146
S11	Detailed pictures of the experiments	148
S12	Detailed pictures of the experiments	149
S13	Detailed pictures of the experiments	153
S14	Additional test of the MCMC strategy	154
S15	Vertical GPS movement's from continuous GPS stations GV01, 02 and 04 situated on Sierra Negra's summit	158

List of Figures

S16	Interferograms of Sierra Negra spanning the sill propagation phase of the 2018 eruption	159
S17	Interferograms of Sierra Negra spanning the whole propagation and early eruption phase of the 2018 eruption	161
S18	Magnitude of stress gradients, topographic vs buoyancy	163
S19	Half-space effects on K_I at the upper and lower tips of a dipping penny-shaped crack	164
S20	Profiles used to estimate intrusion geometry	165
S21	Summary of changes in K due to different effects on the sill at Sierra Negra	166
S22	Comparison of K_I around a penny-shaped and elongated penny-shaped crack	167
S23	Forecasting propagation directions along the Bárðarbunga dyke track	168

Abbreviations & Notation

Abbreviations

BEM	Boundary element method
DDM	Displacement discontinuity method
LEFM	Linear elastic fracture mechanics

Symbols

ν	Poisson's ratio	
ρ	Density	$\text{kg}\cdot\text{m}^{-3}$
σ	Stress	Pa
ε	Infinitesimal strain	
$I II III$	Opening, sliding and tearing displacement, local crack-tip coordinates	m
$n_{ss ds}$	Normal, strike-slip and dip-slip displacement, local coordinates	
c/a	Half-length or radius of a crack	m
D	Movement of a dislocation (Burger's vector)	m
E	Young's Modulus	Pa
G	Shear Modulus	Pa
K	Stress intensity factor	$\text{Pa}\cdot\text{m}^{0.5}$
K_c	Fracture toughness	$\text{Pa}\cdot\text{m}^{0.5}$
t	Traction	Pa
u	Displacement	m
V	Volume	m^3
$x y z$	Coordinates	m

Chapter 1

Introduction

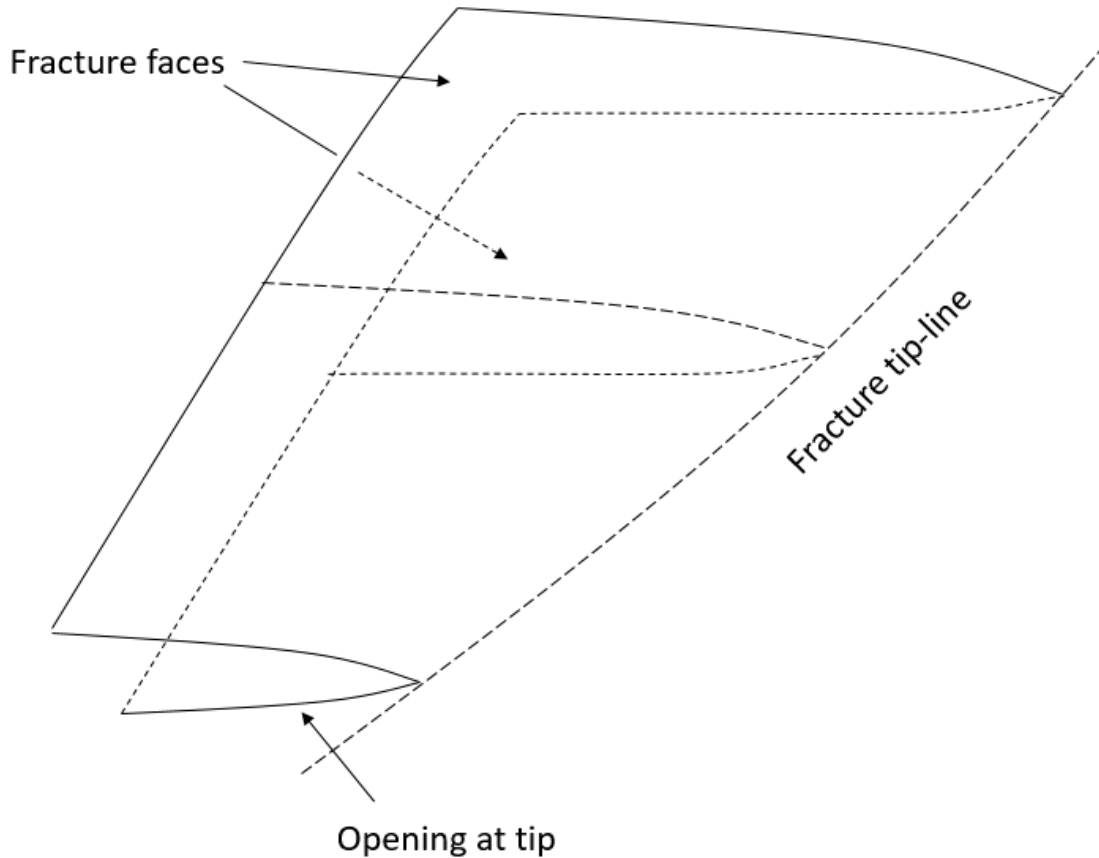
1.1 Motivation

1.1.1 An introduction to fluid-filled fractures

Across a fracture surface a material has been mechanically separated. The opposing surfaces of the material that have been displaced are defined as the ‘faces’ or ‘walls’ of the fracture. At the extremities of the fracture are its tips, at these there is no displacement between the faces of the fracture. The extent of the fracture is defined by a line that circumscribes its tips, this boundary is known as the fracture’s tip-line, see Fig. 1.1. Fracturing is a non-linear irrecoverable process. Fractures grow when the stress at the tips exceeds the material strength, breaking molecular bonds. Once a fracture has been created forcing the fracture walls back into contact will not remove the fracture from the material. Fractures are ubiquitous in nature, existing across multiple length scales, from millimetre aperture veins with lengths of centimetres to meter-wide radial dyke swarms with lengths of hundreds of kilometres (Scholz, 2010). A continuum mechanics framework can be used to formally describe the process of fracturing, as outlined in section 1.4.2. Broadly speaking, the size and shape of the fracture as well as internal and external stresses acting on its faces define how these faces separate. This separation causes intense disruptions in the stress field in the vicinity of the fracture tips, ultimately allowing the fracture to grow. In this work, the focus is on a sub-field of this discipline; fractures that propagate due to a pressurised fluid inside the fracture.

The growth and propagation of fluid-filled fractures encapsulates a number of phenomena related to geosciences: magma transport by dyking (Pollard and Segall, 1987; Dahm, 2000a), drainage of crevasses in melting glaciers e.g. (Weertman, 1973; Veen, 1998), production of veins in hydrothermal systems e.g. (Okamoto and Tsuchiya, 2009; Bons, 2001) and industrial processes that aim to create fractures within a rock mass (Bunger and Detournay, 2007; Warpinski, Branagan, and Wilmer, 1985). Fractures can be described using continuum mechanics models, as widely

Figure 1.1: Schematic diagram of fracture features.

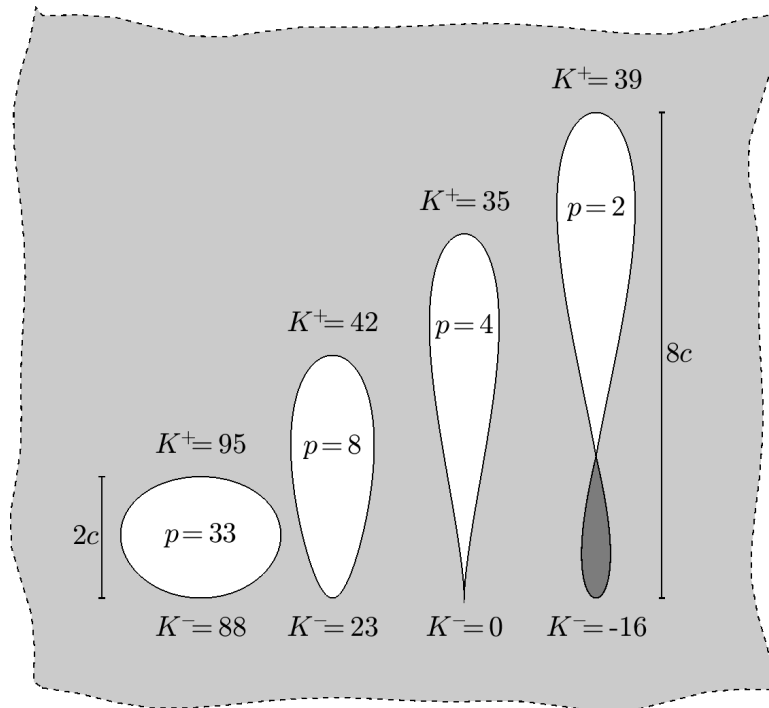


adopted in engineering literature (Tada, Paris, and Irwin, 2000). Such techniques have been applied to model geological phenomena with great success. Concerning the propagation of fractures within stress gradients, many studies in geoscience have been performed in 2D. Many of the factors controlling the path of such fractures are well understood including the influence of the free surface, topographic loading and fluid/rock weight gradients, (Fig. 1.3) (Muller, Ito, and Martel, 2001; Pollard and Segall, 1987; Dahm, 2000a; Maccaferri, Bonafede, and Rivalta, 2011). Note for a fracture to be influenced by a ‘stress gradient’ the stress and fracture must be orientated such that on the faces of the fracture the stress exerts a gradient in traction.

Early studies concerning dyke/sill trajectories postulated that these propagate parallel to the most compressive stress direction (Anderson, 1937). This assumption is relatively accurate and continues to be used despite its simplicity (Muller and Pollard, 1977; Roman and Jaupart, 2014). 2D models of fracturing within a rock mass impose a plane strain boundary condition. Here there is zero strain out

of the plane of interest, defined simply, the fracture has a blade-like form and is of infinite extent in its third plane. Early studies of dykes as elastic fluid-filled cracks with a constant internal pressure were proposed in Anderson (1939), following the seminal work of Inglis (1913).

Figure 1.2: Reproduction of Fig.6 from Weertman (1971a), showing how the cross-sectional shape of a 2D crack with a constant fluid volume (area) changes as its length is extended. An external stress gradient acts on the walls of the crack closing the tail and opening the upper tip. Cross sectional area = $\pi(10^{-4})$, $\mu/(1 - \nu) = 1$, length $c = 37/15$ m and stress gradient = 10^{-6} Pa·m⁻¹. The internal fluid pressure p decreases as this is extended (value at centre of the crack shown in μ Pa). The stress intensity at the upper and lower tip are denoted as K , shown in μ Pa·m^{1/2}. The dark grey portion at the longest fractures tail shows non-physical overlap of the crack walls. Note the horizontal displacements are exaggerated to emphasize changes in geometry.



Geophysical studies later began to integrate new advances from the field of fracture mechanics approximating the stress field around a fractures tip, this concept significantly reduced the complexity of the fracture growth theory (Sneddon, 1946; Irwin, 1957; Williams, 1957). The study of Weertman (1971a) described how the opening distribution of the walls of a pressurised 2D fracture within a stress gradient changes as it is extended, from an elliptical to a teardrop like form (Fig. 1.2). In this study, the stress gradient in question was due to the increasing weight of overlying material with depth, acting due to the internal fluid and the surrounding rock. Secor and Pollard (1975)

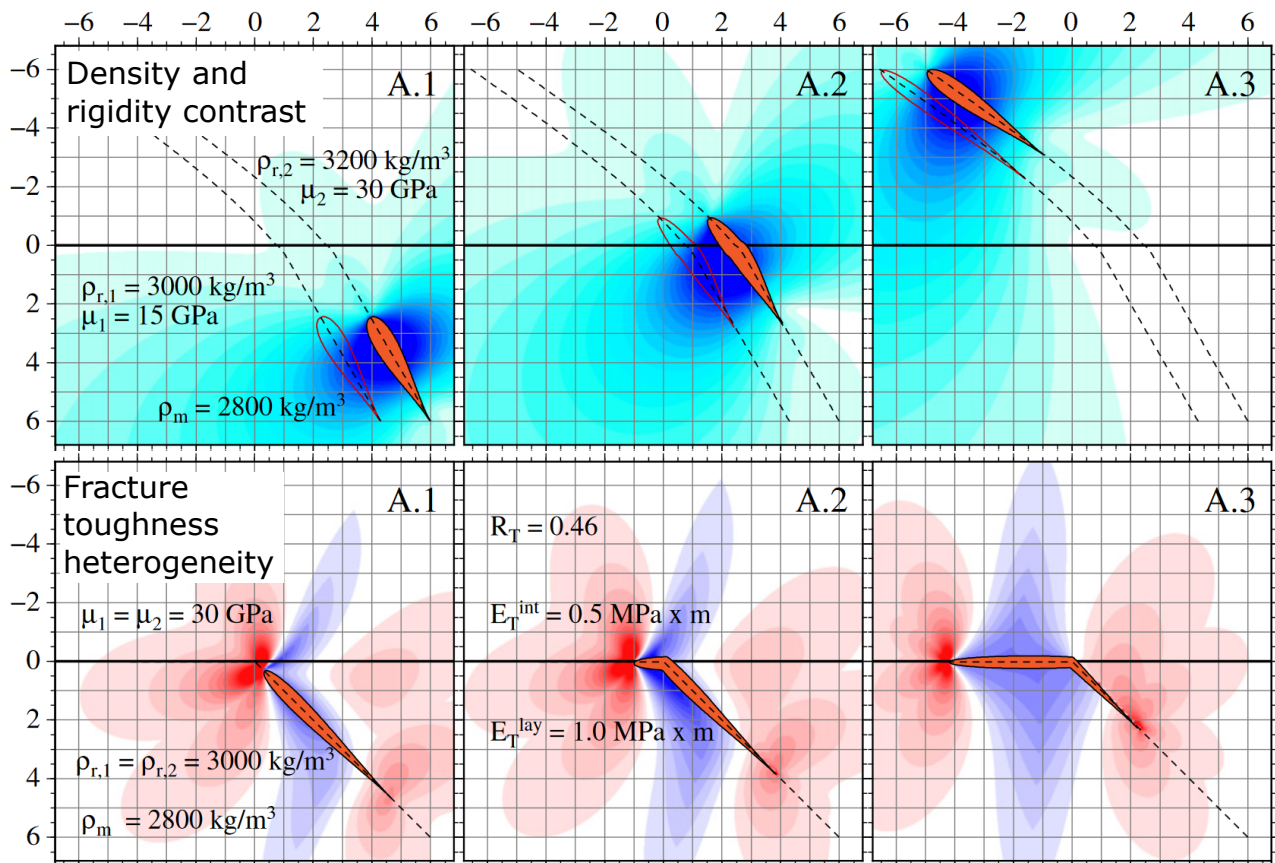
Chapter 1. Introduction

and Pollard and Muller (1976) extended this analysis using Irwin's fracture mechanics concepts, describing both the internal pressure and critical length of a fracture such that the tail pinches shut and the stresses at the upper tip are at the limit of the rock strength. For a formal definition of fracture mechanics see section 1.4.2. It is of note that although fracture apertures are small in rock, the opening distribution still controls the stress intensity that develops at the tip of the fracture, and defines how this will grow.

Novel analog studies showed that air, water, oil and mercury-filled cracks all propagate within a gelatin solid, with a form that fits the theoretical shape described in earlier studies. It was shown that once a given volume of fluid was injected, the fractures were no longer stable and ascended/descended through the gelatin block. These studies also showed how a fractures ascent speed and 3D shape change due to different properties (Takada, 1990; Heimpel and Olson, 1994). Additionally, they showed how the path of these fluid-filled cracks could be deflected by the placement of loads on top of the gelatin blocks. This observation promoted the implementation of numerical techniques, as this process could not be modelled using analytical analysis alone (Muller, Ito, and Martel, 2001; Dahm, 2000a). It is known that topography perturbs near-surface gravity induced stresses, and these studies provided quantitative insights into how this affects the direction of propagating cracks (Savage, Powers, and Swolfs, 1984).

Numerical studies have additionally quantified how elastic interfaces, the free surface and other effects change the trajectories of such cracks, as shown in Fig. 1.3 (Maccaferri, Bonafede, and Rivalta, 2011). Recently, these concepts have also been adapted and applied to explain neo-tectonic observations, showing potential as a method to understand and forecast future dyke paths. Such studies use concepts in earlier publications to understand the 2.5D path of propagating dykes from observations and, as such, can currently only be applied to vertical fractures (dykes) (Sigmundsson et al., 2015). Note that the fracture mechanics models of this process above are all in quasi-static equilibrium (dynamic terms omitted), under the assumption that the process is relatively slow, and that the fluid-flow inside the crack reaches an equilibrium and the fluid maintains a constant internal pressure during propagation. This assumption is discussed in chapter 7. Progress has also been made in modelling fluid-flow inside these fractures both independently, and also more recently, using fully coupled hydro-mechanical models, allowing for such assumptions to be tested (Lister and Kerr, 1991; Nakashima, 1993; Dahm, 2000b; Roper and Lister, 2007; Pinel et al., 2019; Zia and Lecampion, 2020; Salimzadeh, Zimmerman, and Khalili, 2020).

Figure 1.3: Subset of 2D dyke propagation paths from Maccaferri, Bonafede, and Rivalta (2011) with permission from Elsevier. Snapshots of the dyke (orange) path (dotted) are shown from left to right, scales shown are in km. Top row: Interface across which both density and elastic rigidity change, the dyke deflects as it passes through this. Colourmaps show the displacement of the surrounding medium. Bottom row: Halved value of fracture toughness K_c along an interface, here the dyke is trapped as a sill at the interface. Colourmaps show the Coulomb stress change on horizontal planes (red is positive).



1.1.2 Fluid-filled fractures in 3D

In some cases, it is hard to reconcile understanding and observations with the assumption that fluid-filled fracture propagation can be modelled as a 2D process, where the fractures have infinitely long lateral extent. Understanding from theoretical models show that in certain instances propagation is likely to occur out of plane (Townsend, Pollard, and Smith, 2017). Alongside this, neo-tectonic insights show many examples of dykes twisting, segmenting and propagating laterally following ascent (Bagnardi, Amelung, and Poland, 2013; Xu and Jónsson, 2014; Sigmundsson et al., 2015). The relevance of 3D aspects is confirmed by observations of out of plane fluid-filled propagation in gelatin, see Fig. 1.4, where the fracture grows laterally at the interface before breaking through this (Rivalta, Böttlinger, and Dahm, 2005; Urbani, Acocella, and Rivalta, 2018). This contrasts with many assumptions used in 2D propagation models, and are not accounted for in the models such as those shown in Fig. 1.3.

Figure 1.4: Air-filled crack ascent across an interface with a rigidity contrast (upper μ /lower $\mu=5.5$) from (Rivalta, Böttlinger, and Dahm, 2005) with permission from Elsevier. Snapshots of the fracture are shown in alphabetical order, and the scale shown is in cm. For each snapshot the crack is shown from two perpendicular directions. Note that additional air is injected in frames b to d.

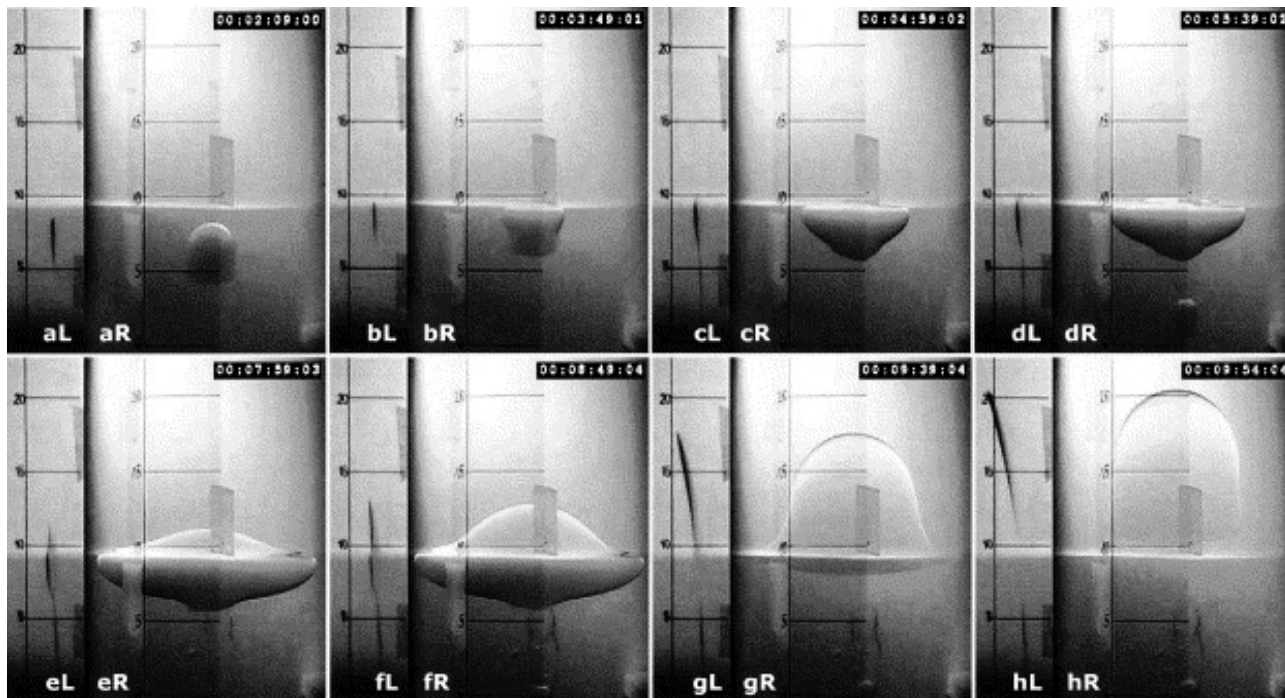
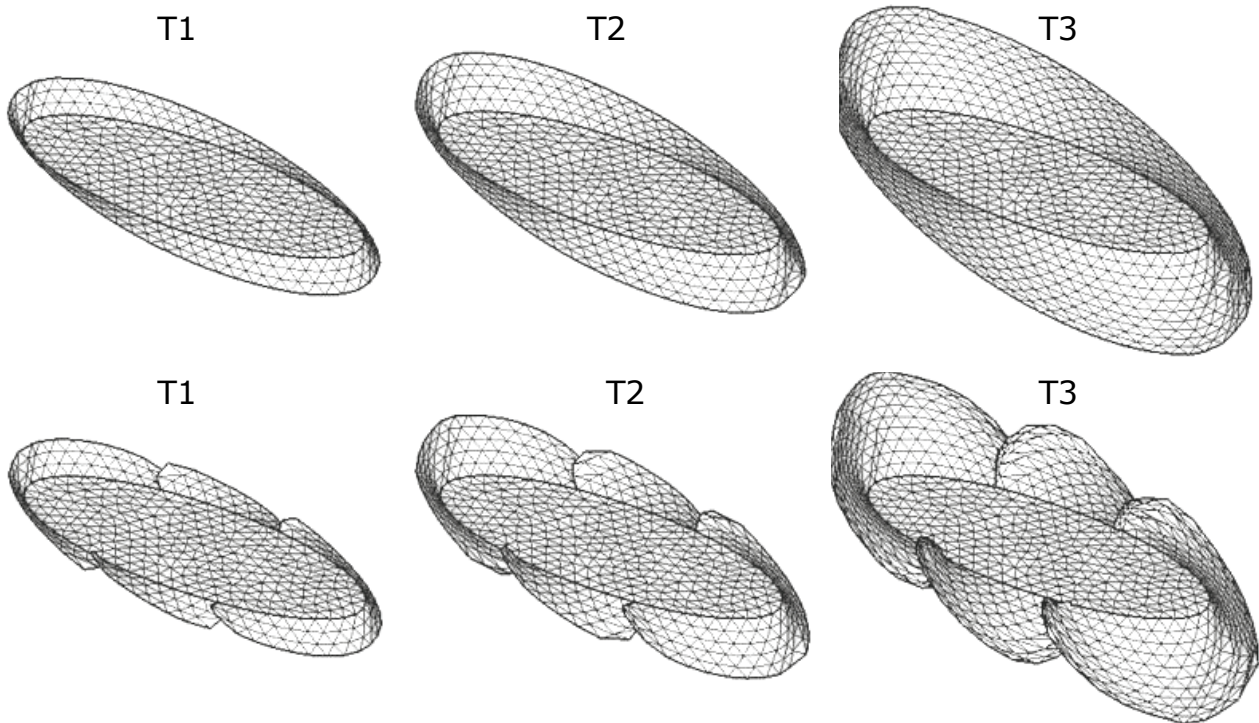


Figure 1.5: Figure from Meng, Maerten, and Pollard (2013) with permission from Springer. This shows an early example of triangular dislocations used to model non-planar fracture propagation. Snapshots of growth shown from left to right. The model in the top row doesn't allow for tip-line segmentation, whereas the model in the bottom row explicitly accounts for this.



A number of studies modelling ground deformation due to dykes and sills have discretised the fractures using triangular dislocations e.g. Cayol et al. (2014) and Smittarello et al. (2019). These studies retrieve reasonable estimates of the evolving fracture shape and internal pressure required to cause the observed deformation pattern at a snapshot in time. Few studies have mechanically modelled the evolution and growth of such fractures in 3D. One convincing example of fracture growth that uses triangular dislocations, as adopted in this thesis, is that of Meng, Maerten, and Pollard (2013). Importantly, this study showed how this discretisation could capture an evolving non-planar fracture shape, Fig. 1.5. This study focussed on growth of fractures in tension, and due to the aims of the study, did not implement a rigorous growth criterion or a scheme to evaluate the mechanics of fracture wall contact, both of which would be useful in extending existing 2D numerical methods of fluid-filled fracture growth to 3D. Little work in 3D has focussed on fluid-filled fracture propagation, with the majority of this focussing on growth time-scales within

industrial hydro-fracturing, for example Bungler and Detournay (2007). How such fractures react to stress gradients or how external stresses control their shape and trajectories as studied extensively in 2D, remains unstudied in 3D.

Figure 1.6: Left: previous numerical 2D growth schemes, the opening of dislocation elements is shown as rectangles (Dahm, 2000a; Maccaferri, Bonafede, and Rivalta, 2011; Sigmundsson et al., 2015). Right: 3D fracture growth described in this thesis, with triangular dislocation elements. In this diagram, blue elements are filled with fluid. In 2D the white elements represent those that interpenetrate, whereas in 3D these are elements that have closed shut.

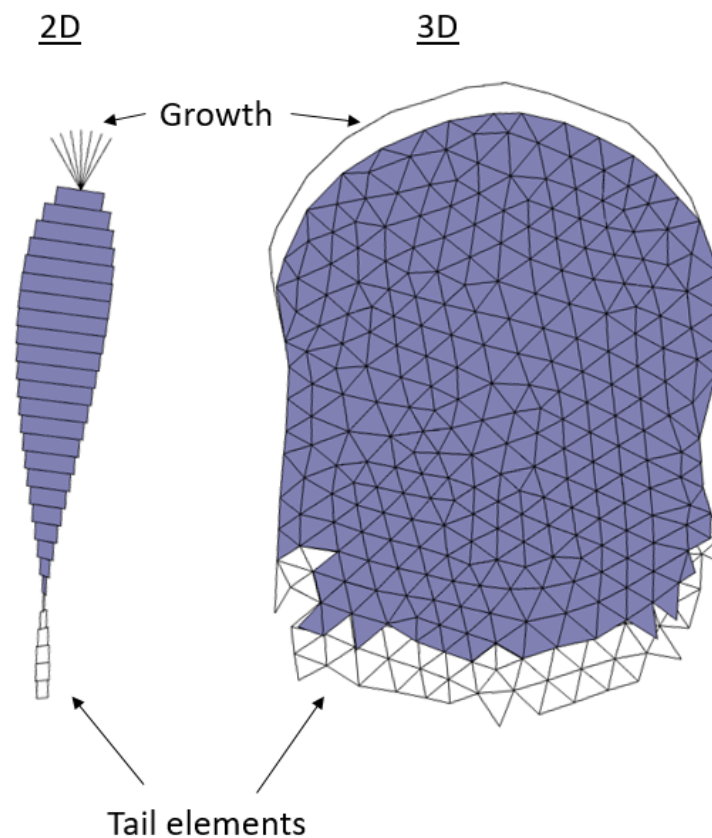


Fig. 1.6 shows the scheme used to model growth and propagation of 2D fluid-filled fractures in Dahm (2000a) and Maccaferri, Bonafede, and Rivalta (2011). In this 2D scheme, when tail elements interpenetrate, one tail segment of the fracture is removed and the opening distribution is recomputed. This process is performed iteratively until there is no interpenetration at the tail of the fracture. A second iterative scheme is then entered, in each iteration a new tip segment is added at a given angle, and the total strain energy induced by the lengthened fracture is then computed. The tip then grows in the direction which exerts the lowest strain energy. It is hard to reconcile how such a scheme can be adapted to model growth of a fracture's tip-line in 3D. This is both because

Chapter 1. Introduction

the number of computations required quickly becomes unwieldy, but additionally, this involves a conceptual problem, as many parts of the 3D tip-line will extend simultaneously. Such growth will result in a change in the fracture's shape, instantaneously changing the stress intensity along the tip-line.

It is therefore hard to extend the existing fluid-filled fracture propagation schemes to 3D. Here I propose an alternative method to perform this in 3D. Using a method that explicitly accounts for frictional contact of the walls stops interpenetration and allows for removal of multiple tail elements at once (Ritz, Mutlu, and Pollard, 2012; Kaven et al., 2012). Once removed, and the fractures opening is known, if the stress intensity around the tip-line can be computed, then the tip-line can be extended by lengths based on the local K magnitude (Peng et al., 2017). Additionally, this removes any need to iteratively search for the next propagation direction of the tip in question, as many schemes exist to compute this based on the ratios of the different modes of K at the fractures tip (see section 1.4.2) (Lazarus et al., 2008). As such, an implementation of frictional contact described above, as well as a method to compute K around the fractures tip-line, will allow for 3D propagation, as shown in Fig. 1.6.

1.2 Objectives

1.2.1 Research goals

Understanding how fluid-filled fractures propagate in 3D is complex, there is a dearth of existing analytical analysis as it is harder to derive such equations, and numerical modelling techniques are only recently powerful enough to tackle this problem efficiently. The goal of the current research is to develop and validate 3D crack propagation models and apply these to outstanding problems in geoscience.

More specifically, the following research objectives are carried out:

- To understand the tipping point, which once exceeded causes fluid-filled fractures to ascend in a 'self-sustaining' manner.
- To perform analysis of the mechanisms controlling magma movements beneath volcanic edifices. Testing whether the techniques I propose can be applied to real world examples, and exploring the additional insights these bring.

Chapter 1. Introduction

- To constrain the state of stress in volcanic regions using physical models describing trajectories of magma migration.

To tackle these problems the following solutions are required:

- To use, adapt and manipulate existing 2D analytical formulas describing critical crack lengths to 3D.
- To adopt the use of triangular dislocations within a 3D boundary element code, to simulate non-planar fracture geometries with a continuous fracture tip-line.
- To efficiently apply a criterion describing fracture growth within such 3D models. The resulting fracture propagation model must be able to handle growth of the fracture tip-line and closure of the fracture's walls.
- Application of the 3D numerical scheme to understand the extent to which analytical formulations can be used to provide insight into fluid-filled fracture propagation.
- Adoption and integration of techniques to model stresses within and beneath volcanic topography.

1.2.2 Thesis outline

A summary of how each chapter tackles the research objectives is provided below.

- Chapter 2: Details the boundary element method using triangular dislocations, with proof of its ability to model non-planar geometries. A non-linear numerical scheme is described in detail that can solve for contact and friction problems at closed dislocations. Lastly, a way of approximating the three modes of stress intensity around a fractures tips is derived, described and its accuracy is explicitly quantified.
- Chapter 3: Describes in detail how to perform 3D propagation simulations: a numerical scheme that includes re-meshing, tip-line growth and closure of tail elements is outlined. 2D analytical formulas describing critically stressed cracks are adapted to 3D with focus on the internal fluid volume.

Chapter 1. Introduction

- Chapter 4: This chapter describes a novel statistical scheme to invert for stresses in volcanic regions based on the locations of monogenetic vents. It focusses on the case study of the Campi Flegrei volcanic field, retrieving topographic and tectonic stress ratios. This provides an explanation of the inward migration of volcanism over time within the caldera.
- Chapter 5: This improves upon and tests the technique introduced in chapter 4, evaluating how effective this is in retrieving the stress field and forecasting ‘vent’ locations in controlled analytical experiments.
- Chapter 6: Extends the 3D simulation technique so the fractures can twist out of plane, the possibility to incorporate free surface effects is also detailed. Simple analytical analysis along with more complex numerical analysis is applied to understand mechanisms that caused the InSAR observations of a long curved sill trajectory at Sierra Negra in the Galápagos islands. This explicitly shows how to apply techniques described in this thesis to gain insight into the mechanics of neo-tectonic observations.

1.3 Publications and authors contribution

I now list the articles that have been published during this research.

1.3.1 Published articles

- Chapter 2: **Davis, T.**, Healy, D. and Rivalta, E., 2019. Slip on wavy frictional faults: Is the 3rd dimension a sticking point? *Journal of Structural Geology*, 119, pp.33-49. <https://doi.org/10.1016/j.jsg.2018.11.009>
T. Davis wrote the first draft, implemented the numerical method, derived the approximation of K and performed the analysis in this manuscript.
- Chapter 3: **Davis, T.**, Rivalta, E., Dahm, T. (2020): Critical fluid injection volumes for uncontrolled fracture ascent. *Geophysical Research Letters*, 47, 14, e2020GL087774. <https://doi.org/10.1029/2020GL087774>
T. Davis implemented the numerical method, as well as performing the analytical derivation, figure creation and first manuscript draft.

Chapter 1. Introduction

- Chapter 4. Rivalta, E., Corbi, F., Passarelli, L., Acocella, V., **Davis, T.**, Di Vito, M. A. (2019): Stress inversions to forecast magma pathways and eruptive vent location. *Science Advances*, 5, 7, eaau9784. <https://doi.org/10.1126/sciadv.aau9784>
T. Davis helped to develop the statistical concepts in this manuscript and provided insights into the structural evolution of the area.
- **Not included as a chapter in this thesis.** Cesca, S., Malebrán, C V., López-Comino., J Á., **Davis, T.**, Tassara, C., Oncken, O., Dahm, T. (2021): The 2014 Juan Fernández microplate earthquake doublet: Evidence for large thrust faulting driven by microplate rotation. *Tectonophysics*, 801. <https://doi.org/10.1016/j.tecto.2021.228720>
T. Davis worked on the text and performed the Coulomb stress analysis in this study.

1.3.2 Submitted/in revision articles

- Chapter 5. Mantiloni, L., **Davis, T.**, Gaete Rojas, A., Rivalta, E., (**submitted** to GRL: 17/Aug/2020). Stress inversion in a gelatin block: testing eruptive vent location forecasts with analog models. <https://doi.org/10.1002/essoar.10504091.1>
T. Davis helped with concepts, created the numerical code used and wrote the original scripts to predict the trajectories of the dykes in a gelatin box.
- Chapter 6: **Davis, T.**, Bagnardi, M., Lundgren, P., Rivalta, E. (**submitted** to Nature Geoscience: 3/Nov/2020): Extreme curvature of shallow magma pathways controlled by competing stresses. <https://doi.org/10.31223/X5FK56>
T. Davis and Dr. E. Rivalta conceptualised and implemented the mechanical analysis in this study.

Appendices are included, for any associated supplementary files, see the published texts.

1.3.3 Published code

- MATLAB boundary element code: "CutAndDisplace" <https://doi.org/10.5281/zenodo.3694163>

1.4 Theory

1.4.1 General linear elasticity

The field of fracture mechanics is well established and is routinely used in engineering analysis. It has been shown that the local stresses at the tip of a crack control the process of crack growth. Basic fracture mechanics relies on linear elasticity where stress linearly relates to strain. Infinitesimal strain in 2D can be defined as

$$\begin{bmatrix} \frac{\delta u_x}{\delta x} & \frac{1}{2} \left(\frac{\delta u_y}{\delta x} + \frac{\delta u_x}{\delta y} \right) \\ \frac{1}{2} \left(\frac{\delta u_y}{\delta x} + \frac{\delta u_x}{\delta y} \right) & \frac{\delta u_y}{\delta y} \end{bmatrix} = \begin{bmatrix} \varepsilon_{xx} & \varepsilon_{xy} \\ \varepsilon_{yx} & \varepsilon_{yy} \end{bmatrix} \quad (1.1)$$

where u_x is the displacement in the x direction from coordinate x , and partial derivative $\frac{\delta u_x}{\delta x}$ is the extension of an element over its original length. Note that infinitesimal rotations have not been included here as these do not contribute to the strain field. It is obvious how the 2D definition of strain in Eq. 1.1 can be extended to 3D with a 3x3 matrix that includes z components. Following from this definition of strain, the linear stress to strain relationships in 3D are:

$$\begin{aligned} \varepsilon_{xx} &= \frac{1}{E} [\sigma_{xx} - \nu(\sigma_{yy} + \sigma_{zz})] \\ \varepsilon_{yy} &= \frac{1}{E} [\sigma_{yy} - \nu(\sigma_{zz} + \sigma_{xx})] \\ \varepsilon_{zz} &= \frac{1}{E} [\sigma_{zz} - \nu(\sigma_{xx} + \sigma_{yy})] \\ \varepsilon_{xy} &= \frac{1 + \nu}{E} \sigma_{xy} \\ \varepsilon_{xz} &= \frac{1 + \nu}{E} \sigma_{xz} \\ \varepsilon_{yz} &= \frac{1 + \nu}{E} \sigma_{yz} \end{aligned} \quad (1.2)$$

where subscripts use an ‘on-in’ convention, i.e. for xy , the stress or strain acts on planes with normals aligned with the x -axis, acting in a direction aligned with the y -axis. ε is the infinitesimal strain as defined above and σ the force per unit area (stress). E and ν are material constants. E , the Young’s modulus, is the change in stress divided by the corresponding shortening/extension in the direction the force is applied. ν is the Poisson’s ratio, the shortening/extension in the perpendicular direction to the applied stress divided by the shortening/extension in the direction the force was applied (Pollard and Fletcher, 2005).

1.4.2 Linear Elastic Fracture Mechanics

Linear Elastic Fracture Mechanics (LEFM) is used for problems concerning the growth of fractures. Pioneering studies, showed that the stress concentration at the tips of fractures is infinite, but that the strength of this singularity is directly related to the square root of the fracture length and the far field stress (Inglis, 1913; Griffith, 1921; Griffith, 1924; Westergaard, 1939). It was also shown that a measurable set of material properties controls the rate of crack extension. Later, studies showed how to approximate the stress distribution at a fracture's tip, using local crack tip coordinates (Sneddon, 1946; Irwin, 1957; Williams, 1957). This is important as the stress due to the traction free faces close to the tip, dominate the stress field in this location. Although this was initially derived for 2D line cracks in tension (Fig. 1.8), it was shown that solutions describing the local crack tip stresses are valid regardless of the boundary conditions. This is provided that the cracks faces are free from stress in the vicinity of the crack tip and no additional changes to the boundary conditions or crack shape occur in this location. The crack shape and loading conditions only effect the intensity of this local stress field. The plane strain approximation of the tip stress distribution is also accurate for 3D geometries at distances close to the crack tip. Irwin (1957) demonstrated how tip stresses (K) relate to strain energy (\mathcal{G}) in plane strain and plane stress configurations. \mathcal{G} here is the energy exchange associated with a unit extension of a crack, i.e. the force required to cause crack extension. In Irwin (1958) K was formalised as a value that describes the stress magnitudes at a fracture's tip and the different modes of K were introduced (I , II and III). For opening mode fractures in plane strain the relationship between K and \mathcal{G} can be written as (Tada, Paris, and Irwin, 2000):

$$K_I = \sqrt{\frac{\mathcal{G}_I E'}{1 - \nu^2}} \quad (1.3)$$

Two examples are now provided to show how K changes due to the crack geometry and loading stresses. K_I for a line crack of length c loaded by a constant remote stress/pressure (σ) perpendicular to the walls of the fracture (Fig. 1.7a), is defined as (Tada, Paris, and Irwin, 2000):

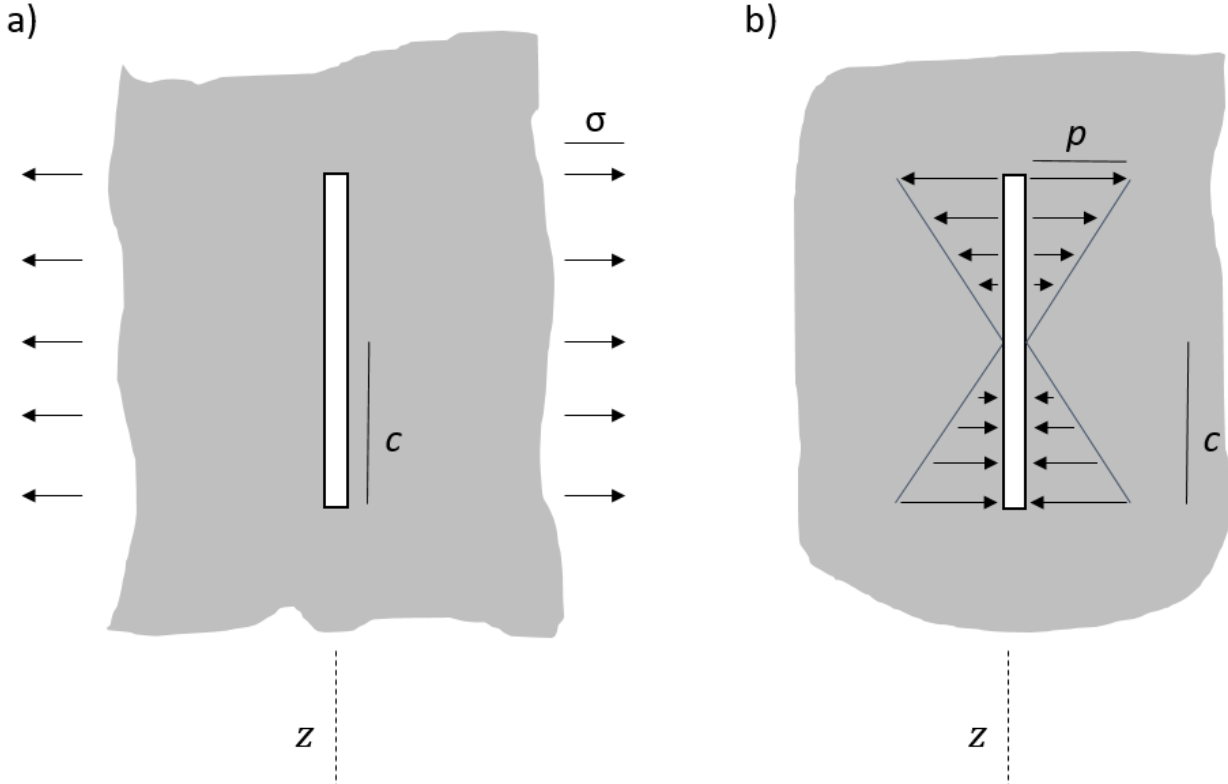
$$K_I = \sigma \sqrt{\pi c} \quad (1.4)$$

and for a crack under a linear stress gradient which is zero at the crack's centre, magnitude $-p$ at one tip and p at the opposing tip (Fig. 1.7b), is (Tada, Paris, and Irwin, 2000):

$$K_I^\pm = \pm 0.5p\sqrt{\pi c} \quad (1.5)$$

Summation of Eq. 1.4 and 1.5 can be used to describe stresses at the tips of fluid-filled fractures, like shown in Fig. 1.2.

Figure 1.7: 2D fracture loaded by a) uniform remote stress (or internal pressure) σ , b) a linear stress gradient p .

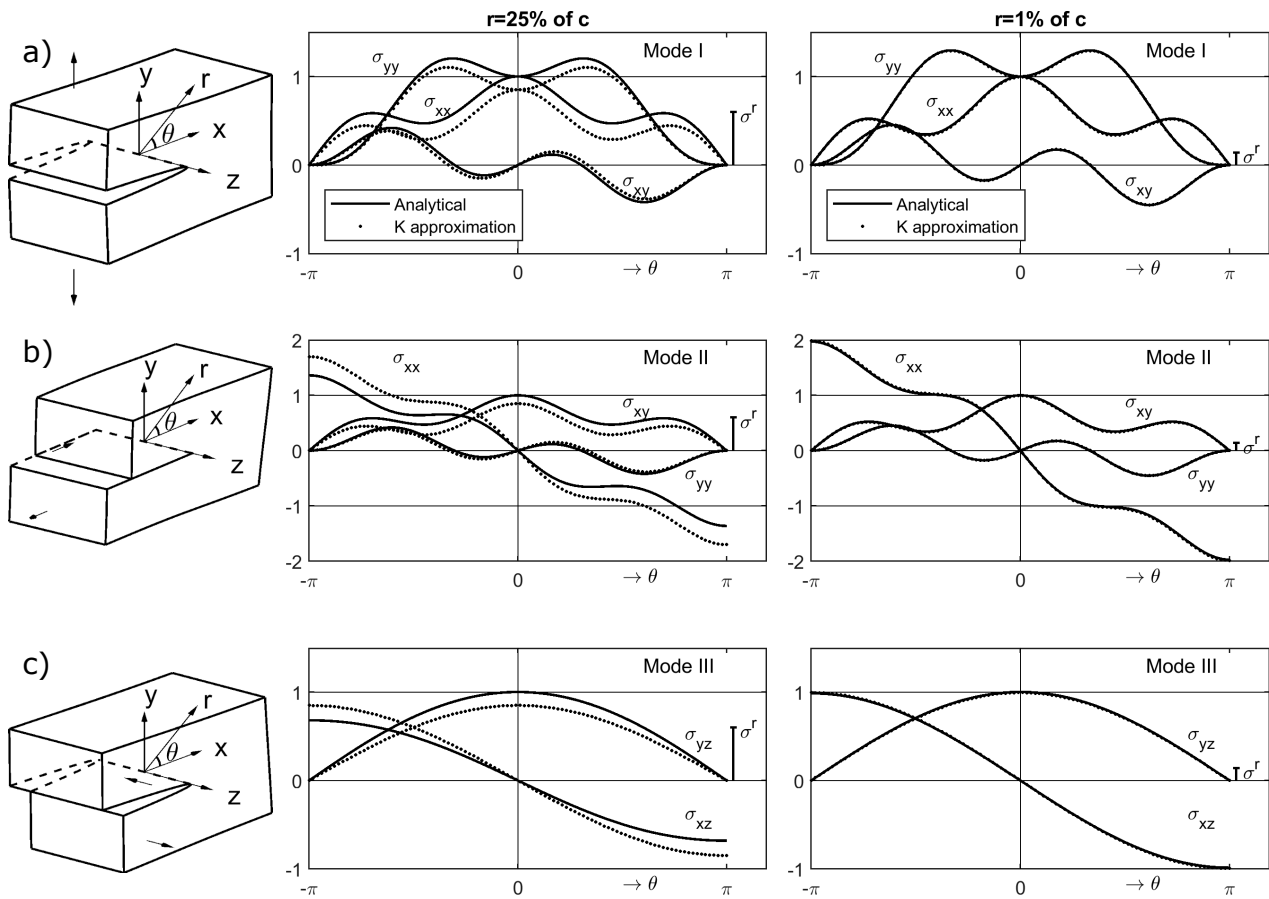


The different modes introduced in Irwin (1958) are a set of classes that describe how the fracture's faces at the tip move in relation to one another, Fig. 1.8. As the medium is a linear elastic, the results from these different modes can simply be summed. Here I introduce a local crack-tip coordinate system; the crack lies along the x -axis, with θ the angle away from the x -axis and r the radial distance from the crack tip, Fig. 1.8 (Pollard and Fletcher, 2005, p.372). Once K for a given geometry and loading is known, the plane strain stress distribution when the surfaces at the tip of the crack separate (opening or mode I , Fig. 1.8a), can be written succinctly as (Tada, Paris, and Irwin, 2000):

$$\begin{Bmatrix} \sigma_{xx} \\ \sigma_{yy} \\ \sigma_{xy} \end{Bmatrix} = \frac{K_I}{\sqrt{2\pi r}} \begin{Bmatrix} \cos(\theta/2)(1 - \sin(\theta/2) \sin(3\theta/2)) \\ \cos(\theta/2)(1 + \sin(\theta/2) \sin(3\theta/2)) \\ \sin(\theta/2) \cos(\theta/2) \cos(3\theta/2) \end{Bmatrix} \quad (1.6)$$

Assuming a flat-lying crack, when the upper fracture surface moves towards the tip of the crack and

Figure 1.8: Variation of stress tensor components relative to angle θ at the tip of a line crack. Each row shows a different mode of fracture tip displacement, as shown in the left column (Pollard and Fletcher, 2005, p.372). Stresses are shown at a given radial distance from the crack tip: $0.25c$ (left graphs) and $0.01c$ (right graphs), where c is the crack half-length. The analytical solution is that of a line crack under constant remote stress, as detailed in Pollard and Segall (1987), is shown as lines. The remote stress σ^r is included in these plotted components, and is biaxial for the mode I crack. The stress intensity approximation for this geometry is shown as dots (Tada, Paris, and Irwin, 2000). These graphs show the approximate stress distribution from Eqs. 1.6:1.8 converges towards the analytical result as the crack tip is approached.



the lower away from this (shearing or mode *II*, Fig. 1.8b), these stresses are:

$$\begin{Bmatrix} \sigma_{xx} \\ \sigma_{yy} \\ \sigma_{xy} \end{Bmatrix} = \frac{K_{II}}{\sqrt{2\pi r}} \begin{Bmatrix} -\sin(\theta/2)(2 + \cos(\theta/2) \cos(3\theta/2)) \\ \sin(\theta/2)(\cos(\theta/2) \cos(3\theta/2)) \\ \cos(\theta/2)(1 - \sin(\theta/2) \sin(3\theta/2)) \end{Bmatrix} \quad (1.7)$$

and when the upper and lower surface both move parallel to the tip-line but displace in opposite directions (tearing or mode *III*, Fig. 1.8c), the stresses at the tip are:

$$\begin{Bmatrix} \sigma_{xz} \\ \sigma_{yz} \end{Bmatrix} = \frac{K_{III}}{\sqrt{2\pi r}} \begin{Bmatrix} -\sin(\theta/2) \\ \cos(\theta/2) \end{Bmatrix} \quad (1.8)$$

In these equations only the magnitude of the stress distributions are dependant on the value of K . In a strict mathematical sense, K describes the strength of the stress singularity at the tip. Fig. 1.8 shows that as the crack tip is approached, the approximations of stresses at the fracture tip outlined above converge towards the values described by complete stress solutions (Pollard and Segall, 1987). The error associated with the approximation will change with the crack geometry and boundary condition, but will always decrease to zero as the tip is approached. It is clear that the stresses at the tips of cracks are asymptotic in relation to the radial distance from the tip i.e. the stresses are infinite at the tip itself. As shown in Eq. 1.4/1.5, all the information pertaining to the size and shape of the crack, as well as the stresses loading this, are wrapped inside the stress intensity factor K . In reality, materials cannot sustain infinite stresses and process zones around the fracture's tip will redistribute stress allowing the fracture to remain stable. Once a given material threshold is exceeded (K_c), micro-cracks and voids in the tip zone rapidly coalesce, causing the fracture tip to grow (Tada, Paris, and Irwin, 2000).

As K can be computed for known geometries, material properties such as fracture toughness K_c , can be determined empirically by comparing these formulations to controlled experiments in a laboratory (Atkinson and Meredith, 1987a). It is of note that extensive lists of equations exist describing the magnitudes of K for different geometries and loading conditions, which are widely available in handbooks e.g. Tada, Paris, and Irwin (2000) and Murakami et al. (1987).

1.4.3 Analytical and numerical solutions to LEFM problems

There are two ways to solve LEFM problems: the first, analytical methods, solve elastic boundary problems mathematically. Such solutions are constrained to the simplest of geometries and boundary conditions. Due to mathematical constraints, such solutions are typically plane strain,

Chapter 1. Introduction

either in Cartesian coordinates ($\sigma_{zz} = \nu(\sigma_{xx} + \sigma_{yy})$) or cylindrical coordinates ($\sigma_{zz} = \nu(\sigma_{rr} + \sigma_{\theta\theta})$), but this is not a requirement. As described above, the stresses and displacements around a 2D line crack loaded by a remote stress formed the basis of LEFM theory (Westergaard, 1939), with the solutions of penny-shaped cracks loaded in tension and shear allowing for the introduction of different modes of crack tip displacement (Sneddon, 1946). An additional solution important to this work, in the context of the numerical method, is the analytical solution of a constant displacement dislocation, for an out of plane shear dislocation this is simple to derive from first principles (Weertman and Weertman, 1964). For the 3D fluid-filled crack analysis in this work, analytical solutions describing the displacement and stress intensities due to 3D cracks, under constant and linear stress gradients are used (Tada, Paris, and Irwin, 2000).

An alternative approach to solving LEFM problems is to use numerical methods. In this work the numerical method adopted is the semi-analytical Displacement Discontinuity Method (DDM), which remains popular in geophysical studies (Crouch and Starfield, 1982). Unlike other numerical methods, Boundary Element Methods (BEM) only require discretisation of the problem along its boundaries. The medium surrounding these is approximated as a continuum with specified material properties, such as a linear elastic. DDM methods (a subclass of BEM's) separate such a problem's boundaries into patches, where each patch is represented by an analytical solution that describes the stress at any distance from the patch due to its walls displacing. A boundary condition (stress and/or displacement) is then applied along the boundary at each patches' face, and a solution is found such that the sum of stress and or displacements due to all patches displacing results in the prescribed condition along the boundary. For planar elements of constant displacement, asymptotic stresses due to singularities at the element's tips cancel at the element's centre, such that stresses can be evaluated here. A detailed evaluation of the method in 2D (plane strain or plane stress) can be found in Crouch and Starfield (1982), with each element in the method represented by the summation of two edge/climb dislocations (Eshelby, 1966). Here a 3D method is used with constant displacement planar patches, for flat boundaries rectangular patches could be used (Okada, 1992). For irregular boundary geometries, triangular patches are required to capture the surface geometry (Thomas, 1993). Recently, analytical solutions for triangular patches that avoid any singularities that arise from the combination of dislocations required to create such patches have been explicitly accounted for, making the method both more accessible and less prone to 'random' errors that arise from certain boundary geometries (Nikkhoo and Walter, 2015). In 2D, various solutions to approximate stress intensity factors with this method exist i.e. Crouch and Starfield (1982), Olson (1991), and Dahm (2000a). The 2D solution described in Crouch and Starfield (1982) and Olson (1991) works with the 'edge' elements that define the tip of a fracture. Once the opening and shearing of the fracture is solved for using the DDM, an analytical solution with both a length and displacement at

its centre that corresponds to that of the tip element, is then used to approximate the stress intensity of the tip in question (Eq.1.4). Olson (1991) provides the following formula:

$$\begin{Bmatrix} K_I \\ K_{II} \end{Bmatrix} = \begin{Bmatrix} D_n \\ D_s \end{Bmatrix} x \frac{\sqrt{\pi} E}{4(1 - \nu^2)\sqrt{c}} \quad (1.9)$$

where c is the elemental half length. Constant x accounts for the error associated with this approximation which was originally reported as $x=0.806$, it was later reported that $x=0.798$ has less error (Olson, 1991; Mériaux and Lister, 2002). In 3D, for planar fractures using rectangular dislocations, this approximation has also been used (Sheibani, Olson, et al., 2013), noting the errors in this approximation of K can reach up to 20% when the fracture's tip-line is not straight.

The ability to approximate K using DDM methods is described as one of the research goals, see section 1.2.1. The DDM method can model frictional contact of a fracture's walls; it is straightforward to apply half-space conditions and the discretisation of fractures is simple, Fig. 1.6 (Crouch and Starfield, 1982; Ritz, Mutlu, and Pollard, 2012; Kaven et al., 2012).

Chapter 2

Friction on wavy faults

The content of this chapter has been published in **Davis, T.**, Healy, D. and Rivalta, E., 2019. Slip on wavy frictional faults: Is the 3rd dimension a sticking point? *Journal of Structural Geology*, 119, pp.33-49.

Abstract

The formulation for the 3D triangular displacement discontinuity boundary element method with frictional constraints is described in detail. Its accuracy in comparison to analytical solutions is then quantified. We show how this can be used to approximate stress intensity factors at the crack tips. Using this method, we go on to quantify how slip is reduced on fault surfaces with topography, where the asperities are approximated as a sinusoidal waveform, i.e. corrugations. We use stress boundary conditions (compressive) orientated such that frictional contacts shear. We show that slip reductions relative to planar faults for 2D line and 3D penny-shaped crack models are comparable within 10% when slip is perpendicular to the corrugations. Using the 3D model, we then show how slip is reduced more when corrugation wavelengths are doubled compared to the reduction due to corrugation alignment with the slip direction. When slip is parallel with the corrugation alignment we show that reducing the out-of-plane stress, from the normal traction acting on the fault when planar to that resolved on a perpendicular plane, has the same effect as halving the length of the corrugation waveform in terms of slip reduction for a given amplitude.

2.1 Introduction

2.1.1 Fault slip profiles

Discontinuities within rock masses such as faults are commonly simplified as broadly planar structures, and relative displacement of the fault faces generates deformation in the surrounding rock. The aim of this paper is to assess the degree to which non-planar fault surfaces influence both the slip (fault parallel) and opening (fault normal) displacements for faults oriented such that they slide in the regional stress field. In the geological literature, an early theoretical treatment of discontinuities in the context of Linear Elastic Fracture Mechanics (LEFM) was outlined by Pollard and Segall (1987). Their text supplies analytical solutions for shearing and opening of the faces of a line crack and the resultant stresses and strains induced in the surrounding material. For these solutions, the medium surrounding the discontinuity is treated as a linear elastic material and the resultant deformation is static, satisfying a uniform stress drop prescribed at the fracture surface. The resultant displacement of the faces is such that these are traction free. Despite the many idealisations, the equations in Pollard and Segall (1987) can be used to gain insight into the slip distribution of faults. A quantitative understanding of fault slip profiles is of interest because:

- Fault slip profiles, combined with fault length scaling relationships, can be used to constrain fault displacement on structures where data is sparse (e.g. Kim and Sanderson (2005), e.g. in the subsurface).
- Slip on non-planar faults may promote local opening (or closing) of fault faces, and such movements can impact fault zone permeability, e.g. Figure 4 of Ritz, Pollard, and Ferris (2015).

Numerical models have shown that several parameters can perturb the slip distributions of fault surfaces away from the simple elliptical profiles described in Pollard and Segall (1987). These are:

- Fault overlap Crider (2001) and Kattenhorn and Pollard (2001).
- Fault corrugations Marshall and Morris (2012), Ritz and Pollard (2012), and Ritz, Pollard, and Ferris (2015).
- Fault tip-line shape Willemse (1997).

- Non-uniform stresses and friction distributions on the fracture surface Cowie and Scholz (1992) and Bürgmann, Pollard, and Martel (1994).

The focus of this paper is to quantify the effects of non-planar fault surfaces on the slip and opening distributions of isolated faults in three dimensions (3D).

2.1.2 Motivation: non-planar faults

In this study, we use the term ‘faults’ for surfaces with shear displacement and the term ‘fractures’ or ‘cracks’ more generally for surfaces with low offset where both opening and/or shear displacement is observed, these terms are common in LFM literature. We focus on metre-scale faults to avoid the additional complexities of gravitational stress gradients, inhomogeneous material interfaces, and damage Ritz, Pollard, and Ferris (2015). Several mechanisms cause the faces of fractures in rock masses to deviate from planar, these can occur both during initial fracture growth, and later, as slip accumulates on the fault surface. Examples of such mechanisms are:

1. Mixed mode fracture propagation during fracture growth, which introduces relatively cohesionless curved or stepped surfaces into the rock as the fracture tip deviates from a planar path as it grows, this has been shown experimentally (e.g. Thomas and Pollard (1993), Cooke and Pollard (1996), and Dyskin et al. (2003) and several numerical criteria exist to evaluate this phenomenon (e.g. Erdogan and Sih (1963), Lazarus et al. (2008), and Baydoun and Fries (2012));
2. Fracture growth by linkage of discontinuities, pores, or inclusions (e.g. Olson and Pollard (1989), Janeiro and Einstein (2010), Huang et al. (2015), and Davis et al. (2017));
3. Roughening of fault walls during shearing (e.g. Renard, Mair, and Gundersen (2012) and Brodsky, Kirkpatrick, and Candela (2016)).
4. Non-uniform stresses and friction distributions on the fracture surface Cowie and Scholz (1992) and Bürgmann, Pollard, and Martel (1994).

For all these mechanisms parts of the fracture surface will evolve geometrically as it shears. Relative to the final direction of shearing mechanisms 1) and 2) should introduce complex steps in the fracture that have a spread of orientations relative to the direction of shearing, dependent on the

boundary conditions driving growth and on the distribution of initial cracks. Assuming the rock is under compression and that the fracture grows by linkage of wing cracks the final fracture will be stepped with steps that are perpendicular to the final direction of shearing (e.g. Yang et al. (2008)). For 3) asperities will be aligned parallel with the shear direction. Note the far field stresses driving shearing of the fractures faces can change over time, relative to the alignment of asperities. It is therefore reasonable to question how deviations from a planar surface affect the evolving fault slip profile as a fault shears and slips. In this study, we idealise fault surface roughness as a smoothly and continuously corrugated sinusoidal waveform. Although this is an oversimplification of the roughness of mm-metre scale fault surfaces, it is a useful end member situation for the evaluation of the effects of roughness (and its orientation), on the resultant slip distributions of faults.

2.1.3 Previous numerical work

The 2D numerical study of Ritz and Pollard (2012) explored how non-planarity affects the resultant slip profiles of fracture surfaces, where non-planarity is modelled as sinusoidal waveforms or ‘corrugations’. As the study of Ritz and Pollard (2012) is 2D, fracture walls shear perpendicular to the asperities on the fracture faces. The boundary conditions are set such that the two principal stresses driving shearing are both compressive, and the ratio between these is calculated empirically, based on the observations of shearing pre-cut fractures from Byerlee (1978). Ritz and Pollard (2012) showed that as the asperity wavelength decreases, or its amplitude increases, mean slip is reduced. The slip distribution deviates significantly from that of a planar fault. Greater complexity of asperity geometry was introduced in the study of Dieterich and Smith (2009) where fault plane topography was modelled as random fractal roughness. This study also models slip on 2D frictional surfaces and the faults satisfy a uniform shear stress drop aligned with the tips of the fault line. The positive shear stress boundary condition used is equivalent to the stress in a body induced by perpendicular inclined tensional and compressional stress of equal magnitude. This boundary condition puts planes of certain orientations into net tension and is unrealistic for a fault under confining crustal conditions. The 3D numerical analysis of Marshall and Morris (2012) examined the net slip for 3D ‘frictionless faults’ driven by a uniaxial compressive stress, typically 45° to the fault surface. Constraints were imposed such that the fault faces do not interpenetrate but frictional resistance itself was not considered. The study states that total scalar seismic moment release is not significantly different between rough and planar faults, but this contrasts strongly with the findings of the 2D study of Ritz and Pollard (2012), which has more physically realistic boundary conditions and includes friction. Therefore, we surmise that an analysis in 2D alone cannot provide insights into the mechanics of slip along the corrugation direction. The aim of the current study is to extend

the comprehensive 2D analysis of Ritz and Pollard (2012) into 3D. We question how the corrugation orientation in relation to the far field stresses affects slip distributions (including openings) of the fault surfaces. Referring to ‘in-plane’ stresses in our 3D model as those in the plane containing both the faults normal and shear vector direction, we also quantify the effect the ‘out-of-plane’ stress has on 3D slip distributions. Using similar boundary conditions to Ritz and Pollard (2012), we also quantify the differences between 2D and 3D analyses of such phenomena when corrugations in 3D are also perpendicular to the slip direction.

2.2 Background

2.2.1 Theoretical background and terminology

As in the study of Pollard and Segall (1987) this study focuses on faults confined within a linear isotropic elastic medium. The material can therefore be described by two elastic constants; here we use Poisson’s ratio (ν) and the shear modulus (G). For planar 2D and 3D faults loaded by a constant shear traction as shown in 2.1, these constants are related to slip in the following manner Pollard and Segall (1987) and Eshelby (1963):

2D line crack, at $L < a$:

$$D_s = \frac{(1 - \nu)t_s}{G} \sqrt{a^2 - L^2}. \quad (2.1)$$

3D penny-shaped crack, at $L < a$:

$$D_s = \frac{4(1 - \nu)at_s}{\pi(2 - \nu)G} \sqrt{1 - \frac{L^2}{a^2}}. \quad (2.2)$$

Eqs. 2.1 and 2.2 supply the displacements D_s of the planar cases of a 2D line crack and 3D penny-shaped crack walls loaded by a constant shear traction t_s . Note this is the displacement of one wall of the crack away from its starting position. The result of these equations is that the faces are free of the shear traction imposed due to the resultant slip, note that we ignore tilting of the crack in this study. Here, a is the radius or half-length of the crack and L is the length from the crack centre to an observation point on the crack wall. We use traction in these equations instead of a remote stress driving slip on the crack for two reasons: 1) this removes the dependence on local coordinate systems and relative fracture orientation, and 2) we can directly input friction into these

equations without the need for coordinate system transformations. For these equations, both in 2D and 3D, lower values of ν and G cause greater slip of the crack walls. Note that the equations for the opening of a line crack are found by simply replacing t_s by t_n in Eq. 2.1. For a penny-shaped crack under a tensile stress the opening displacement and its corresponding stress intensity are found using the line crack equations for this boundary condition and multiplying these by $2/\pi$.

Integrating Eq. 2.1 and applying shell integration to the radially symmetric curve from Eq. 2.2 between the interval 0 to a we can find the total ‘area’ (A) or ‘volume’ (V) of slip of one of the cracks walls. The results are:

2D line crack:

$$A = \frac{\pi(1 - \nu)t_s a^2}{2G}. \quad (2.3)$$

3D penny-shaped crack:

$$V = \frac{8(1 - \nu)t_s a^3}{3(2 - \nu)G}. \quad (2.4)$$

Contextually, Eq. 2.3 is the area under the curve of static slip distributions typically shown for a 2D fracture, e.g. Ritz, Pollard, and Ferris (2015). These terms can also be converted to seismic moment using:

$$M_0 = VG \quad (2.5)$$

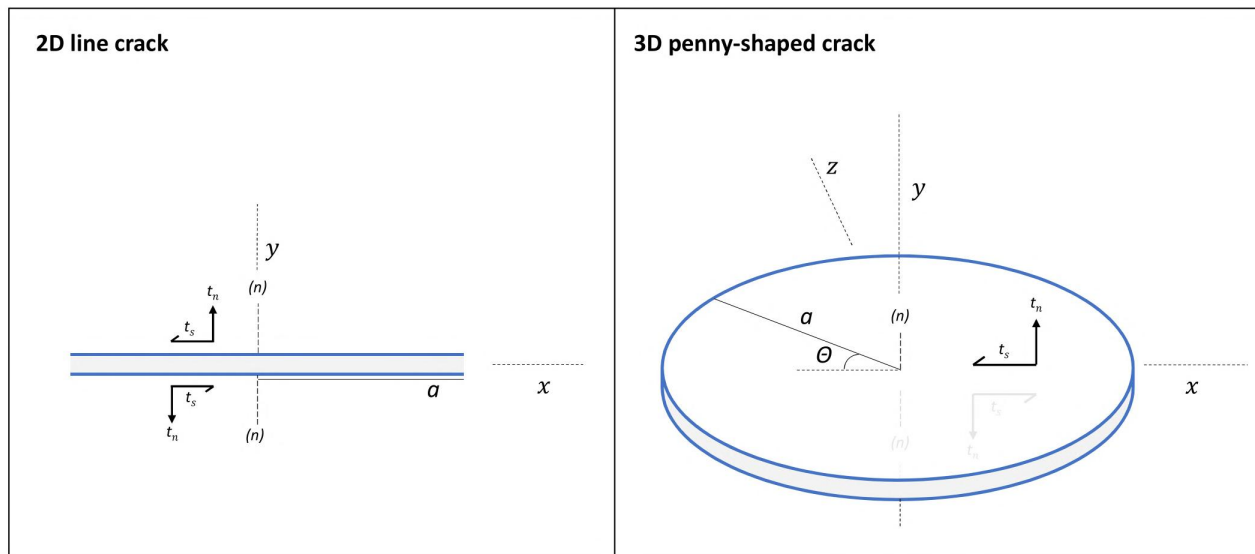
Faults buried in the subsurface will be subject to a non-zero confining stress, depending on depth. A proportion of this force resolves as a compressive force directed along the surfaces normal; resolving the force as a traction we adopt the notation t_n . The normal and shear tractions on the surface can be combined with friction to find the resolved shear traction driving slip on the fault surface Pollard and Fletcher (2005):

$$|t_{s_res}| = |t_s| + \mu t_n - S_f \quad (2.6)$$

The result of Eq. 2.6 can be put into Eqs. 2.1 – 2.4 to find the slip profile of a fault under crustal stress conditions. Eq. 2.6 describes the resultant shear traction t_{s_res} on a plane under compression after the frictional properties, the coefficient of friction (μ) and cohesion (S_f), have been considered. The bars surrounding t_s represent the use of absolute values. We adopt a convention where a

negative value in t_n represents a compressive force. Note that Eq. 2.6 ignores the sign and therefore the relative direction of the input t_s .

Figure 2.1: Geometry and boundary conditions of the elastic boundary-value problem of a line and penny-shaped crack subject to uniform shear or tensile loads. Traction directions are relative to the fractures normal (n) and Θ is the angle away from the direction of shearing. The crack surfaces have been artificially separated (grey area) in order to see its faces and the respective tractions acting on these.



2.2.2 Motivation

Visual examples of fault roughness show it is ubiquitous but varied e.g. Cann et al. (1997), Sagy, Brodsky, and Axen (2007), Jones, Kokkalas, and McCaffrey (2009), Griffith et al. (2010), and Ritz, Pollard, and Ferris (2015). Many previous studies of rough fault surfaces have focussed on the scaling of roughness Resor and Meier (2009) and Candela et al. (2011). Other studies look at how such corrugations deflect slip, at both kilometre fault scales Roberts and Ganas (2000) and locally on the fault surface Kirkpatrick and Brodsky (2014). Recent experimental studies have attempted to model how friction changes with the contact area and development of asperities and shear surfaces (e.g., Harbord et al. (2017)). The aim of such studies is to look at how roughness and pressure change the contact area of the asperities and hence the friction. Fracture geometry and roughness also influences fracture stiffness and has been shown experimentally to control nucleation points

of slip surface displacement Choi, Bobet, and Pyrak-Nolte (2014) and Hedayat, Pyrak-Nolte, and Bobet (2014). Although much of the previous work on rough faults has centred on the roughness itself and the scaling, there has been less work on the mechanics of rough faults, especially in 3D. In this study, a single-scale ‘roughness’ wavelength is used in each model. This neglects roughness below a certain scale, assuming that small-scale asperities and their contact mechanics can be reduced to the mechanical problem of a planar surface with a uniform coefficient of friction, which is the underlying assumption of Coulomb’s friction law Persson (2006). This study therefore focuses on how the larger scale geometrical asperities of a surface, in relation to both the remote stresses and the shearing over these irregularities, inhibits or promotes the sliding of faults.

2.3 Displacement discontinuity method with friction

In this section, we detail the numerical method used to model sliding surfaces with frictional properties. A frictional adaptation of the displacement discontinuity boundary element method (DDM) is employed. Such adaptations in 3D have been described in previous works Kaven et al. (2012). For the sake of clarity in notation and in defining a clear convention we describe the matrix system here.

2.3.1 3D DDM formulation: equations, elements and convention

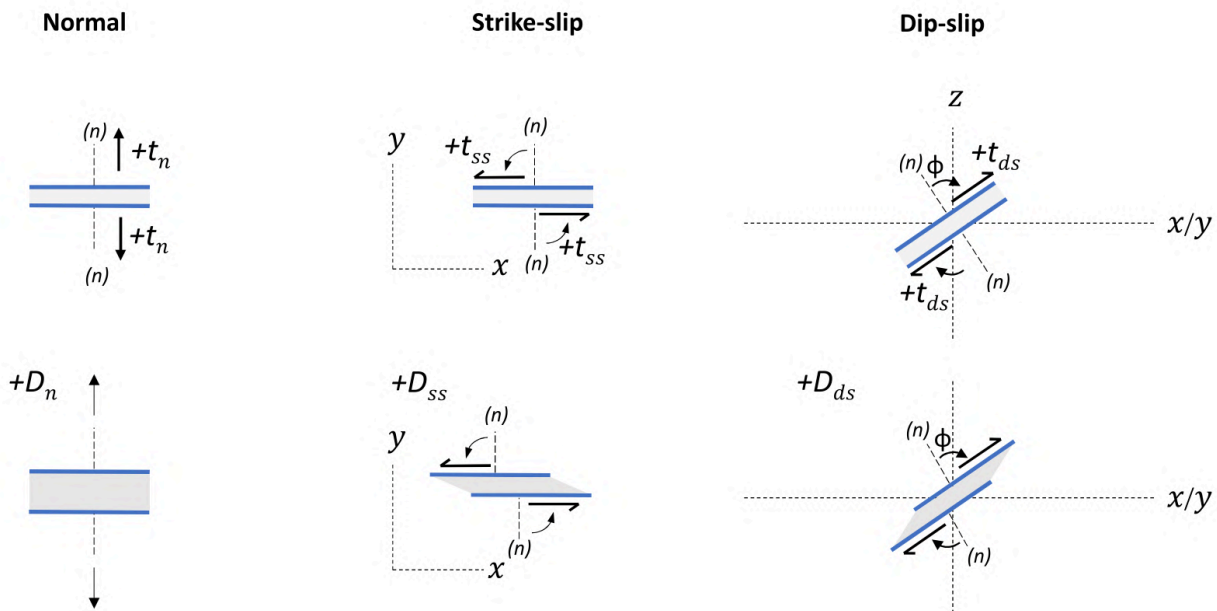
The whole space triangular element formulations of Nikkhoo and Walter (2015) are used as the basic displacement discontinuities in our method. The elements in this publication describe the stress perturbations and displacements in an isotropic linear elastic medium caused by the face of a planar triangle displacing with a constant mirrored movement. In the method, boundaries are meshed as 3D triangulated surfaces, where each face of the mesh acts as a triangular dislocation. Coefficient matrices $[A]$ are built and a vector is supplied that describes the remote stresses resolved as a traction $[t^\infty]$ at each face of the boundary. The displacement discontinuity method in 3D is then solved as:

$$D = -A^{-1}t^\infty \quad (2.7)$$

Expanding Eq. 2.7 for the 3D DDM method the matrix system is as follows:

$$\begin{bmatrix} D_n^i \\ D_{ss}^i \\ D_{ds}^i \end{bmatrix} = \begin{bmatrix} A_{D_n t_n}^{ij} & A_{D_{ss} t_n}^{ij} & A_{D_{ds} t_n}^{ij} \\ A_{D_n t_{ss}}^{ij} & A_{D_{ss} t_{ss}}^{ij} & A_{D_{ds} t_{ss}}^{ij} \\ A_{D_n t_{ds}}^{ij} & A_{D_{ss} t_{ds}}^{ij} & A_{D_{ds} t_{ds}}^{ij} \end{bmatrix}^{-1} \begin{bmatrix} t_n^i \\ t_{ss}^i \\ t_{ds}^i \end{bmatrix} \quad (2.8)$$

Figure 2.2: Positive displacement and traction component convention adopted for the 3D DDM formulation. Traction and discontinuity convention match, positive D_n and t_n are opening and tension respectively. In the xy -plane positive D_{ss} and t_{ss} are left lateral, i.e. along the direction counter-clockwise from the element normal (n). For D_{ds} and t_{ds} positive directions are those where the angle between the normal and the shear direction in question (ϕ) contains the z -axis. For flat triangles the convention of Nikkhoo and Walter (2015) is used, for normal vectors facing upwards, D_{ss} and D_{ds} are positive when shearing south and west, whereas when the normal vector points downward, positive directions face north and west.



In this system, D is a vector containing the movement of each triangles face (i.e. a displacement discontinuity), where subscripts n , ds and ss represent displacement of the faces in the normal, dip-slip, and strike-slip directions respectively. Vector t^∞ represents the remote stress resolved as a traction on the mid-points (geometric incenter) of each triangular face. The sign of A is flipped as we have adopted the same sign convention for the displacement of discontinuities and direction of traction, summarised in Fig. 2.2.

For each sub-matrix of square coefficient matrix A in Eqs. 2.7 and 2.8, the first subscript D represents the displacement of an element with its direction defined by the lower subscripts. The second subscript t represents the traction in the direction of its respective subscript. For example, $A_{D_n t_{ss}}^{ij}$ is a square matrix that describes how much an opening displacement of one unit length at element j effects the strike-slip shear traction on element i . Each column in this matrix is the effect of one element on the mid-point of every other element.

2.3.2 Aims of the DDM solution

In Eqs. 2.7 and 2.8, the aim is to find a static slip distribution that approximates the mid-point of each face of the boundary as traction free (t_n, t_{ss} and $t_{ds} = 0$) under the given remote stress defined in the vector t^∞ on the right-hand side of the equation. Once D is found, DA results in traction vector t^B , which represents the stresses at each mid-point induced by the displacement of the cracks walls. The result of Eq. 2.7 is that t^B and t^∞ should oppose each other resulting in a solution where there is no traction at any triangle mid-point along the meshed boundary:

$$\begin{aligned} 0 &= t_n^B + t_n^\infty \\ 0 &= t_{ss}^B + t_{ss}^\infty \\ 0 &= t_{ds}^B + t_{ds}^\infty \end{aligned} \tag{2.9}$$

2.3.3 DDM formulation with friction

To add frictional constraints to this problem, the system of equations 2.7 and 2.8 is reformulated as a linear complementarity problem Kaven et al. (2012). We use the open source complementarity solver of Niebe and Erleben (2015) implemented in MATLAB. For full details on the accuracy and convergence criterion of the complementarity solver see Niebe and Erleben (2015). For our analysis we have used the default converge criterion of 10 times the numerical precision and the zero Newton equation strategy supplied in the code. Following the notation of Niebe and Erleben (2015) the linear complementarity problem can be stated as:

$$y = ax + b \tag{2.10}$$

In Eq. 2.10 x , y , and b are vectors and a is a square matrix. For this problem, the following constraints are set:

$$x \cdot y = 0 \quad (2.11)$$

$$y \geq 0 \quad (2.12)$$

$$x \geq 0 \quad (2.13)$$

In this formulation vectors x and y are unknowns representing tractions and or displacement discontinuities as the solver progresses. They are created such that each pair of corresponding values in the vectors contains a traction and displacement discontinuity and that the sign convention in vector x is flipped. Vector b is filled with the results from Eq. 2.8, if all displacements are positive according to our convention all constraints are already met, D_n must be positive so the coefficient of friction does not need to be considered. If any displacements in b are negative, then the constraint in Eq. 2.12 is not met and x will begin to fill with opposing with non-zero values. The expanded form of Eq. 2.10 for a 3D DDM problem is:

$$\begin{bmatrix} DF_n^{i+} \\ DF_{ss}^{i+} \\ DF_{ds}^{i+} \\ t_{ss}^{i+} \\ t_{ds}^{i+} \end{bmatrix} = \begin{bmatrix} (C_{D_n t_n}^{ij} - (C_{D_n t_{ss}}^{ij} I \mu^i) - (C_{D_n t_{ds}}^{ij} I \mu^i)) & C_{D_n t_{ss}}^{ij} & C_{D_n t_{ds}}^{ij} & 0 & 0 \\ (C_{D_{ss} t_n}^{ij} - (C_{D_{ss} t_{ss}}^{ij} I \mu^i) - (C_{D_{ss} t_{ds}}^{ij} I \mu^i)) & C_{D_{ss} t_{ss}}^{ij} & C_{D_{ss} t_{ds}}^{ij} & I & 0 \\ (C_{D_{ds} t_n}^{ij} - (C_{D_{ds} t_{ss}}^{ij} I \mu^i) - (C_{D_{ds} t_{ds}}^{ij} I \mu^i)) & C_{D_{ds} t_{ss}}^{ij} & C_{D_{ds} t_{ds}}^{ij} & 0 & I \\ 2I \mu^i & -I & 0 & 0 & 0 \\ 2I \mu^i & 0 & -I & 0 & 0 \end{bmatrix} \begin{bmatrix} t_n^{i-} \\ t_{ss}^{i-} \\ t_{ds}^{i-} \\ DF_{ss}^{i-} \\ DF_{ds}^{i-} \end{bmatrix} \quad (2.14)$$

$$+ \begin{bmatrix} D_n^{i+} - (C_{D_n t_{ss}}^{ij} S_f^i) - (C_{D_n t_{ds}}^{ij} S_f^i) \\ D_{ss}^{i+} - (C_{D_{ss} t_{ss}}^{ij} S_f^i) - (C_{D_{ss} t_{ds}}^{ij} S_f^i) \\ D_{ds}^{i+} - (C_{D_{ds} t_{ss}}^{ij} S_f^i) - (C_{D_{ds} t_{ds}}^{ij} S_f^i) \\ 2S_f^i \\ 2S_f^i \end{bmatrix}$$

Where:

$$\begin{bmatrix} C_{D_n t_n}^{ij} & C_{D_n t_{ss}}^{ij} & C_{D_n t_{ds}}^{ij} \\ C_{D_{ss} t_n}^{ij} & C_{D_{ss} t_{ss}}^{ij} & C_{D_{ss} t_{ds}}^{ij} \\ C_{D_{ds} t_n}^{ij} & C_{D_{ds} t_{ss}}^{ij} & C_{D_{ds} t_{ds}}^{ij} \end{bmatrix} = \begin{bmatrix} A_{D_n t_n}^{ij} & A_{D_{ss} t_n}^{ij} & A_{D_{ds} t_n}^{ij} \\ A_{D_n t_{ss}}^{ij} & A_{D_{ss} t_{ss}}^{ij} & A_{D_{ds} t_{ss}}^{ij} \\ A_{D_n t_{ds}}^{ij} & A_{D_{ss} t_{ds}}^{ij} & A_{D_{ds} t_{ds}}^{ij} \end{bmatrix}^{-1} \quad (2.15)$$

Eq. 2.14 describes the 3D complementarity equation system for friction on fault surfaces in the 3D DDM method. C is the matrix inverse of the collated coefficient matrix A from Eq. 2.8; the sub-matrices of C are extracted as in Eq. 2.15. Matrix C can be described as follows: the summed influence of all elements displacing the amount described in each column of matrix C will cause

a traction of one stress unit, t^B on element i in the direction defined by the subscript. The other traction components at this element and all tractions at every other element will be 0. S_f (the cohesive strength of the material) and μ (the coefficient of friction) are defined as vectors, with one value for each element. I is an identity matrix (a square matrix of zeros with ones on the main-diagonal). DF represents the resultant displacement discontinuities when friction is considered. Values of D in vector b (Eq. 2.14) are the results of Eq. 2.8. Negative superscripts in Eq. 2.14 (vector x) are values with the opposite sign to the convention shown in Fig. 2.2. This means that once solved, positive values in x of Eqs. 2.10 and 2.14 must be flipped in sign so the boundary displacements cause stresses that satisfy Eq. 2.10. The resultant displacement discontinuities at each face are therefore calculated from the results of Eq. 2.10 as:

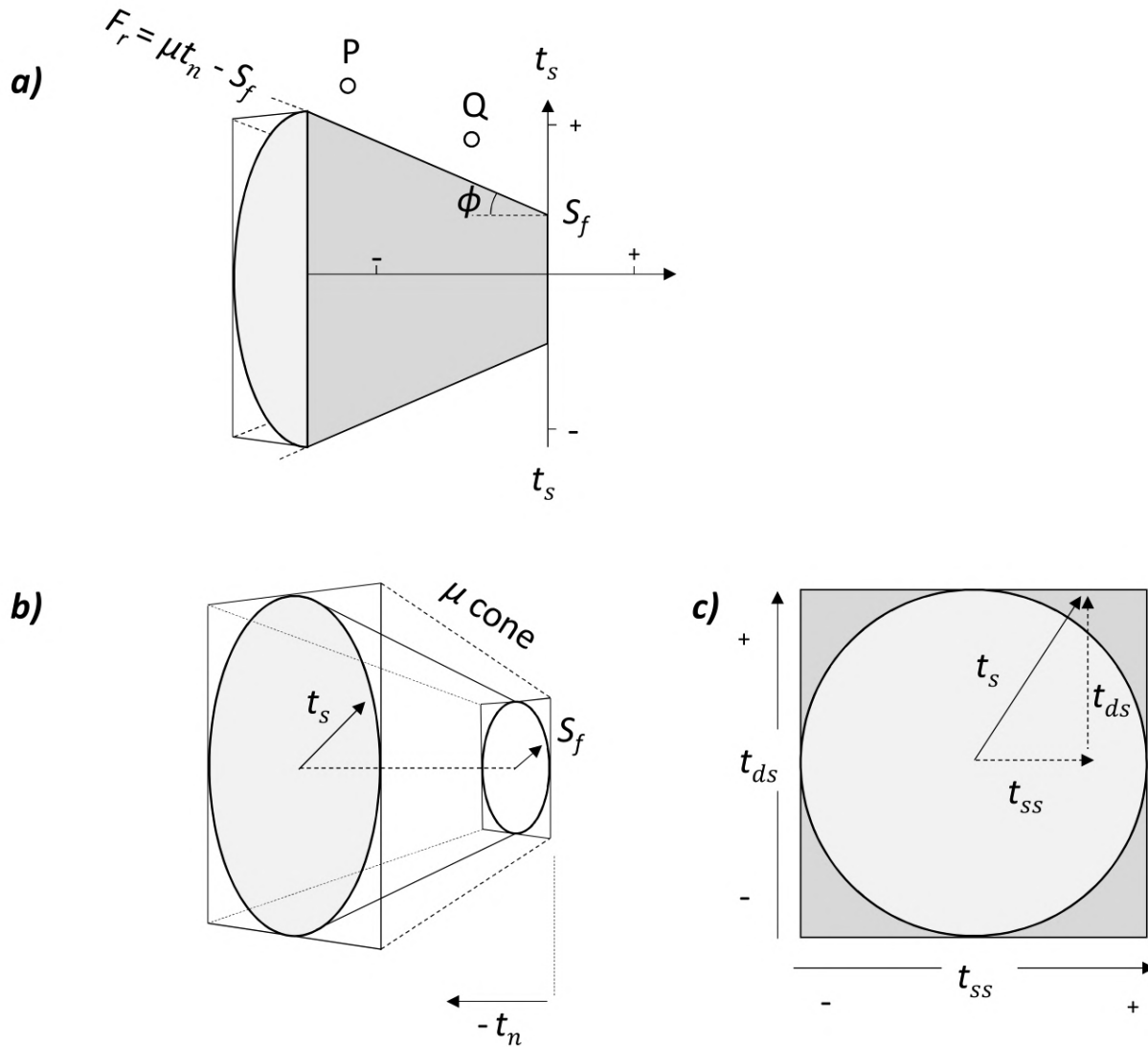
$$D = y - x \quad (2.16)$$

Note, this assumes that the corresponding vectors from x and y are extracted and aligned before this is performed. To stabilise the implementation, matrix conditioning is used. The matrix A in Eq. 2.15 is scaled by a constant before it is inverted. This constant is the mean value of the half-perimeter length of all the triangles divided by the shear modulus. In the 2D code for line elements we use a similar scaling, the mean element half-length divided by the shear modulus, multiplied by 100. The output element displacements of Eq. 2.14 are simply multiplied by this scalar value to find the true displacements. Without this scaling, the solver may fail to converge if both the coordinates and/or driving stresses are not scaled around values close to one. Note that the scaling described here assumes that the elements in the model have similar length scales and shapes.

2.3.4 Aims of the frictional DDM solution

Eqs. 2.8 and 2.14 attempt to reach a solution where all elements are free of t_{s_res} , which is the shear traction calculated using Eq. 2.6, either through shearing or opening of elements. Note that each element only shears if its frictional constraints allow it. The resultant boundary should also be free of tensile tractions defined in vector t^∞ . This solution explicitly factors in changes in the normal or shear traction and the associated frictional resistance due to the displacement of elements in the result as the solver progresses. In the formulation described, the input mesh represents an infinitesimally thin crack with initially coincident faces. To allow given surfaces to interpenetrate in this formulation an arbitrarily large value bigger than the amount needed to close the fracture in the stress field can be added to D_n for the necessary elements vector b in Eq. 2.8/2.14. This

Figure 2.3: A summary of the 3D friction cone used in the numerical calculation. Figure adapted from Kaven et al. (2012) and Niebe (2009)



value is then subtracted from these elements in the outputs of Eq. 2.16. An example use case is modelling both fractures and stresses due to topographic loading, such topographic stresses can be modelled with the BEM as described in Martel and Muller (2000) where elements representing the topography must be able to both open and close. This manipulation also allows for the modelling of initially open fractures, the value added to the vector b in this case would be the fractures initial opening profile.

Fig. 2.3 shows the polygonal frictional approximation as described in Kaven et al. (2012). Fig. 2.3a) shows a cross section through the 3D friction cone; in 2D this takes a form comparable to the typical failure envelope of a Mohr-Coulomb plot. Both points P and Q are the same distance in y from the grey cone, therefore have the same resultant traction driving shearing. Fig. 2.3b) shows a) extended to 3D space. In 3D space, the pyramidal approximation is shown by the dotted lines. In this numerical approximation, the elements with shear tractions large enough to plot outside of the ‘pyramid’ will displace, rather than those that plot inside the cone. Fig. 2.3c) shows an end-on view of the cone shown in b). The approximation overestimates friction for any part of vector t_s that passes through the dark grey area between the pyramidal approximation (square) and the isotropic friction cone (circle). It is clear that this is highest at faces where t_{ds} and t_{ss} are equal. For this situation friction is overestimated by 41% Kaven et al. (2012).

2.4 Benchmarking and model setup

2.4.1 Boundary conditions and shear profile of the crack

This test of the numerical method uses the same boundary conditions, initial geometry, and sampling as the remainder of the analysis in this study.

Fig. 2.5 is a comparison of the numerical result to the slip profile of a penny-shaped crack as described by Eq. 2.2. The geometry of the problem is shown in Fig. 2.5. The stress convention used puts σ_1 as the least compressive stress. The boundary conditions have been chosen such that in the xy -plane these match the empirically defined boundary conditions of Ritz and Pollard (2012). Here we summarise the motivation behind the chosen boundary conditions in Ritz and Pollard (2012), Byerlee (1978) finds that the maximum friction of rocks in the upper crust (normal stress of up to 200 MPa) occurs when $0.85t_n = t_s$. Maximum friction being the point in experiments when the contact between two separate blocks of material suddenly shears. Using the ratio 0.85 as the

coefficient of friction and placing Eq. 9.45 into Eq. 6.55 of Pollard and Fletcher (2005) as the value of ax and rearranging to find the ratio between σ_{xx} and σ_{yy} (treating these as principal stresses by ignoring σ_{xy}) the following equation is found:

$$\frac{\sigma_3}{\sigma_1} = 2 \frac{t_s}{t_n} \sqrt{\left(\frac{t_s}{t_n}\right)^2 + 1} + 2 \left(\frac{t_s}{t_n}\right)^2 + 1 \quad (2.17)$$

For a ratio of t_n to t_s of 0.85 this results in a principal stress ratio of 4.68, Eq. 9.45 of Pollard and Fletcher (2005) supplies the angle of these principal stresses away from the fracture plane, 24.8° . The friction coefficient of the fractures face in our model is set to a value less than 0.85, this takes the fracture surface past failure, allowing it to slip in the defined stress field. We orientate the 3D surface so that its normal points along the y -axis, i.e. an extension of a 2D model. Here Θ is set at 24.8° and is the angle of the normal away from σ_3 . The results supplied in the rest of the analysis are scaled relative to these analytical solutions so are dimensionless and can be scaled as necessary.

For the modelling the following parameters were used: the fault radius (a) was set to 1 metre and σ_1 and σ_3 were set to -50 MPa and -233.8 MPa respectively, adhering to the ratio defined above. When resolved into Cartesian tensor components with the fault plane oriented as above these are: $\sigma_{xx} = -201.5$ MPa, $\sigma_{yy} = -82.3$ MPa and $\sigma_{xy} = -70.0$ MPa. The shear modulus (G) was set at 12 GPa while the Poisson's ratio (ν) was set to 0.25. The frictional properties were as follows: no cohesive strength was imposed and the dimensionless value of μ was set to 0.6 Pollard and Fletcher (2005) and Harbord et al. (2017). For these parameters, the maximum slip from Eq. 2.2 scales with fracture length ($2a$) in a 1:1,000 relationship. Such a scaling lies at the lower end of shear fractures observed in the field Kim and Sanderson (2005).

The analytical solution from Eq. 2.2 is plotted on Fig. 2.4 with the boundary conditions stated above driving slip. The surface is meshed using a grid of points within a circle on the xz -plane that have a spacing of 1/65 m. Points on this grid 0.02 m from the circles edge were removed and equilateral triangles were added to approximate a smooth outer boundary of the crack, see Fig. S3. The overestimation of the crack shear displacement at the tip region of the fracture is $30\% \pm 5\%$ as shown in Fig. 2.4. Note that the angular dependency of error is dependent on the mesh used. In the subsequent analysis, we plot the relative area (or volume) of slip on the fault surface to indicate how it is reduced by the fault geometry. This can be calculated numerically with the 2D and 3D DDM using:

Figure 2.4: Benchmarking of the numerical results against analytical solutions. D_s represents the slip of the penny-shaped crack normalised to the maximum slip value from 2.2. The sampling used is described in the text. c) shows the crack tip elements overestimation of the analytical slip profile in percent vs Θ .

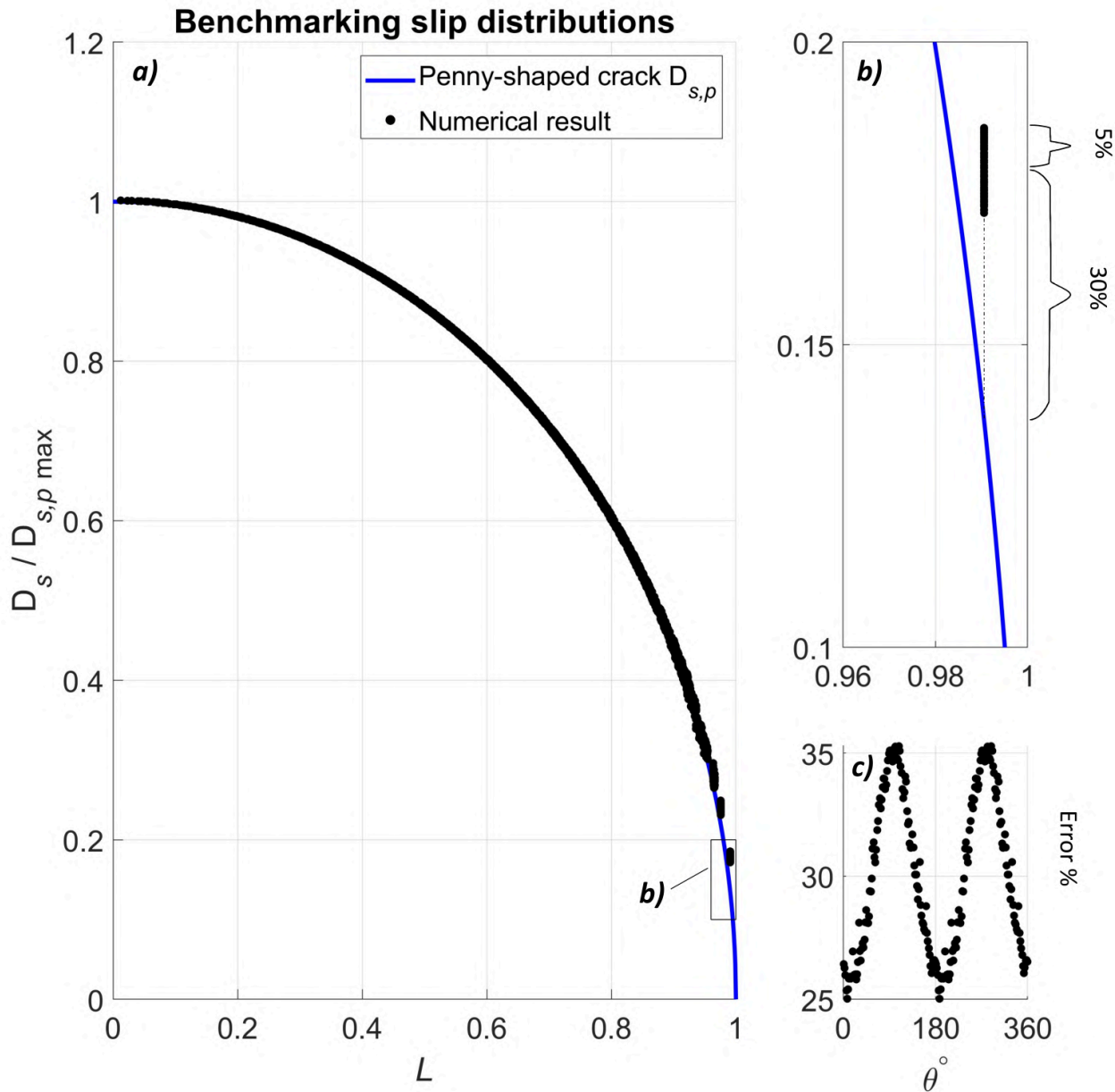
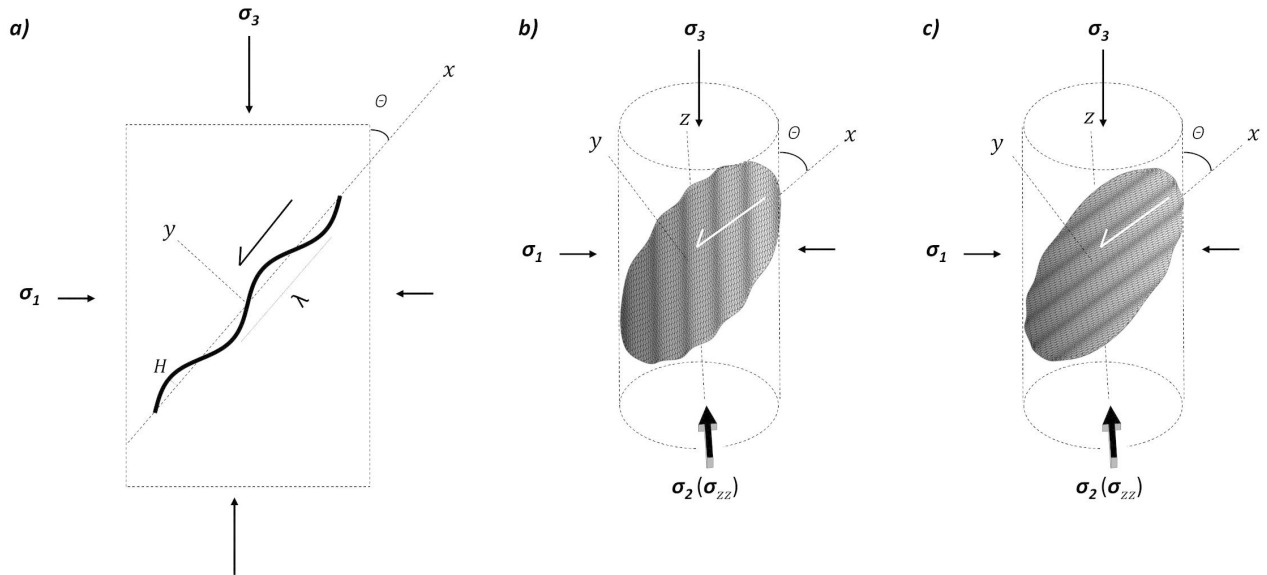


Figure 2.5: a) Boundary conditions used in the numerical analysis that lie in the xy -plane. λ is the wavelength and the amplitude is H . b) Slip direction (white arrow) perpendicular corrugations. c) Slip direction parallel with corrugations. Note that the dashed boundaries are included to highlight the principal stress directions, the fracture surfaces modelled lie within an infinite elastic medium.



2D:

$$A = \frac{\sum(2aD_s)}{\sum 2a} \tag{2.18}$$

3D:

$$V = \frac{\sum(TD_s)}{\sum T} \tag{2.19}$$

Where A and V are the area and volume of slip of the 2D or 3D fracture, respectively. T in Eq. 2.19 is the area of each triangles face and a is the half-length of the 2D elements. D_s is the shear displacement calculated at each element. The following equation is used to evaluate the slip decrease on wavy faults from the reference slip observed for a planar penny-shaped crack:

$$\%A_{reduction} = (100/A_p)(A_p - A_w) \tag{2.20}$$

$$\%V_reduction = (100/V_p)(V_p - V_w) \quad (2.21)$$

where the subscript p is the slip of a planar fault, i.e. Eq. 2.3 and 2.4 and the subscript w that of a wavy fault. Fig. 2.6 shows diagrammatically the slip distribution for a planar and a wavy fault. Eq. 2.21 here would describe the volume between the planar and wavy surfaces.

A second test of the accuracy of the numerical setup in 3D is to calculate how well Eq. 2.19 approximates Eq. 2.4 when the fault is planar. Using Eq. 2.21 this results in a value of 1.08%. The error is deemed acceptable for the current analysis as our results look at levels of slip reduction greater than 1%. This gives an insight into the numerical accuracy of results shown later, where the sampling in 3D described above is used. We have also run our 3D analysis for a mesh as described previously but with half the number of triangles to test how sensitive our results are to sampling. Comparing for the waveform where the observed change in volume and stress intensity reductions is steepest ($H = 1\%$ of a and $\lambda = 25\%$) we see a maximum difference of 1.5% for the stress intensity and volume of slip reductions reported in our results (Fig. 2.8 to Fig. 2.12). Our mesh sampling is therefore deemed high enough to provide stable results at the scales of reduction in these properties that we report.

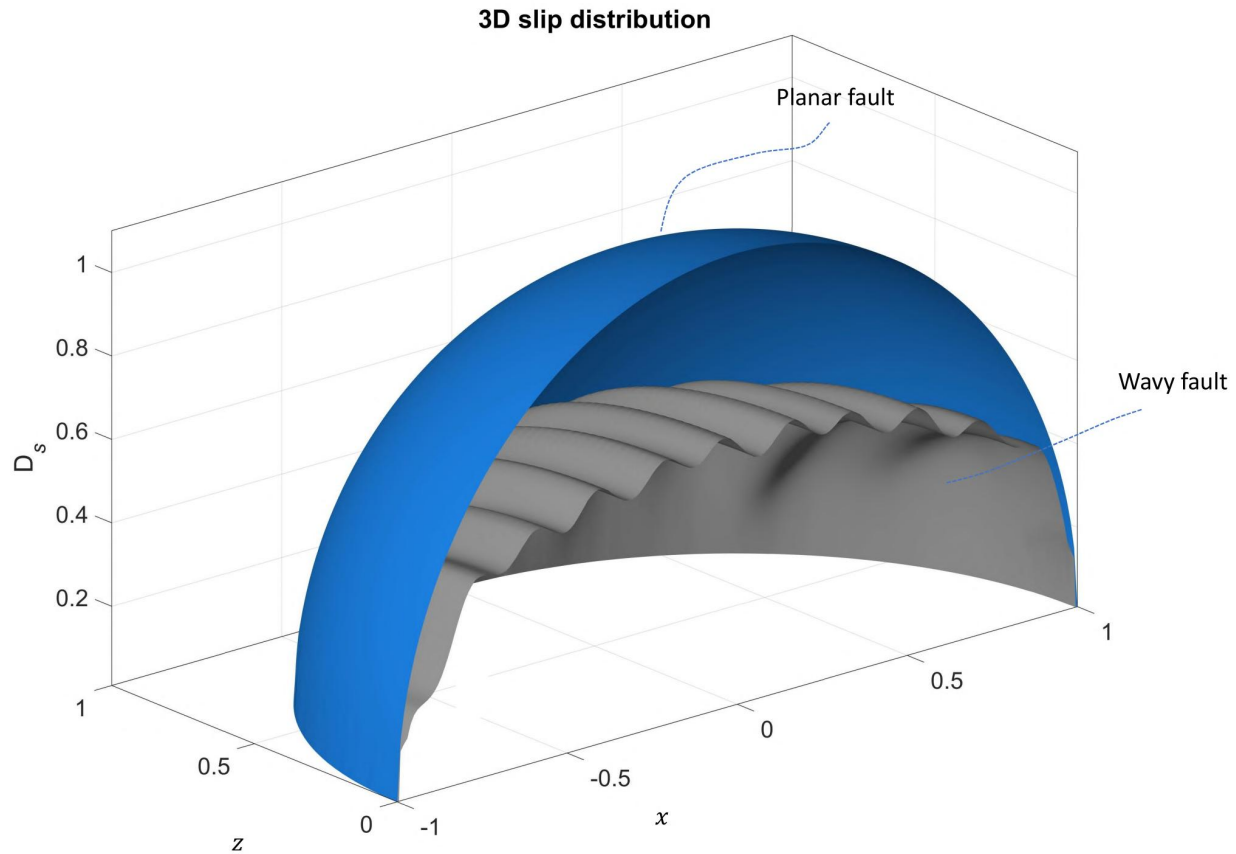
Our last test of accuracy is to use the output slips from Eq. 2.16 and compute the tractions using Eq. 2.8. Converting the boundary conditions to tractions and using Eq. 2.6 we find the analytical resultant traction. Comparing the analytical and numerical tractions at every elements midpoint, the highest error observed is $1E-7\%$ of the analytical value. This is deemed sufficiently accurate in capturing the boundary condition set.

Corrugations were introduced onto the surface using Eq. 2.22. The resultant undulations are aligned along the z -axis created by moving each triangles corner point by the y value of the prescribed waveform. To orient these corrugations at different angles to the slip sense a rotation of the surface around the y -axis was then applied (Fig. 2.5b to c).

$$y = H \sin\left(\frac{2\pi x}{\lambda}\right) \quad (2.22)$$

Where H is the waveform amplitude and λ the wavelength. Note that we have set an upper limit to the waveforms used in this analysis such that the inflection points on the waveforms (where $y = 0$) are never angled more than 45 degrees away from the x -axis.

Figure 2.6: Cross section through 3D slip distributions for a planar and wavy fault. Here $a=1$ and the xz axes of the graph are the location on the cracks walls. The wavy fault has an H and λ that are 2% and 37.5% of a respectively. D_s here is slip normalised to a planar faults maximum slip value from Eq. 2.2.



2.4.2 Stress intensity approximation

Stress intensity factors approximate stress distributions and magnitudes at distances very close to a fracture's tip. For a 2D fracture (shear or opening) these have been shown to approximate stress distributions at distances of 10% of the fractures half-length from the tip with less than 15% error Pollard and Segall (1987) and Pollard and Fletcher (2005). The accuracy of this approximation increases with decreasing distance from the fracture's tip. In 2D the formula for the stress intensity of a line crack subjected to shearing is:

$$K_{II} = ts\sqrt{a/\pi} \quad (2.23)$$

Following Tada, Paris, and Irwin (2000) the formulas for the stress intensity factors around a penny-shaped crack subject to shearing are:

$$\begin{Bmatrix} K_{II} \\ K_{III} \end{Bmatrix} = \begin{Bmatrix} \cos \theta \\ \sin \theta(1 - \nu) \end{Bmatrix} \frac{4t_s\sqrt{a/\pi}}{2 - \nu} \quad (2.24)$$

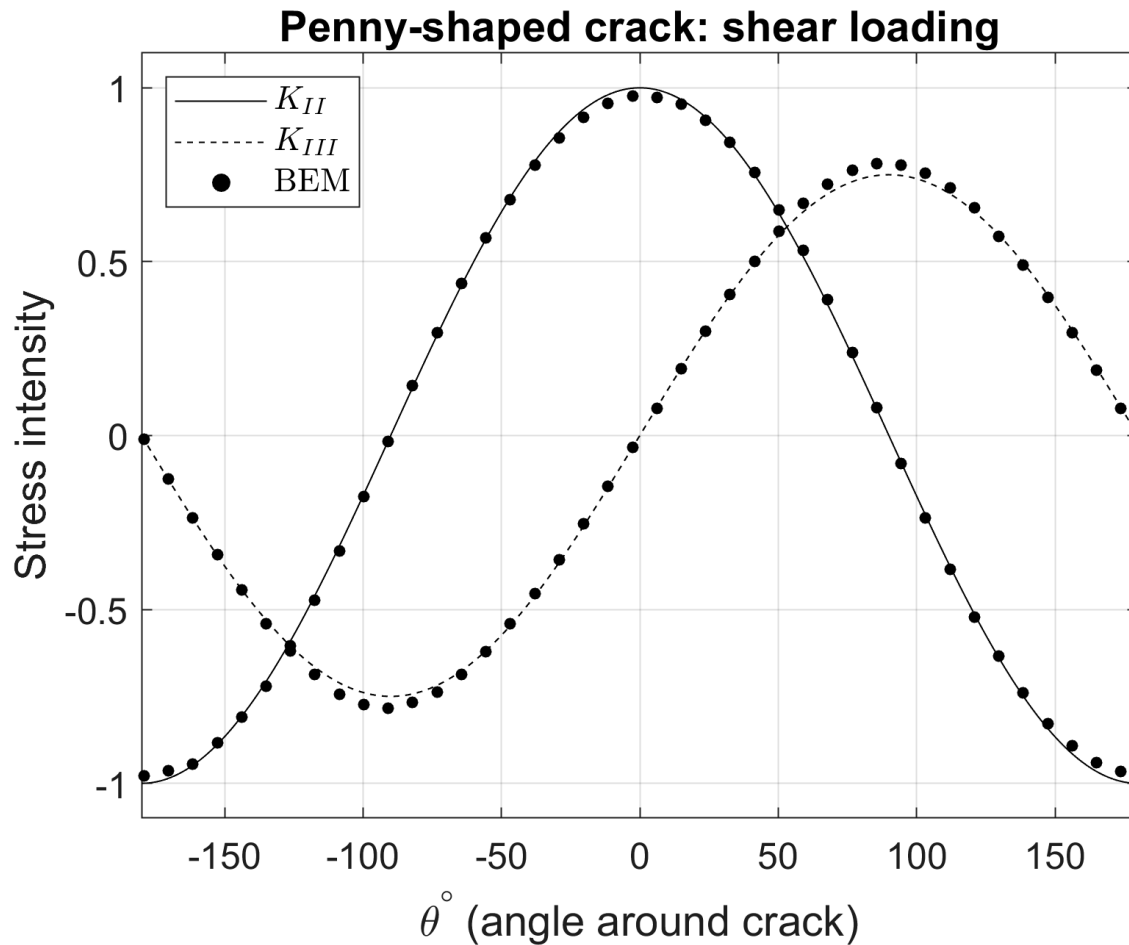
Where Θ is measured from the crack centre and defines the angle between the shear direction and a location on the crack's tip-line, (Fig. 2.1). The results of the DDM method can be used to approximate the stress intensity factors at a fracture's tip Olson (1991). We have followed the method of Olson (1991) but re-derived the formulas using the equations for a 3D penny-shaped crack (chapter 7.3). The 3D formulas are:

$$\begin{Bmatrix} K_I \\ K_{II} \\ K_{III} \end{Bmatrix} = \begin{Bmatrix} D_n \\ D_{II} \\ D_{III}(1 - \nu) \end{Bmatrix} \frac{\sqrt{\pi G}}{\sqrt{h}(1 - \nu)^2} c \quad (2.25)$$

In these equations, h is the distance from the mid-point (geometric incenter) of the boundary element to the fracture's tip Ritz, Mutlu, and Pollard (2012), D_n is the normal displacement of this element, D_{II} is the displacement perpendicular to the crack edge, and D_{III} is the displacement parallel with the edge. The correction factor c is used to correct for the errors due to the numerical approximation. This is set to 1/1.834. See the chapter 7.3 for the reasoning.

The accuracy of the 3D DDM in matching Eq. 2.24 is shown in Fig. 2.7. The maximum vertical separation between the analytical curve and points (residual) shown in Fig. 2.7 is 0.032 for K_{II} and

Figure 2.7: Stress intensity factor approximation using the 3D DDM method. Analytical curves shown are for a penny-shaped crack subject to shear stress; Eq. 2.24. All results are normalised the maximum analytical value of K_{II} . The numerical approximation is shown as dots. The sampling used, and boundary conditions on the fracture are those described in the benchmarking section. The signs here follow the shear direction convention shown in Figure 9.30 of Pollard and Fletcher (2005). The positive direction of the crack y -axis in Fig. 2.5b corresponds to the y -axis in the local coordinate system of their figure.



0.035 for K_{III} , this is for the surface as described in the benchmarking section.

2.5 Model results

2.5.1 Effect of corrugation amplitude and wavelength: comparison to 2D results

We now compare the slip reduction differences for 2D and 3D geometries with the same shaped corrugations. The results of Eqs. 2.20 and 2.21 are plotted to compare the slip area or volume reduction relative to a planar fault. The fault in 3D is oriented as in Fig. 2.5b. For this configuration, the ‘out-of-plane stress’ σ_{zz} in 3D makes no difference to the results as this is not resolved as a traction at any point on the surface.

Fig. 2.8 shows a comparison between the results for 2D and 3D wavy faults with several amplitudes and four different wavelengths. The 2D sampling has been set to 1,000 equally spaced elements on the fault plane in the x -axis before the waveform is introduced. Slip reductions relative to a planar penny-shaped and line cracks are plotted in Fig. 2.8 as a function of the surface waveform, and both 2D and 3D results are shown. This shows the simple trends observed in previous 2D studies where resultant slip is reduced by corrugations with higher amplitudes and/or shorter wavelengths (Ritz and Pollard, 2012).

Trends, due to both changes in amplitude (H) and wavelength (λ), in the reduction in slip are similar for the 2D and 3D results. The largest difference between 2D and 3D reductions in slip due to corrugations is less than 10%. Some notable differences are that the 2D results have greater reductions in slip for all modelled wavelengths, except for when the wavelength is larger than the fault half-length (in this case the opposite is true). As the numerical accuracy of the DDM has been quantified as accurate to approximately 1%, the difference between the two results is due to the shape and area of the crack in 3D and the lack of the plane strain boundary condition. From these results, we suggest that the slip distribution profiles documented by Ritz and Pollard (2012) for 2D fractures can be extrapolated to 3D penny-shaped fractures when shearing is perpendicular to the alignment of asperities.

Figure 2.8: Comparison between numerical results for 2D (A) and 3D (V) slip reduction due to changes in a wavy fault surfaces amplitude and wavelength. Squares are the resultant 2D slip area and diamonds are the 3D slip volume. Results on the y -axis are relative to Eqs. 2.3 and 2.4. Different colours on the graph correspond to different wavelengths relative to half-length a . On the right of the figure we show our mesh captures the most extreme waveform we show this looking down the corrugations for a waveform where H and λ are 3.5% and 25% of a respectively. The slight deviations at the wave crests are caused by the added equilateral edge triangles.

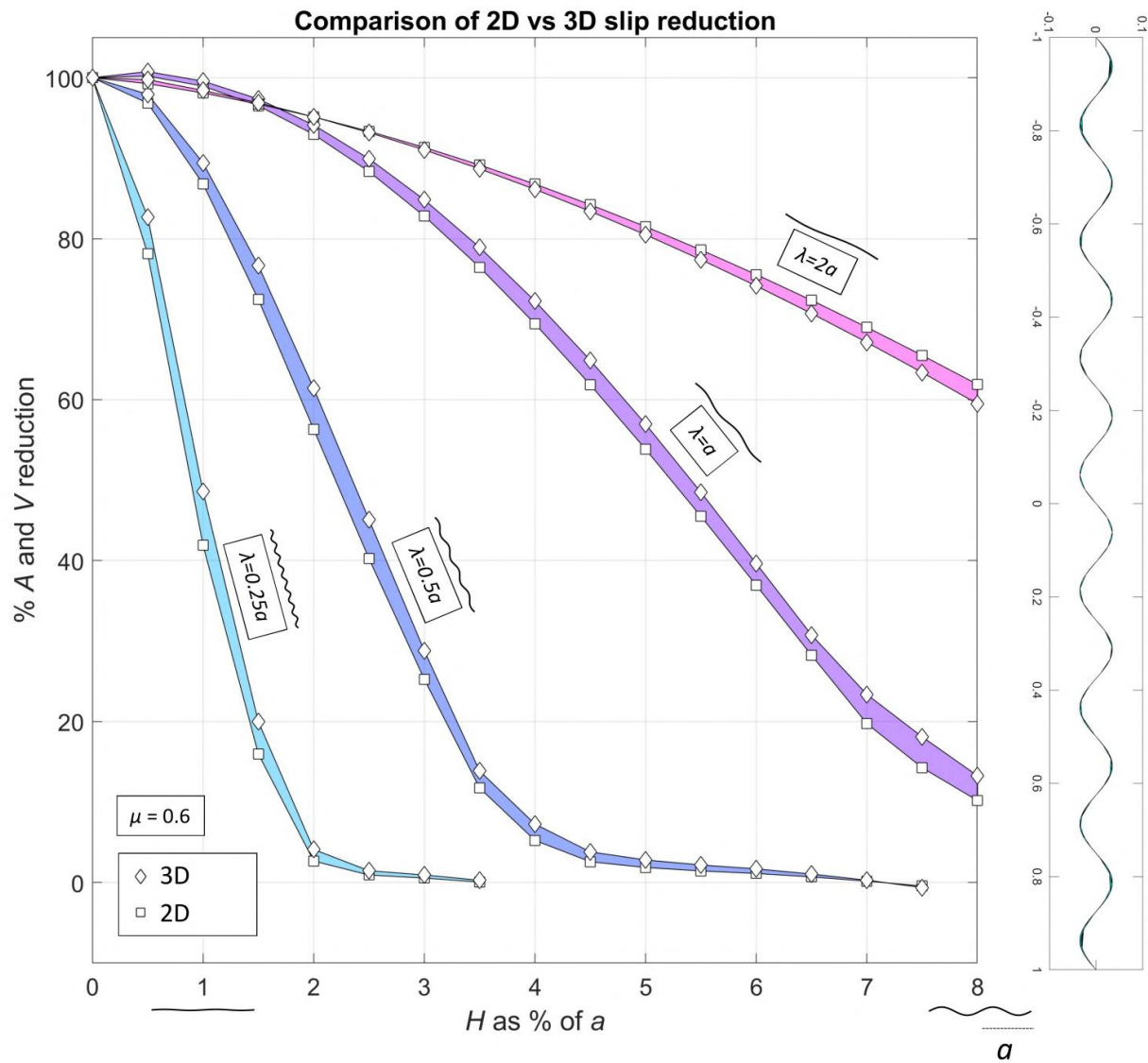


Figure 2.9: (Continued on the following page.)

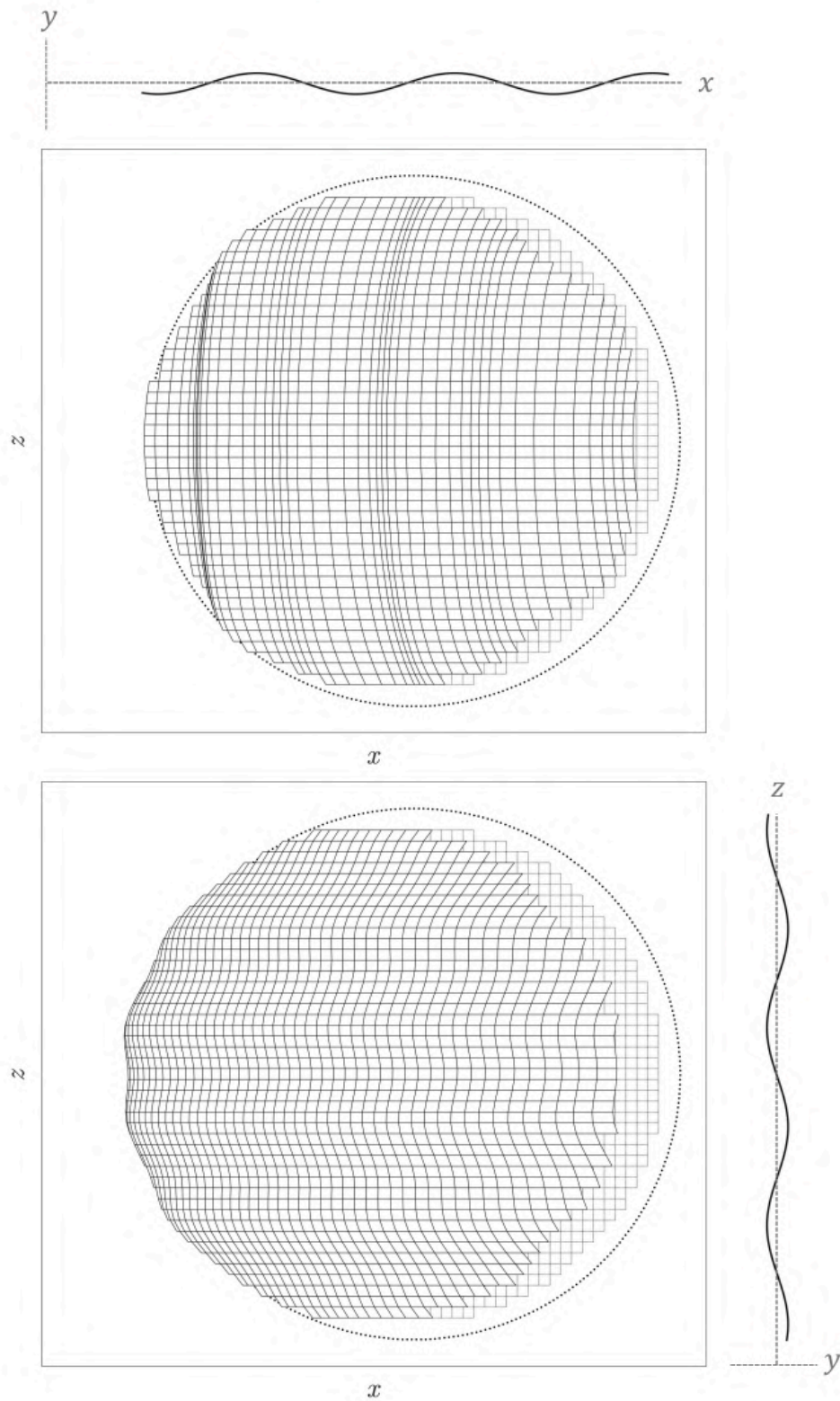


Figure 2.9: Deformation pattern of the fracture walls when slip is perpendicular (top) and parallel (bottom) to corrugations. The dotted line represents the fractures boundary. The light uniformly gridded squares in the background represent one of the fracture walls before deformation. The deformed grid is the resultant displacement once this wall shears. The topography of the surface is shown as the 2D lines at the side; this waveform corresponds to an H and λ that are 4% and 75% of a respectively. Boundary conditions are as stated but the displacement is exaggerated by 300 times. xz -axes correspond to those shown in Fig. 2.5b) and c). σ_{zz} here has been set equal to σ_{xx} .

2.5.2 Effect of corrugation orientation in 3D

In this section, we explore the effects of corrugation orientation in relation to the direction of shearing, i.e. changing from the geometry shown in Fig. 2.5b to that in Fig. 2.5c. When corrugations are oriented as in Fig. 2.5c this means σ_{zz} is resolved as a normal traction on some parts of the surface. We start by exploring the changes in slip volume when σ_{zz} is set to the same magnitude as the stress component, σ_{xx} ; this is t_n acting on the plane if it was perpendicular to its orientation shown in Fig. 2.5a. Changes in the magnitude of σ_{zz} are explored later.

Fig. 2.9 is an example that shows the shearing of a faults faces for the geometries in Fig. 2.5b and Fig. 2.5c. An important observation from this figure is that there is no slip in the z direction. The lines running parallel with the x -axis are not perturbed. This is different to the findings of Marshall and Morris (2012) where deviations in slip vector rake are analysed on frictionless faults. For high values of friction and for these boundary conditions the fault plane only slips in directions parallel to the greatest resolved shear traction vector.

Fig. 2.10 has the same axes and plots the same corrugation waveforms as Fig. 2.8 but compares slip reductions when corrugations are parallel and perpendicular to the slip direction (Fig. 2.5b to c). Reviewing the trends in this graph shows that:

- The range in slip reduction due to doubling the wavelengths of corrugations (vertical distance between lines with the same symbol) is almost always greater than the reduction due to corrugation misalignment for a given corrugation waveform (vertical extent of each shaded patch).
- Faults with shorter corrugation wavelengths are more sensitive to corrugation angle relative to slip. These have greater ranges in slip as the corrugation directions change from parallel to perpendicular in relation to the plane containing the most compressive stress.

Figure 2.10: 3D slip V reduction due to changes in a wavy fault surfaces amplitude and wavelength. Diamonds are when slip is perpendicular with corrugations and squares parallel. Note perpendicular results match those in Fig. 2.8. Results on the y -axis are relative to a planar fault described by Eq. 2.4. Different colours on the graph correspond to different wavelengths relative to half-length a .

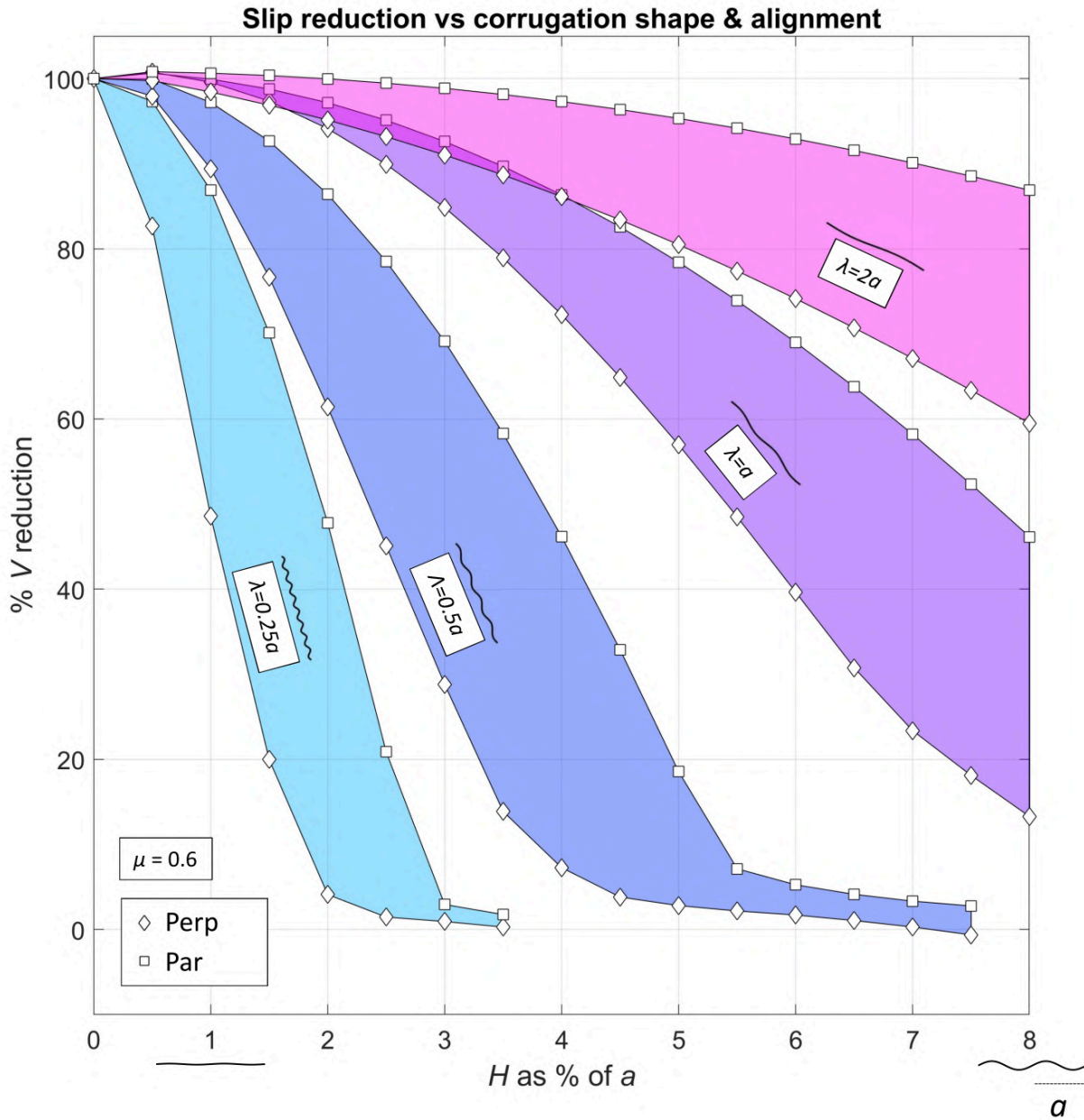


Figure 2.11: 3D slip V reduction due to changes in a wavy fault surfaces amplitude and wavelength. Diamonds are when the stress out of the plane of shearing is low (equal to σ_{yy}) and squares when this is high (equal to σ_{xx}). Results on the y - axis are relative to a planar fault described by Eq. 2.4. Different colours on the graph correspond to different wavelengths relative to half-length a . Values of μ shown on the right of y -axis are adjusted coefficients of friction for planar faults, these will reduce the slip volume by the amount shown on the left y -axis (relative to the volume when μ is 0.6).

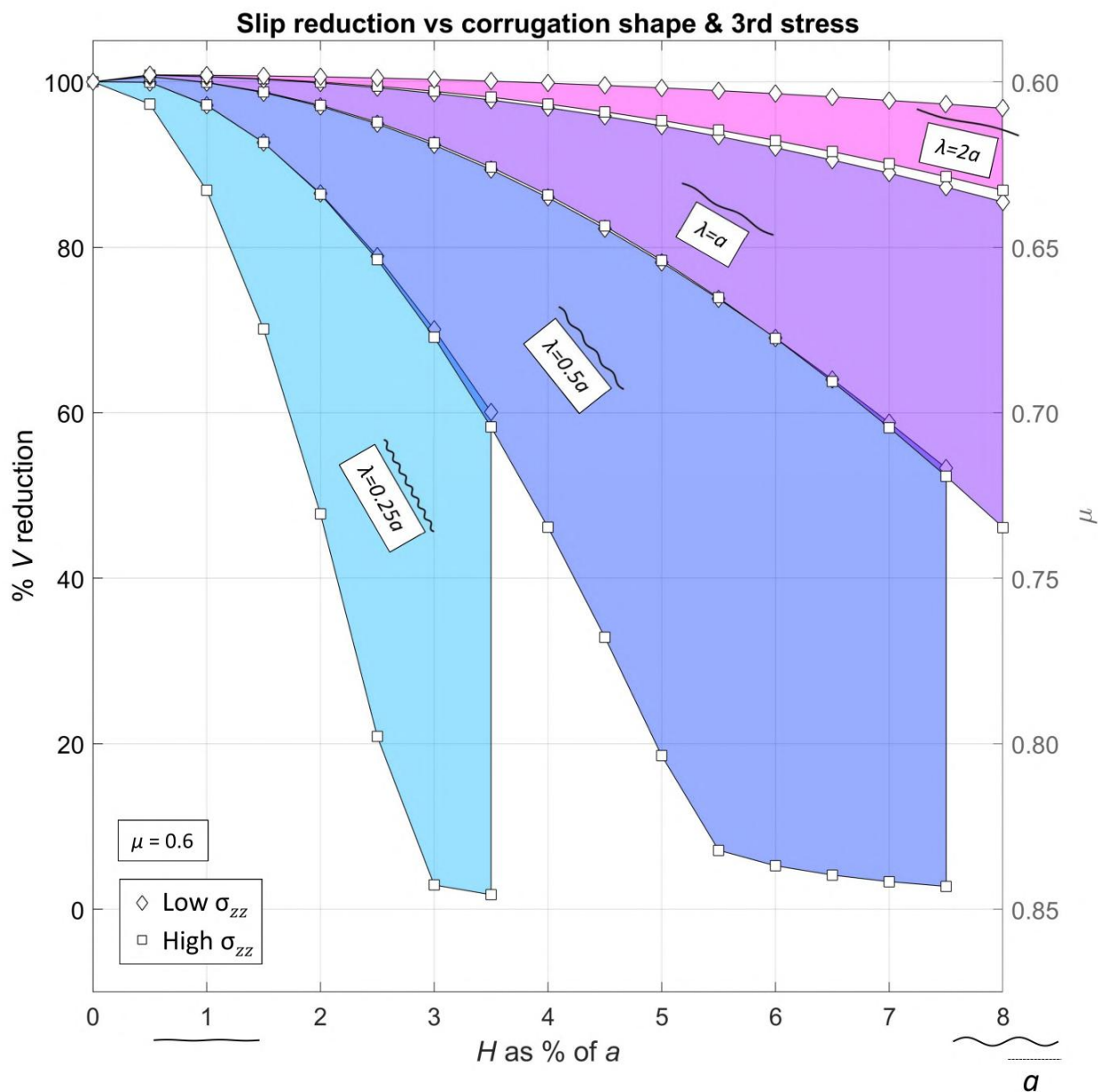


Figure 2.12: Stress intensity factor reductions due to corrugations, comparison between 2D and 3D results. Results on the y -axis are relative to a planar fault described by Eq. 2.24. Different colours on the graph correspond to different wavelengths relative to half-length a .

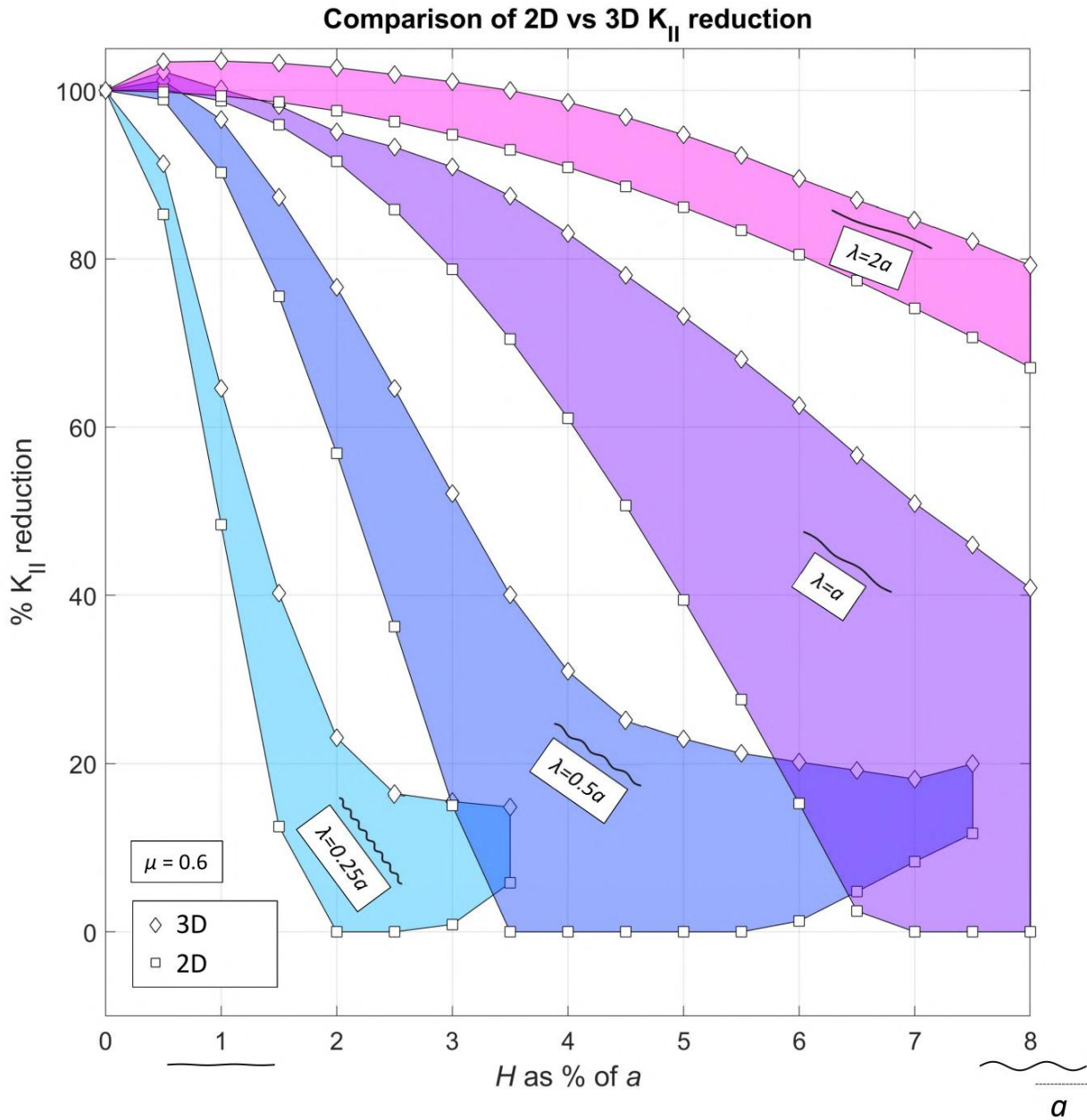


Fig. 2.11 explores what the out-of-plane stress (here σ_{zz}) does to the results of Fig. 2.10. Two cases are shown: a) σ_{zz} is set equal to σ_{xx} ; b) σ_{zz} is equal to σ_{yy} (i.e. t_n when planar). The figure shows slip reductions when corrugations are parallel with the slip direction. For cases when σ_{zz} is reduced so is the additional frictional resistance which allows the fault to slip a greater amount. Here it can be seen that doubling the wavelength of the corrugations (vertical distance between lines with the same symbol) has close to the same effect in reducing slip as decreasing the out-of-plane stress σ_{zz} to the magnitude of the lowest stress driving slip (vertical extent of each shaded patch). Adjusted coefficients of friction are supplied for planar faults in Fig. 2.11 to give an idea of how this parameter reduces slip volume in comparison to the reductions due to fault waveform. Note these values also apply to Fig. 2.8 and Fig. 2.10 also. This gives some idea of the ‘effective’ friction that would be calculated by fitting a planar fault model to slip data from a wavy fault surface that was subject to the boundary conditions we have described.

2.5.3 Stress intensity factors

Reductions in stress intensity between the 2D and 3D results are shown in Fig. 2.12. This figure plots results relative to the result from Eq. 2.24. Note that the 3D results plot the maximum stress intensity on the crack edge. Unlike in Fig. 2.8 the trends between 2D and 3D results are quite disparate, <40% in places. This is due to the crack tip in 2D being a single point. Fig. 2.9 shows that parts of the fault surface slip less due to the waveform of the fault surface and its relation to the principal stresses. In 2D if the crack tip is at a location where the slip is reduced then so is the stress intensity. In 3D, the crack has a tip-line so even if slip along parts of its tip-line are reduced, locations along parts of the tip-line in ‘releasing bends’ will continue to slip. This results in some edges of the fault maintaining higher stress intensities. Note that reductions in K_{III} for the 3D case follow very similar trends to that of K_{II} . This observation highlights the need for careful consideration of geometry and local departures from the general trends when analysing the results of the previous graphs, Fig. 2.8, Fig. 2.10, and Fig. 2.11.

2.5.4 Effect of waveform on opening aperture

This part of the study focuses on the ‘lenticular’ openings as described by Ritz, Pollard, and Ferris (2015). The same basic boundary conditions and constants are used as before, but with an additional pore pressure inside the fracture. In this part of the study a 2D plane strain code is used to model slip perpendicular to the asperity direction. In the 2D study of Ritz and Pollard (2012) a ratio a/λ

greater than 11 (when λ is less than 9% of a) was required before opening was observed on parts of the fractures face. We look at openings for faults with longer corrugation wavelengths when there is a pore pressure (P) acting to reduce the effective normal stress confining the surface. From Eq. 2.6 we can state that increases in pore pressure should increase the overall slip on the fracture surface, this should also promote opening of the surfaces faces:

2D line, at $L < a$:

$$D_n = \frac{2(1 - \nu)P}{G} \sqrt{a^2 - L^2} \quad (2.26)$$

We choose to scale the maximum apertures observed on the wavy faults, so they are relative to the maximum opening observed for a planar line shaped crack dilating due to an internal pressure, (Eq. 2.26). D_n here being the total separation between the faces not just the displacements of one wall of the crack. Note that the maximum opening here is found by simply setting the term L inside the square root to zero, i.e. the centre of the crack (Fig. 2.1). This allows us to scale our results to a problem that uses both the same elastic constants and has the same surface geometry (when planar) making our results dimensionless. The internal pressure opening the crack is set to half the magnitude of the normal stress that confines our shear fault when it is planar. In terms of pressure this is a value P , 41.15 MPa.

Fig. 2.13 shows how openings on the fracture surface change as a function of the waveform of the fracture. The two axes show the parameters that control the waveform and the coloured squares are openings as a percentage of Eq. 2.12. Note that the dashed lines shown are where waveform slopes are deemed excessive. The graph shows that lenticular openings on confined shear fractures can reach up to 25% of the maximum apertures of an unconfined pressurised crack. Maximal openings are found for waveforms with ratios of λ/H of around 15. Such a ratio and the opening magnitudes will change with friction, pore pressure and driving stresses.

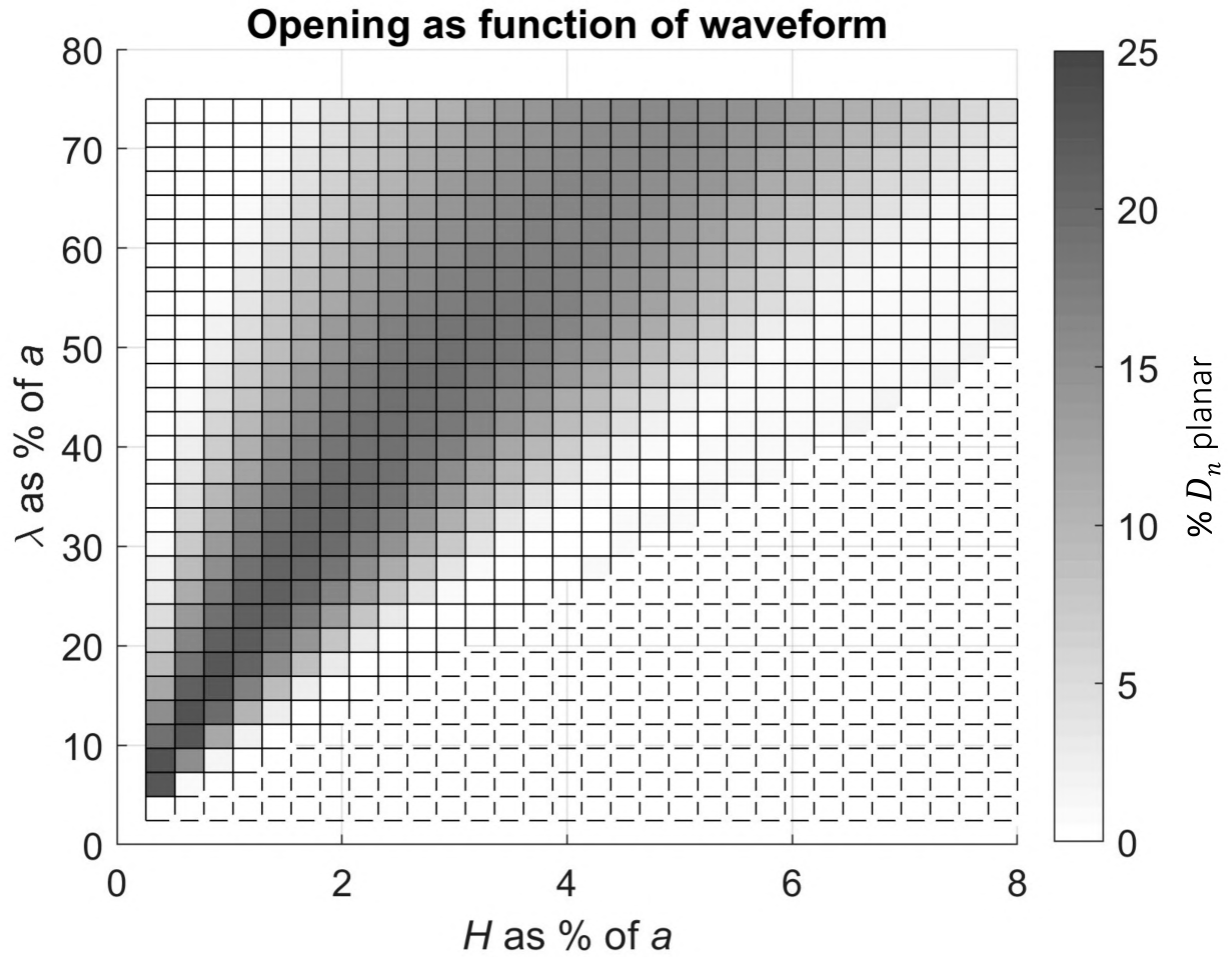
2.6 Discussion

2.6.1 Relationships in slip reduction

From the modelling results, the following statements can be made:

1. When slip is perpendicular to the corrugations, results from 2D studies match closely with

Figure 2.13: Waveform and associated lenticular opening apertures on the fault surface. Results scaled relative to Eq. 2.26.



3D results (Fig. 2.8). This suggests that the slip reductions due to the shape of corrugations are not greatly affected by the tip-line shape of the fracture so plane strain (2D) modelling is adequate in this case.

2. When slip is parallel to corrugations, reductions due to doubling corrugation wavelength are greater than the slip reduction due to rotation of the corrugations out of alignment with the slip direction (Fig. 2.10). This is provided that the out-of-plane stress is high, high being the value of t_n resolved on the crack face when planar.
3. For slip parallel with corrugations, the maximum reduction in slip when changing the out-of-plane stress from low to high matches the reduction in slip when halving the corrugation wavelength. Low here being the value of t_n resolved on a planar crack orientated perpendicular to the crack in our setup (with its normal in the xy -plane).

These results should give some indication as to which fault shapes will preferentially accrue more slip in a given slip direction. Such results rely on both an estimation of fault roughness at a larger scale and the stresses driving failure. Note the two latter relationships detailed here are dependent on the coefficient of friction being at 0.6. We have tested if these statements hold true for values of μ between 0.4 – 0.67. Statements 1 and 3 hold true between these values. Statement 2 is still valid when μ is higher, i.e. 0.67, but begins to break down for lower values i.e. 0.4. Here results for the different wavelengths would begin to overlap in Fig. 2.10. It is worth reviewing the statements earlier that friction is overestimated by 41% on faces where the two shear traction components (t_{ds} and t_{ss}) are of equal magnitude. We can therefore state that trends for the slip parallel with corrugations in Fig. 2.10 and Fig. 2.11 will show greater reductions due to friction than would be observed if we modelled this using an isotropic friction cone.

2.6.2 Additional complexity

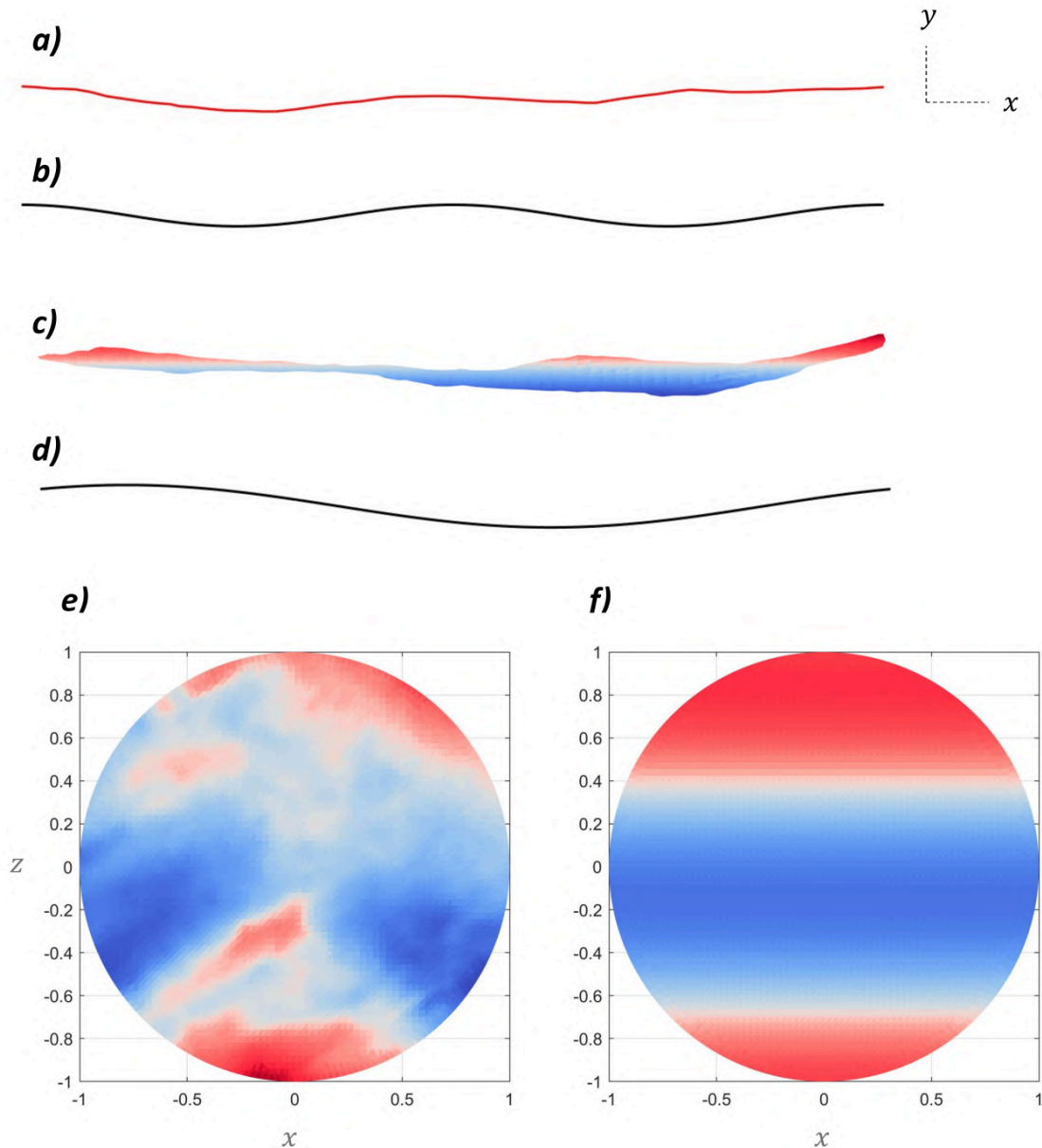
In 2D the correlation between slip reduction and stress intensity is clear; see Fig. 2.8 and Fig. 2.12. This breaks down in 3D where high stress intensities remain even when the total volume of slip is significantly reduced. Similar examples of local departures from the global trend of slip on the fault surface were presented by Ritz and Pollard (2012); here we have shown an example where 3D geometry also introduces such a complexity. Changing the start location and sign of the waveform (phase shift) for faults with longer corrugation wavelengths changes the slip distributions Ritz and Pollard (2012). Changing these parameters will only have substantial effects on slip reductions for

corrugations of longer wavelengths, for example the greatest slip reduction shown for the longest wavelength in Fig. 2.8 increases by up to 10% for a waveform shifted positively by 90 degrees. The other wavelengths modelled here are broadly unaffected (less than 5%).

An obvious question related to the results shown here is how well does the approximation of a smoothly undulating roughness compare to slip on surfaces with real fracture surface roughness? To give some indication of the limitations of the approximation adopted here, we numerically simulate slip on two more complex geometries to quantify how slip is reduced on such surfaces. We have found slip distributions relative to planar faults for 2D and 3D fracture surface geometries observed in the field. The first is from Ritz, Pollard, and Ferris (2015) and the second an exposed fracture face on a sandstone outcrop reconstructed using 3D photogrammetry. The sampling of this face is such that roughness below a 10th of the half-length is not captured and additional artefacts may have been introduced during processing. Fig. 2.14 also shows approximations of these two fractures with waveforms. For the 2D results for the surface shown in Fig. 2.14 we observe a slip reduction of 17% compared to planar. This compares well to that for the waveform approximation shown, that has an approximate slip reduction of 12% (Fig. 2.8). For the 3D fracture surface, the slip reduction is 25%. For the approximate waveform from Fig. 2.10 the slip reduction is 5%. Therefore, for the two surfaces shown here the results suggest that first order approximation will overestimate the volume of slip compared with a natural fracture shape that has multiple length scales of asperities. Intuitively, this will be especially apparent when 3D surface roughness is close to isotropic, i.e. lacking alignment of the asperities. This is seen for small faults (slip < 1 m), which in general are characterised by roughness that is closer to isotropic than larger faults (~10-100 m slip) Sagy, Brodsky, and Axen (2007). Power and Durham (1997) show that roughness on fracture surfaces of both natural and experimental tensile fractures is close to isotropic, at scales of 0.001 to 2 cm. To provide a conflicting example, Pollard, Bergbauer, and Mynatt (2004) show clear examples of joint surfaces with clear anisotropic roughness perpendicular to the fracture tip lines, on the scale of cm's, formed during mixed mode fracture propagation.

We have provided some potential mechanisms that create or cause non-planarity of fractures. None of these mechanisms create the sinusoidal structures observed on some fault surfaces, that are typically above the metre scale Resor and Meer (2009) and Brodsky, Kirkpatrick, and Candela (2016). Are our results applicable to such structures? Our model results can be scaled up to a larger scale using the appropriate values in the analytical solutions provided. This is dependent on the assumption that the roughness is not destroyed or modified during slip and that the boundary conditions we have used are still suitable.

Figure 2.14: a) 2D fracture profile from Ritz, Pollard, and Ferris (2015), Fig.2.8, fracture is approximately 3 m long. b) 2D approximation with waveform: $\lambda = a$, $H = 2.5\%$ of a . c) 3D fracture surface from photogrammetry on a sandstone block (self-defined edges), the exposed fracture surface was 2 m wide, looking into the x -axis (slip direction). The height of the surface in the y -axis varies by 14 cm. d) Approximation of c) with the waveform: $\lambda = 200\%$ of a , $H = 5\%$ of a . e) 3D fracture surface front coloured for height/depth away from 0. f) 3D fracture surface front approximation of d) with the same colour scale as e).



2.6.3 Fluid flow

We have quantified the opening of apertures when wavy fault surfaces shear at fluid pressures close to hydrostatic conditions. These open even when confined by remote stresses driving shearing. This is contrary to the assumption that fluid pressure must exceed the normal stress acting on a fracture face before openings are observed (e.g. Mildren, Hillis, and Kaldi (2002)). Fig. 2.13 uses internal pressure as the variable controlling opening of the fracture. To use the data presented in this figure the input pressure must be scaled so there are reasonable values for the remote stresses that drive shearing. Using the elastic parameters and stresses described previously this suggests that a 10 m-long shear fracture with the correct waveform could have had 1.25 cm lenticular openings. It is of interest to know if in a laboratory, an experiment using pre-cut rock samples would also show increases in the permeability during shear loading, for certain cut shapes.

2.7 Conclusions

We have quantified the amount that slip is reduced by friction on 3D fault surfaces with variations in fault topography. We use a first order approximation where topography is modelled as a sinusoidal waveform, i.e. parallel corrugations. Firstly, when typical friction values are considered the fault plane only slips in directions parallel to the resolved traction vector, independent of its direction in relation to the corrugation alignment. Slip reductions due to corrugations are comparable for both 2D line cracks and 3D penny-shaped cracks when shearing is perpendicular to corrugation alignment. Differences in slip reductions when the slip is aligned and misaligned with corrugations appear to be less than the differences in slip reductions when the corrugation wavelength is doubled, when the out-of-plane stresses are high. When the slip vector is aligned with the corrugations on the fault surface, halving the corrugation wavelength has almost the same effect at reducing slip volume as increasing the out-of-plane stress from close to the lowest stress in the plane of shearing up until it matches the normal stress acting on the plane. For lenticular openings on fault surfaces we have quantified which waveforms have the greatest openings: for typical shearing conditions, this is a λ/H ratio of around 15. Note that opening apertures are observed even when the internal pore fluid pressure does not exceed the remote stresses clamping the fault surface.

Acknowledgements and funding

We thank both reviewers for the constructive reviews which resulted in improvements to the manuscript, the editor Cees Passchier and lastly, Lydia Jagger who helped improve the language of the initial draft. The work here was funded through the Deutsche Forschungsgemeinschaft / International Continental Scientific Drilling Program, grant agreement N. RI 2782/3-1.

Chapter 3

Critical fluid injection volumes

The content of this chapter has been published in **Davis, T.**, Rivalta, E., Dahm, T. (2020): Critical fluid injection volumes for uncontrolled fracture ascent. *Geophysical Research Letters*, 47, 14, e2020GL087774.

Abstract

Hydro-fracturing is a routine industrial technique whose safety depends on fractures remaining confined within the target rock volume. Both observations and theoretical models show that, if the fluid volume is larger than a critical value, pockets of fluid can propagate large distances in the Earth's crust in a self-sustained, uncontrolled manner. Existing models for such critical volumes are unsatisfactory, most are two-dimensional and depend on poorly constrained parameters (typically the fracture length). Here we derive both analytically and numerically in three dimensions scale-independent critical volumes as a function of only rock and fluid properties. We apply our model to gas, water and magma injections in laboratory, industrial and natural settings, showing that our critical volumes are consistent with observations and can be used as conservative estimates. We discuss competing mechanisms promoting fracture arrest, whose quantitative study could help to assess more comprehensively the safety of hydro-fracturing operations.

Plain Language Summary

Fractures in rocks can act as channels for fluids. Fracking, or hydro-fracturing, involves injection of fluids at high pressure in order to grow fractures within the rock and increase its permeability. Fluid volumes need to be kept below a threshold value: if the fluid volume is larger, then the stresses at the tips of the fluid pocket will be large enough for the fluids force their way around by fracturing the

rock ahead of them. Previous theoretical models for the critical volumes are unsatisfactory as they are two-dimensional and based on poorly constrained parameters. We derive and test a new three-dimensional equation that uses only rock and fluid parameters. We find that typical volumes injected in hydro-fracturing operations are over the limit we define. We argue they are still mostly safe as additional processes often hinder fracture growth. Further work is needed to comprehensively quantify mechanisms that hinder hydro-fracture arrest.

3.1 Introduction

Official guidelines for hydraulic fracturing (e.g. Mair et al., 2012; EPA, 2016), outline safe operational practices for regulators. Such reports often state that during routine operations fractures are unlikely to grow out of the target rock formation, as typical injection pressures are too low for this to occur. These claims are substantiated with empirical observations from closed access microseismic data of scarce vertical fracture growth following injection (Fisher and Warpinski, 2012). Evidence for unsafe vertical migration of such fluids remains ambiguous (Vidic et al., 2013).

Natural analogues of fluid migration by hydro-fracturing include drainage crevasses in melting glaciers and magma transport by dyking. Field and experimental observations provide some indication of typical rates of fracture ascent, in the order of mm/s to around half a m/s (Das et al., 2008; Tolstoy et al., 2006). For water-filled fractures in rock this has not been observed; estimates from geochemical analysis supply similar rates of ~ 0.01 - 0.1 m/s, (1 km/day) (Okamoto and Tsuchiya, 2009). Theoretical arguments suggest that the migration velocity should have a dependency on volume (Heimpel and Olson, 1994; Dahm, 2000b).

According to theory, tip-propagation occurs when a critical amount of fluid has accumulated inducing enough stress to overcome the medium's fracture toughness, K_c (Secor and Pollard, 1975). So far, critical 'volumes' are given in terms of the fracture length, which is not directly observable and difficult to estimate from observations (Secor and Pollard, 1975; Dahm, 2000b; Taisne, Tait, and Jaupart, 2011); moreover, such analyses have been carried out in 2D only, not capturing the fracture's 3D shape and scaling of volume vs length.

Here, after deriving a theoretical model and validating it with numerical simulations, we apply this to cracks filled with air, water, oil and magma in solids of varying stiffness and toughness, across a wide range of length scales.

Methods

3.1.1 Hydrofracturing and stress gradients

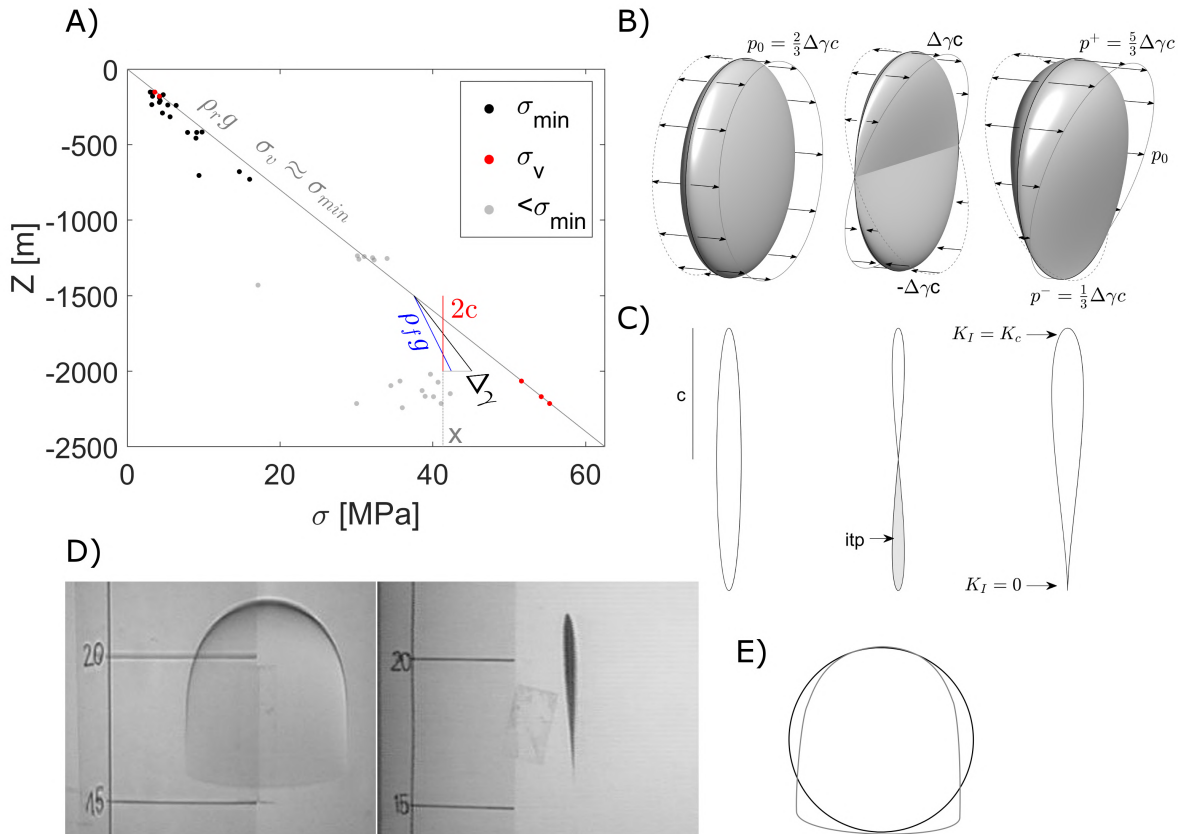
We consider a pressurised penny-shaped crack of radius c and volume V in an elastic medium. The crack can only grow when the stress intensity K_I at its tip-line exceeds K_c . The elastic parameters of the medium (shear modulus, μ , and Poisson's ratio, ν) control the fracture's aperture. The internal pressure p_0 must overcome the stress normal to the crack walls (generally the minimum compressive stress, σ_{min}) by an amount accommodating the volume V against the elastic forces, Fig. 3.1A/B.

When the crack is vertical, the gradient in the normal stress acting to close the crack and the gradient in the load due to the overlying fluid acting to open the crack, i.e. $\rho_r g$ and $\rho_f g$ in Fig. 3.1A, where ρ_r and ρ_f are the densities of the host rock and fluid, respectively, result in a net stress gradient $\Delta\gamma$ acting to push open the crack walls in an inverse 'teardrop' shape, Fig. 3.1B/C. When the crack is inclined $\Delta\gamma$ needs to be adjusted by $\cos(\theta)$, where θ is the cracks' angle away from vertical. Quantitative formulations used to assess industrial fracture heights neglect stress gradients (e.g. Xu et al., 2019; Yue, Olson, and Schultz, 2019). This contrasts with routine observations of stress gradients from industry data (Fig. 3.1A) and the fact that these gradients are considered in the well design of industrial operations (Lecampion et al., 2013; Mair et al., 2012). When this gradient is included in formulations, stress intensity varies around the fracture's tip-line (Fig. 3.2). Where K_c is exceeded, the upper tip-line advances. The contained fluid flows into this newly created fracture surface while the bottom edge of the fracture is pinched shut as the internal pressure drops. With a great enough volume this fluid movement maintains a critically stressed upper tip-line and the fracture reaches a state of 'self-sustaining propagation'. Fluid viscosity will cause some fluid to stay trapped in the tail trailing behind the fracture; if fluid viscosity is low enough, the contained fluid is virtually all transported. Provided the fracture's shape and volume are maintained, no additional forces, such as pressure from injection, are required to aid this state of propagation.

3.1.2 Analytical formulation

Secor and Pollard (1975) define in 2D the size and pressure inside a vertical fracture subject to $\Delta\gamma = (\rho_r - \rho_f)g$ such that at the upper tip $K_I^+ = K_c$ and at the lower tip $K_I^- = 0$. We derive an analytical expression for the fluid volume needed for a three-dimensional crack to propagate in a self-sustained manner.

Figure 3.1: A) Stress vs depth in the crust, data from Bell, Price, and McLellan (1990), crack shown in red with length $2c$. B) Stress boundary conditions and 3D crack wall displacement. C) Cross sections of crack wall displacement, itp=interpenetration. D) Shape of an ascending air filled crack in gelatine from (Rivalta and Dahm, 2006). E) Air filled cracks tip-line vs a penny-shaped tip-line.



K_I for a mode I penny-shaped fracture of radius c subject to a generic linear stress gradient can be expressed as the superposition of K_I for a penny-shaped fracture subject to a uniform pressure p_0 :

$$K_I = \frac{2}{\pi} p_0 \sqrt{\pi c} \quad (3.1)$$

and that for a penny-shaped fracture subject to a linear pressure gradient $\Delta\gamma$ where pressure is equal to 0 at the fracture's midpoint (Tada, Paris, and Irwin, 2000, p. 355):

$$K_I^\pm = \pm \frac{4}{3\pi} \Delta\gamma c \sqrt{\pi c} \quad (3.2)$$

where the + refers to the propagating tip and the - to the basal tip. Requiring $K_I^- = 0$ results in $p_0 = 2\Delta\gamma c/3$ and thus:

$$p^\pm = \left(\frac{2}{3} \pm 1 \right) \Delta\gamma c \quad (3.3)$$

Requiring $K_I^+ = K_c$ and rearranging for c yields:

$$c = \left(\frac{3\sqrt{\pi} K_c}{8\Delta\gamma} \right)^{2/3} \quad (3.4)$$

We note that the 2D plane strain critical length is $\approx 0.9c$. The volume of the crack can be calculated based on the equation for a crack pressurised by uniform pressure p_0 , as the antisymmetric pressure contribution integrates to zero. Thus using (Tada, Paris, and Irwin, 2000):

$$V = \frac{8(1-\nu)}{3\mu} p_0 c^3 \quad (3.5)$$

results in:

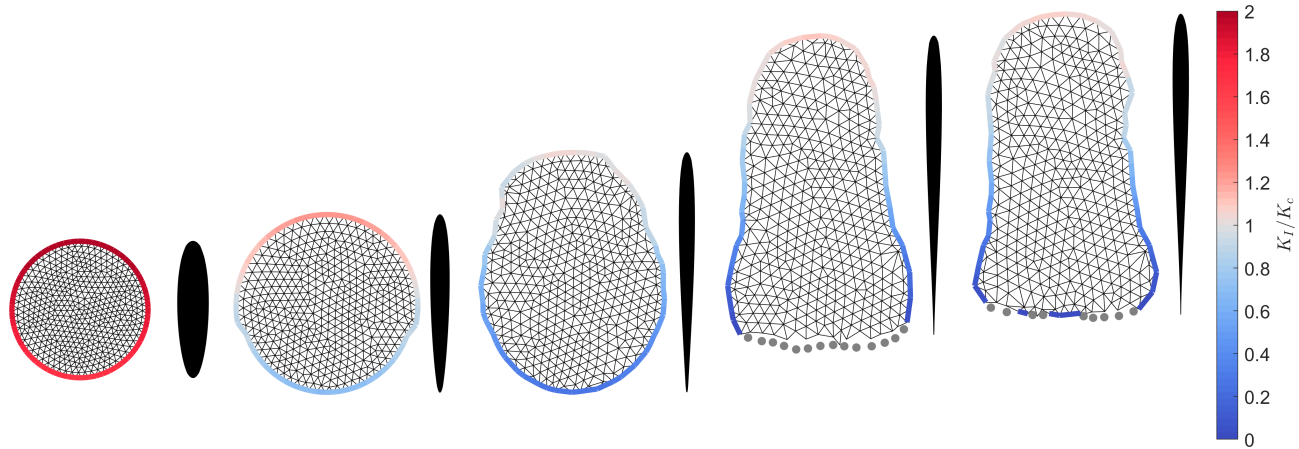
$$V_c^{an} = \frac{(1-\nu)}{16\mu} \left(\frac{9\pi^4 K_c^8}{\cos(\theta)\Delta\gamma^5} \right)^{1/3} \quad (3.6)$$

This equation requires validation in order to evaluate the bias due to approximating the shape of the propagating crack as circular (Fig. 3.1D/E).

3.1.3 Numerical model

To simulate propagation, we use a 3D Boundary Element program where each element is a triangular dislocation with constant displacement (Fig. 3.2) (Nikkhoo and Walter, 2015). The program computes fracture opening and stress intensities, based on fracture shape, rock and fluid parameters and external stresses Davis, Healy, and Rivalta (2019). Our workflow during each iteration is as follows:

Figure 3.2: Numerical simulation of crack propagation (from left to right), looking at the fractures' face (left) and cross section (right). Grey points are edges that closed in the previous iteration.



1. We invert for the uniform internal fluid pressure, p_0 , necessary to open the crack to match the required volume against all external and internal tractions. Non-linear complementarity conditions are imposed such that the crack's faces cannot interpenetrate (Davis, Healy, and Rivalta, 2019).
2. We calculate the crack opening and the stress intensity at the tipline using the method of Davis, Healy, and Rivalta (2019). In order to reduce artefacts, we smooth the stress intensity along the tip line by averaging the local K_I with its two neighbouring edges.
3. We calculate the advance or retreat of the tipline. At elements where K_I exceeds K_c , the tipline will advance proportional to K_I/K_c . This approximation is akin to the "Paris fatigue law" (Lecampion, Bungler, and Zhang, 2018). The maximum crack advance will occur at the triangle where K_I is maximum; this advance is set equal to the mesh's average triangle size. The triangular elements that close are removed. The simulation assumes the fluid is inviscid, and, as such, we cannot retrieve time-dependent propagation rates.
4. Once the fracture's edge has been updated, it is re-meshed and cleaned such that the triangles on the fractures tip-line are approximately equal size and isosceles (Da and Cohen-Steiner, 2019).

For a description of the numerical methods accuracy, see chapter 7.3. We start the simulation with a vertical penny-shaped crack. We fix the number of elements, K_c , $\Delta\gamma$, μ , ν and the volume

of fluid, V . We set the initial radius to $0.4c$, (Eq. 3.4). In our 350+ simulations we use variables spanning several orders of magnitude: $G=190\text{--}5\cdot 10^{10}\text{Pa}$, $\nu=0.25\text{--}0.49$, $\Delta\gamma=7.8\cdot 10^2\text{--}2.2\cdot 10^4\text{Pa}\cdot\text{m}^{-1}$ and $K_c=1\text{--}1\cdot 10^8\text{Pa}\cdot\text{m}^{0.5}$. We state the fracture has reached self-sustaining ascent when its upper tip has travelled $4c$ upwards.

For all simulations, independent of mesh sampling, we find that if $V = 0.7V_c^{an}$ the numerical code returns a trapped fracture and if $V = 0.8V_c^{an}$ the fracture always reaches self-sustaining propagation. Therefore, scaling Eq. 3.6 by 0.75 supplies the numerical estimate of V_c , independent of the scale we use:

$$V_c^{num} = 0.75 \frac{(1 - \nu)}{16\mu} \left(\frac{9\pi^4 K_c^8}{\cos(\theta)\Delta\gamma^5} \right)^{1/3} \quad (3.7)$$

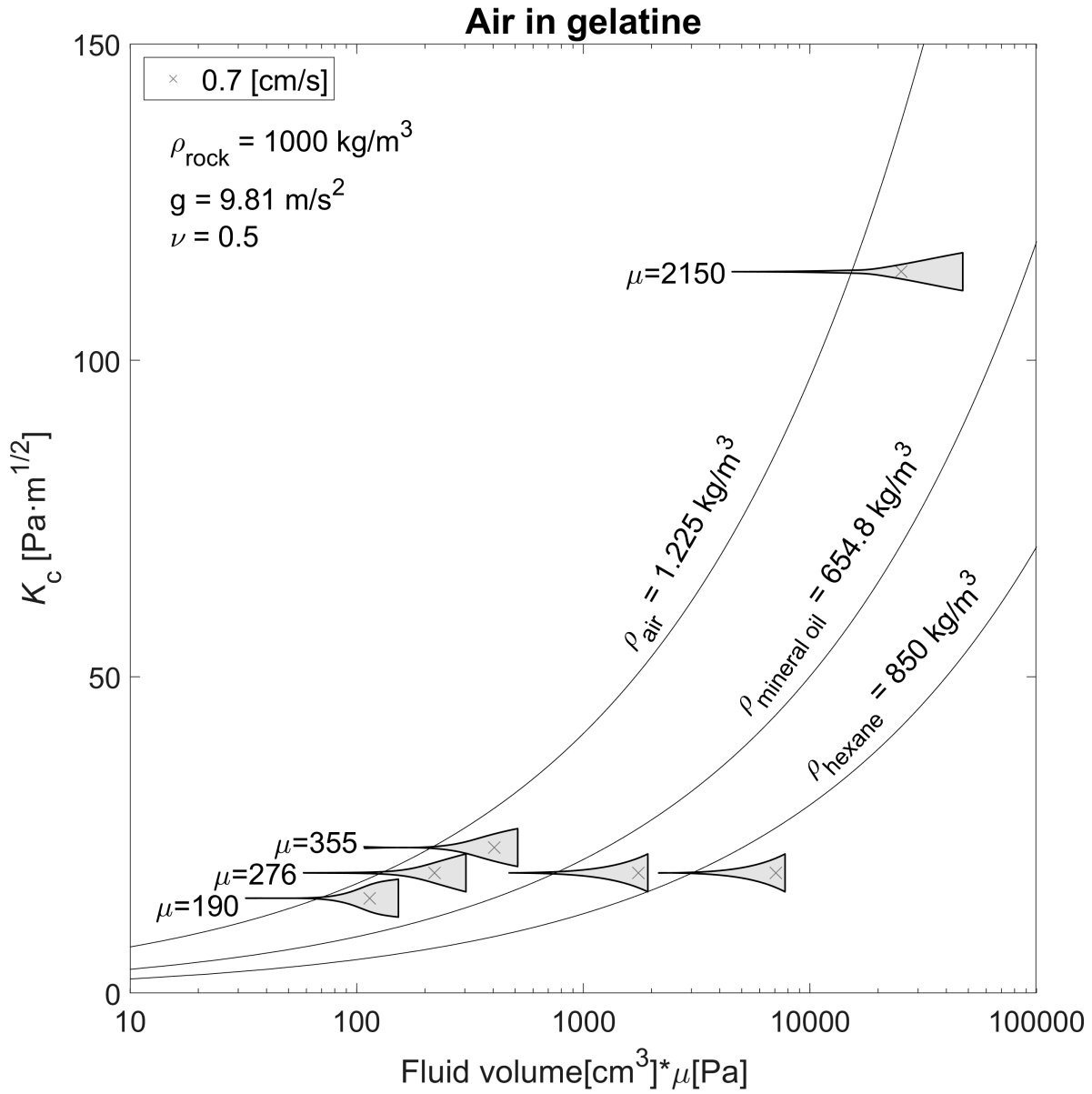
For all cracks that reached self-sustaining propagation the horizontal and vertical lengths were greater than $\sim 0.6c$ and $\sim 1.14c$, respectively.

3.2 Applications

3.2.1 Analog gelatine experiments

The analog study of Heimpel and Olson (1994) inspects critical volumes of fluids ascending in gelatine blocks of different stiffness and fracture toughness (Fig. 3.3). The graph of volume vs speed from their experimental results shows a rapid increase in speed past a certain volume. The authors interpret that at velocities past $\sim 0.7\text{ cm/s}$ (crosses in Fig. 3.3), the ascent transitions from a sub-critical propagation regime ($K_I < K_c$); where the fracture growth speed at the tip limits the velocity (Atkinson and Meredith, 1987b), to a dynamic propagation regime. We test if our equation can predict volume of fluid that causes this transition in ascent speed. As Heimpel and Olson (1994) estimate K_c directly from this change in velocity, to verify that we can use this estimation, we calculate K_c differently; directly from the measured value of G . Strain energy release \mathcal{G} increases with greater stiffness in gelatin solids: $\mathcal{G}[\text{N/m}] \approx 6.66 \cdot 10^{-4} G[\text{Pa}]$ (Czerner et al., 2016). This second independent estimate of K_c lies within $5\text{ Pa}\cdot\text{m}^{1/2}$ of the original estimate. Using $\rho_r=1000\text{ kg}\cdot\text{m}^{-3}$, $\nu=0.5$ and setting μ , ρ_f and K_c to match the experiments of Heimpel and Olson (1994), we find that our value of V_c^{num} independently captures the point at which the velocity transitions, described above, supporting the previous interpretation that this describes the transition to dynamic fracture propagation.

Figure 3.3: $V^*\mu$ vs K_c from Heimpel and Olson (1994). Eq. 3.7 predictions shown as black lines. The thickness of the grey filled patches represents the velocity of the crack as the volume increases, normalised by maximum observed velocity.



3.2.2 Magmatic dykes

We consider magma propagation volumes at Piton de la Fournaise, La Réunion, to see how our equation matches observed dyke volumes. The volumes of the dyke intrusions observed between 1998-2016 range from $0.05\text{-}3.2 \cdot 10^6 \cdot \text{m}^3$ (Froger et al., 2004; Fukushima, Cayol, and Durand, 2005; Fukushima et al., 2010; Smittarello et al., 2019). Using $\rho_r - \rho_f = 100 \text{ kg} \cdot \text{m}^{-3}$, $\mu = 5 \text{ GPa}$, $\nu = 0.25$ and K_c ranging from 29 to $112 \text{ MPa} \cdot \text{m}^{1/2}$ (Fukushima et al., 2010; Delaney and Pollard, 1981), we retrieve $V_c^{num} = 0.05 \cdot 10^6$ and $2 \cdot 10^6 \cdot \text{m}^3$, respectively. The critical volumes we estimate are consistent with the observed dyke sizes. As such our approximation predicts the correct scale in natural settings, provided K_c values estimated from field data are used, noting such field values appear to correct due to a number of additional processes that we have disregarded, instead of being representative of the rock strength at the scale of a laboratory sample.

3.2.3 Water injection into stiff rock

The UK government defines hydraulic fracturing as operations that use over $1,000 \text{ m}^3$ of fluid per frack stage. During a hydro-fracturing procedure, proppant is injected in the final phase to maintain an open fracture (e.g. spherical quartz grains). After the operation, not all injected fluid is recovered when the wellhead valve is opened: Vidic et al. (2013) report an average of only 10% fluid recovery in flowback waters, noting that this recovery volume decreases when shut-in times are longer. Using $\rho_r = 2700 \text{ kg} \cdot \text{m}^{-3}$, $\rho_f = 1000 \text{ kg} \cdot \text{m}^{-3}$, $\mu = 8.9 \text{ GPa}$, $\nu = 0.25$ and K_c in the range $0.36\text{--}4.05$ to $7\text{--}25 \text{ MPa} \cdot \text{m}^{1/2}$, we obtain $V_c^{num} = 6 \cdot 10^{-2}$ and 500 m^3 respectively. These K_c values are for laboratory-sized shale samples from 100 to 1000 m confining pressure and effective K_c values estimated for veins in the field, respectively (Gehne et al., 2020; Olson, 2003). Current operations use volumes around double our highest predicted limit. Few observations attest to the fact that industrial operations can cause ascent of fluids in fractures. One such example, are the spectacular surface fissures created due to steam injection documented in Schultz (2016); additional examples can be found in Schultz, Mutlu, and Bere (2016). Geochemical data from aquifers above fracking operation sites has shown some evidence of the contamination of overlying units, which is attributed to poor well casing design, rather than fracture ascent (Vidic et al., 2013). Usually, microseismic monitoring of actual fracking operations show limited vertical extents of the fractures, however, these data are proprietary and methodological descriptions are scarce (Fisher and Warpinski, 2012). Experimental fracturing data is of little help as volumes injected are typically below or close to our volumetric limit, with injected volumes of 2 to 20 m^3 (Warpinski, Schmidt, and Northrop, 1982;

Pandurangan, Chen, and Jeffrey, 2016).

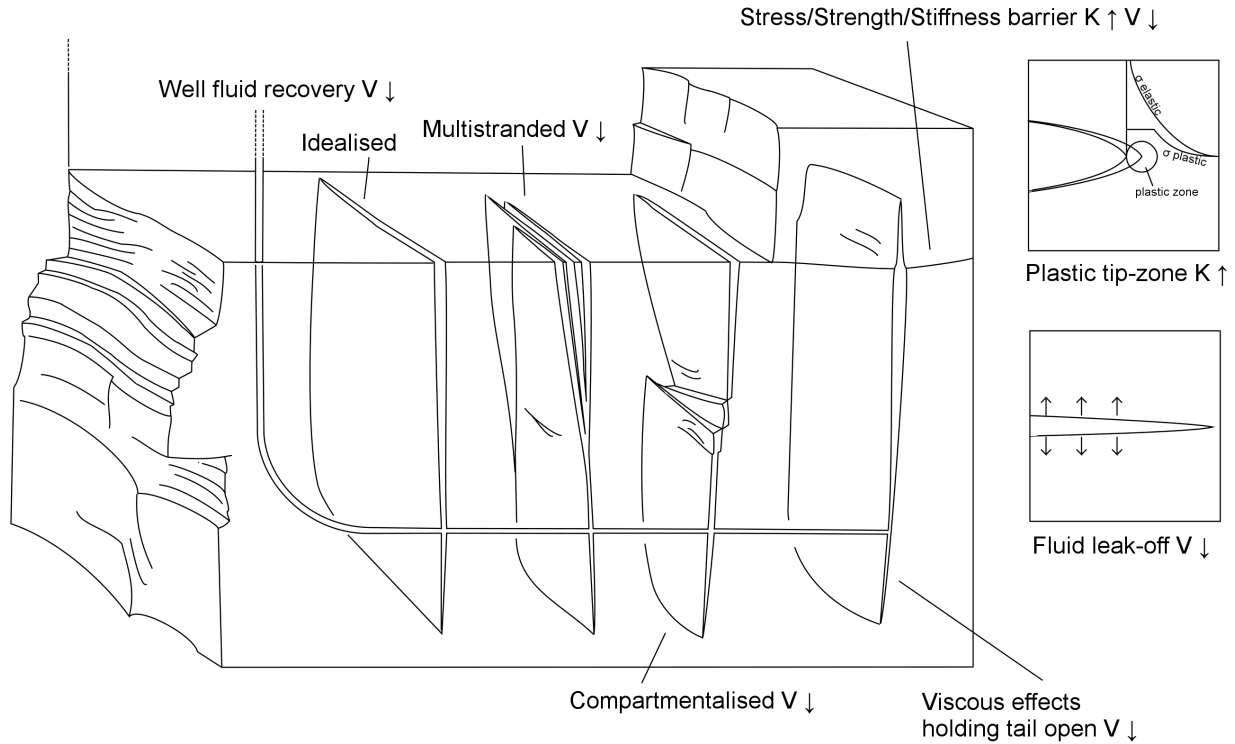
Natural degassing, such as CO₂ in the Cheb basin, Czech Republic, has chemical signatures of fluids that have ascended over 20 km through the crust (Weinlich, 2014). Fracture driven ascent can explain this phenomena without the requirement of permanent highly conductive fluid pathways at great depths. Supercritical CO₂ at depth has a similar density to water, and as such may be a good natural analog for water filled fracture ascent. We saw that in analogue and magmatic examples Eq. 3.7 predicts the correct order of magnitude of critical volumes; at the same time, it appears that this equation is conservative for high volume water injection as fracture ascent in these settings has rarely been observed.

3.3 Discussion and conclusions

In summary, Eq. 3.7 provides an estimate of the minimum fluid volume for self-sustained propagation of fluid-filled fractures, ranging from cm to tens of km. V_c is dependent on $K_c^{8/3}$; since K_c is often poorly constrained V_c suffers from large uncertainties. Values of K_c obtained in laboratory experiments show a strong dependency on pressure and temperature. Field estimates of effective K_c from trapped fractures can be orders of magnitude larger. An effective way to estimate K_c in Eq. 3.7 incorporating all processes affecting the energy needed to extend the fracture at different scales would clearly be beneficial for any fracture mechanics based analysis of rock masses and the resultant interpretations.

In our derivation we have neglected the effects of viscosity. Whether these effects will dominate over toughness in determining fracture growth can be assessed by evaluating the time scale needed for the fluid pressure to equilibrate within the crack, as this will mean that viscous dissipation is low and crack growth will be toughness-dominated (Bunger and Detournay, 2007). The model of Bunger and Detournay (2007) assumes a constant injection rate with no stress gradients, we assume this still provides a rough estimate of the timescale until this transition. Typical industrial operations use fluid viscosity of 0.001-0.01 Pa·s, injection rates between 0.5-10 m³/min and stiffness's of 10-40 GPa. Using low values of K_c from laboratory experiments in shale, 0.36 MPa·m^{1/2}, this transition time ranges between 1 minute to times exceeding the end of injection. Whereas, setting K_c higher, values for shale at depth, e.g. 4 MPa·m^{1/2} this significantly reduces this range from milliseconds to a maximum of 5 hours. This suggests that, depending on K_c , Eq. 3.7 can be a relevant estimate of V_c^{num} , independent of viscous forces.

Figure 3.4: Processes that can hinder fracture ascent, K and V relate to effective K_c and V_c operating in Eq. 3.7



While theory and experiments support Eq. 3.7, this appears to be overly conservative in practice, as injections of quantities of fluid exceeding this do not result in significant ascent in most cases. In part, this discrepancy results from our simplification of the process, as mass conserving propagation in a homogeneous linear-elastic medium. Fig. 3.4 shows a schematic of processes not quantified in relation to critical fluid volumes which we review in detail below.

1. A series of mechanisms can reduce V during propagation and thus promote crack arrest. These include leak-off from the fractures faces, the fracture becoming multistranded/compartimentalised, fluid recovery (extraction), or fluid remaining in the tail of the fracture due to added proppant or viscous forces (Taisne and Tait, 2009).
2. Mechanisms that can lead to an effective increase of K_c , and thus also promote crack arrest, include plastic tip processes, the fracture entering in a zone of damage of the host rock (Sih, Paris, and Irwin, 1965; Kaya and Erdogan, 1980), or seismicity surrounding the fracture,

causing reduction in the system's energy/blunting the fracture's tip (Rivalta et al., 2015).

3. Heterogeneous μ or K_c or stress barriers may also lead to arrest of fractures by deflection or promoting lateral growth (Maccaferri, Bonafede, and Rivalta, 2011; Bungler and Lecampion, 2017; Warpinski, Branagan, and Wilmer, 1985),
4. Eq. 3.7 has a clear dependency on the fracture's dip. If the minimum compressive stress is vertical, this promotes flat lying fractures.

Quantification of processes acting to halt fracture ascent, especially in the context of the variables in our equation, are critical to understand which volumetric limits can be deemed safe. In particular, the gradient in stress with depth must be included to assess this process. Without such quantification, regulation of this industrial process will continue to rely on empirical evidence for safe rates, volumes and depths from select operations that may not be representative.

Acknowledgements and funding

The authors would like to thank the reviewers Meredith Townsend and Dmitry Garagash for their insightful and constructive reviews of the manuscript. T Davis is funded by the DFG-ICDP grant N. RI 2782/3-1. The code used for the numerical analysis of this study was the open source code <https://doi.org/10.5281/zenodo.3694163> with an interface with the Computational Geometry Algorithms Library software (C++) for meshing.

Chapter 4

Forecasting magma pathways

The content of this chapter has been published in Rivalta, E., Corbi, F., Passarelli, L., Acocella, V., **Davis, T.**, Di Vito, M. A. (2019): Stress inversions to forecast magma pathways and eruptive vent location. *Science Advances*, 5, 7, eaau9784.

One-sentence summary (teaser) We forecast where magma will breach the Earth's surface to erupt based on how the volcano's shape and size have evolved

Abstract

When a batch of magma reaches the Earth's surface it forms a vent from which volcanic products are erupted. At many volcanoes, successive batches may open vents far away from previous ones, resulting in scattered, sometimes seemingly random spatial distributions. This exposes vast areas to volcanic hazards and makes forecasting difficult. Here we show that magma pathways and thus future vent locations may be forecast by combining the physics of magma transport with a Monte Carlo inversion scheme for the volcano stress history. We validate our approach on a densely populated active volcanic field- Campi Flegrei (Italy), where we forecast future vents on an onshore semi-anular belt comprised between 2.3 and 4.2 km from the caldera center. Our approach offers a mechanical explanation for the vent migration over time at Campi Flegrei and at many calderas worldwide and may be applicable to volcanoes of any type.

4.1 Introduction

A basic, poorly investigated problem in volcano hazard studies is that we do not know where the next eruptive vent might form. This problem affects to some extent all active volcanoes, as there is

always at least some chance of eruptive fissures opening in unexpected locations distant from the volcano summit. At central volcanoes with a characteristic cone shape (e.g. Hawaii or Etna) many eruptions are expected to occur on, or close to, the volcano summit. Eruptions also punctuate rifts zones branching from the volcano summit, showing that new fissures may open at low altitude along the rifts, endangering populated areas. Some types of volcanoes, however, do not show any cone-shaped edifice, and lack a summit focusing eruptive activity. This is the case of calderas, km-sized sub circular depressions resulting from the drainage of magma chambers and collapse of their roof. Calderas have fed some of the most catastrophic eruptions on Earth and are extremely hazardous (Newhall and Dzurisin, 1988). However, their eruptions are generally few and far apart, so hazard is often underestimated by the local population, which at some calderas approaches one million. As calderas are associated with large volcanic fields, with past eruptive vents scattered throughout, the problem of forecasting the location of future eruption is extremely challenging.

Volcano hazard models, including lava and pyroclastic flow or plume expansion and fallout models, have reached high levels of sophistication, but remain poorly constrained due to the large uncertainties on where magma will breach the Earth's surface to create eruptive vents, especially at calderas (Neri et al., 2015). The need of probabilistic maps of future eruptive vents have typically been addressed empirically, based on the surface distribution of past vents (Wadge, Young, and McKendrick, 1994; Connor and Hill, 1995; Cappello et al., 2012). This is generally more or less implicitly justified based on two different underlying assumptions. On one hand, it is sometimes assumed that previous vents mark weaknesses or paths in the host rock that will guide ascending magma. This assumption is not supported by observations, as many volcanoes are punctuated by monogenetic (e.g. used by only one eruption) vents, surrounded by tens of other monogenetic vents. According to a second rationale, the observed vents' patterns reflect an unknown physical controlling mechanism (Cappello et al., 2012), thereby justifying a data-driven approach to create probabilistic maps. An animation of the eruptive history in the last 15 ka at Campi Flegrei caldera (<http://hazard-mapping.org/Campi-Flegrei.html>) illustrates that after the initial phase, where vents are scattered, most vents open relatively close to clusters of previous vents. This qualitatively shows how data-driven approaches work better and better as the density distribution gets populated. However, the number of observed vents at volcanoes rarely exceeds a few tens, so that the underlying physical mechanism remains sampled by too few eruptions to provide a sharp representation of the vent distribution probability; this results in very coarse maps. Indeed, the animation shows that occasional eruptions (including the last 1538 Monte Nuovo eruption) hit locations distant from previous vents: forecasts for such low probability locations will be affected by large uncertainties, as interpolation or extrapolation are needed where data are scarce or lacking. Such eruptions would have been hard to anticipate. Some studies have attempted to complement the

limited statistics by considering fractures (Selva et al., 2012; Bevilacqua et al., 2015), seismicity, tomographic images, geochemistry and gravity (Alberico et al., 2002; Martin et al., 2004). This is also problematic, as there is no clear evidence that including such additional information improves vent forecasts. In fact, fumaroles and fractures may have been caused by, rather than having been a driver of, dike propagation, thus forcing interpretation to a wrong conclusion. These approaches may be difficult to validate or falsify retrospectively.

Forward validation is an outstanding issue for vent forecasts, as these maps are not routinely subject to testing. Performance testing generally involves partitioning the data into calibration and validation datasets. In the case of probabilistic vent opening maps, this translates into recalculating the maps based on the earliest eruptions and verifying the performance on the most recent eruptions. Calculating maps for an arbitrary point in time may not be straightforward if the calculations rely on poorly dated datasets; some of these predictive models may be thus inherently hard to test. Moreover, partitioning the data would lower the number of points used to set up the map, exacerbating the issues linked to the need of extrapolating or interpolating vent density. Despite these limitations, no better method has been proposed to address vent forecasting, hampering progress in volcano hazard modeling.

Here we propose a new concept to vent forecasting based on the combination of physical models of magma transport with Monte Carlo statistics. Numerous theoretical and field studies have established that host rock stresses dictate magma pathways: magma-filled fractures (dikes) feed eruptions, and during ascent to the surface the dikes align themselves with the most energy efficient orientation, which is roughly perpendicular to the least compressive principal stress axis, σ_3 (Pollard, 1987; Anderson, 1951; Gudmundsson, 1995; Roman and Jaupart, 2014; Dahm, 2000a; Fialko, 2001; Maccaferri, Bonafede, and Rivalta, 2010). Contrary to intuition, pre-existing faults appear of subordinate importance in guiding magma (Pollard, 1987; Anderson, 1951; Gudmundsson, 1995; Roman and Jaupart, 2014), as their orientation in respect to the stress field is optimized for shearing movements so opening along such planes is inefficient. In this framework, dike trajectories can be predicted, provided we know with sufficient resolution the volcano stress field and the dike starting location (the magma chamber). Stress magnitudes and directions in crustal rocks, however, are generally very poorly constrained. Despite this, we show that magma trajectories, and thus eruptive vent locations, are so sensitive to stress variations that the previous vent locations at a volcano can be used to constrain the stress field to a sufficient degree of accuracy to render reliable physics-based vent forecasts possible.

4.2 Model and inversion scheme

4.2.1 Concept of the vent forecast scheme

We propose a scheme based on three independent blocks: 1) a deterministic model for magma trajectories and thus vent opening where the dike trajectories intersect the Earth's surface, 2) a deterministic model for the volcano stress field, needed to calculate the dike trajectories, 3) a probabilistic scheme to constrain, based on the observed vents, the posterior distributions of all models' parameters. In other words, under the assumption that crustal stresses govern dike trajectories, we will retrieve the model parameters' distributions that lead magma to propagate from the known magma reservoir's location to the location of the observed vents. Finally, probabilistic forecasts are obtained by combining the deterministic models with the posterior parameter distributions. In the following, we first introduce the general scheme and outline some of the options available to deal with the three blocks described above. Next, we apply the scheme to vent forecasting at Campi Flegrei caldera. For this first application, we opt for the simplest deterministic and statistic models in order to enhance ease of explanation and model transparency.

State-of-the-art models for magma propagation trajectories are based on maximizing tensile stresses at the dike tipline (Fialko, 2001) or energy release rate on prospective dike incremental elongations (Dahm, 2000a; Maccaferri, Bonafede, and Rivalta, 2010). These models account for magma buoyancy pressure and allow for mixed-mode propagation, and are thus capable of treating accurately the effects of layering or the free surface. These methods however involve several parameters. In our application to Campi Flegrei we use a simpler option: magma propagates strictly perpendicular to the least compressive principal stress axis, σ_3 . According to this approximation, magma-driven fractures will be pure opening fractures (Pollard, 1987; Anderson, 1951). In other words, development of mixed-mode fractures resulting e.g. from the interaction of the dike with layering or the free-surface will be neglected; the resulting bias on the trajectories is discussed below. In 3D, the directions perpendicular to σ_3 in every point of space identify a family of surfaces on which magma is assumed to propagate; these will intersect the Earth's surface as a curve on which the eruptive fissure will lie. In 2D, the surfaces become σ_3 -perpendicular streamlines, i.e. curves aligned in every point to σ_1 . These surfaces or curves are obtained from the eigenvalues and eigenvectors of the stress tensor in every point of the crustal volume under investigation. Deterministic simulations of magma trajectories rely on a well-balanced stress model for the volcano. Layering affects edifice stresses and magma trajectories (Maccaferri, Bonafede, and Rivalta, 2010) but the benefit of considering it should be weighed against the need of including

detailed information on numerous, often poorly constrained, structural parameters. For our application to Campi Flegrei we take a simpler approach and assume a homogeneous half-space.

For the parameters inversions, efficient Bayesian resampling methods, such as Markov Chain Monte Carlo (Moorkamp et al., 2016), are probably the best option for the general case. In our application to Campi Flegrei we resort to the computationally inefficient but simple Sampling/Importance Resampling (SIR) algorithm (Rubin, 1988; Passarelli et al., 2010). The SIR is a non-iterative Bayesian Monte Carlo “perfect sampler” (Moorkamp et al., 2016): a large number of magma propagation trajectories are calculated at the beginning of the procedure based on prior distributions for the model parameters; from this set, a subset is selected (resampling) so that the modelled arrivals at the Earth’s surface reproduce exactly the empirical distribution of observed vents. The resampling results in posterior distributions of the model parameters, which can then be used in forward mode to compute a large number of magma trajectories and thus well-populated probabilistic vent forecasts.

In the following, we describe the details of the general conceptual scheme and present a simple application to Campi Flegrei. Finally, we discuss the potential and limits of the approach, considering the physical plausibility of the inversion results and testing the forecasts’ performance.

4.2.2 Parametric volcano stress model

We assume the background state of stress (i.e. before the establishment of any volcanic edifice) is Andersonian (i.e. the Earth’s surface is stress free and one of the principal stress axes is vertical). Under this assumption, given that the equations of elasticity are linear, trajectory calculations may rely just on the perturbations from a lithostatic stress state (Fialko, 2001). We assume that the local state of stress will evolve at any time, t , and point in space, $(x, y, z > 0)$, as the linear superposition of both slow and sudden processes affecting the volcano history:

$$\begin{aligned} \sigma_{TOT}(x, y, z, t) = & \sigma_t(x, y, z, t) + \sigma_C(x, y, z, t) + \\ & \sigma_L(x, y, z, t) + \sigma_U(x, y, z, t) + \sigma_I(x, y, z, t) + \sigma_E(x, y, z, t) \end{aligned} \quad (4.1)$$

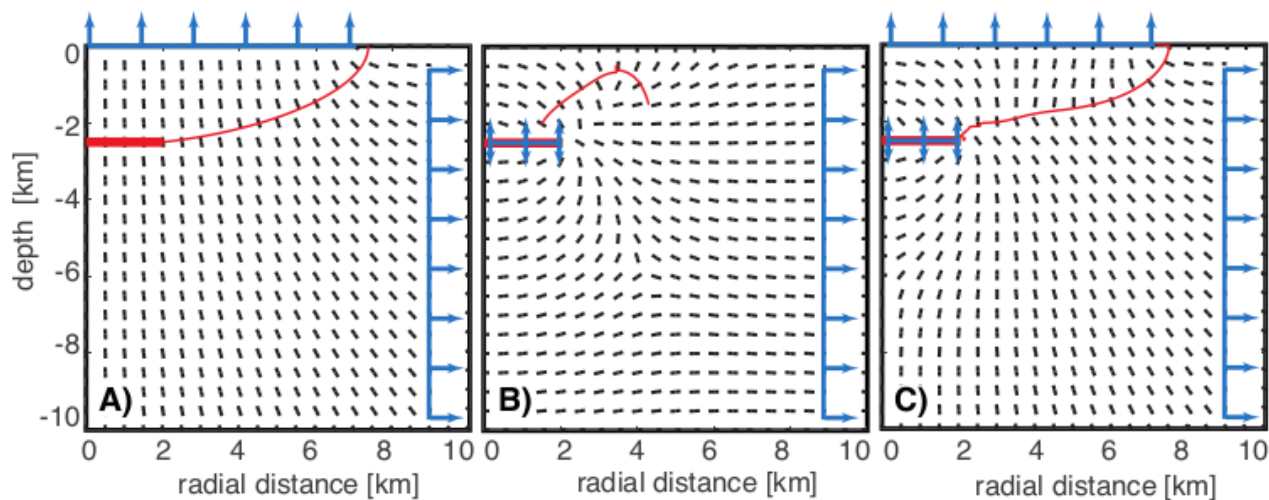
where $\sigma_{TOT}(x, y, z, t)$ is the supra-lithostatic full stress tensor, $\sigma_t(x, y, z, t)$ is the regional tectonic stress tensor, $\sigma_C(x, y, z, t)$ is the stress perturbation due to magma chamber pressurization (Chadwick Jr and Dieterich, 1995; Gudmundsson, 2012), $\sigma_L(x, y, z, t)$ is the stress perturbation due to edifice load (Roman and Jaupart, 2014; Dahm, 2000a; Pinel and Jaupart, 2000), $\sigma_U(x, y, z, t)$ is

the stress perturbation due to unloading caused by mass redistributions due e.g. to icecap melting (Hooper et al., 2011), excavation of a caldera (Corbi et al., 2015) or a flank collapse (Ventura, Vilardo, and Bruno, 1999; Maccaferri, Richter, and Walter, 2017), $\sigma_I(x, y, z, t)$ is the stress tensor due to previous magmatic intrusions, $\sigma_E(x, y, z, t)$ is the stress tensor due to previous large earthquakes or slow slip events. Multiple or additional terms may be appropriate in special cases. Coupling between these terms, where for example edifice loading influences magma chamber shape and thus its stress perturbation, are neglected in this first-order linear approach. Fully interacting approaches, relying e.g. on boundary element calculations, is also compatible with our general scheme and can be considered in future studies.

The terms in Eq. 4.1 are not all equally important: they are roughly ordered according to a decreasing extent of the stressed rock volume, since these stresses decay away from the source over a distance that scales with the size of the pressurised area (Roman and Jaupart, 2014). This translates in the list being ordered roughly according to expected relevance. so that σ_T , σ_L and σ_U are often dominant. Stresses around a pressurized magma chamber control the location of magma chamber rupture and have been commonly considered the dominant component of edifice stresses (Chadwick Jr and Dieterich, 1995; Gudmundsson, 2012; Pinel and Jaupart, 2000). However, evidence is accumulating that their importance in determining magma trajectories may have been overestimated. Recent volcano stress models considering a combination of tectonic and edifice loading and unloading stresses have successfully explained magma trajectories, dike orientation and vent location in diverse settings (Roman and Jaupart, 2014; Hooper et al., 2011; Corbi et al., 2015; Ventura, Vilardo, and Bruno, 1999; Maccaferri, Richter, and Walter, 2017), as opposed to corresponding ones involving only magma chamber stresses (Chadwick Jr and Dieterich, 1995). Loading/unloading stresses scale with the height of the edifice or the caldera effective depth (i.e. including the contribution of low-density infill). Depending on the case this may amount to large loading or unloading, e.g. a 4000 m tall edifice or a 1000 m deep caldera correspond to 100 MPa and 25 MPa loading or unloading, respectively. Moreover, loading/unloading decays approximately as R^{-1} over a vertical distance R that scales with the edifice or caldera radius. The distance over which magma chamber pressurization stresses decay depend on magma chamber shape, but in general they are only intense in the proximity of the chamber and decay very fast away from it, e.g. as R^{-2} for a spherical chamber (Roman and Jaupart, 2014). We further stress the relative importance of magma chamber and loading/unloading by calculating a simple finite element model comparing stress trajectories due to a shallow topographic depression of 200 m with those around a pressurized sill and those with both depression and sill (Fig. 4.1A, B, C). Results show, consistent with previous studies comparing the effect of edifice loading and magma chamber stresses on magma trajectories Roman and Jaupart, 2014, that even for such a shallow caldera the model

that only contains unloading stresses has trajectories like those of the composite model, while the magma chamber stress model does not. Thus, the purely unloaded model is preferable, as it describes magma trajectories satisfactorily, with a lower number of parameters. Moreover, magma chambers depressurize upon magma transfer into a dike, so that magma chambers stresses further lose importance over the course of the pre-eruptive phase. In conclusion, tectonic stresses and stresses due to mass redistribution at the surface often dominate in volcano edifices except for very close to the magma chamber.

Figure 4.1: Numerical FE models of principal stresses orientation and resulting magma trajectories. σ_3 is represented by the black segments, the thick red line represents the location of a sill-shaped pressurised melt lens, the thin red lines represent σ_3 -orthogonal streamlines. A) “unloading scenario” where we applied 9 MPa of vertically oriented tensional stress due to overburden removal (blue arrows); B) “inflating sill scenario” where we applied 5 MPa pressure to a thin flat cavity; and C) “unloading + inflating sill” scenario where we combined the two previous cases. We added a weak (1 MPa) horizontal stretching to all models.



Similar to magma chamber pressurization stresses, σ_I and σ_E are very intense in the near field but decay rapidly with distance, thus are in general of smaller magnitude than σ_L and σ_U except for very close to the intrusion or fault (Roman and Jaupart, 2014). In other words, it takes many intrusions or large earthquakes to compensate for stresses induced by edifice growth or partial collapse. However, the effect of previous intrusions may still be important to consider: subsequent intrusions may preferably arrange in a complementary fashion to cumulatively compensate for strains caused e.g. by loading or flank dynamics. Unfortunately, old intrusions are often poorly constrained, and we neglect this effect in our application to Campi Flegrei.

Even if the stress model is well balanced, magma trajectories calculated deterministically based on Eq. 4.1 may poorly match observations, as stresses are generally ill-constrained. Indeed, during the lifetime of volcanoes loading/unloading stresses may evolve in complex ways, with stress-releasing and homogenizing processes such as earthquakes or magma intrusions periodically alternating with collapse episodes and stress build-up processes, e.g. superposition of layers of erupted products. Thus, loading stresses calculated based on the 3D topography of the volcano, as if it was built instantaneously, are generally overestimated (Chadwick Jr and Dieterich, 1995; Corbi et al., 2015; Maccaferri, Richter, and Walter, 2017). We propose a probabilistic scheme to constrain poorly known stresses based on empirical data. To this aim, we rewrite Eq. 4.1 in parametric form as:

$$\begin{aligned} \sigma_{TOT}(x, y, z, t) = & \sigma_T(t) + P_C(t)G_C(x, y, z) + P_L(t)G_L(x, y, z) + \\ & P_U(t)G_U(x, y, z) + P_I(t)G_I(x, y, z) + \tau_E(t)G_E(x, y, z) \end{aligned} \quad (4.2)$$

where P_C , P_L and P_U are scalar chamber supra-lithostatic pressurization, and gravitational loading and unloading pressures, respectively, P_I is magma pressure minus the stress normal to the intrusions, τ_E is the static shear stress released by any significant earthquake and $G_C, L_U, I, E(x, y, z, t)$ incorporate the variability in space and time of the stress perturbations induced by the individual processes, respectively. $\sigma_t, P_L, P_U, P_C, P_I, \tau_E$ are the parameters to be inverted for. The assumption behind Eq. 4.2 is that the uncertainties on the stress field are represented by uncertainties on the scaling factor of each contribution, while their spatial variability is known to a much better degree of certainty.

4.2.3 Location of dike nucleation

Eruptive vents are often interpreted as originating from vertical magma propagation from a “mirror” location directly below the vent. Thus, when the vent distribution shows migration patterns, this is often attributed to a migration of the magma source. Here we argue that the curvature of stress-controlled magma pathways may offset significantly vent location from their source at depth (Dahm, 2000a; Corbi et al., 2015; Maccaferri, Richter, and Walter, 2017), adding uncertainty to the starting location of the dikes. In our approach, the dike starting location can be either assumed based on independent observations, or treated as an additional unknown to be inverted for. We will show below that stresses and magma starting locations cannot be both determined independently with a high degree of accuracy, as they suffer from a strong trade-off. Thus, incorporating independent

information on the magma starting location may be critical to an accurate resolution of edifice stresses. Crustal deformation may provide the most reliable constraint, as magma chamber shape strongly influences the location of magma chamber rupture (Gudmundsson, 2012; Pinel and Jaupart, 2000). At many calderas, crustal deformation is often consistent with thin horizontal penny-shaped cracks as sinks of melt accumulation. Such penny-shaped cracks are expected to rupture somewhere at their tip-line, at a depth d and radial distance from the center r .

4.2.4 Probabilistic scheme and inversion procedure

First, the stress field due to the individual contributions in Eq. 4.2 is estimated from the 3D topography, edifice history and structural information, e.g. by applying a distribution of loads on the Earth's surface to mimic topography (Roman and Jaupart, 2014; Dahm, 2000a; Corbi et al., 2015; Ventura, Vilardo, and Bruno, 1999; Maccaferri, Richter, and Walter, 2017). Once all G terms in Eq. 4.2 have been estimated, prior distributions for the P terms, $p(\theta)$, are defined according to plausible ranges or any other prior information available. Based on those prior distributions, a set of random parameters are drawn, the stress tensor (Eq. 4.2) is calculated and diagonalized to obtain the principal stresses. Trajectories are then calculated starting from the known location of the magma chamber, or, alternatively, depth d and radius r of dike nucleation can be included among the parameters inverted for. The dike arrivals at the Earth's surface for all combination of random parameters result in a modelled vent distribution $p(x)$. A Bayesian resampling scheme will return the likelihood $p(x|\theta)$ and the posterior distributions of the model parameters $p(\theta|x)$.

In the SIR scheme the distribution $p(x)$ is resampled by only retaining in each bin x_i a fraction of modelled vents:

$$w(x_i) = [Y^0(x_i)/Y^m(x_i)] / \sum_i [Y^0(x_i)/Y^m(x_i)] \quad (4.3)$$

where $w(x_i)$ are the importance weights (Rubin, 1988; Passarelli et al., 2010) and $Y^0(x_i)$ and $Y^m(x_i)$ are the distribution of the observed and modelled vents, respectively. The resulting likelihood replicates exactly the distribution of the observations and restitutes posterior probabilities for the model parameters. Combining such posteriors with the deterministic stress and trajectory models results in a probabilistic stress field model that can be used to compute forecasts.

4.2.5 Explanatory models and forecasts

We now illustrate how our stress inversion procedure can help both improving the understanding of vent migration patterns during a volcano's history as well as producing probabilistic forecasts that are testable at least in retrospective. We illustrate below this explanatory and predictive potential with application to Campi Flegrei. For our explanatory model, we invert for stress parameters and location of dike nucleation. For our forecasts, we will reduce the set of parameters by fixing the magma chamber depth and radius to take advantage of information from inversion of crustal deformation data. Precondition for a stress inversion is that tectonic and edifice stresses were roughly stable over the period of formation of a set of vents. Such a stationary stress state is an idealization of reality, as each batch of magma will change the stress field with its eruption deposits or from permanent host rock deformation. Nevertheless, as discussed above, a volcano eruptive history is often punctuated by a few dominant events. These events ideally partition the volcano's eruptive history in a series of approximately stationary stress epochs that we can use to partition the vent data for the inversions. Inversion results from different epochs can then be compared with the edifice history to learn about how major edifice-modifying events are reflected in the estimated stresses. In particular, estimates of P_L and P_U obtained from the inversion, $P_{L,m}$ and $P_{U,m}$, are expected to amount to a fraction of $P_{L,o} = \rho_L g h_L$ and $P_{U,o} = \rho_U g h_U$, i.e. those expected from the observed 3D volcano structure, with ρ_L and ρ_U average density of the added crustal material and the excavated volume, respectively, g acceleration due to gravity, h_L and h_U height of the edifice and thickness of the overburden removal, respectively. The fractions $R_L = P_{L,m}/P_{L,o}$ and $R_U = P_{U,m}/P_{U,o}$, where subscripts m and o indicate pressures resulting from the inversion and modeled based on the stratigraphy, respectively, are a proxy for the longevity of elastic stresses in the volcanic edifice.

4.3 Results and discussion

4.3.1 Application to Campi Flegrei caldera

We test our approach against the high-risk Campi Flegrei caldera (Italy). Campi Flegrei (CF; Fig. 4.2A) caldera formed during the eruptions of the Campanian Ignimbrite ~ 39 ka and the Neapolitan Yellow Tuff (NYT) ~ 15 ka (Rosi and Sbrana, 1987; Deino et al., 2004). Post-caldera volcanism developed >70 monogenic vents focused in the NE, presently onshore, sector of the

Figure 4.2: (Continued on the following page.)

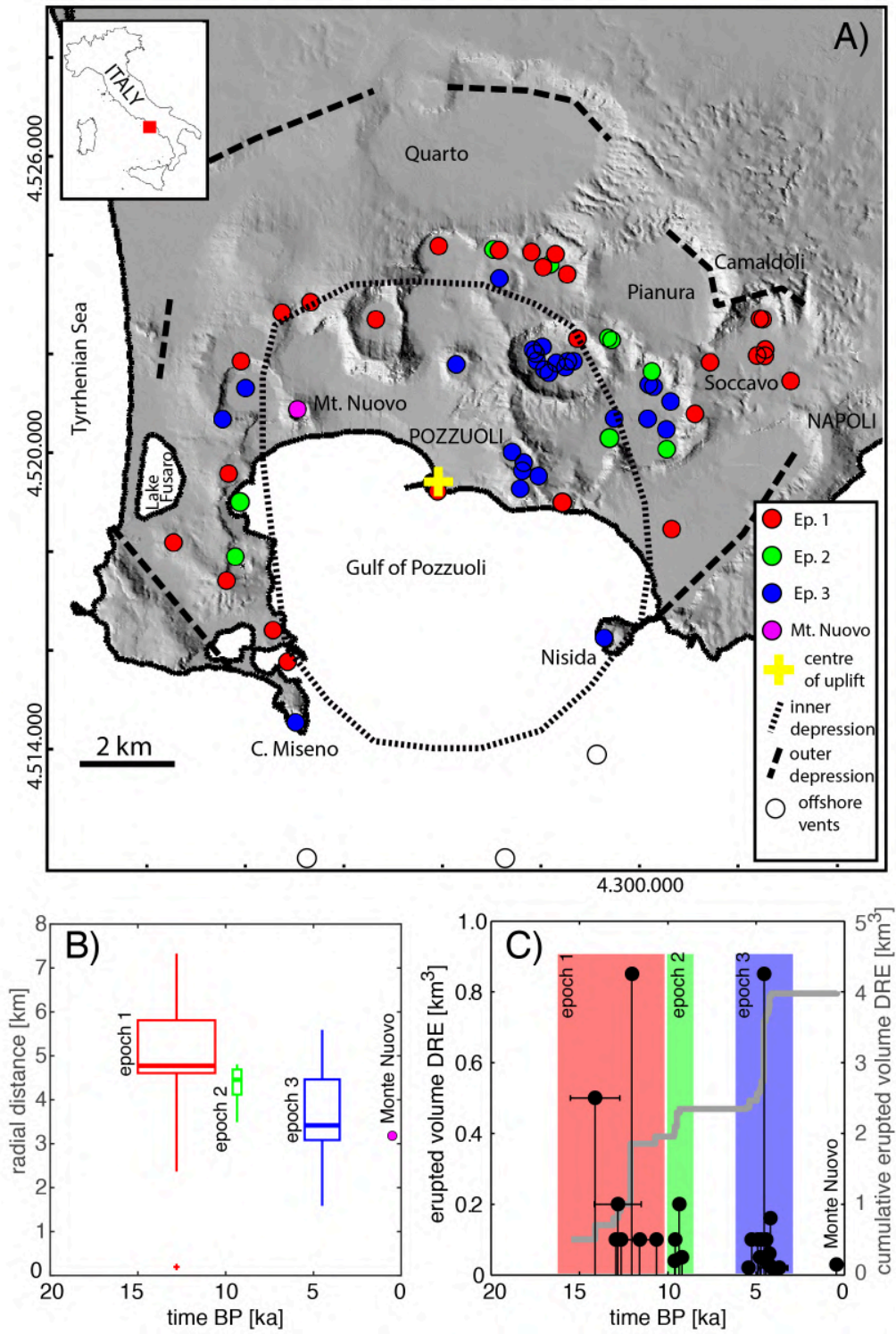


Figure 4.2: Eruptive history of the Campi Flegrei caldera during the last 15 ka. A) Shaded relief map of the caldera with location of eruptive vents (Isaia, Marianelli, and Sbrana, 2009). B) Boxplot showing the radial distribution of eruptive vents. The boxes have horizontal lines at the 1st quartile q_1 , median, and 3rd quartile q_3 . The whiskers correspond to 99.3 percent data coverage. The red circle at epoch 1 is an outlier (i.e., data point that is smaller than $q_1 - w(q_3 - q_1)$; where w is the whisker length). The horizontal size of the boxes represents the time interval of the epoch. C) Volume of eruptions and cumulative (gray line) erupted volume (Isaia, Marianelli, and Sbrana, 2009).

caldera. Eruptive activity migrated progressively inward over epochs 1 (15-9.5 ka), 2 (8.6-8.2 ka), and 3 (4.8-3.7 ka) (Fig. 4.2A, B) (Di Vito et al., 1999; Orsi, Di Vito, and Isaia, 2004; Isaia, Marianelli, and Sbrana, 2009; Smith, Isaia, and Pearce, 2011). Deposition of 25-300, 3-25 and 5-80 m thick eruptive products over the three epochs, respectively, has partially refilled the inner caldera (Di Vito et al., 1999). Coeval resurgence uplifted the caldera central sector of 180 m, of which >60 m in the last ~5 ka (Steinmann, Spiess, and Sacchi, 2018). The last eruption occurred at Monte Nuovo, in 1538 (Di Vito et al., 1999; Di Vito et al., 2016), whereas the most recent activity consists of four unrest episodes in 1950-1952, 1969-1972, 1982-1984 and 2005-Present, with uplift of ~0.7 m, ~1.7 m, ~1.8 m and ~0.4 m, respectively (Amoruso, Crescentini, and Sabetta, 2014)(Amoruso et al., 2007). Inflation of a caldera-centered oblate spheroidal magma chamber at depth ~3.5 km is consistent with the deformation in the last ~600 years at least (Di Vito et al., 2016; Amoruso et al., 2007). The inward migration of post-collapse volcanism (Fig. 4.2B) and the onshore focusing of vents (Fig. 4.2A) are both currently unexplained. In fact, a progressive shrinking of the magma chamber (Barberi et al., 1991), invoked to explain the observed inward vent migration, is inconsistent with the approximately constant eruptive rates in the last 15 ka (Fig. 4.2C) (Amoruso, Crescentini, and Sabetta, 2014) and the inferred size of the stationary shallow magmatic source in the last ~5 ka (Di Vito et al., 2016). Also, the onland focusing of the vents, previously explained by the activity of a tilted resurgent block (Orsi, De Vita, and Di Vito, 1996), is in contrast with later studies highlighting a non-tilted resurgent dome (Acocella, 2010).

4.3.2 Forward explanatory model for Campi Flegrei

Our working hypothesis is that the inward vent migration observed over the last 15 ka has been caused by stress variations. We simplify drastically Eq. 4.2 with the aim of keeping the number of parameters low. Loading from the volcanic edifice may be neglected due to the lack of an important

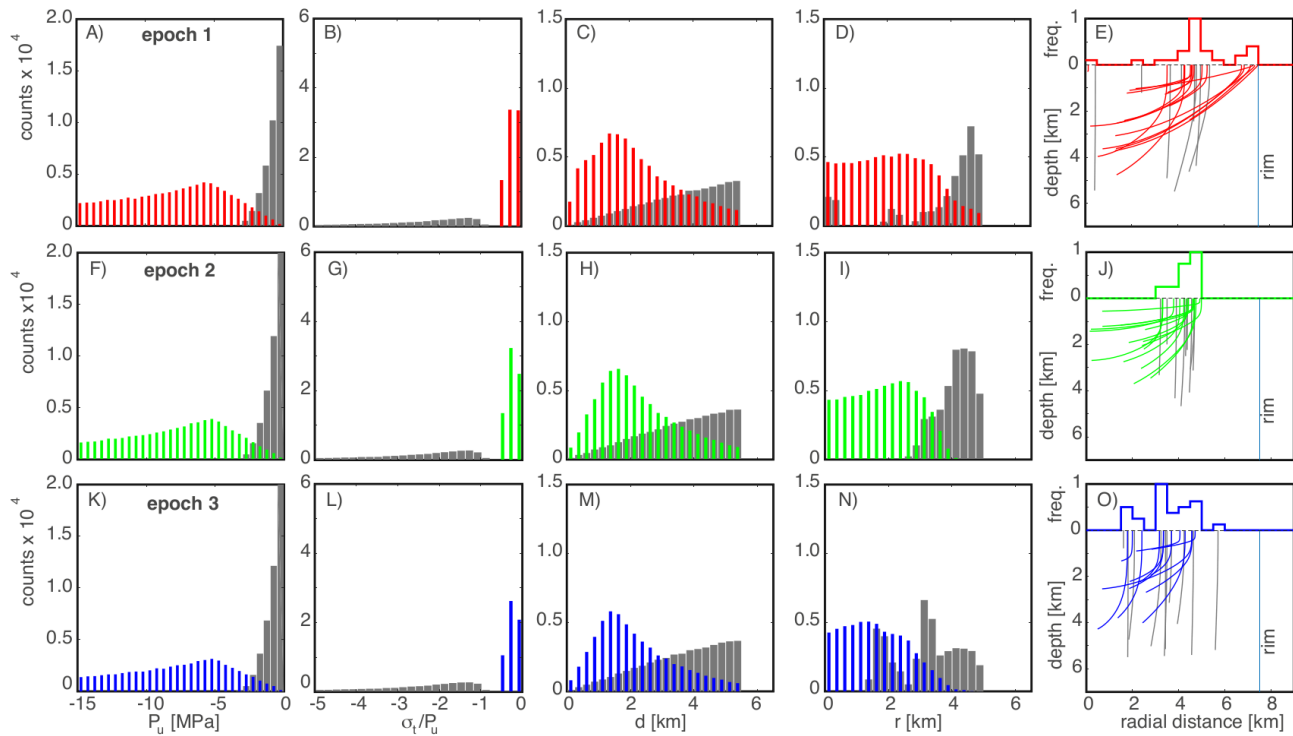
topography (we explore the effect of the existing approximately SW-NE topography gradient below). We also neglect previous intrusions, earthquakes and also magma chamber stresses for the reasons explained above. Moreover, we assume axisymmetric geometry so that Eq. 4.2 will write:

$$\sigma_{TOT} = \sigma_t(t) + P_U(t)G_U(r, z) \quad (4.4)$$

where r is the distance from the caldera axis. The only stresses left in the equation are a homogeneous tectonic stress and a uniform unloading stress applied to the caldera floor due to the caldera excavation. We assume $\sigma_t(t)$ and $P_U(t)$ are piecewise constant functions with discontinuities at the time of transition between different epochs. We calculate the function G_U analytically by means of equations describing the stress perturbation due to a rectangular negative (unloading) pressure source located at the surface. We fix the caldera radius ($a=7.5$ km) and select as free parameters P_U , the ratio σ_t/P_U (the latter ratio for reasons explained later). In this section, we consider as additional free parameters d and r .

We run 10^7 Monte Carlo trajectory simulations based on random parameter sets drawn from uniform distributions: $P_U=-15-0$ MPa; $\sigma_t=0-3$ MPa; $d=0-5.5$ km; and $r=0-6$ km). The resampled distributions of P_U , σ_t/P_U , d and r for the three epochs are bi-modal (Fig. 4.3), indicating two distinct solution subsets according to whether σ_t or P_U is dominant. If $\sigma_t > 2P_U\pi$ (Fig. 4.3B, G, L) dikes ascend vertically (Fig. 4.3E, J, O, gray) from the edge of a magma reservoir that shrinks laterally over the three epochs (Fig. 4.3D, I, N, gray). We deem such reservoir shrinking scenario unlikely, as discussed above. Conversely, $\sigma_t < 2P_U\pi$ corresponds to an ‘unloading-dominated scenario’. Here dikes nucleate at shallow depth at $r < 4$ km (Fig. 4.3C, D, H, I, M, N, colored) and propagate to the surface in trajectories with upward concavity (Fig. 4.3E, J, O, colored). The likeliest value (mode) of P_U decreases from -5.75 to -5.25 MPa from epoch 1 to 3 (the average P_U varies from ~ -7.9 to -7.7 MPa for epoch 1 to 3), equivalent to depositing 10-25 m of volcanic products over 200-300 m of overburden removal following the NYT eruption. The ratio between the inverted unloading pressure $P_{U,m}$ and that estimated from stratigraphy $P_{U,o}$ is $R_L \sim 0.8$, without significant variations between the three epochs (Methods), suggesting that inelastic processes have partially relaxed and homogenized stresses (Chadwick Jr and Dieterich, 1995; Maccaferri, Richter, and Walter, 2017). The mode and average of σ_t/P_U are 0.275 and ~ 0.26 , so that $\sigma_t=1.5-2$ MPa, consistent with evidence of weak extension from earthquake focal mechanisms (Amoruso, Crescentini, and Sabetta, 2014) and fracture patterns (Vitale and Isaia, 2014). The wide spread around the likeliest values results largely from a trade-off between stress parameters and d (explored below), from simplifying the geometry to axisymmetric, from neglecting local stresses due to second-order topographic features and from merging vents in discrete epochs instead of considering them individually. Notwithstanding such spread, the mean values of the stress probability density

Figure 4.3: Forward model. Summary of the resampled Monte Carlo simulations shown as histograms for epoch 1 (red), epoch 2 (green), and epoch 3 (blue). Gray and colored bars refer to simulations where σ_t is larger and smaller than $2P_U/\pi$, respectively, corresponding to “shrinking magma chamber” and “unloading controlled” scenarios. Panels A-D, F-I and K-N represent the resampled distributions for the input parameters as indicated. Panels E, J and O show representative streamlines for the two scenarios and the frequency of observed eruptive vents in the upper part of the panel.



function resolve a small unloading stress change of $\sim 0.2\text{-}0.5$ MPa. This is consistent with the reloading expected from a thickness of $\sim 10\text{-}25$ m of eruptive deposits revealed by field and borehole data (Di Vito et al., 1999; Orsi, De Vita, and Di Vito, 1996) assuming a density of $2000\text{-}2500$ kg/m³. Thus, the ‘unloading-dominated’ solutions describe a shallow source of substantially stable size and depth, broadly consistent with geophysical and geological evidence (Steinmann, Spiess, and Sacchi, 2018; Amoroso, Crescentini, and Sabbetta, 2014), overlaid by a progressively refilling caldera depression. The parameters appear affected by some tradeoff (Fig. S5S6S7). In particular, d is correlated with both P_U and σ_t/P_U , demonstrating that the two problems of magma source location and stresses cannot be easily separated based on eruptive vent location. A tradeoff between P_U and σ_t is removed by considering P_U and σ_t/P_U instead (Fig. S8A-F) Moreover, d

appears stable with respect to r , consistent with a melt accumulation zone over a relatively narrow depth range (Figs. S5S6S7). Parameters tradeoff appear limited for a narrow range (e.g., 0.5 km) of d (Fig. S9), suggesting that a robust inversion is obtained if d is well constrained. We conclude that our model is capable to capture the stress variations following the NYT eruption and the subsequent caldera infilling, only based on vent distribution.

4.3.3 Discussion on model assumptions

Sharp contrasts between layers of different rigidity and the interplay between propagation and the free surface affect dike trajectories (Fialko, 2001; Maccaferri, Bonafede, and Rivalta, 2010). Layering is common in volcanic areas, including Campi Flegrei (Barberi et al., 1991). If rigidity decreases with decreasing depth (as commonly is the case), then trajectories become increasingly vertical, and vice versa. Ignoring such transitions may introduce a bias in the inversion results: propagation into less rigid layers may be mapped into a larger extensional stress, and vice versa. The inversions will average out similar effects and return “effective” stress parameters. This is similar to the bias resulting from assuming the melt source deeper than it actually is: it will be mapped into biased stress parameters. If the inversion results are then used to make physical inferences on the the stress field, such bias should be considered and discussed. But if the stress parameters are only used for predictive models, the bias are not critical; on the contrary it is an element of strength of the proposed approach: instead of complicating the model by accounting for the internal structure of the volcano, which is generally very poorly constrained, the simplest model possible will have the advantage of incorporating multiple effects into few effective parameters that will reflect a number of known and unknown processes into the forecast. If the deep structure of the volcano was known in detail, this could be incorporated into the method, but then simple principal stress trajectories would need to be abandoned for a dike propagation approach that can deal with crustal inhomogeneities by allowing for mixed-mode propagation, with the price of increased computing time and number of parameters. The question whether accounting for layering and mixed-mode propagation results in an increased predictive power for the proposed approach is an interesting point for future studies. As for the interplay between dike propagation and the free surface, numerical and analog studies have shown that the free surface induces mixed-mode propagation, and increased curvature towards the free surface into a saucer-shaped intrusion (Fialko, 2001; Polteau et al., 2008). Strong deviations occur when horizontal intrusions (sills) are very close to the free surface, i.e. their diameter is 4 to 5 times the thickness of the overburden (Polteau et al., 2008), but trajectories start to bend slightly when their diameter is double their depth (Fialko, 2001). σ_3 -perpendicular propagation pathways are pure opening pathways and thus cannot account for

this complexity. However, this issue, while important, is not very critical in most cases, including Campi Flegrei, as the diameter of the sill-shaped magma chamber is similar to its depth. Cases of sill-shaped magma chambers with diameter larger than three times their depth can be addressed by using propagation models that can account for mixed-mode propagation (Dahm, 2000a; Fialko, 2001; Maccaferri, Bonafede, and Rivalta, 2010).

4.3.4 Forecast for Campi Flegrei

We now construct and test a predictive version of our approach. We reduce the number of free parameters by fixing the probability distribution for magma chamber depth to a generalized beta function ($\alpha = \beta = 2$) ranging between 3 and 4 km, based on the inversion results by Barberi et al., 1991, and the nucleation radius to $r = 0$, thus inverting for only P_U and σ_t/P_U . Generalized beta functions are chosen here as they seem to provide good fits. Note that no loss of generality occurs due to the $r = 0$ condition, because dike trajectories are horizontal for small radii, i.e. they lie on the assumed sill-shaped melt lens before bending towards the surface.

We use the data from epoch 1 to illustrate a stable-stress forecast, assuming that the condition of a stable state of stress is met. We use a random subset (2/3 of the sample size, thus 20 of 31 vents) of the observed vent radii to resample P_U and σ_t/P_U . Based on the obtained posterior distributions we produce a forecast by running 104 Monte Carlo simulations. Finally, we test the forecast with the remaining 1/3 of the vents (Fig. 4.4, top). We find that this 2D forecast well matches the distribution of radii for those vents not used to set up the forecast. Note that having the magma chamber geometry fixed leads to stress parameters that are numerically different from those obtained with the explanatory model above; this is expected due to the tradeoff highlighted above, and does not invalidate either model.

We have demonstrated that based only on a few stress parameters (here two parameters) it is possible to forecast the location of future vents, provided the stress field has maintained approximately stable over the time interval used for the stress inversion. But what if we want to forecast vents following a major stress-modifying event for the volcano, with no observed vents available to invert those new stresses and constrain such forecast? With this purpose in mind we have developed a forecast approach to extrapolate the modelled stresses into the future. The approach takes advantage of the link between inverted and stresses and stresses modelled according to the observed stratigraphy. We illustrate and test such evolving-stress forecast by using vent maps for epochs 1 and 2, along with stratigraphy information, to produce forecasts for epoch 3 and Monte

Figure 4.4: (Continued on the following page.)

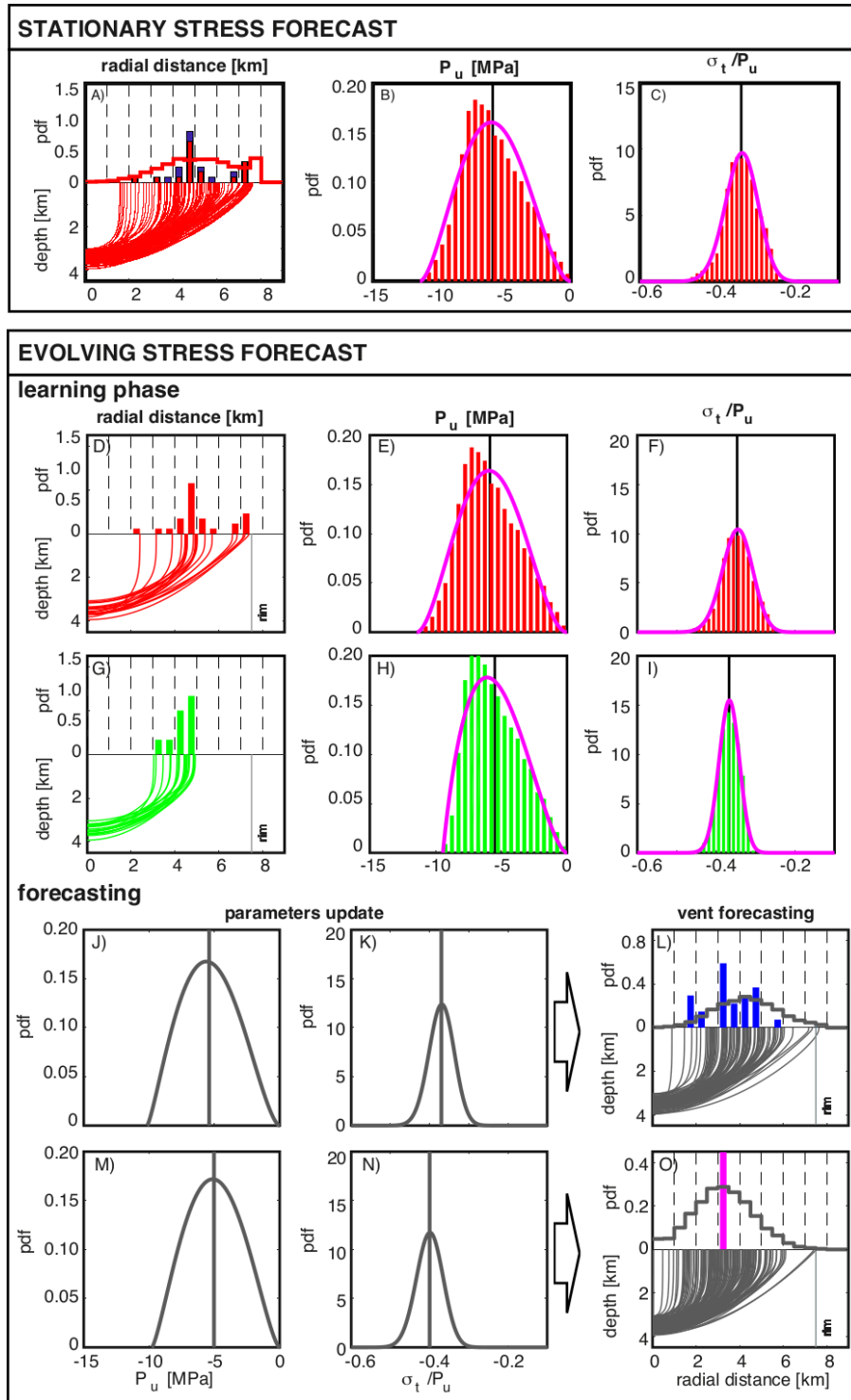


Figure 4.4: Vent forecasts. Top: Stationary stress forecast. A) Thin red lines are forecasted magma trajectories, red stairs indicate the distribution of arrival radii based on 66% of the observed vents of epoch 1. The blue and red bars show the distribution of observed vents and a random 66% of them, respectively. B) and C) show the marginal distributions of inverted P_U and σ_T/P_U (red bars) fitted by beta functions (magenta lines), respectively. Bottom: evolving vent forecasts. D) Observed vent radii and resampled trajectories for epoch 1 (we excluded the outlier vent of Rione Terra). E) and F) show resampled distributions of P_U and σ_T/P_U for epoch 1 fitted with a generalized beta function (magenta lines panels E, F, H, I). Panels G, H, and I represent the same as D, E and F but for epoch 2. Panels J and K) are distributions for P_U and σ_T/P_U projected for epoch 3. L) Vent forecasting for epoch 3 (grey stairs) compared with observed vent radii (blue bars). Panels M, N and O represent the same as G, H and I but for the Monte Nuovo cone.

Nuovo. We first resample the distributions of P_U and σ_t/P_U for epochs 1 and 2 using all available vents (Fig.2.4 bottom, D-I). We then assume a linear relationship between inverted unloading and excavation stresses estimated from stratigraphy (and any other geological or geophysical information). This is equivalent to assuming that R_U is approximately constant over the volcano history. We then assume the average of the unloading pressure distribution $P_{U,m}$ and its support (minimum and maximum stress value) evolve as $R_U \Delta P_{U,0}$ that is proportional to the unloading stress due to the deposition observed during the successive epochs (Fig. 4.4E, F, H, I, Fig. S10).

P_{U0} is calculated as follows:

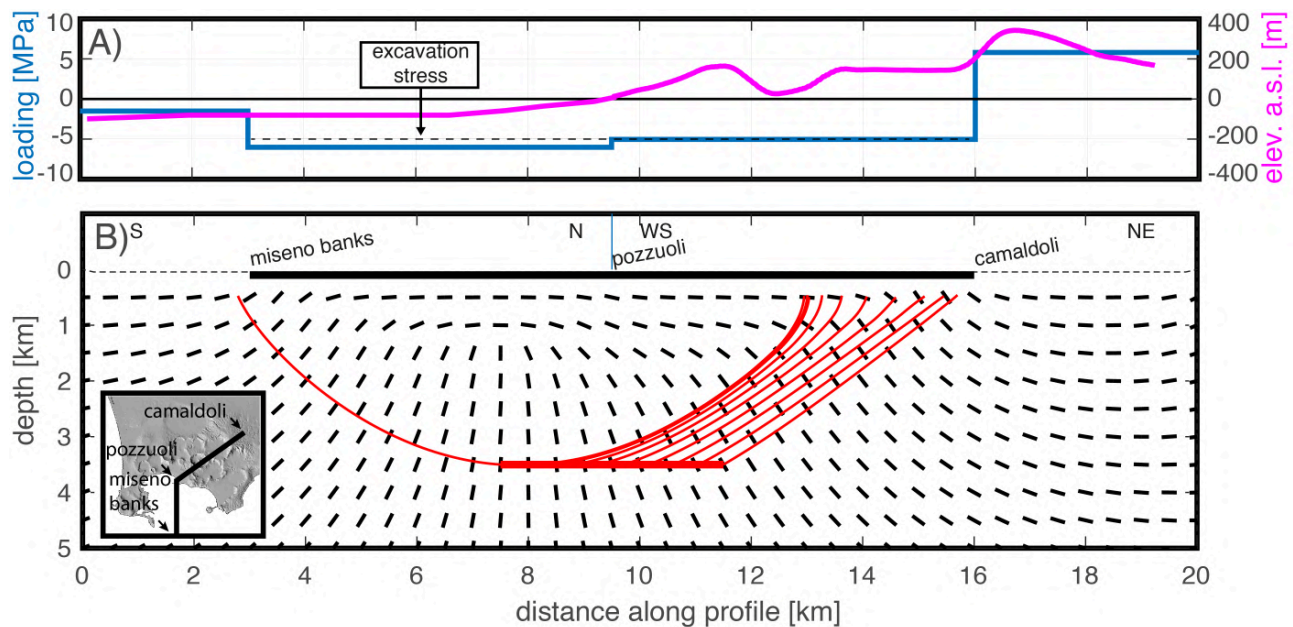
$$P_{U0} = -g(d_b \rho_b + \sum h_i \rho_i) \quad (4.5)$$

where g is the acceleration due to gravity, $d_b=2$ km is the 40 ka Campanian Ignimbrite collapse depth, h_i and ρ_i are the thickness and density of the post-Campanian Ignimbrite deposits (ρ_i ranges from 2400 to 2000 kg/m^3), respectively and $\rho_b=2600$ kg/m^3 is the density of the basement (Table. S1). Beside updating the average of the unloading distribution (Fig. S10A), we update also to the lower limit of the support of $P_{U,m}$, $Min(P_{U,m})$, by applying the same shift $\langle \Delta P_{U,m} \rangle$, on the assumption that a reloading of the caldera will affect both best guess and its lower limit. Since two possible updates of $Min(P_{U,m})$ are available (starting from epoch 1 and 2), we take their average. The upper limit remains 0. The estimated $\langle P_{U,m} \rangle$ for epoch 3 and Monte Nuovo are used to update σ_t/P_U for the respective periods, assuming that the product $\langle P_{U,m} \rangle \langle \sigma_t/P_U \rangle$ remains constant (Fig. S10B).

The forecast vent radii for epoch 3 has 56% of the observed vents falling within the 1st and 3rd quartile (where 50% are expected) of the forecast distribution (Fig. 4.4L). For Monte Nuovo, the

mode of the resampled distribution, corresponding to a 3.25 km radius, coincides with the observed distance of Monte Nuovo from the caldera center (Fig. 4.4O). While only one vent is insufficient to validate a forecast, we highlight that Monte Nuovo is located in a low probability area from previous studies and would have been hardly anticipated if those maps had been available before the eruption.

Figure 4.5: Explaining asymmetric volcanism. Topographic/loading profiles (panel A, magenta and blue lines, respectively) and modelled stress field below Campi Flegrei caldera for the two half cross-sections highlighted in the inset of panel B. The black segments represent the direction of σ_3 . The thick red line represents the pressurized melt zone according to ref. (Barberi et al., 1991), and likely active in the last 5 ka at least (Steinmann, Spiess, and Sacchi, 2018). Thin red lines are σ_3 -perpendicular streamlines.



4.3.5 Explaining non-axisymmetric volcanism

Our axisymmetric approach returns a forecast for the radial distance, but not for the sector of the caldera (radial location) where the vent may open. This information may be approximately obtained from our 2D model by combining the stresses we inverted for the end of epoch 3 ($P_U = -5.0$ MPa and $\sigma_t/P_U = -0.4$) with a first-order 2D stress perturbation created by the asymmetric topography of the caldera. We consider two end-member cross-sections: a S-N offshore section with maximum

unloading (negative relief) and a SW-NE onshore section including the highest relief outside the caldera (Camaldoli). We consider an average bathymetry of -100 m (offshore area) and an average topography of 300 m for Camaldoli (Fig. 4.5A). We use plane strain approximation and assume a homogeneous elastic half-space. The computed minimum compressive stress under the caldera floor is subvertical below 1.5 km and rotates progressively to sub-horizontal towards the caldera rim (Fig. 4.5B), leading to concave trajectories. The larger surface loading towards the NE rim results in an asymmetric stress pattern, which drives most streamlines northeastwards away from the magma lens. Eruptions occur mainly within this NE, onland part of the caldera (Fig. 4.5B). Only a few streamlines propagate southward and erupt outside the offshore caldera rim, consistent with the low number of observed vents (Fig. 4.2A). This suggests that the non-axisymmetric distribution of the topography around the caldera may control the inhomogeneous distribution of its volcanism.

Our 2D results are broadly consistent with previous maps, that indicate high probability of vents opening in the NE part of the caldera (Fig. S9&S10). Yet, our results imply substantial vent opening density in locations where previous studies give a low probability, i.e. the 1st and 3rd quartile of the forecast describe a predominantly onshore, approximately annular belt comprised between 2.3 and 4.2 km from the caldera center, on which the Monte Nuovo vent lies.

4.3.6 Forecast potential for other calderas

Our method may be applied to other calderas and volcanoes of different shapes. Below we propose a general diagram forecasting the location of future vents for calderas based on their geometry (radius and depth), inferred depth to the magma reservoir and stress conditions. This is intended to be purely demonstrative as important stress sources are ignored, including the presence of any stratocone, the density profile below the caldera floor, not to mention the high uncertainty related to tectonic stresses. We calculate how the chamber depth/caldera radius ratio, d/a , and the tectonic/unloading stress ratio, σ_t/P_U , determine the arrival distance of the dikes feeding the vents; this arrival distance is classified into intra-, along rim (i.e., $0.85a$ - $1.15a$), or off-caldera; these three domains correspond to the colored background in Fig. 4.6. We then locate on the diagram 17 approximately circular calderas (Table. S2) with a sufficient knowledge of the above-mentioned parameters (caldera geometry, depth to the magma reservoir, vent location, regional stress). P_U was calculated considering only the maximum caldera depression and taking into account any water level. The regional stress was set more arbitrarily, assigning a stronger extension of 1–3 MPa to calderas in extensional settings and a weaker extension of 0.2-0.5 MPa induced by inflation or resurgence to calderas in neutral tectonics (Newhall and Dzurisin, 1988; Neri et al., 2015). In

Figure 4.6: (Continued on the following page.)

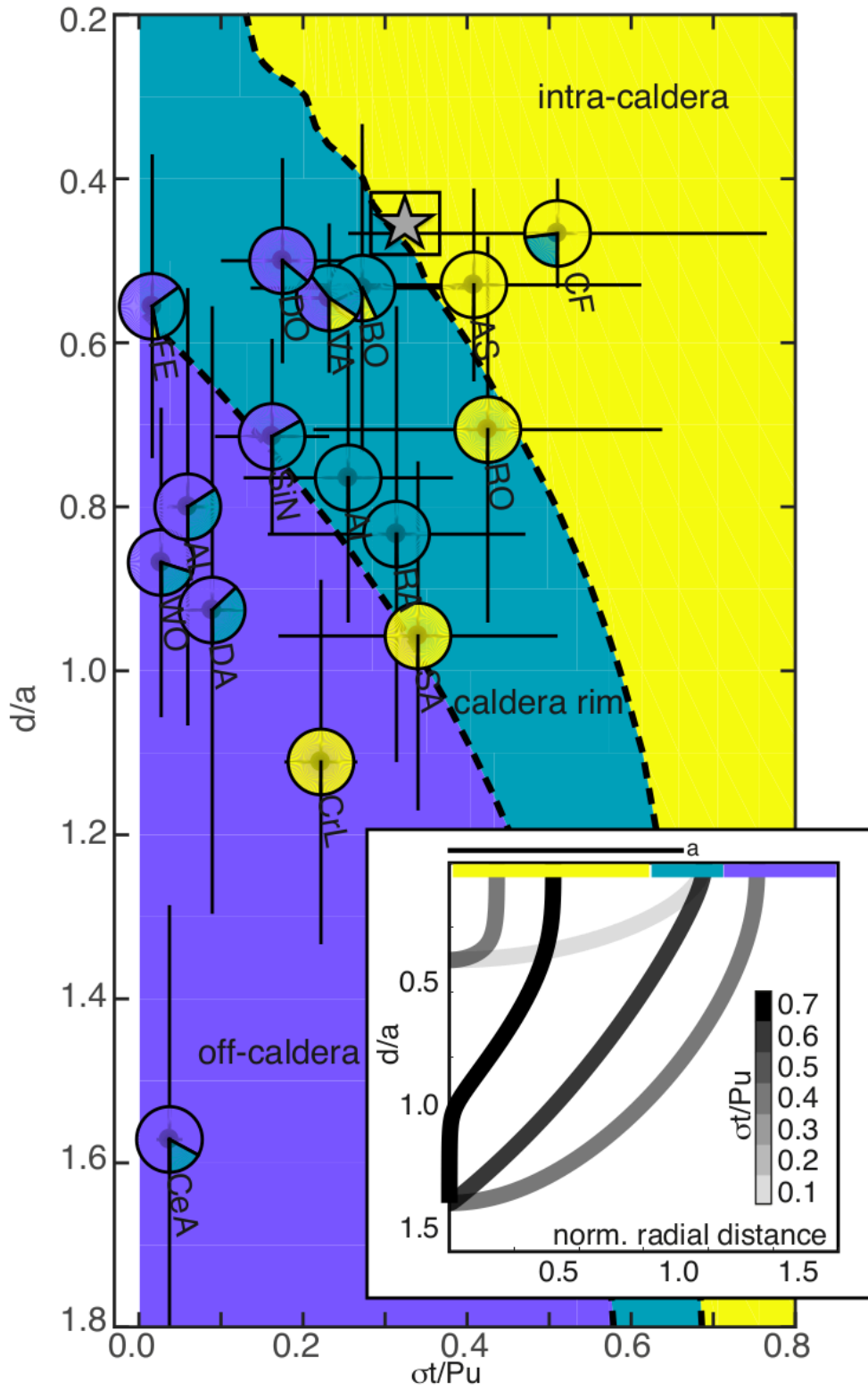


Figure 4.6: Performance of the unloading model for notable worldwide calderas. The background color represents the phase diagram for intracaldera, rim or off-caldera vent location according to model prediction, as specified. The caldera rim field is bounded by $0.85a$ and $1.15a$ (inset). Estimates for calderas in nature are represented by pie plots according to the proportion of observed intracaldera, rim or off-caldera vents, with the same colorcoding as the background. Uncertainties are shown as black lines. The star highlights the position of CF according to the σ_t/P_U calculated in this study. The inset shows streamlines of selected models with $d/a=0.4$ and $d/a=1.4$ and variable σ_t/P_U , as a reference. d/a is depth d normalized to the caldera radius a , while σ_t/P_U is the normalized stress controlling trajectories concavity. Caldera acronyms as follows: FE, Fernandina; WO, Wolf; DA, Darwin; SiN, Sierra Negra; Al, Alcedo; CeA, Cerro Azul; RaK, Rano Kau; CF, Campi Flegrei; AS, Aso; CrL, Crater Lake; Ro, Rotorua; SA, Santorini; BO, Bolsena; RA, Rabaul; AI, Aira; VA, Valles; DO, Dolomieu.

spite of its simplicity, our forecast broadly matches the observed dominant vent location (intra-, rim and off-caldera, shown as pie diagrams for each caldera). In particular, depending mostly on σ_t/P_U , vents distribute from predominantly intra-caldera to predominantly along the caldera rim and finally to off-caldera, confirming the importance of the stress ratio in determining their location. The considered calderas appear shifted to the left with regard to the theoretical domains, possibly depending on our limited and indirect knowledge of σ_t . This shift may also explain, at least partly, the two outliers from the overall pattern (Crater Lake and Santorini). These outliers may result from underestimating σ_t or magma buoyancy, or stress conditions different from those at the time of the past eruptions.

4.4 Conclusions

In contrast to traditional approaches for vent forecasting, our method directly links observations, i.e. the distribution of observed vents, to properties of the volcanic edifice and the magmatic system, providing a physics-based forecast of future vent locations. The ability of our approach to resolve small stress variations developing during the eruptive history of a caldera represents a first validation of its potential. In the ideal case of detailed knowledge on the (re)distribution of surface loads during each individual eruption, and even stress change caused by any intruded magma, it would be possible to perform a stress inversion for each eruption. This could provide a quantitative approach to understand the evolution of stress over time and re-calculate vent radii probability based on any

future stress perturbation.

Unlike previous models, our approach performs well on retrospective tests: our high-probability forecast for the location of Monte Nuovo was obtained after removing knowledge of its location from the model. Other geological and geophysical information on the structure and dynamics of a caldera may be included to better constrain the stress field in the volcano edifice, and in particular the terms $G_L(x, y, z)$ and $G_U(x, y, z)$ from Eq. 4.2, which should improve the quality of the forecasts.

By improving the individual components of the present forecasting model (3D stress computation, including an accurate distribution of deposit coverage in time), our method may be also used to produce maps of probability of vent opening at calderas and in volcanic edifices of different shape. Combining our method with hazard simulation tools may result into more reliable hazard assessment, especially for systems characterized by large vent location variability.

Acknowledgements and funding

We thank M. Bagnardi and D. Bindi for discussion. E.R. and F.C. were funded by the European Union Supersite MED-SUV project, grant agreement no. 308665.L.P. was funded by the German Federal Foreign Office through the German Humanitarian Assistance program, grant S05-41-321.50 IDN 03/16. V.A. was funded by the DPC-INGV project V2, “Eruptive Precursors”. T.D. was funded by the DFG-ICDP, grant agreement no. RI 2782/3-1. M.A.D.V. was funded by the DPC-INGV projects V1 and V2.

Chapter 5

Analog stress inversion

The content of this chapter has been submitted to GRL.

Abstract

Assessing volcanic hazard in regions of distributed volcanism is challenging because of the uncertain location of future vents. A statistical-mechanical strategy to forecast future vent locations was recently proposed. Here we further develop and test that strategy with analog models. We stress a gelatin block laterally and with surface excavations, and observe air-filled crack trajectories. We use the observed surface arrivals to sample the distributions of parameters describing the stress state of the gelatin block, combining deterministic crack trajectory simulations with a Monte Carlo approach. While the individual stress parameters remain unconstrained, we effectively retrieve their ratio and successfully forecast the arrival points of subsequent cracks.

Plain Language Summary

In regions of distributed volcanism eruption locations (vents) are scattered over a large area. Forecasting the new eruption locations over such regions is critically important, as many are densely populated. One of the main difficulties is dealing with few known past eruptions, that is, the data available to constrain forecast models are scarce. Thus, we develop a forecast strategy by applying extensional or compressional stress to blocks of gelatin with surface excavations and observing the propagation of air-filled cracks. Such models, if properly scaled, are an analog for magma propagation in the Earth's crust. We use the surface arrival points of some observed cracks to retrieve the statistical distributions of a few parameters controlling the stress field. Next, we use such distributions to forecast the arrival points of other observed cracks. Although we could not

retrieve all the stress parameters accurately, the forecasts we perform are reliable. Our strategy may help retrieving the state of stress in volcanic regions and forecast the location of future vents.

5.1 Introduction

In many volcanic regions, eruptive vents may be spatially scattered: they sometimes cluster along rift zones or are distributed over areas that may exceed 10,000 km². Some of these regions are densely populated. In order to better protect human life and infrastructure, it is important to better understand the factors determining vent distributions and improve vent location forecasts.

The most common approaches to probabilistic forecasts of future vent opening locations rely on the spatial density of past eruptive events, sometimes complemented with the surface distribution of structural features, such as faults and fractures (Connor and Hill, 1995; Martin et al., 2004; Selva et al., 2012; Bevilacqua et al., 2015). Such models, however, often remain poorly constrained due to scarce or spatially sparse data, and cannot be easily validated in volcanic systems where eruptions are infrequent.

Recently, Rivalta et al. (2019) proposed a mechanical-statistical approach to inversely constrain the state of stress, and thus magma pathways, of a volcanic region on the basis of the known location of magma reservoirs and past eruptive vents. Dike trajectories are assumed to follow a "least resistance to opening" path calculated from the elastic stress field, which is optimized so that any magma batch released from the magma reservoir reaches one of the past eruptive vents. Once the stress field is constrained, the trajectories of future dikes can be forecast. Rivalta et al. (2019) applied the concept only to Campi Flegrei caldera in Italy, performing inversions on two stress parameters: namely, the tectonic and the unloading stress. As independent estimates of such parameters in nature are affected by large uncertainties, it remains unclear how accurately the model can capture them. Secondly, it is unclear how much other factors, such as medium layering, were biasing the results, and how this would affect the forecast.

Here we delve deeper into the stress inversion concept, investigating these issues in a controlled setting: air-filled cracks propagating in a gelatin box. Such analog experimental setups have proven useful in validating dike propagation models (Watanabe et al., 2002; Maccaferri et al., 2019), e.g. assessing the influence of surface loads (Muller, Ito, and Martel, 2001; Gaete et al., 2019), rigidity layering (Maccaferri, Bonafede, and Rivalta, 2010) and external stress fields (Acocella and Tibaldi, 2005). We stress the gelatin with extension/compression and surface excavations, shown in

previous works to be the dominant stressing mechanisms in volcanic regions (Roman and Jaupart, 2014; Maccaferri et al., 2014; Corbi et al., 2016). Here we do not intend to reproduce a specific geologic setting, but rather to test the ability of our statistical-mechanical strategy to retrieve the state of stress and the relative importance of surface excavations and regional stresses. We chose a valley-shaped surface geometry so that the stresses within the gelatin block can be approximated by plane strain, but our setup may provide insights on the same stress-generating mechanisms also in caldera-like settings. First, we run a series of experiments where we track the propagation of injected air-filled cracks. Secondly, we use a boundary element (BE) model to calculate expected crack trajectories with a realistic topography, combined with a Markov Chain Monte Carlo (MCMC) algorithm to sample two parameters describing the state of stress within the gelatin. This improves on Rivalta et al. (2019) both in terms of numerical modelling and sampling algorithm used. Thirdly, we validate our strategy by running forecasts for additional cracks, which we compare to further injections.

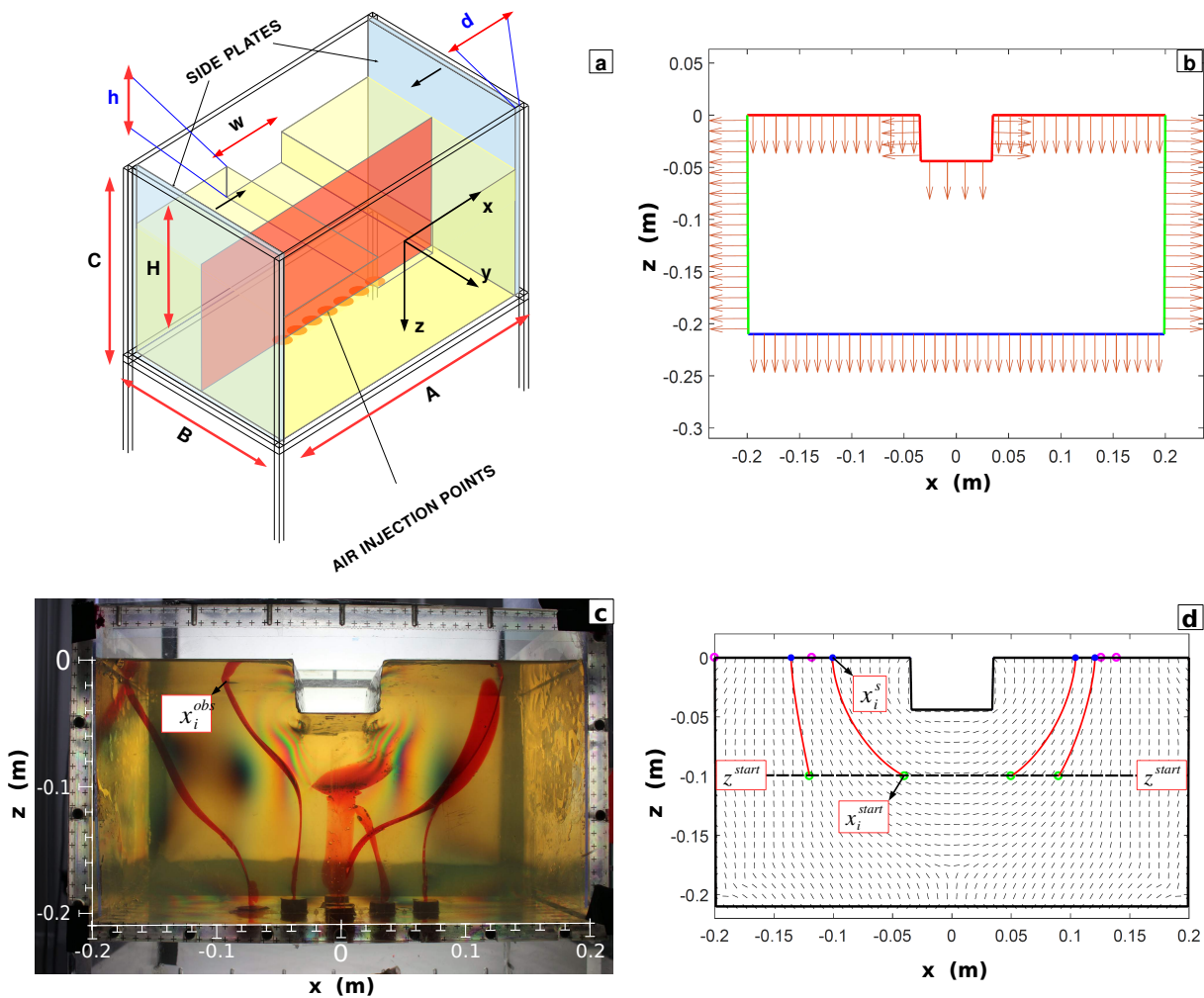
5.2 Methods

5.2.1 Experimental Setup

We use a perspex container of size $A \times B \times C = 40 \times 20 \times 20$ cm (Fig. 5.1a). A 2.0 wt% or 2.5 wt% aqueous solution of 220 Bloom pig gelatin powder was let solidify in the box at $T = 8^\circ$ C for 20 h. These concentration values have been used in previous works (e.g. Di Giuseppe et al., 2009; Kavanagh, Menand, and Daniels, 2013; Gaete et al., 2019; Smittarello, 2019), so they are well characterized. Compression or extension were imposed on the set gelatin by inserting or removing two plastic plates of thickness $d = 2.5 \pm 0.1$ mm at the box sides, separated from the medium by a transparent plastic film (Fig. 5.1a). We chose $d = \pm 2.5$ mm both to work with a small strain $e = 2d/A$ and to obtain ratios between extensional/compressional and unloading stresses comparable with estimates in nature (see below). The gelatin block surface is moulded to include along the y-direction a rectangular excavation of width $w = 6 - 7$ cm and varying depth h (Fig. 5.1a), creating surface unload. The height of the gelatin block, H , varied throughout the experiments (see Fig. 5.1a).

Air is injected into the gelatin from the bottom of the box, resulting in ascending air-filled cracks. Different injections are made through different holes at 1 cm intervals, both to avoid the reopening of previous cracks and to observe trajectories over as wide a section of the gelatin block

Figure 5.1: a) Schematic view of the gelatin box: the side plates are highlighted in blue, the median plane of the block in red. The quantities are defined in section 5.2.3. b) discretisation of the box and its surface over the median plane. Arrows: normals to BEs. The length of the illustrated BEs is larger than the one we employed. c) Front view of the gelatin box at the conclusion of experiment 2DLA-2 (compression): crack trajectories are marked post-intrusion with red ink. d) Numerical simulation of the experiment in c): blue dots represent the x_i^s simulated from a random set of parameters, while x_i^{obs} are marked with magenta circles. Simulated trajectories are highlighted in red and σ_1 directions are drawn in black. z^{start} is marked by a black dashed line.



as possible. Air has been used as a magma analog in gelatin-based models in previous works (Menand, Daniels, and Benghiat, 2010; Corbi et al., 2016). Air is nearly inviscid, so that we avoid any effect on the trajectories due to viscous effects, which are treated in other works (e.g. Smittarello, 2019; Pinel et al., 2019). All experiments were carried out at room temperature, with time-scales short enough (≤ 1 h) to maintain the experiments in an elastic regime (Kavanagh, Menand, and Daniels, 2013). The Young's modulus E of the gelatin was determined case by case by applying a small cylindrical load on the surface and measuring the resultant subsidence under the assumption of a half space (Kavanagh, Menand, and Daniels, 2013). E was mostly within the 2000 – 3500 Pa range (Supplement, Table S12). We assumed a $\nu = 0.49$ Poisson's ratio (Otterloo and Cruden, 2016) and take $\rho_{gel} = 1020 \text{ kg} \cdot \text{m}^{-3}$ for the gelatin density (Smittarello, 2019). We attached polarized sheets on the box front and back walls (Fig. 5.1c) to observe stress inhomogeneities during the experiments. The resulting sequences of colored fringes (Table 5.1) visualize the differential stress ($\sigma_1 \sim \sigma_3$) perpendicular to the light direction (Gaete et al., 2019).

We present seven experiments (2DLA- i , $i= 1, \dots, 7$), involving extension (2DLA-1,3,4,5,6,7), compression (2DLA-2) and layering (2DLA-3,4). In a set of three more experiments we imposed compression but we discarded them as most of the cracks hit the box walls (see Fig. S13). We measure the surface arrival points of the cracks (x_i^{obs}). All the respective data sets are collected in the Supplementary material. In 2DLA-5,6,7 we changed the state of stress midway in the experiments, in between injections: we performed N^I injections, then removed the side plates (2DLA-5) or partially refilled the surface excavation with water (2DLA-6,7), and finally injected N^F more cracks (see Table 5.1 and Fig. S12). The data from 2DLA-6 and 2DLA-7 were also pooled to test the method with a larger data set.

Inhomogeneities of various nature affect the outcome of the experiments. Some of them are unplanned, such as temperature gradients within the gelatin block (a temperature difference of $\sim 3^\circ \text{ C}$ was measured between the gelatin surface and the bottom, leading to gradients $\leq 0.15^\circ \text{ C/cm}$ and thus to heterogeneities in the gelatin Young's modulus, see Table S4), and localised strain concentrations induced when removing and, especially, inserting the side plates. Conversely, rigidity layering is intentionally introduced in experiments 2DLA-3 & 2DLA-4 (Table 5.1): elastic interfaces were welded by pouring a $\sim 25^\circ \text{ C}$ second layer (Kavanagh et al., 2017). In 2DLA-3, the bottom layer had a higher gelatin concentration, and thus rigidity, than the top one, and reverse in 2DLA-4. The Young's modulus E of the bottom and top layers was measured and estimated from other measurements for the same concentration, respectively (Table S4). For these two experiments, we assume a homogeneous medium in the numerical model and an 'effective' Young's modulus obtained by carrying out the measurement on the whole block. The aim here was to test the

performance of the strategy when ignoring an existing layered structure in the simulations.

5.2.2 Scaling

The length scaling factor between our experiments and nature is given by the buoyancy length (Secor and Pollard, 1975):

$$L = \left(\frac{K_c}{\pi^{\frac{1}{2}} \Delta \rho g} \right)^{\frac{2}{3}} \quad (5.1)$$

where K_c is the medium fracture toughness and $\Delta \rho$ is the density contrast between the host medium and the injected fluid. Taking $\Delta \rho_r = 100 \text{ kg}\cdot\text{m}^{-3}$, $\Delta \rho_{gel} = 1000 \text{ kg}\cdot\text{m}^{-3}$ as the rock-magma and gelatin-air density contrasts, respectively, $K_c^r = 0.2 - 1 \cdot 10^9 \text{ Pa}\cdot\text{m}^{\frac{1}{2}}$ as the rock fracture toughness and $K_c^{gel} = 60 - 80 \text{ Pa}\cdot\text{m}^{\frac{1}{2}}$ for a gelatin with Young's modulus in the range of $E = 2000\text{-}3000 \text{ Pa}$ (Kavanagh, Menand, and Daniels, 2013; Smittarello, 2019), we obtain $L^* = 3.3 \cdot 10^{-6} - 1.2 \cdot 10^{-5}$, where the asterisk refers to the ratio between analog and natural values. Thus, the excavation width range $w = 6 - 7 \text{ cm}$ we measured (Table S4) corresponds to 6-20 km in nature, compatible with the broad range of lateral scales (100 m - 100 km) displayed by unloading mechanisms on Earth, such as the development of rifts or calderas or icecap melting. Likewise, a typical starting depth of 100 - 150 mm (Table 5.1) corresponds to $z^{start} = (-10) - (-50) \text{ km}$ in nature. Such a starting depth for dikes is deep, but not unreasonable.

The stress scaling factor is calculated by dividing the unload stress $\sigma_U = \rho_{gel}gh$ for the excavation in the gelatin by the one for the natural case. Taking $h = 2 - 5 \text{ cm}$ (Table 5.1) and excavations in the range 0.3 - 1 km, assuming $\rho_r = 2500 \text{ kg}\cdot\text{m}^{-3}$, we obtain $\sigma^* = 1 \cdot 10^{-5} - 1 \cdot 10^{-4}$. We also require the ratio between the stress arising from lateral strain and the unloading one to be comparable to natural cases. In our experiments, such ratio $Ee/\rho_{gel}gh$, where $e = 2d/A = 1.25 \cdot 10^{-2}$, is in the range 0.06 - 0.20. The same ratio in nature, for rifts or calderas 100 - 1000 m deep, assuming $\rho_r = 2500 \text{ kg}\cdot\text{m}^{-3}$ and a typical range for absolute values of tectonic stresses of 1 - 10 MPa (Heidbach et al., 2016), is 0.04 - 4.00, which comprises our experimental range, even if the latter lies close to its lower limit. An overview of our scaling factors is reported in the Supplement (Table S3).

5.2.3 Numerical Modelling

We assume an elastic rheology in the numerical model. This is commonplace in previous works (Anderson, 1937; Muller and Pollard, 1977; Roman and Jaupart, 2014) and supported by field observations on dikes (Lister and Kerr, 1991; Gudmundsson, 2002). There is, however, evidence of non-elastic dike propagation in nature (Spacapan et al., 2017; Poppe et al., 2020), which are reproduced in different analog models (e.g. Poppe et al., 2019).

To calculate the elastic stresses within the gelatin, we use the two-dimensional (2D) Boundary Element (BE) code "Cut&Displace" (Crouch and Starfield, 1982; Davis et al., 2017; Davis, Healy, and Rivalta, 2019). As explained above, we approximate the experiment's geometry as plane strain, as we observed little strain in the analog model's y-direction (Fig. 5.1a). The box bottom, top and walls are discretised into BEs of length $l_{BE} = 2$ mm. Displacement is set to zero on the bottom elements, while we impose fixed displacement on the side walls, equal to d or $-d$ (Fig. 5.1) for extension or compression, respectively. The free surface is shaped to model the excavation; stress boundary conditions are imposed on them to reproduce the gravitational stress due to the unload (Martel and Muller, 2000, eqs. 1). We assume that w and the position of the excavation are known exactly, and we employ the measured values of E for each experiment. In the case of the data pooling in 2DLA-6&7 (see section 5.2.1), we assumed average values for E and h , as these were similar but not identical in the two experiments (Table 5.1).

We calculate the principal stress directions on a dense grid of observation points within the box. We simulate the crack trajectories assuming that the cracks open against, and propagate perpendicular to, the least compressive stress axis σ_3 (Anderson, 1951). This assumption makes a good approximation of real trajectories provided the size and volume of the cracks are not too large (Watanabe et al., 2002; Maccaferri et al., 2019) and the effects of its viscosity can be neglected, as well as those of external stress gradients (Dahm, 2000a). The more these assumptions are far from reality, the larger the mismatch between real and σ_3 -perpendicular trajectories. More complex dike trajectory models exist for simulations in 2D (Dahm, 2000a; Maccaferri, Bonafede, and Rivalta, 2011) and recently also in three dimensions (3D) (Davis, Rivalta, and Dahm, 2020). However, the predictive power of models increases if model complexity is reduced with regard to accurate explanatory dike trajectory models (e.g. Forster and Sober, 1994). Thus, we opt for the simpler option of σ_3 -perpendicular trajectories, which also necessitate much shorter computation time and better serve the stochastic part of our strategy.

If the cracks are misaligned with the stress field at injection, they will require some distance

to realign (Menand, Daniels, and Benghiat, 2010; Maccaferri et al., 2019). The starting depth in the simulations is shallower than the injection depth to allow for this readjustment to occur at least partly.

5.2.4 MCMC Scheme

Our sampling procedure relies on the Delayed Rejection and Adaptive Metropolis MCMC algorithm (Haario et al., 2006; Laine, 2013). The set of N observed arrivals (x_i^{obs} , $i = 1, \dots, N$) is first divided into two subsets N^I and N^F ("I" and "F" stand respectively for "inversion" and "forecast"). The N^I set is used to sample the two parameters d and h . The size of our data sets varies from a minimum $N^I = 2$ in 2DLA-2 to a maximum of $N^I = 5$ in 2DLA-6&7 (see the Supplement, Tables S5:S6).

At start, ranges and guesses for the parameters d and h are fixed together with a common starting depth for the cracks, z^{start} . Starting locations, x_i^{start} , are assigned as the horizontal coordinate of the upper tips of the observed cracks at z^{start} . At each iteration, we simulate N^I crack trajectories and sample d and h in order to minimize the objective function

$$S = \sum_{i=1}^{N^I} (x_i^s - x_i^{obs})^2 \quad (5.2)$$

where x_i^s are the simulated arrivals.

The squares of the uncertainties on the two parameters ($\Delta d = \pm 0.1 \text{ mm}$; $\Delta h = \pm 1 \text{ mm}$) populate the diagonal of the covariance matrix. $M = 10^4$ iterations were made for every chain. Our runs highlight a correlation between d and h , as expected from Rivalta et al. (2019), so we consider a further parameter: $R = d/h$, which partly removes the trade-off, and use the posterior probability distributions (PPDs) of d and R to perform the forecasts.

5.2.5 Forecasting Approach

After performing the inversions, we run $M^F = 10^3$ iterations of N^F simulations for the forecasts, where we sample the parameters (d , R) from their PPDs. Starting points are drawn from Gaussian distributions centred on $x_i^{start,F}$, $z_i^{start,F}$, with standard deviation $\sigma = 1 \text{ mm}$. The combined distribution of simulated arrivals is compared to the observed arrivals set aside for the forecast

Table 5.1: (Continued on the following page.)

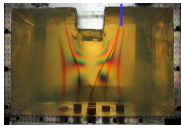
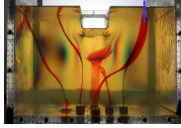
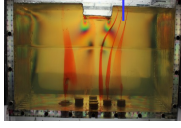
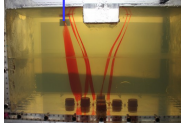
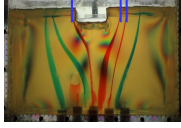
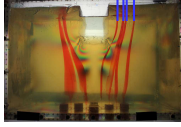
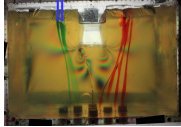
Experiments		Measured Parameters			Results			Forecasts			
# Exp.	Picture	h	d	R	h^{med}	d^{med}	R^{med}	$x_i^{med,F}$	δx_i^F	Δx_i^F	
		± 1	± 0.1	$(\times 10^{-3})$			$(\times 10^{-3})$				
		mm	mm		mm	mm		mm	mm	mm	
2DLA-1 Extension		50	2.5	63 ± 4	51	4.9	100	67	7	2	
2DLA-2 Compression		44	-2.5	-57 ± 4	73	-3.5	-55	115	39	11	
2DLA-3 Extension Layered		21	2.5	120 ± 10	63	3.9	69	75	9	1	
2DLA-4 Extension Layered		24	2.5	104 ± 8	59	5.8	102	-85	6	1	
2DLA-5 Updated Extension		24	0 2.5	0 ± 10^{-2} 104 ± 8	64	0.4	8×10^{-3}	-54 66 77	43 36 34	1 6 10	
2DLA-6 Extension Refilled		58 28	(65) (35)	2.5 (2.5)	(43 ± 2) (89 ± 7)	64	2.5	39	63 76 84 102	10 7 6 4	3 1 2 1
2DLA-7 Extension Refilled		72 32	(65) (35)	2.5 (2.5)	(43 ± 2) (89 ± 7)				-84 -73	8 6	4 0

Table 5.1: Experiments, measured parameters and results. Note: blue markers in the pictures indicate the arrivals used for the forecast (see Fig. 5.2b): in 2DLA-5, 2DLA-6 and 2DLA-7 these coincide with the injections following the stress update (differently coloured trajectories in pictures of 2DLA-5 and 2DLA-7 stand for pre-update and post-update). Mean values assumed for the pooled data of experiments 2DLA-6&7 are indicated in parentheses. Updated d and h are in boldface. h^{med} , d^{med} , R^{med} : medians of the respective PPDs (section 5.3.2). Quantities $x_i^{med,F}$, δx_i^F and Δx_i^F are defined in section 5.2.5 and refer to forecasts for individual $x_i^{obs,F}$. For further information see the Supplement, Tables S12:S14.

$x_i^{obs,F}$. We measure the success of a forecast from how far the median $x_i^{med,F}$ of the simulated arrivals lies from $x_i^{obs,F}$. Thus, for each individual i -th forecast, we define $\Delta x_i^F = |x_i^{obs,F} - x_i^{med,F}|$ and compare it to the standard deviation δx_i^F of the distribution (see Table 5.1).

A different approach is adopted in experiments 2DLA-5 and 2DLA-6&7 to account for the modified state of stress between the N^I and N^F cracks. In 2DLA-5 we fit the PPDs of d and R with Beta functions and then update them by shifting the mean value and their upper and lower limits to account for the added extension. In 2DLA-6&7 we use the same strategy, except that we update h and R .

5.3 Results

5.3.1 Experimental Results and Numerical Modelling

Experiments with extension and compression resulted in markedly different observations. Extension competes against surface unloading and leads to more vertical crack trajectories. This is clearly observed in 2DLA-5, where extension was applied after N^I cracks were injected and propagated, by comparing green (early) to red (late) trajectories (Table 5.1). The partial refilling in experiments 2DLA-6 and 2DLA-7 had a similar effect (Table 1), reducing the influence of the unloading and leading to less deflected trajectories. We find that our trajectory simulations for the experiments with extension are not identical to, but closely match the observations, if the measured d and h are employed.

As mentioned above, the trajectories in compressional settings (2DLA-2 and discarded

experiments, see Fig.S13) tend to diverge significantly from each other and spread the uncertainty of the initial location into scattered arrival locations. Simulations with the imposed parameters fail to reproduce these data sets. This is reflected in the outcome of the inversions and forecasts, as we explain later on.

Dike trajectories are deflected towards the vertical direction when passing from a high-rigidity layer to a low-rigidity one and vice versa, as theoretically predicted by Maccaferri, Bonafede, and Rivalta (2010) (see experiments 2DLA-3 and 2DLA-4, Table 5.1).

5.3.2 Parameters sampling

We find that in most cases the PPDs retrieved from the inversions fail to constrain the individual parameters d and h , though they generally succeed in constraining their ratio R . This is clearly seen in the joint distributions for R and h (Fig. 5.2a). In the homogeneous extensional cases, the PPDs for d and especially h are generally spread. In spite of this, the imposed value of d is well recovered in 2DLA-5 and 2DLA-6 & 7 (see Table S7). In contrast, the PPD for R is always peaked around or close to the imposed value (Fig. 5.2a). The distributions of h tend to be uniform. The PPDs, including those of h , are more peaked when more data are available (2DLA-6&7). In the layered cases, the medians of all the PPDs are rather far from the respective imposed values, except for R in 2DLA-4. This was expected, since we purposely neglected the medium layering in the modelling (see section 5.2.1).

In the only compressional case (2DLA-2), the PPDs are extremely spread and fail to constrain the parameters, though the median of R is close to the imposed value (Fig. 5.2a).

5.3.3 Forecasts

In spite of the PPDs for d and h being often spread or even uniform, the forecast distribution generally shows N^F sharp peaks (Fig. 5.2b, Table 5.1). Moreover, in spite of the PPDs for d and h failing to accurately recover the imposed values, the peaks of the forecast distribution generally coincide or are very close to the observed arrivals (Fig. 5.2b, Table 5.1). This includes the layered cases. Again, the compressional case 2DLA-2 marks an exception: the forecast is rather spread (see σ^F values in Table 5.1) and shows two maxima, one closer to the box centre and a sharp one at the box margin (Fig. 5.2b); this is due to the fact that many simulated cracks hit the right side of the

Figure 5.2: a): PPDs for parameters d , h and R and joint PPD for (R, h) . Red lines show the measured values; green lines the medians (Table 5.1). The Beta functions used to fit and update the distributions in 2DLA-5 and 2DLA-6&7 are plotted in magenta. Last column from left: the starting guess, measured and median values are represented, respectively, by a blue, red and yellow star. The colour palette shows the value of S (Eq. 5.2) for every sampled point in the parameters' space, from dark red (higher S) to blue (lower S). b): counts of forecast arrivals displayed on a scheme of the box (the surface topography shown is before the refilling in 2DLA-6&7). Positions of $x_i^{obs, F}$ are marked with red lines, while green lines represent the medians of the forecasts for individual $x_i^{obs, F}$ (see also Tables 5.1 and S5).

box. Neither of the maxima coincides with the observed arrival, and the median falls ~ 1 cm away (Fig. 5.2b, Table 5.1).

Two secondary peaks are also obtained in the combined forecast distribution for 2DLA-5 ($N^F = 3$), as the sampling range for d allowed for both positive (extension) and negative (compression) values. This is reflected also in the spread of the individual distributions (Table 5.1). The two main maxima are here close to the box centre and show good agreement with $x_i^{obs, F}$. Considering the three individual distributions separately, the distances Δx_i^F between the three $x_i^{obs, F}$ and the medians $x_i^{med, F}$ are well within σ_i^F of the respective distributions. In 2DLA-6&7 ($N^F = 6$) three clear maxima are observed in the combined forecast distribution, showing again good agreement with the $x_i^{obs, F}$, which are ≤ 4 mm away from the medians of the respective individual distributions (Table 5.1).

In all extensional experiments with $N^F = 1$, the observed arrivals $x_i^{obs, F}$ are always within 2 mm from the medians (Table 5.1).

5.4 Discussion

While the inversion algorithm generally failed to retrieve the imposed values of the parameters d and h (Fig. 5.2a), the forecast strategy proved very effective in identifying high-probability regions for crack arrivals on the surface (Table 5.1 and Fig. 5.2). This apparent contradiction arises from the fact that the inversions are able to recover the imposed value of $R = d/h$. Physically, this is because the curvature of the trajectories is controlled by R , rather than d or h individually, as also found by Roman and Jaupart (2014).

Forecasts are successful in spite of the sampling being carried out on scarce data sets and when layering of the medium is neglected. If data sets are larger (5 data points for 2 parameters), the state of stress is recovered more accurately. In principle, our procedure could be used also to constrain the elastic parameters, but information on the stress state would be necessary as they trade off. To test this possibility, we ran an inversion for E on the N^F data set of 2DLA-5, and we found the sampled E distribution peaks very close to the measured value (results are shown in Fig. S14b).

The forecast strategy applied in experiments 2DLA-5 and 2DLA-6&7 also proved effective in accounting for the modification of the stress field over time, validating the evolving-stress forecast method by Rivalta et al. (2019).

Several factors may contribute to the failure of the approach in compressional settings. Both unloading and compression lead to more horizontal σ_1 directions within the medium. Thus, the mismatch between the crack orientation and σ_1 right after the injection is larger and they need more space to align. Moreover, a horizontal σ_1 may encourage cracks to propagate towards the back or the front walls of the box, whose effect on the gelatin may undermine the plane strain assumption (in compressional cases, these walls prevent the gelatin to expand along the y-axis, thus inducing compression also in this direction). Furthermore, side plate insertion and the non-frictionless contact between gelatin and box walls induced local stress concentrations at the box corners, affecting nearby trajectories (Fig. S13). However, dike propagation in compressional settings, including nature, may be inherently more challenging to forecast: σ_3 -perpendicular trajectories tend to diverge, especially in case of unloading, and simulations are therefore more sensitive to any variability of initial and boundary conditions or model parameters.

A further limitation arises from the limited number of experiments we carried out. In spite of such small number, we did observe clear common patterns in experiments with similar settings (section 5.3.1). Our experimental setup allowed for several factors, including variable starting crack length and orientation, elastic heterogeneities and possible interactions between successive injections, to play a role. This is reflected in the fact that observed and modeled trajectories do not coincide in general (section 5.3.1), though the forecasts are fairly good. This is not contradictory, as our forecast strategy includes a stochastic model to treat such variability.

Another remarkable issue is the nearly-uniform trend observed in the PPDs for h (Fig. 5.2a), which appears to be systematic even when larger data sets are available (as opposed to the PPDs of d , cfr 2DLA-1 and 2DLA-5). This arises from the fact that very shallow or very deep surface unloads, for the same d and starting points, lead to similar arrivals. We surmise that this effect, observed both in the numerical simulations and in a separate experiment (Fig. S14a), is due to the

relaxation of the surface excavation's walls under gravity.

5.5 Conclusions

We conclude that a mixed deterministic-stochastic strategy is effective in constraining the ratio of different stress-generating mechanisms and forecasting the arrival points of air-filled cracks in gelatin blocks. The strategy performs well on small data sets and may be therefore suitable for applications to volcanic regions where few vent locations are available. Future developments may focus on relaxing some of the limitations in our current numerical simulations, such as upgrading to 3D, including the viscous flow in the cracks, or addressing rheologies different from elastic. This will facilitate direct application to producing probabilistic maps of vent location for volcanic systems in nature.

Acknowledgements and funding

We are grateful to Thierry Menand and Sam Poppe, whose thorough and constructive reviews greatly improved the quality of our work. L.M. and T.D. are funded by the grants N. RI 2782/6-1|ZO 277/3-1 and DFG-ICDP N. RI 2782/3-1, respectively. The numerical model is based on the open source code at <https://doi.org/10.5281/zenodo.3694164>.

Chapter 6

Unstable sill trajectories

The content of this chapter has been submitted to Nature Geoscience.

Summary paragraph

To feed off-summit eruptions at volcanoes, magma moves by creating and passing through cracks that can propagate many kilometres downslope. Typically, these cracks are vertical (dykes). Here we analyse the propagation of a flat-lying magma-filled crack (sill) at Sierra Negra volcano, Galápagos Islands, using space-borne radar interferometric data spanning the 2018 eruption. This sill propagated along a 15-km-long curved trajectory, which is hard to explain with current understanding and models. We perform both a simple analytical analysis and three dimensional (3D) numerical crack propagation simulations, which incorporate the effects of magma buoyancy, realistic topography and tectonic stresses that may control the sill's propagation. We show that sill trajectories can only be understood and predicted if accounting for the interaction of all these factors, and explain the observed trajectory at Sierra Negra as the result of competing stresses being close to one another throughout the propagation of the sill. Under certain conditions, these events may be inherently unstable but remain predictable by combining high resolution observations with sophisticated theoretical understanding.

6.1 Introduction

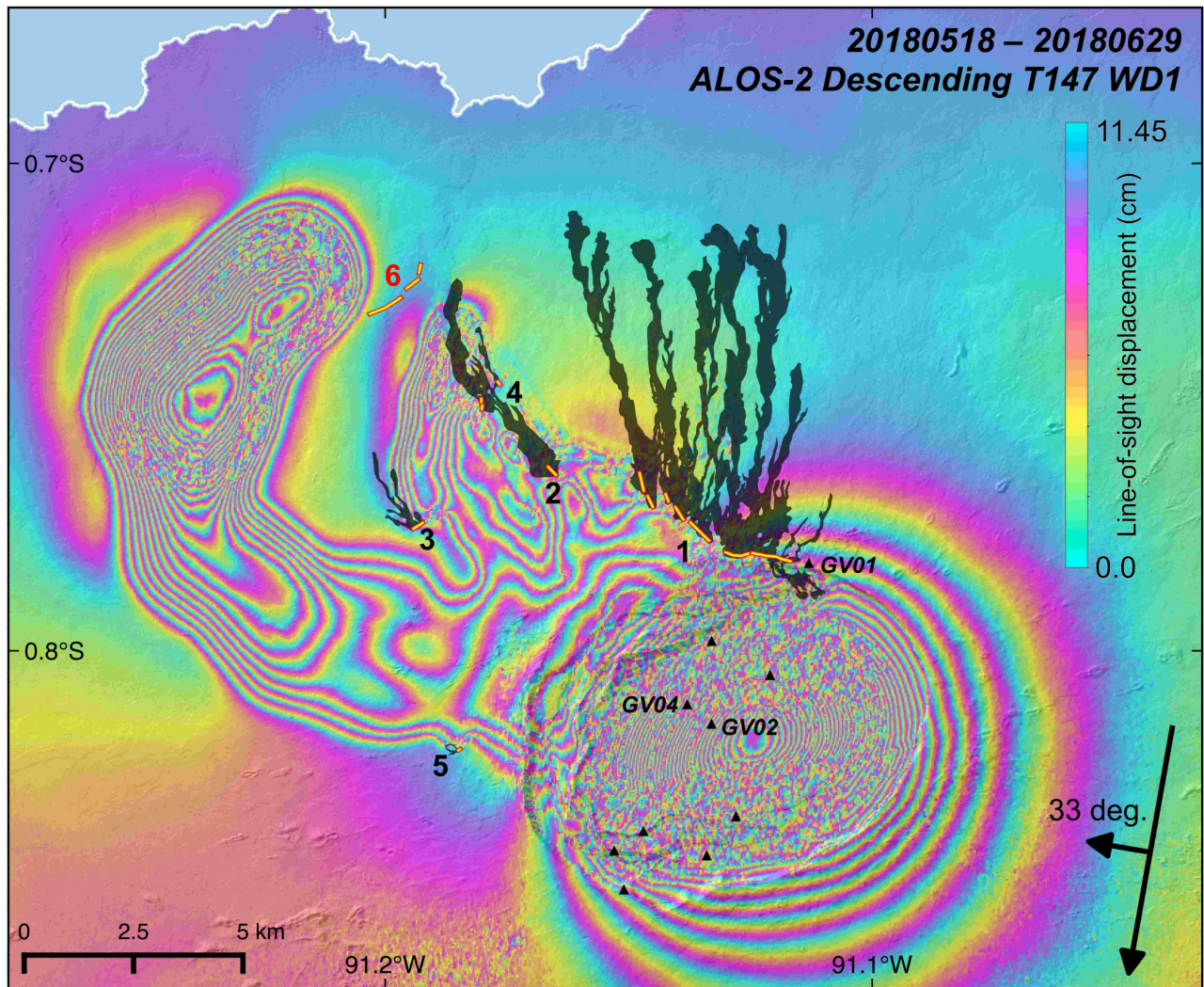
Sierra Negra is an intra-plate basaltic shield volcano with a maximum elevation of 1140 m above sea level (a.s.l.), a shallow (110 m) and structurally complex 7 x 10 km elliptical caldera, and is the most voluminous of the five coalescing volcanoes that form Isabela Island in the western Galápagos Archipelago, Ecuador (Reynolds, Geist, and Kurz, 1995). Thirteen effusive eruptions have occurred

at Sierra Negra since 1813. The three most recent eruptions (Vasconez et al., 2018) all occurred in the northern flank of the volcano and produced 0.90 km^3 in 1979, 0.15 km^3 in 2005, and 0.19 km^3 in 2018. While the 1979 and 2005 eruptions were fed by vents high on the northern flank and with eruptive fissures aligned parallel to the caldera rim, the vents of the 2018 eruption were scattered with no preferred orientation up to 9.5 km from the caldera rim, at a minimum elevation of 90 m a.s.l. Vents at such low elevation do not seem to be common in the recent history of the volcano. On the other hand, some of the higher-elevation eruptive vents of the 2018 eruption reactivated existing fissures. The 2018 eruption interrupted a thirteen-year semi-continuous period of uplift that raised the floor of the summit caldera by up to 5.2 m since the 2005 eruption as measured by GPS (Fig. S15), presumed to be re-pressurization of a ~ 2 km deep magma reservoir. On the 26 June 2018 at 19.40 the appearance of volcanic tremor marked the beginning of the eruption. Throughout the eruption, seismicity was mainly located along the caldera fault system with fewer events in the northwestern upper flank. Caldera deflation rapidly started with the onset of eruptive activity and by the time the eruption ended on August 25th 2018, GPS stations measured a cumulative intra-caldera subsidence of up to ~ 8.5 m (Fig. S15).

Short-lived (< 24 hrs) effusive eruptions from multiple fissures (Fissure 1 - 5, Fig. 6.1) on 26-27 June were followed by a long-lasting effusive eruption from the most distal fissure (Fissure 6) between July 1st and August 25th. Geodetic monitoring by continuous GPS at Sierra Negra is limited to the summit caldera, such that the feeder-induced surface displacements were only measured by interferometric synthetic aperture radar (InSAR). The first co-eruptive synthetic aperture radar (SAR) image was acquired on 29 June at 17:50 UTC by the Japan Aerospace Exploration Agency's ALOS-2 satellite, approximately 70 hours after the onset of the seismic swarm (Fig. 6.1). Further SAR images were acquired on 30 June and 1 July by the European Space Agency's Sentinel-1 satellite constellation, right before the opening of Fissure 6 (Fig. S16a and b). Additional SAR images were captured during the eruption of Fissure 6 (Fig. S17a and b).

Surface deformation patterns before and after Fissure 6 erupted show a surprising trajectory for the propagating feeder. The deformation patterns point at a flat-lying magma body (sill, see Methods) with a propagation direction that turned by over 90 degrees, whilst the sill remained flat-lying. Even though turning and twisting of dykes has been observed frequently (Sigmundsson et al., 2015; Bagnardi, Amelung, and Poland, 2013; Smittarello et al., 2019), such a 90 degree turn has never been observed before.

Figure 6.1: Interferogram spanning the sill propagation phase of the 2018 eruption. SAR data from the ALOS-2 satellite. Each colour cycle represents 11.45 cm of line-of-sight (LOS) surface displacement. Gray polygons show the extent of the lava flows emplaced during the time period spanned by the interferogram. Yellow lines mark the location and extent of all eruptive fissures. Black triangles mark the location of GPS stations. Black arrows show the satellite orbit direction (\sim N-S), look direction (\sim E-W), and the incidence angle in degrees. Descending pass, Track 147, ScanSAR mode.



6.2 Parameters and numerical result

In order to understand why the sill turned as observed, before proceeding with a 3D simulation, we reduce the physics of this problem to its component parts and evaluate how these affect the sill's direction of propagation. Previous studies have found that dyke trajectories are dependent on the ratio of tectonic to topographic loading stresses (Roman and Jaupart, 2014; Sigmundsson et al., 2015; Rivalta et al., 2019). Here we propose that contrasting magma and rock weight gradients (buoyancy) must also be considered as one of the dominant forces.

Propagation directions of dykes have typically been predicted by maximizing the strain energy release rate (Dahm, 2000a; Sigmundsson et al., 2015), on test elongations at the leading tip, thereby finding the path of least resistance. Such a method is unwieldy for true 3D propagation, as it would involve computing a large number of potential tip-line growth patterns. Here we use a theoretically equivalent, but more flexible, approach based on the maximum stress intensity, K (see Methods). In our analytical approach, we reduce the sill geometry to that of a penny-shaped crack subject to stress gradients (Chapter 7.3), with an opening that is compatible with the surface displacements observed along the short-axis of the sill (see Methods). At selected points along the sill's path, we calculate K around the tip-line (Davis, Healy, and Rivalta, 2019), and assume the greatest tip-line advance occurs in the direction where K is largest (Paris fatigue law (Davis, Rivalta, and Dahm, 2020)). In our numerical simulations, we discretise the sill into triangular elements (Nikkhoo and Walter, 2015; Davis, Rivalta, and Dahm, 2020) and update the tip-line at each step using the local value of K as compared to the critical rock strength, K_c .

In our analytical approach, we employ stress intensity equations in a full-space. We then go on to numerically test how the free surface and the real topography would affect these results. In the numerical simulations, we compute stresses under an arbitrary topography in 3D with an external elastic stress field. As in previous 3D studies we neglect viscous effects of the contained fluid and chamber pressure.

We constrain the parameters in both models using inversions of co-eruptive InSAR data along the propagation path (Fig. 6.1, see Methods): depth $d=950$ m, radius $c=1900$ m and volume $V=1.6\pi c^2 d$ m³. V represents the volume of the inflated nose of the propagating fracture, which is around a 10th of the estimated erupted volume (Vasconez et al., 2018) (0.018 km³). We set the rock properties to: $\rho_r=2900$ kg·m⁻³, $\mu=2\cdot 10^9$ Pa and $\nu=0.35$ corresponding to the rock density, shear modulus and Poisson's ratio, respectively.

6.3 Effects defining the sill's path

Opening stress intensity K_I around the edge of a penny-shaped crack of volume V in a full-space, subject to a constant pressure (Tada, Paris, and Irwin, 2000) is:

$$K_I = \frac{3\mu V}{4(1-\nu)c^2\sqrt{\pi c}} \quad (6.1)$$

$K_{I\alpha}$ around a crack under a pressure gradient (Tada, Paris, and Irwin, 2000) is:

$$K_{I\alpha} = \frac{4}{3\pi} \Delta\gamma c \sqrt{\pi c} \cos(\alpha) \quad (6.2)$$

where α is the angle away from the direction of the linear stress gradient ($\Delta\gamma$) on the crack's walls. The pressure gradient in equation (6.2) defines the direction of K_{max} (blue lines in Fig. 6.2a). As such, ignoring other effects, the direction and magnitudes of competing pressure gradients acting on the crack define its propagation direction.

We now estimate stress gradients at Sierra Negra. First, we use an analytical solution describing stresses beneath a ridge-like topography (Savage, Powers, and Swolfs, 1984). h and v are the horizontal and vertical axis, respectively. We compute the horizontal gradient of vertical stress: $\delta\sigma_v/\delta h$, i.e., the normal stress gradient driving a flat-lying crack away from the caldera rim, at the inferred sill depth along its track. Linear stress gradients due to the difference between rock and fluid density (buoyancy) (Pollard and Townsend, 2018) are $(\rho_r - \rho_f)g \sin(\beta)$, where ρ_f is the magma density. The factor $\sin(\beta)$ means that if the crack is flat this gradient is zero. We set (Vigouroux et al., 2008) $\rho_f = \rho_r - 300 \text{ kg}\cdot\text{m}^{-3}$. For the parameters above, 15 km from the caldera center (around where the sill began to turn) the dip needs to be around 10° for the buoyancy gradient to exceed the stress gradient due to the overlying slope (Fig. S18) and drive the sill to turn away from the downslope direction (Fig. 6.2a).

As shown in Fig. S19, a dipping sill is attracted towards the free surface. For $c/d=2$, as observed, a dip of 15° results in the same K_I increase for both buoyancy and free surface, doubling dip's effects.

Lastly, we test if the other intrusions to the east that fed fissures 2, 3 and 4 (Fig. 6.1) may have attracted the sill. Two penny-shaped cracks subject to equal internal pressure (Tada, Paris, and Irwin, 2000; Fabrikant, 1987) separated 5 km from each other, as observed (tip separation of 1.2 km)

Figure 6.2: (Continued on the following page.)

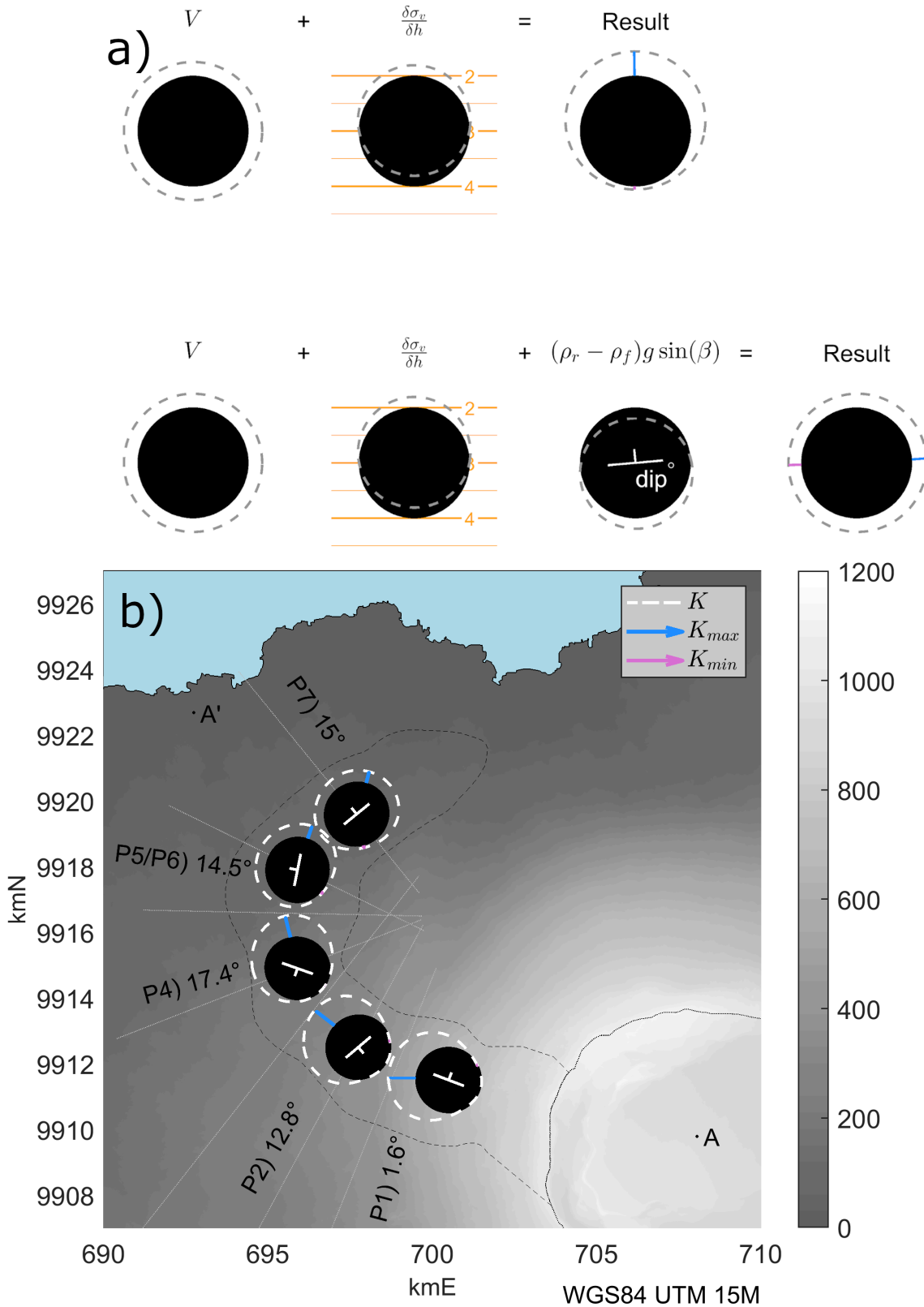


Figure 6.2: Simulating the propagation direction of fracture at selected locations. a) Analytical K_I diagram. Black circles represent the fracture, distance of the dashed gray line to the fracture edge represents K_I magnitude, blue segment represents K_{max} direction. Topographic contours in orange. b) Numerical simulation of the propagation direction at Sierra Negra. Fractures are scaled down to a 1 km radius, white dashed-line represents K_I magnitude as in a). Dip and strike directions shown, defined by inversions (see Methods). For P7 a dip of 15° is used. Dashed grey outline is a contour of sill-induced deformation from Fig. S17. Background $\sigma_h/\sigma_v=0.5$ in topographic loading model.

experience a maximal K_I increase of $\sim 3\%$. Such an increase is minor compared to the processes described earlier.

To summarise the analytical analysis, the stress gradient due to topography drives the sill away from the caldera rim. As the slope shallows, the buoyancy gradient begins to dominate even for shallowly dipping cracks, causing the sill to turn. The free surface amplifies this effect (Fig. S21). This analytical method of assessing the sill path is flexible and fast. In spite of its simplicity it can explain the trajectory of previous intrusions, including curved dyke trajectories such as the 2014 Bárðarbunga dyke path (chapter 7.3).

In order to allow interaction between all factors discussed above, we develop a 3D Boundary Element Model (Davis, Healy, and Rivalta, 2019; Davis, Rivalta, and Dahm, 2020) to simulate a penny-shaped crack beneath the real edifice's topography. We include stresses due to gravitational loading and traction-free boundary conditions on the surface (Martel, 2000; Davis, Healy, and Rivalta, 2019). Using orientations of the crack in the 3D space obtained by inverting surface deformation (see Methods), our model explains the turning of the sill for snapshots along its path (6.2), showing that it is the interaction between sill dip, slope gradients and the free surface that causes the observed turning. Note that increasing the ratio of the horizontal to vertical stress (σ_h/σ_v) in the topographic loading model results in better fits.

6.4 Full 3D propagation model

Lastly, we run full 3D fracture propagation simulations (Davis, Rivalta, and Dahm, 2020). Here the crack is neither constrained to be planar nor circular in shape, only such that it maintains a constant V . The tip-line shape is recalculated at every iteration moving it forward in proportion to K/K_c , if

Figure 6.3: Numerical simulation of the sill propagation. a) Map view, b) cross-section looking along the downslope direction and c) cross-section looking along the x -axis c). The fracture is shown at chosen locations along its computed path. Grey points are edges that closed in the previous iteration. The shaded patch in a) is the sill track and the dotted line is the caldera rim. In c) the solid line is the topographic slope used to load the body and the dashed line is the simulations free surface. Parameters used: $\beta = 1^\circ$, $\rho_f = \rho_r - 300 \text{ kg/m}^3$, start depth of 1000 m, $K_c = 70 \text{ MPa} \cdot \text{m}^{0.5}$, $V = 1.6\pi c^2 \text{ m}^3$ and $\sigma_{yy} = -4.5 \text{ MPa}$.

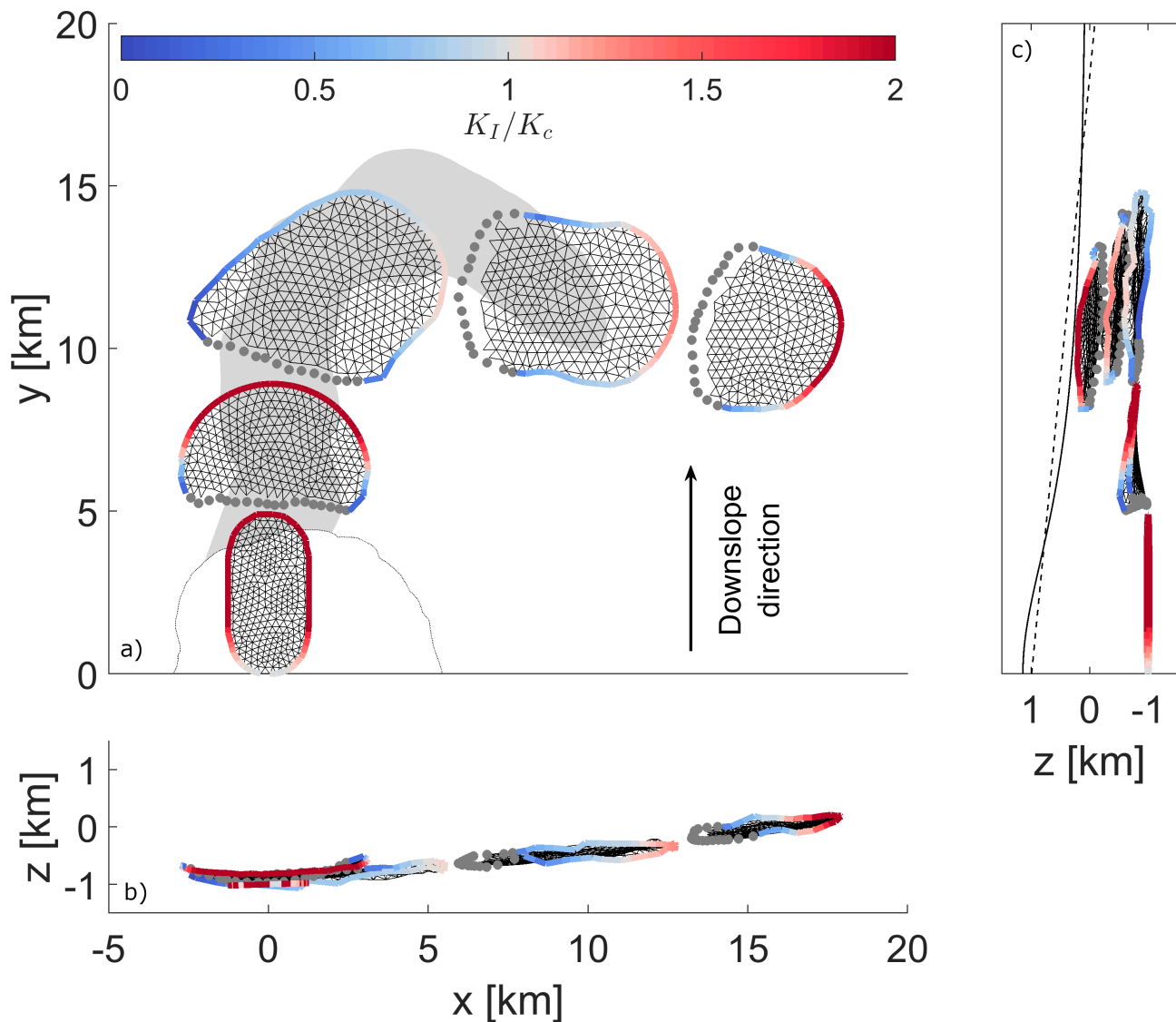
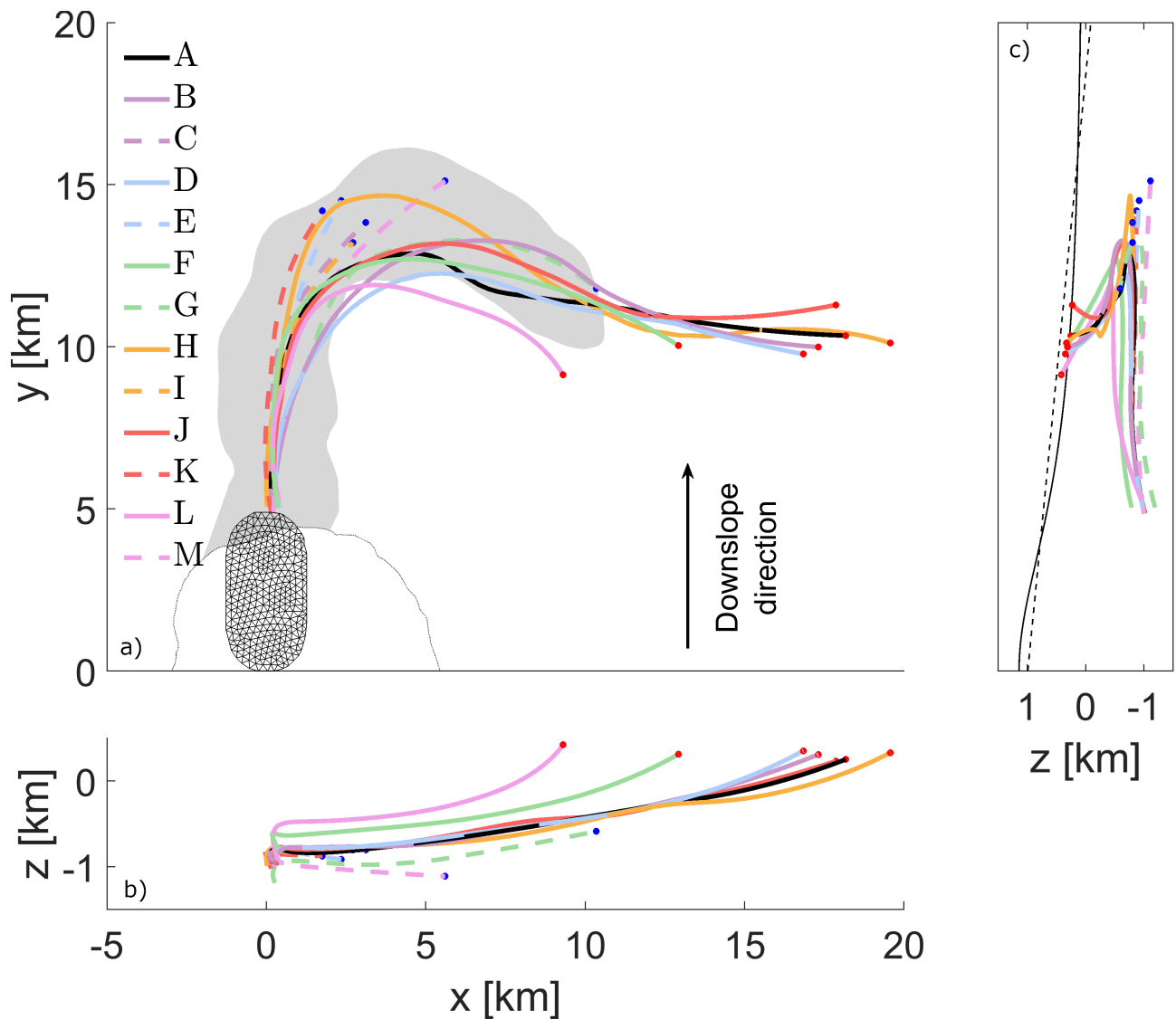


Figure 6.4: Effects of parameters on the simulated sill path. Fracture paths from simulations as in Fig. 6.3, defined by the triangle with the maximum K value at each iteration. Dashed lines with blue dots are fractures that stalled, solid lines with red dots reached the free surface (erupted). In each simulation we changed one parameter with respect to Fig. 6.3, as follows: A is reference simulation from Fig. 6.3, B: $\beta = 1.5^\circ$, C: $\beta = 0.5^\circ$, D: $\rho_f = \rho_r - 450 \text{ kg/m}^3$, E: $\rho_f = \rho_r - 150 \text{ kg/m}^3$, F: Start depth=800 m, G: Start depth=1200 m, H: $K_c = 55 \text{ MPa} \cdot \text{m}^{0.5}$, I: $K_c = 85 \text{ MPa} \cdot \text{m}^{0.5}$, J: $V = 1.8\pi c^2 \text{ m}^3$, K: $V = 1.4\pi c^2 \text{ m}^3$, L: $\sigma_{yy} = -3 \text{ MPa}$, M: $\sigma_{yy} = -6 \text{ MPa}$.



$K/K_c > 1$, at each triangle. We remove triangular elements that shut closed. Bending or twisting of the fracture's tip-line out of its plane is calculated using the maximum circumferential stress criterion (Pollard and Fletcher, 2005).

In this last approach, we use a planar free surface with a start height at $y = 0$ of 990 m with a slope of 3° facing to the north. The lithostatically stressed body ($\sigma_h = \sigma_v$) is loaded due to topography (Savage, Powers, and Swolfs, 1984) (S18). We also apply throughout the body a compressive tectonic stress of 4.5 MPa directed along σ_{yy} , with σ_{xx} the mean between σ_{yy} and σ_{zz} , as suggested by stress indicators (Heidbach et al., 2018). Shear stresses from the topographic loading solution (Savage, Powers, and Swolfs, 1984) are set to zero, on the assumption that these stresses are diminished over time by faulting, diking and longer term rock deformation processes in the edifice's flanks.

The initial crack is an ellipse 1000 m wide and 5000 m long at a depth of 1000 m below sea level, dipping to the west by $\beta=1^\circ$. K_c is set to $70 \text{ MPa}\cdot\text{m}^{0.5}$. We find when the fracture gets a certain distance away from the caldera centre, it begins to turn and propagates east (6.3). By changing the values of the parameters one at a time, we investigate the sensitivity of the path to the input parameters and initial geometry (6.4). Reducing the initial start dip β or the buoyancy reduces the force driving the sill eastwards, causing the sill to stall as the topography shallows (6.4, curves B to E). The start depth defines when the free surface attraction takes effect (S21F), such that only shallower sills can propagate eastwards (6.4, curves F,G). The fracture toughness and volume define how far the sill can travel downslope as the topography shallows. These also control the sill width, reducing the buoyancy force when this is smaller, again trapping the sill (6.4, curves H to K). When the tectonic compressive stress is reduced, in places σ_v becomes the most compressive stress, causing the sills track to become very unstable with the sill quickly rising to the surface (6.4L).

The simulations compare well with the observed trajectory; the sill was destined to turn, although it could have stalled or erupted earlier on its path.

6.5 Conclusions

Previous flank volcanism at Galápagos volcanoes has been fed by radial and circumferential dykes (Chadwick Jr and Dieterich, 1995; Bagnardi, Amelung, and Poland, 2013). Here we have shown evidence of flank volcanism fed by a long curving sill. We find that trajectories of shallow sills underneath topography will be unstable and defined by a delicate balance between buoyancy forces,

topographic load, external stresses and the free surface. Still, trajectories may be anticipated, provided all those factors are well-constrained and their interaction is accounted for. By combining such models with careful analysis of high-resolution crustal deformation data, we showed that such parameters as well as the state of stress of the volcano can be well constrained, reducing the uncertainties in the hazard.

6.6 Methods

6.6.1 GPS data

S15 shows the continuous GPS time series for three stations located at the summit of Sierra Negra (see Fig. 6.1 for station locations). Data downloaded from <http://geodesy.unr.edu>.

6.6.2 Definition of K

The total stress intensity which is compared to the fracture toughness at a point of a cracks tip-line can be defined by a combination of the opening, sliding and tearing mode stress intensity factors (Pollard and Fletcher, 2005) (K_I , K_{II} and K_{III}).

$$K = \sqrt{K_I^2 + K_{II}^2 + \left(\frac{1}{1-\nu}\right) K_{III}^2} \quad (6.3)$$

which relates to strain energy release rate (Tada, Paris, and Irwin, 2000) (\mathcal{G}) through:

$$K = \sqrt{\frac{\mathcal{G}E}{1-\nu^2}}; \quad (6.4)$$

where E is the Young's modulus.

6.6.3 InSAR processing and additional observations

All interferograms were created using the InSAR Scientific Computing Environment (ISCE) software (Rosen et al., 2015) and by applying conventional differential InSAR processing techniques for stripmap, ScanSAR (ALOS-2), and Terrain Observation by Progressive Scans (TOPS) (Sentinel-1) data. Topographic contributions to the interferometric phase are removed using the Deutsches Zentrum für Luft und Raumfahrt (DLR) 12-m resolution digital elevation model based on TanDEM-X satellite measurements (Wessel et al., 2018), and interferograms are phase-unwrapped using the Statistical-cost, Network-flow Algorithm for Phase Unwrapping (SNAPHU) (Chen and Zebker, 2001) implemented in ISCE.

6.6.4 InSAR inversions along track

Deformation source parameters and uncertainties are estimated using a Bayesian approach implemented in the Geodetic Bayesian Inversion Software (Bagnardi and Hooper, 2018). The inversion algorithm samples posterior probability density functions (PDFs) of source parameters using a Markov chain Monte Carlo method, incorporating the Metropolis-Hastings algorithm, with automatic step size selection. Posterior PDFs are calculated considering errors in the InSAR data, which we directly quantify using experimental semivariograms to which we fit an unbounded exponential one-dimensional function with a nugget (Bagnardi and Hooper, 2018). The exponential function is then used to populate the data variance-covariance matrix. Prior to inversions, all InSAR data sets are subsampled using an adaptive quadtree sampling (Decriem et al., 2010) to reduce the computational burden when calculating the inverse of the data variance-covariance matrix and in forward model calculations. For all models, we assume that the deformation sources are embedded in an isotropic elastic half-space with Poisson's ratio $\nu = 0.25$. Since no detailed prior information on the deformation source parameters are available, prior probability distributions are assumed to be uniform between geologically realistic bounds. In each inversion, posterior PDFs are sampled through 10^6 iterations. Depth estimates are referred to as distance from the surface.

At profile locations P1, P4 and P5 in Fig. S20 we estimate source parameters of a rectangular dislocation with constant opening (Okada, 1985) and retrieve openings of 0.74 ± 0.03 , 1.73 ± 0.03 and 2.80 ± 0.03 m respectively, where the value after \pm brackets the 2.5 and 97.5 percentile of the results from our Bayesian inversion scheme (Bagnardi and Hooper, 2018) (S8). Using such solutions the depth of this sill along its path is consistently 900-1000 m below the ground surface with a half-width of approximately 1.5 km.

6.6.5 Choosing physical parameters

We approximate the sill in our analytical analysis as a penny shaped crack. To retrieve c and V for this geometry, we compare the ground deformation of a flat lying rectangular dislocation where the faces open 2 m with a depth d of 950 m and its third axis extending far out of the plane of observation, to the analytical solution describing the uplift due to a pressurised penny-shaped crack under a half-space (Sun, 1969) with the same d . The penny-shaped crack's ground deformation supplies a radial deformation pattern, therefore we only fit this to the ground deformation relative to the short-axis of the sill. Once fitted, we retrieve a radius $c = 1900$ m and volume $V = 1.6\pi c^2$ (with the largest error 1.5% and 15% less than the maximum u_z and u_x value from the dislocation solution, respectively).

6.6.6 Comparison of different effects on stress intensity factors

S19 is computed using a numerical scheme to evaluate how K_I in equation (6.1), decreases as the crack approaches the free surface (Davis, Healy, and Rivalta, 2019). For $c/d=2$ as observed, a dip of 15° causes a relative increase and decrease of K_I of +30% and -10% at its highest and lowest edge respectively. A 30% increase corresponds to the same K_I increase as a sill dip of around 15° due to $(\rho_r - \rho_f)g \sin(\beta)$. As with buoyancy, this effect increases with crack dip.

Acknowledgements and funding

T Davis is funded by the DFG-ICDP grant N. RI 2782/3-1. M. Bagnardi was supported by an appointment to the NASA Postdoctoral Program at the Jet Propulsion Laboratory, administered by the Universities Space Research Association (USRA) through a contract with NASA. Part of this research was carried out at the Jet Propulsion Laboratory, California Institute of Technology, under a contract with the National Aeronautics and Space Administration (grant 281945.02.47.04.51).

Code availability statement

The code used for boundary element numerical analysis in this study was the open source code <https://doi.org/10.5281/zenodo.3694163> with an interface with the Computational Geometry

Algorithms Library software (C++) for meshing.

Author Contributions

T.D and M.B coordinated the work and wrote the initial manuscript. M.B and P.L acquired and analysed the InSAR and GPS data in this study. This analysis provided the evolution and geometry of the sill. T.D and E.R conceptualised the analytical and numerical fracture mechanics that form the interpretation in this work. T.D wrote the analytical and numerical fracture mechanics codes used in this study. All authors have read and revised the manuscript and contributed ideas to the research.

Chapter 7

Summary and discussion

7.1 Summary

In this work, I have extended 2D fluid-filled crack propagation modelling approaches, such that they can be applied in 3D. To adapt these methods to 3D, theoretical advances were required. The resulting method I propose is a combination of the existing 2D methods as well as some theoretical changes, this required implementations of some recent advances in boundary element modelling techniques. The method I propose reproduces the 3D shape of propagating cracks in gelatin, it was previously not clear if this was possible using such methods. These developments and solutions to technical and numerical issues allow for simulation of fluid-filled fracture growth and the resulting fluid migration in 3D. Additionally, I have shown how performing a complimentary 3D analytical analysis vastly improves how such models can be interpreted. The methods proposed can be applied to very different types of problems at different scales. This includes small volume fluid injections in sedimentary basins, sill growth beneath volcanic edifices and hydro-fracturing in glacial settings. Many of the problems tackled here were previously not tractable in 2D.

In chapter 3 I show that quantifiable parameters describe when a fluid-filled crack will start propagating under stress gradients in 3D, and that combinations of these stress gradients define 3D crack propagation paths. Existing 2D analytical formulations describing critical crack lengths have been manipulated and adapted. I use these in combination with 3D numerical models that include stress gradients, to determine a tipping point into ‘self-sustaining’ propagation. This is described by 4 parameters, the two elastic parameters describing the rock mass, the density contrast between the fluid and rock and the fracture toughness of the medium; with a resulting critical volume of fluid. All of these parameters can be quantified in industrial operations, as these properties can be controlled during operation or measured from drill core. This analysis shows that typical volumes of fluids injected in industrial operations are close to this volumetric limit. This has implications on assessments of safety, and the models that inform these operations.

Chapter 7. Summary and discussion

In chapter 6, the idealistic conditions in chapter 3 are dropped and the methods I propose are applied to analyse the observed propagation path of a volcanic sill in 2018. This case is more complex in the sense that it requires an approximation of the actual stress state beneath the volcanic edifice, as well as half-space conditions in the propagation model. For this event, I show that the competition between stress gradients describes the path the sill took, along with the influence of the free surface because the sill was shallow. I analyse the event using both 3D scale independent analytical formulas and a full 3D propagation code. The analytical analysis gives an indication of the stability of crack paths at locations along its track, while sophisticated numerical analysis provides complex insights into the sensitivity of such a system to the initial intrusion parameters.

Uniquely, in chapter 6, I also show how stresses within and beneath an edifice can be constrained from either analytical or numerical models, and that stress gradients from these results are reasonable. This insight is particularly powerful, as these gradients due to the topographic loading, as shown in the studies above, define where a fracture will propagate. These stresses shown in chapter 6 combined with the critical volumes from chapter 3 provides simple constraints on how far a sill can move away from the summit of a volcano, which is important in the context of hazard. A limitation to overcome in future studies is to manipulate the critical volume formula such that it accounts for cracks close to the free surface. For flat-lying cracks close to the free surface, the whole-space values of V_c provided by chapter 3 will be too small, as K_I due to an internal volume and pressure are different.

In chapters 4 and 5 I show how statistical schemes combined with physical models can be used to quantify the ratio of tectonic to topographic stresses accurately. Currently these methods rely on the assumption of dyke propagation along σ_3 trajectories. It is of interest that if such schemes are combined with the mechanically more complex propagation schemes as described in previous chapters, retrieval of additional stress ratios is possible, for example the ratio between magma buoyancy and topographic stress. Additionally, it would be interesting to see if using such schemes would result in smaller bounds on the parameters that can define the path of propagation (more sensitive trade-offs). Noting that use of these more advanced physical models would result in more model parameters.

7.2 Discussion

In the next section I list the assumptions underpinning this work, citing field or laboratory evidence for, or contrary to the assumptions used. I then discuss the possibilities of relaxing such assumptions

and the implications this may have.

7.2.1 Assumptions

Linear elasticity and infinitesimal strain: In engineering analysis linear elastic fracture mechanics has been used routinely for decades, this is because the theory is both simple and works effectively. Rock mechanics testing of cores shows that many rocks closely follow a linear stress strain relationship when deformations are small. In this work it has been assumed that the medium surrounding the fractures can be treated as a linear elastic. Additionally, strain has been assumed to be infinitesimal. These are reasonable assumptions as gradients in displacement around fractures remain small in all regions apart from those close to the fracture tip and material rotations around fractures are negligible. It is of note that a multitude of studies focus on plasticity of the material surrounding a fracture's tip, due to high strains in this region, with analytical formulations available for certain materials and geometries (Tada, Paris, and Irwin, 2000). Including tip-plasticity in propagation models may provide some interesting insights when used in combination with observations. A myriad of numerical solutions exist that can account for both non-linear elastic behaviour and finite strain numerically. Further work in this direction would require evidence that the strains involved with the fracturing process in question are non-linear or large enough to warrant the use of finite strain.

Sharp fractures: There is an increasing number of field observations of blunted dyke tips (Pollard, 1973; Hoek, 1994; Schofield et al., 2012; Healy et al., 2018). In some cases it is assumed this blunting resulted in arrest of the dyke, in others that this was an inflationary process after arrest. In some sedimentary sequences it is thought the dyke can propagate with a blunt tip by 'bulldozing' aside the material in front of this. In this thesis the tip of the fracture has been assumed to be sharp. In the context of blunted intrusions, stress intensity factors for sharp cracks can be applied to thin notches whilst remaining accurate, a notch being a fracture with a rounded tip, see Tada, Paris, and Irwin (2000, p.8). As such, this could be applied to model blunted intrusions. If K is used to compute the stress distribution around the tip of such an intrusion, the tip's radius of curvature would have to be accounted for in Eqs. 1.6:1.8. Therefore, it is possible to use the methods in this work to evaluate potential propagation directions of intrusions with blunted tip-lines, as long as they are adjusted to account for the tip shape. Modelling fluid-filled propagation involving the 'bulldozing' effect mentioned above, requires more work to understand and account for this process (Pollard, Muller, and Dockstader, 1975).

Fracture growth scheme: In engineering literature relationships exist that provide the growth increment of fatigue cracks under cyclic loading, known as Paris' law (Paris and Erdogan, 1963). This involves empirically determined material constants, and is related to the range of K in each loading cycle. In this work a simplified scheme is used, the fracture front extends an amount relative to the local value of K , once K_c is exceeded. The maximal extension length d_{max} is predefined, this occurs at the largest value of K on the tip line, K_{max} . The local tip-line extension d can be found using:

$$\text{subject to } K_{max} > K_c, \quad d = d_{max} \left(\text{Re} \sqrt{\frac{K - K_c}{K_{max} - K_c}} \right)^2 \quad (7.1)$$

This linear relationship lacks experimental verification in rock. Despite this, it is of note that the fracture shapes resulting from the simplistic growth scheme presented here are of reasonable size and shape, as the scheme itself is simplistic but rational.

Quasi-static equilibrium: Ascent rates of fluid-filled fractures are known from field and experimental observations, these are in the order of mm/s to around half a m/s (Das et al., 2008; Tolstoy et al., 2006; Okamoto and Tsuchiya, 2009). Lateral propagation velocities of basaltic dykes lie in this range, and in the early stages, closer than 5-10 km from a chamber these are consistently around 0.4-0.5 m/s, and slow with distance (Brandsdóttir and Einarsson, 1979; Jackson et al., 1975; Sigmundsson et al., 2015; Lengliné, Duputel, and Okubo, 2021). Experimental data and modelling suggests that the speed of this process is governed by the rate of fluid flow (Heimpel and Olson, 1994; Salimzadeh, Zimmerman, and Khalili, 2020). In this analysis it has been assumed the fracturing process is one of quasi-static equilibrium, where acceleration and velocity terms have been ignored. Observations of fluid-filled cracks and models of this process in gelatin show that elastostatic models capture the evolving form of fluid-filled fractures accurately (Takada, 1990). This quasi-static assumption should hold in cases of fluid-filled fracturing where the rate of fluid flow controls the speed of propagation, with this flow rate below the velocity of the fracture rupture speed. It is of note, that following observations, modelling of shear fractures (faulting) has advanced towards dynamic modelling, where the use of quasi-dynamic codes is now routine (Erickson et al., 2020). Such implementations could be applied to fluid-filled fracture propagation in the event that the quasi-static assumption is deemed to have been violated.

Isotropic rock mass and fracture arrest: Fluid-filled fractures pass through interfaces separating elastics of different stiffness as these travel. Observations of this exist in both natural and industrial settings (Warpinski, Schmidt, and Northrop, 1982; Rivalta et al., 2015). Experimental data of this process is also abundant, showing how the aperture and shape of fractures change as these approach such interfaces (Rivalta and Dahm, 2006; Urbani, Acocella, and Rivalta, 2018). An

Chapter 7. Summary and discussion

additional process is that of a freely slipping interface (Weertman, 1980). This causes fractures to arrest as their leading tip advances towards the interface (Warpinski, Schmidt, and Northrop, 1982). How frictional effects on this ‘freely slipping’ interface change this result have been explored, showing they only arrest under certain conditions (Renshaw and Pollard, 1995). This process of arrest has been observed in nature, with dykes stalling as faults shear near their leading tip (Maccaferri et al., 2013; Maccaferri et al., 2016). Such effects remain to be quantified in relation to 3D fluid-filled fractures propagating due to stress gradients. A quantitative analysis on how stiffness contrasts, along with the angle, size and frictional properties of slipping interfaces can cause a propagating fluid-filled fracture to stall are highly relevant to this work. Processes such as these will affect the value of V_c in chapter 3 and also provide constraints for crack propagation simulations.

Equilibrated internal fluid pressure: Observations of arrested dykes in the field show that at the tips of some dykes a vapour phase existed (Hoek, 1994). This suggests that in certain cases there is ‘fluid-lag’ i.e. the fluid front has not reached the tip in question, and as such, the fluid pressure has not yet equilibrated. Time-scales describing the time until the fluid front reaches a fracture’s tip for 3D fractures in the absence of stress gradients are described in Bungler and Detournay (2007). Dykes are especially complex in this regard due to the high temperature contrasts and evolving magma properties. In this work it is assumed that the fluid front has reached the tip in question and the fluid pressure inside the fracture has equilibrated. As such, excluding weight gradients, this exerts a uniform pressure on the fracture’s walls. This fits with experimental results of ascending fluid-filled cracks in gelatin that show no such lag. Additionally, it appears that fluid pressure in these fractures has equilibrated, as K_c calculated using quasi-static models with a uniform internal pressure is comparable to that calculated for a gelatin solid using surface energy arguments (Smittarello, 2019, p.107). For 3D fractures ascending due to stress gradients, I have numerically tested what effect fluid-flow has in this process using the planar hydro-fracture simulator of Zia and Lecampion (2020). I find that over a large range of values, for fluid volumes over the critical volume described in chapter 3, once the fracture starts ascending with a typical ‘tear-drop’ shape, the leading tip has no fluid-lag and is ‘toughness-dominated’. A rigorous analysis to inspect if there are occasions where this no longer holds true is desirable.

State of stress in volcanic regions: Stresses around edifices or calderas are caused by an interplay of a multitude of interacting factors at different spatial and temporal scales, as shown in chapters 5/6. Even the simplest conditions, such as defining the ratio of horizontal to vertical stress, can be hard to constrain as this varies significantly. This can be as low as 0.5, even at 2 km depth (Brown and Hoek, 1978). The magnitude of shear stress that can be sustained over time below topography due to the topographic load is also of interest, a number of processes will act to reduce

Chapter 7. Summary and discussion

these stresses such as faulting or dyking, and this may also be dependant on the rate of loading. In this work an Andersonian stress state is used, where the ratio of horizontal to vertical stress is assumed to be equal (Pollard and Fletcher, 2005). In chapter 6, shear stresses in the numerical propagation simulation were removed. Better constraints on the magnitudes of stresses in volcanic areas would greatly reduce uncertainty in models of dyke propagation. Although extremely rare, constraints from stress measurements describing the stress field at a point significantly constrain free parameters in topographic loading models. This allows for the provision of an accurate estimate of stress magnitudes and stress distributions beneath the topography (Sulistianto, Kido, and Mizuta, 1998; Clair et al., 2015). Alternatively, variations to the stress state could be added as additional parameters to the models in chapters 5:6.

Effective K_c : Laboratory measurements of K_c in rocks typically lie between 0.1–5 MPa·m^{1/2}, greater values tend to exist at increased pressures and lower temperatures (Gehne et al., 2020; Atkinson and Meredith, 1987a). Estimates of K_c from outcrop studies can be orders of magnitude larger (Olson, 2003). These somewhat extreme effective values of K_c required for modelling dykes and veins is not seen in the laboratory data and the processes resulting in such high values of K_c remain poorly quantified experimentally, but are highly relevant.

Tip-line twisting: Many field observations show non-planar tip-line geometries of fractures (Delaney and Pollard, 1981; Healy et al., 2018). Such fractures can be modelled in the laboratory, for example loading a fracture in both tension and shear (Cooke and Pollard, 1996). This is also observed in gelatin experiments of fluid-filled crack ascent, especially when salt concentrations in the gelatin are high (Takada, 1990; Smittarello, 2019). Meng, Maerten, and Pollard (2013) have numerically simulated segmentation of fracture tip-lines during shear, showing it is a highly complex process acting at multiple scales. Despite this, Lazarus et al. (2008) compare a number of tip-line twisting criteria that both include and neglect the value of K_{III} to experimental results. The authors find that the maximum tensile stress criterion that neglects K_{III} , which I use in chapter 6, broadly captures the overall twisting of a 3D fracture surface. It is of note, that the initial facets caused by mode III shearing are of interest, as these may also change the effective value of K_c at the tip-line in question.

A second volumetric transition: Field evidence of giant dykes, shows that extremely large aperture fractures can propagate 100's of km laterally with relatively planar propagation paths. The volumes involved with such events are extreme when viewed in the context of neo-tectonic observations of dyking. The paper of Takada (1990) showed experimentally, what I refer to in this work as the 'critical volume', where the transition to self-sustaining propagation occurs. Additionally, another experimental transition is reported in the study, again this occurs once a

given volume is exceeded. This causes the leading crack front to segment and twist. The author reports that the terminations are akin to viscous fingering of dykes and sills, speculating this is due to high stresses causing ductile deformation at the leading tip. It would be interesting to know if the mechanisms of this segmentation in gelatin analogs could be described using ductile fracture mechanics concepts. If such phenomena are caused by a second transition in volume alone then the straight trajectories of large volume dykes and sills are hard to reconcile. Field evidence of this process operating in rock at the scale of veins, dykes and sills would be of interest.

7.2.2 Comparison to other work

Critical fluid volumes: Since the publication of Davis, Rivalta, and Dahm (2020) (chapter 3) an independent study has analysed fracture propagation under stress gradients using finite element modelling techniques that include fluid flow, as well as an analytical derivation (Salimzadeh, Zimmerman, and Khalili, 2020). Their study results in a semi-analytical equation for the critical volume of fluid before a fracture ascends:

$$V_c = \frac{(1 - \nu)}{2\mu} \left(\frac{16}{27} \frac{\pi^4 K_c^8}{1.578 \Delta \gamma^5} \right)^{1/3} \quad (7.2)$$

Despite using a different analytical approximation, the results are almost identical, with V_c only 3% smaller than the analytical result reported in chapter 3. The numerical results they supply verify the conclusions of my work. It is important to note that their model includes fluid flow and comes to the same result, validating my use of a quasi-static numerical model in chapter 3. The work of Salimzadeh, Zimmerman, and Khalili (2020) focuses on a different problem, hydro-fracturing for waste disposal, but this result also points towards the issue of safety in typical hydro-fracturing operations, as discussed in chapter 3.

Ascent velocities and coupled simulators: Some additional unresolved questions remain after performing this research. Firstly, chapter 3 shows that cracks start ascending after a given volume is injected (V_c). The results of Heimpel and Olson (1994) show that the ascent velocity of fractures scales with the injected volume. Formulas in 2D provide velocities of cracks dependant on their observed length, but fail to predict velocities from controlled settings (Weertman, 1971b; Nakashima, 1993; Nunn, 1996). These formulations supply ascent rates orders of magnitudes faster than velocities and lengths from analog experiments (Smittarello, 2019). If such formulations are adapted to 3D and manipulated, is it possible to predict the rate of fluid ascent due to a given volume analytically, or are numerical methods required? Recently, a number of industry focussed research groups have developed both planar and non-planar 3D coupled elastic/fluid-filled fracture

Chapter 7. Summary and discussion

simulators; Salimzadeh, Zimmerman, and Khalili (2020), Li, Firoozabadi, and Zhang (2020), Napier and Detournay (2020), and Zia and Lecampion (2020). Use of these simulators will allow for numerical inspection of the time-scales of hydro-fracture propagation, due to the explicit coupling of elasticity equations and fluid flow inside the fracture, which this work has neglected. Understanding the speeds of fracture propagation would add an additional constraint to models underpinned by observations, such as those described in Chapter 6. This process also defines the time-scales of dyke-fed eruptions, and as such, has hazard mitigation implications.

Stress intensity approximation: The method to approximate stress intensity described in the chapter 2 (see appendix for detail: chapter 7.3), followed on from the work of Olson (1991) and Sheibani, Olson, et al. (2013). A series of publications using constant dislocation triangular elements to approximate stress intensity have been published both before and after the publication of chapter 2, e.g. Shi et al. (2014) and Li et al. (2019). As shown in the appendices of both chapter 2 and 3, when equilateral edge elements are used, the DDM method can estimate stress intensity factors accurately, with a maximum error of 10%. This accuracy is close to that of more advanced methods, i.e. the finite element method of Nejati, Paluszny, and Zimmerman (2016) has a similar error in approximating stress intensity, noting that they show this error can be reduced to below 4% using refined meshing (see their Fig.12). Approximations of stress intensity factors using novel isogeometric BEM methods have errors below 7%, see Peng et al. (2017). These advanced methods have room to improve on the accuracy with carefully chosen discretisations, unlike the method described in this thesis. Despite this, the DDM method's accuracy shown is surprising given its simplicity. The only additional complexity required to retrieve such accuracies is the constraint of an equilateral edge element discretisation. It is imperative that research using constant dislocation triangular elements to approximate stress intensity maintains isosceles triangular edge elements (close to equilateral) or that studies lacking this provide an explicit description of the errors associated with the meshes used. From experience, without equilateral edge triangles errors increase far beyond 10%. I note that one significant advantage of using this method is that the field of meshing tools for triangular surfaces is advanced i.e. (Da and Cohen-Steiner, 2019), in part due to the pervasive use of triangular surfaces in modern rendering. As such the only additional tools required are those to re-mesh these surfaces such that the edge triangles are equilateral. The higher accuracy techniques described above are more complex in this regard, requiring either the meshing of both the elastic volume and the fracture, or the use of modern discretisation techniques that describe geometry with smooth functions. For boundary element techniques the use of such functions is not well established in geoscience.

7.3 Outlook

The modelling techniques and applications I have presented in this dissertation show how analytical models combined with sophisticated numerical models provide quantitative insights into how fluid-filled fractures migrate. Use of these two techniques in tandem allows for this seemingly complex process to be deconstructed into its component parts and analysed efficiently. As the temporal observations of dyke/sill fed eruptions increase over the coming years, the ability to constrain events using models that include internal fluid-flow will become increasingly pertinent. The development of modelling techniques is now at a point where these can be applied to such events. Theoretical work constraining processes that lead to arrest of such fractures, or potential changes in the effective value of K_c along the tip-line would significantly aid in modelling the paths of such events. Lastly, a combination of fluid-filled fracture propagation modelling techniques and statistical modelling can reduce the great uncertainties in the bounds of the parameters controlling these events. In conclusion, the modelling techniques remain in their infancy, but have great potential to elucidate and constrain many of the processes that control fluid-filled fractures.

Supplementary information

Supplementary information for Chapter 2: Friction on wavy faults

The aim of this section is to detail how we derive the equations for the stress intensity approximation using the 3D displacement discontinuity method. This allows us to provide reasons for the error in the equation and propose a value to correct for this. We then go on to detail the errors for different meshes types and refinements. It is of note to add that other formulations exist for approximating stresses at a cracks tips using the BEM DDM method, these are either directly calculating stress distributions around the tip or using more complex discontinuities on the crack edge Meng, Maerten, and Pollard (2013) and Li et al. (2001). The method of Meng, Maerten, and Pollard (2013) lacks propagation criterion that are related to measurable fracture strengths of materials but could be adapted for this, the method of Li et al. (2001) directly calculates K_I but has does not detail how to work with shear fractures. Sheibani, Olson, et al. (2013) describe a similar method to described here for rectangular dislocation elements in 3D, we go into greater detail, deriving the formulas in 3D to show these are the same as 2D, this derivation allows us to correctly identify the sources of error and appropriately adjust for these. We then quantify the accuracy of our approximation. Tada, Paris, and Irwin (2000) supply stress intensity factors for 3D penny-shaped cracks loaded by remote stresses:

$$K_I = 2t_n \sqrt{a/\pi} \quad (\text{S.3})$$

$$\begin{Bmatrix} K_{II} \\ K_{III} \end{Bmatrix} = \begin{Bmatrix} \cos \theta \\ \sin \theta (1 - \nu) \end{Bmatrix} \frac{4t_s \sqrt{a/\pi}}{2 - \nu} \quad (\text{S.4})$$

And Eshelby (1963) gives the separation distance between the walls of the crack (penny):

$$D_n = \frac{4a(1 - \nu)t_n}{\pi G} \sqrt{1 - \frac{L^2}{a^2}} \quad (\text{S.5})$$

$$D_s = \frac{8a(1-\nu)t_s}{\pi G(2-\nu)} \sqrt{1 - \frac{L^2}{a^2}} \quad (\text{S.6})$$

Rearranging these to give this in terms of traction:

$$D_n \frac{1}{\sqrt{1 - \frac{L^2}{a^2}}} \frac{\pi G}{4a(1-\nu)} = t_n \quad (\text{S.7})$$

$$D_s \frac{1}{\sqrt{1 - \frac{L^2}{a^2}}} \frac{\pi G(2-\nu)}{8a(1-\nu)} = t_s \quad (\text{S.8})$$

Combining Eq. S.3,S.4 with Eq. S.7,S.8, note D_{III} the displacement vector parallel to the crack edge and D_{II} is perpendicular to this, in the plane of the crack. This removes the dependence on Θ in Eq. S.4.

$$K_I = D_n \frac{1}{\sqrt{1 - \frac{L^2}{a^2}}} \frac{2\sqrt{a/\pi}\pi G}{4a(1-\nu)} \quad (\text{S.9})$$

$$\begin{Bmatrix} K_{II} \\ K_{III} \end{Bmatrix} = \begin{Bmatrix} D_{II} \\ D_{III}(1-\nu) \end{Bmatrix} \frac{1}{\sqrt{1 - \frac{L^2}{a^2}}} \frac{4\sqrt{a/\pi}\pi G(2-\nu)}{(2-\nu)8a(1-\nu)} \quad (\text{S.10})$$

As the crack tip is approached the reciprocal term goes to zero. Assuming sufficient sampling of the crack so the edge elements are close to the tip we therefore drop this term.

$$K_I = D_n \frac{2\sqrt{a/\pi}\pi G}{4a(1-\nu)} \quad (\text{S.11})$$

$$\begin{Bmatrix} K_{II} \\ K_{III} \end{Bmatrix} = \begin{Bmatrix} D_{II} \\ D_{III}(1-\nu) \end{Bmatrix} \frac{4\sqrt{a/\pi}\pi G(2-\nu)}{(2-\nu)8a(1-\nu)} \quad (\text{S.12})$$

After some rearrangement:

$$\begin{Bmatrix} K_I \\ K_{II} \\ K_{III} \end{Bmatrix} = \begin{Bmatrix} D_n \\ D_{II} \\ D_{III}(1-\nu) \end{Bmatrix} \frac{\sqrt{a}\sqrt{\pi}G}{a(1-\nu)2} \quad (\text{S.13})$$

As $\sqrt{(x)}/x = 1/\sqrt{(x)}$ then:

$$\begin{Bmatrix} K_I \\ K_{II} \\ K_{III} \end{Bmatrix} = \begin{Bmatrix} D_n \\ D_{II} \\ D_{III}(1 - \nu) \end{Bmatrix} \frac{\sqrt{\pi}G}{\sqrt{a}(1 - \nu)^2} \quad (\text{S.14})$$

The BEM DDM method supplies displacements on the crack wall. If h is substituted for a in Eq.S.14 we simulate a smaller crack with the same opening as the crack tip element close to the fractures tip. Such a crack will have a similar opening profile very close to the tip, i.e. Fig. S1 and therefore a similar stress intensity. This approximation means the terms that specify the crack size in the equations is dropped. Constant c is also added which can be used to correct for the mismatch between the approximation and the analytical solution.

$$\begin{Bmatrix} K_I \\ K_{II} \\ K_{III} \end{Bmatrix} = \begin{Bmatrix} D_n \\ D_{II} \\ D_{III}(1 - \nu) \end{Bmatrix} \frac{\sqrt{\pi}G}{\sqrt{h}(1 - \nu)^2} c \quad (\text{S.15})$$

Fig.S2 shows the error due to the stress intensity approximation described, this is compared to the analytical formula for an inclined crack subject to tension described in Tada, Paris, and Irwin (2000). We have tested different crack geometries: with normals between 5 and 85 degrees away from z , and the errors for each angle are coincident provided the mesh is the same. The figure shows the results of different meshes, triangulated uniform grids (with an edge of equilateral triangles added) like used in this study and unstructured meshes from the code DistMesh Persson and Strang (2004). Note that for both cases we have set a constraint that all the edge triangles are isosceles, see Fig. S3 for examples. The results show the error is relatively stable, with the mean values (shapes) below 4% of the maximum analytical value of each stress intensity. Structured meshes appear to have slightly higher errors, even though for these meshes we have put equilateral triangles around the crack edge. The scatter in the crack tip error as shown in Fig. 2.4 must therefore be larger for such meshes. For the unstructured meshes the number of triangles (numbers above each data point) increases mean mesh quality, there is a trend for K_{II} and K_{III} where mesh density increases the mean accuracy, but the error is only halved as the mesh size is squared. It must be noted that ν changes the scatter of the crack tip element slip distribution error in shown in Figure 4. This only affects the slip profile estimation of the DDM, for opening this scatter is constant, around 3% for the mesh used in our analysis. For a ν of 0.01 the shear component scatter drops from around 5% to 2% and when increased to 0.49 it is close to 10%. These errors are for the mesh we have used

in the rest of the analysis. This change in the scatter with ν in turn affects the error of the stress intensity approximation of K_{II} and K_{III} . In this section we have detailed a method to approximate stress intensities at a fractures tip in 3D where the fracture can have frictional constraints. The method to calculate stress intensities is simple to implement in BEM DDM formulations or in other methods provided the crack opening/slip profile can be estimated. After correcting for the error of the approximation we have described the error in the stress intensities from using this method. This is caused by scatter in the methods estimation of crack tip displacements. Methods to improve the consistency of the crack opening/slip profile near to the tips have potential to reduce this error.

The correction factor c therefore adjusts for error in the approximation detailed above, the fact we drop the reciprocal term when deriving the equations, and that due to the overestimation of crack wall displacements from the BEM-DDM method. Fig. 2.4 shows that the error due to the overestimation of crack wall displacements is $30\% \pm 5\%$, this error is similar for opening displacements. This overestimation is close to being independent of mesh refinement which can be seen when we compute the accuracy of the approximation. Using analytical formulas, we compute one source of error. Comparing stress intensities for cracks under the same boundary conditions between a crack where $a=1$ using Eqs. S.3 and S.4 to the results of Eq. S.15 using a displacement of a crack where a is a 1000th of the width with its max displacement defined by the crack wall displacement of the larger crack (Eqs. S.5 and S.6). The overestimation of the approximation of Eq. S.15 is 41.4%. Combining the two errors the total error of the numerical method is 183.4%. The correction factor is therefore simply $1/1.834$.

Figure S1: Comparison between crack wall displacements for a penny-shaped crack and an approximation of displacements close to the tip for a fracture a 10th of the length.

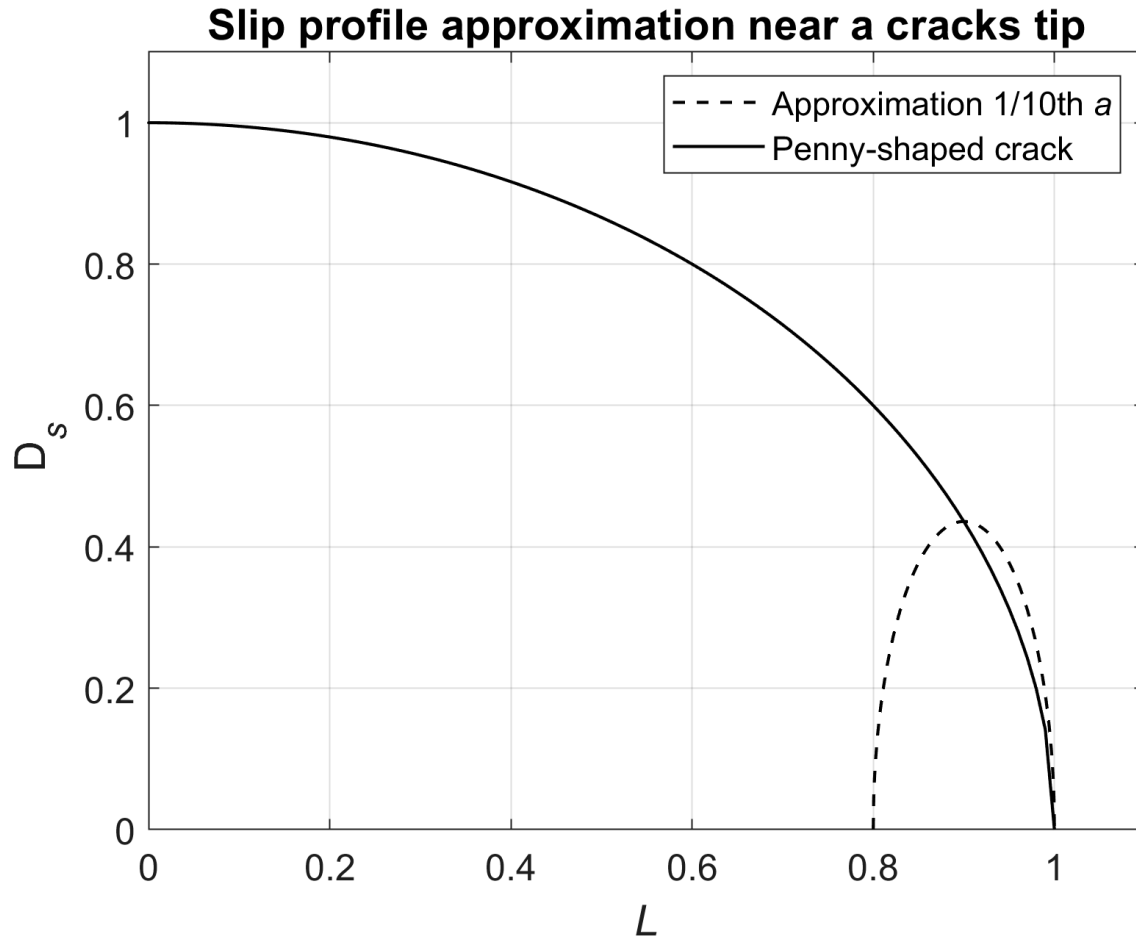


Figure S2: The resulting stress intensity error for multiple meshes, compared to analytical solutions for an inclined penny shaped crack subject to tension. ν was set to 0.25 for all runs. The maximum and minimum errors are shown as solid horizontal lines, mean as shapes. Shades highlight the mode. The mean error shown in the y -axis is the sum of residuals r divided by the number of edge triangles n divided by the maximum value of the stress intensity in question for this geometry. The x -axis shows the mean mesh quality, defined as two times the radius of the triangles inscribed circle to the radius of its circumscribed circle. A value of one is a mesh where all triangles are equilateral, some examples triangles are shown below their respective values. Mesh sizes (number of triangles) are shown above each data point.

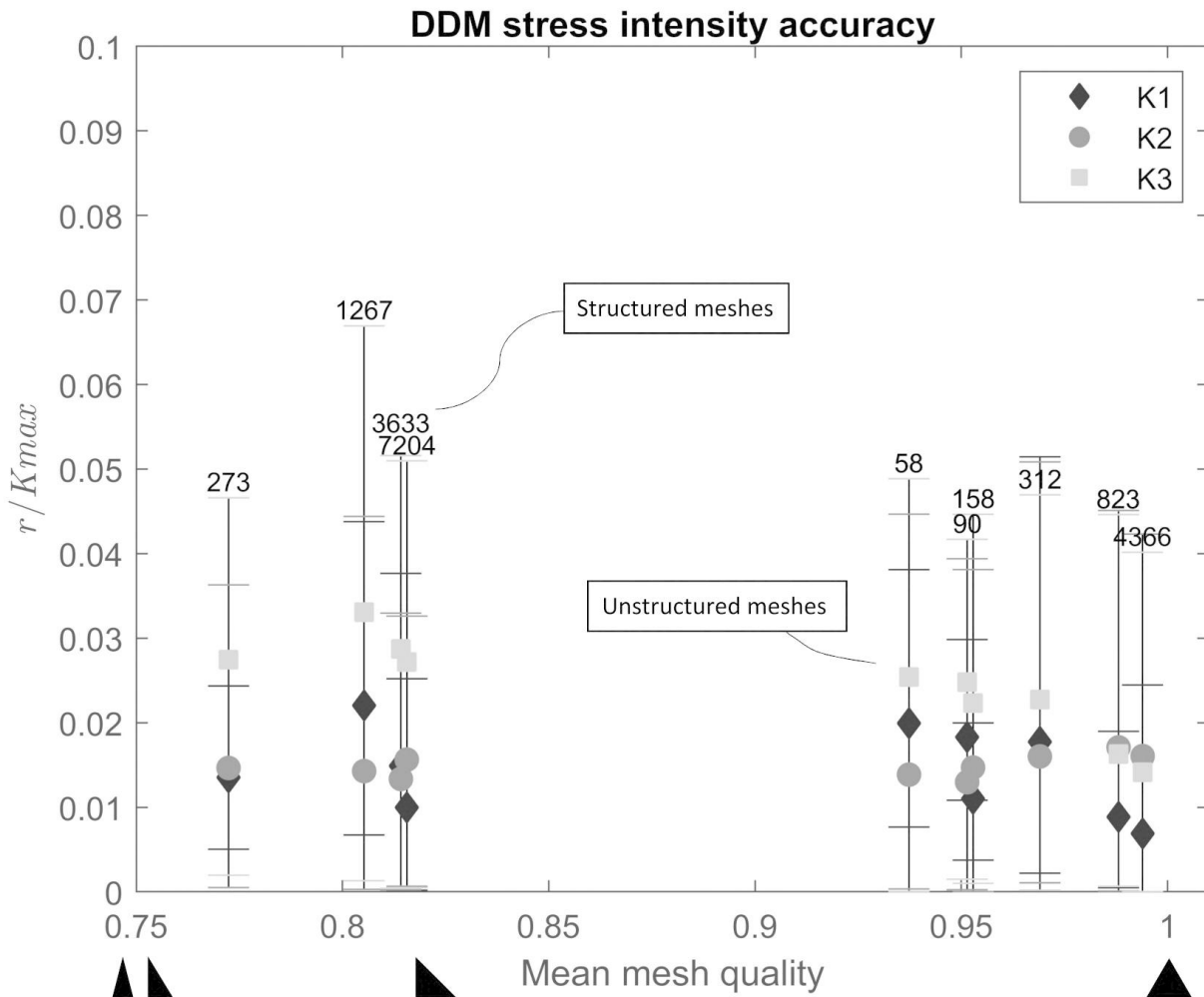
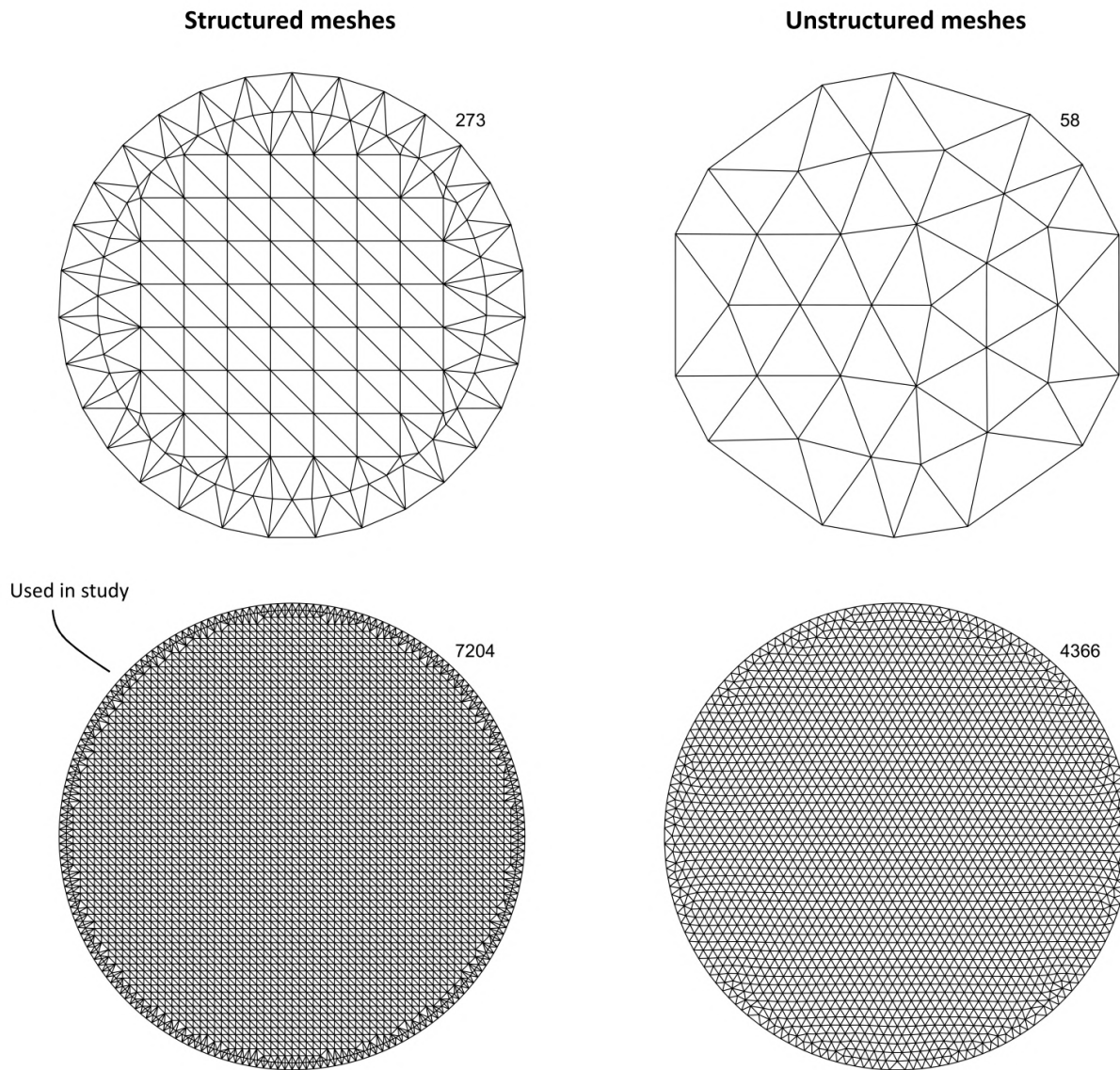


Figure S3: The lowest and highest density meshes used in Fig.S2. The text describes the number of triangles. The mesh used in the bottom left is the mesh used in this study.



Supplementary information for Chapter 3: Critical fluid injection volumes

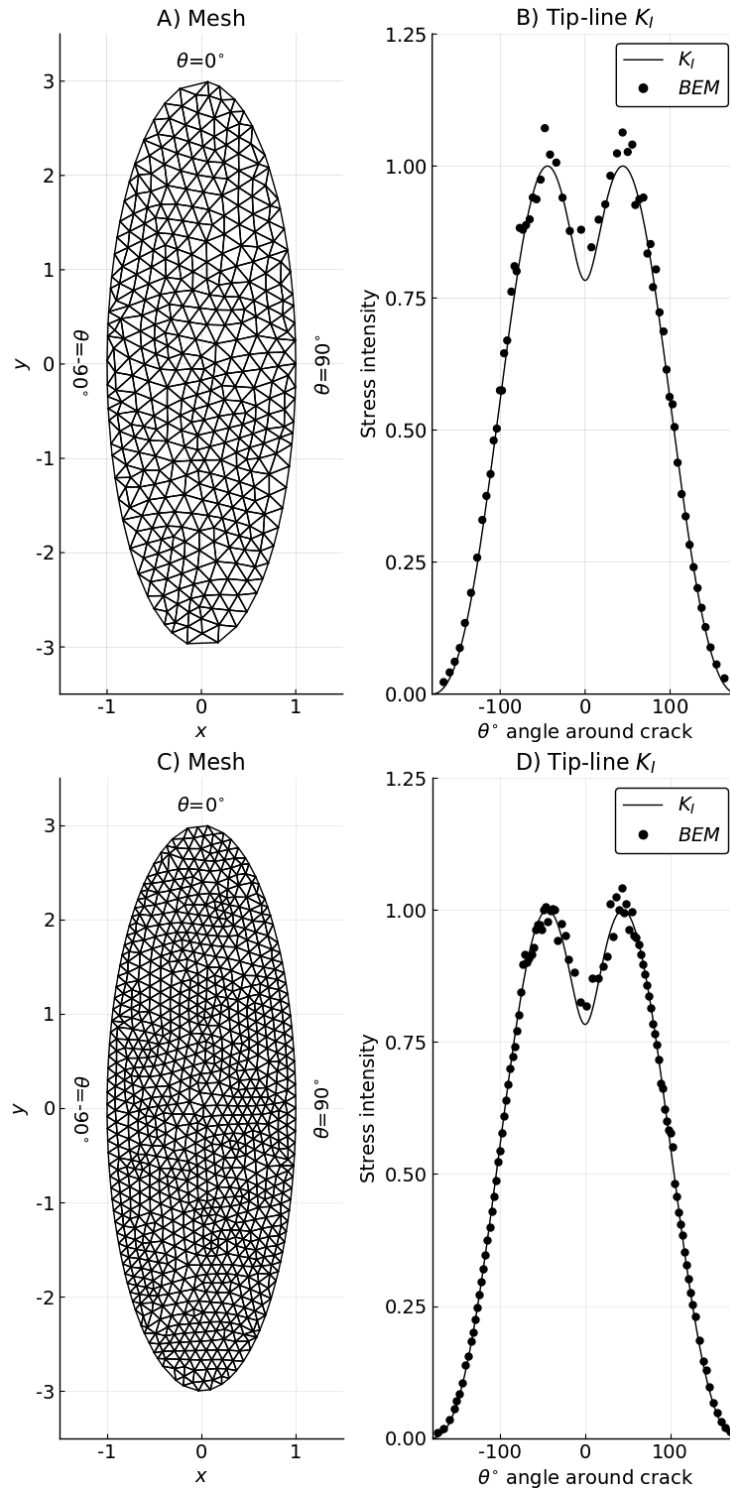
Numerical accuracy

We verify that our method to compute K_I is independent of crack shape and boundary condition. Previously this was only compared to solutions for a circular crack subject to uniform stresses (Davis, Healy, and Rivalta, 2019). We compare this to the analytical solution for the stress intensity around an elliptical crack, subject to a superposition of uniform pressure and a linear gradient of stress, such that, at the basal tip, $K_I = 0$ (Fig. 3.1) (Atroshchenko, Potapenko, and Glinka, 2009). We note that under a stress gradient, K_I for vertically aligned elliptical cracks is not maximal at its upper tip, due to the reduction in crack surface area proximal to this edge.

For a mesh with 650 triangles (Fig. S4A/B), the greatest vertical separation between the numerical points and the analytical line is 0.09. For this test we required the edge points of the mesh's triangles, not the midpoints of the triangles edge where K_I is calculated, to lie on the tip-line defined by the analytical solution. For a mesh with 1500 triangles (Fig. S4C/D), the maximum vertical distance from the analytical solution of is 0.06, noting that greater sampling does not necessarily converge to a improved accuracy, see appendix of Davis, Healy, and Rivalta (2019).

As a further test of numerical accuracy, we compare how well the numerical method approximates the opening volume of a penny shaped crack subject to tension (Tada, Paris, and Irwin, 2000). We find a sampling of 650 triangles overestimates the volume by 5.2%, by increasing the triangle count to 1500 this drops to 3.5%.

Figure S4: Stress intensity factor approximation using the 3D displacement discontinuity method. A/C) Elliptical crack meshed with 650/1500 triangles respectively, B/D) Numerical (dots) and analytical (solid line) results. Results are normalised relative to the maximum analytical value of K_I .



Supplementary information for Chapter 4: Forecasting magma pathways

Supplementary materials include Figs. S5 to S10 and Tables S1 to S2 and references

	layer thickness [m]	density [kg/m^3]	loads [MPa]	cumulative unloading [MPa]
epoch 3	19 (80-5)	2000-1500	0.3	10.3
epoch 2	12 (25-3)	2000-1500	0.2	10.7
epoch 1	120 (300-25)	2000-1500	2.1	10.9
Neapolitan Yellow Tuff	350	2000	6.9	12.9
37 - 12 ka deposits	900	2200	19.4	19.8
Campanian ignimbrite	500	2400	11.8	39.2
depth to caldera floor	2000	2600	51.0	51.0

Table S1: Thicknesses and densities of deposits filling Campi Flegrei caldera with associated loads. Data from Corbi et al., 2015; Deino et al., 2004; Barberi et al., 1991 and unpublished drilling data. For epochs 1, 2 and 3 we report the average values and their range in parenthesis.

Caldera		radius [m]	depth [m]	submerged [m]	min. chamber depth [m]	max. chamber depth [m]	P_U [MPa]
fernandina	FE	2700	1100	-	1000	2000	21.6
wolf	WO	2650	660	-	1800	2800	12.9
darwin	DA	2700	200	-	1500	3500	3.9
sierra negra	SiN	4200	110	-	2500	3500	2.2
alcedo	AL	3750	300	-	2000	4000	5.9
cerro azul	CeA	3500	480	-	4500	6500	9.4
rano kau	RaK	700	160	-	2000	6000	3.1
campi flegrei	CaF	7500	200	-	3000	4000	3.9
aso	AS	8500	250	-	3500	5500	4.9
crater lake	CrL	4500	750	350	4000	6000	11.3
rotorua	RO	8500	250	20	4000	8000	4.7
santorini	SA	4700	400	200	3500	5500	5.9
bolsena	BO	7500	450	150	2500	5500	7.4
rabaul	RA	3600	400	150	2000	4000	6.4
aira	AI	8500	500	200	5000	8000	7.8
valles	VA	11000	550	-	5000	7000	10.8
dolomieu	DO	4000	100	-	1500	2500	2.0
Caldera	σ_t min MPa	σ_t max MPa	vents outside the caldera %	vents on the caldera rim %	vents inside the caldera %		
fernandina	0.2	0.5	65	32	3		
wolf	0.2	0.5	79.9	20	0.1		
darwin	0.2	0.5	62.9	37	0.1		
sierra negra	0.2	0.5	66.9	33	0.1		
alcedo	0.2	0.5	65.9	34	0.1		
cerro azul	0.2	0.5	82.9	17	0.1		
rano kau	0.2	0.5	64.9	35	0.1		
campi flegrei	1.0	3.0	0.1	23	76.9		
aso	1.0	3.0	0.1	0.1	99.8		
crater lake	2.0	3.0	0.1	0.1	99.8		
rotorua	1.0	3.0	0.1	0.1	99.8		
santorini	1.0	3.0	0.1	0.1	99.8		
bolsena	1.0	3.0	18	75	7		
rabaul	1.0	3.0	0.1	99.8	0.1		
aira	1.0	3.0	0.1	99.8	0.1		
valles	2.0	3.0	40	46	16		
dolomieu	0.2	0.5	86	13.9	0.1		

Table S2: Properties of notable worldwide calderas.

Figure S5: Probability distributions for model parameters of epoch 1. The histograms show the distributions for individual parameters. The contour plots show covariance distributions. Bars and contours colored in gray and red refer to simulations where σ_t is larger and smaller than $2P_U/\pi$, respectively.

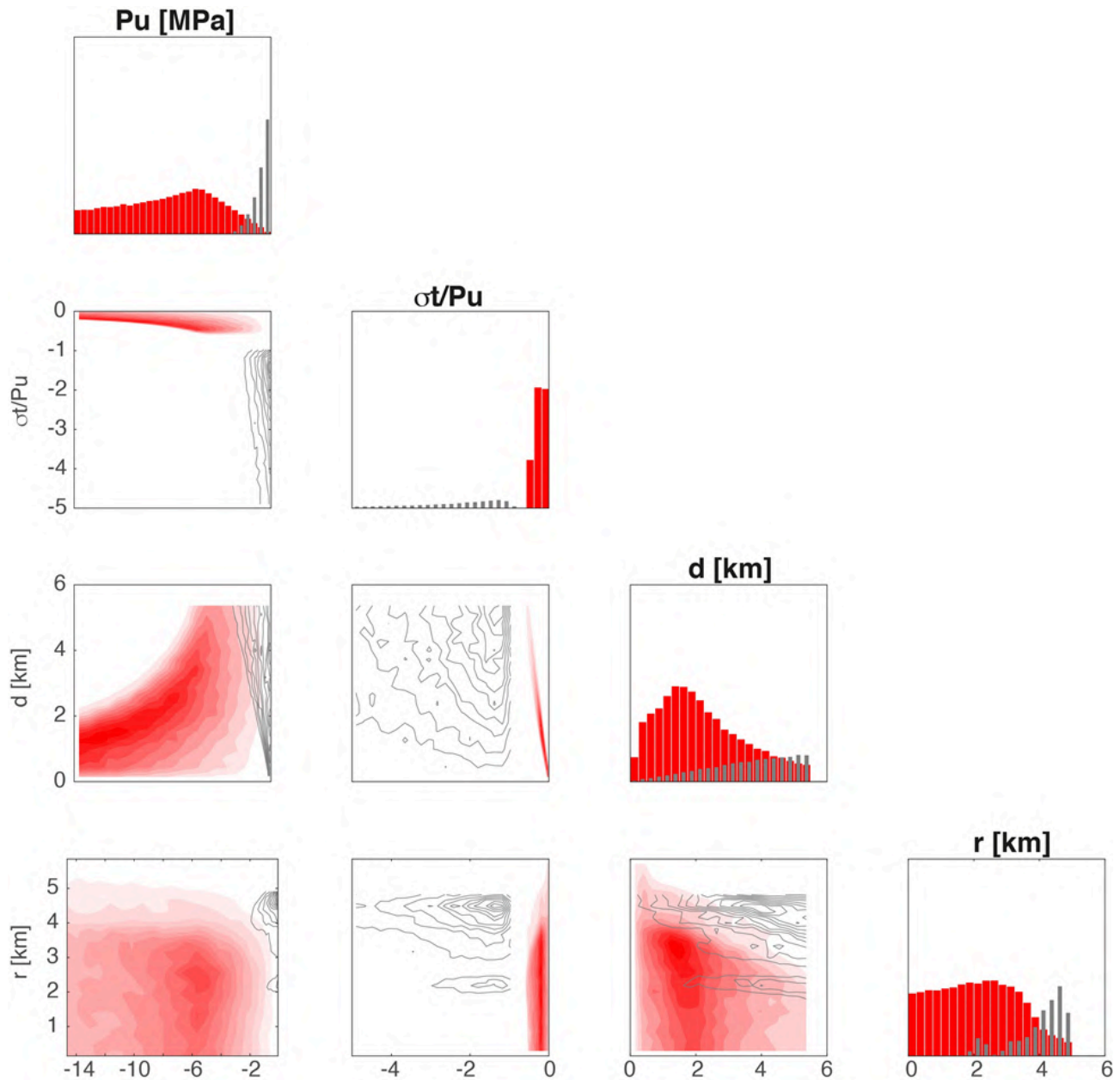


Figure S6: Same as figure S5 for epoch 2.

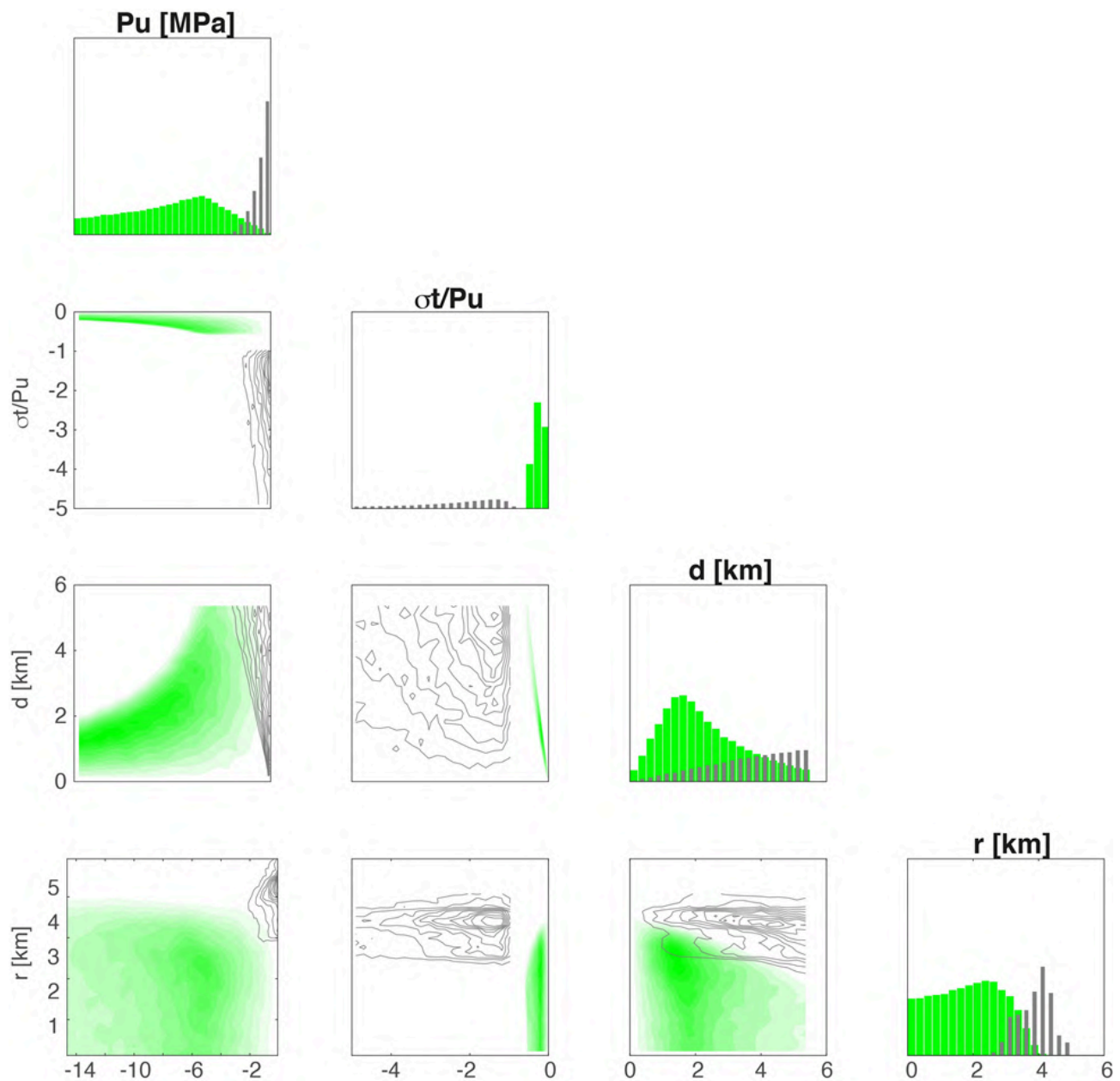


Figure S7: Same as figure S5 for epoch 3.

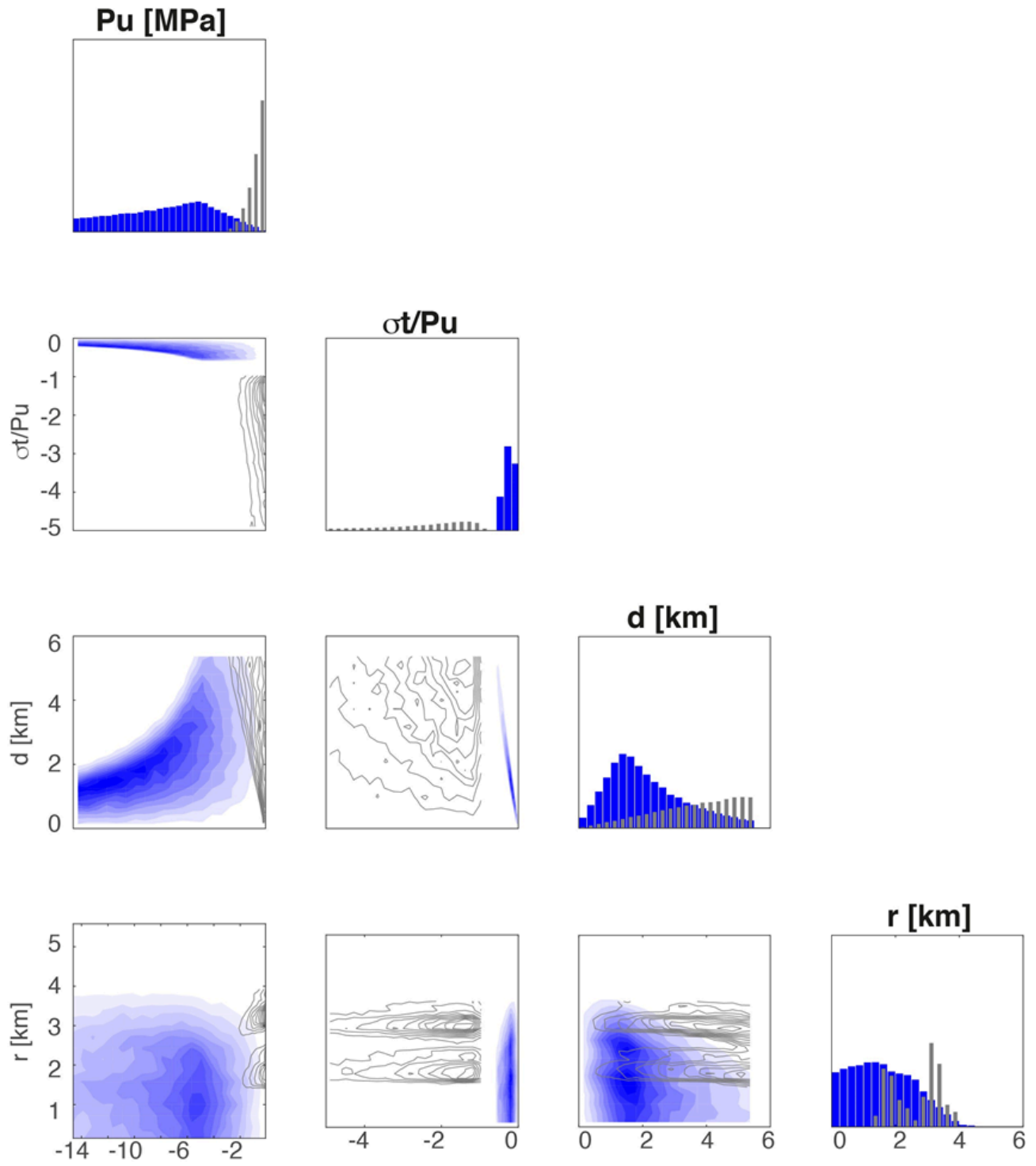


Figure S8: Covariance distributions of σ_t/P_U versus P_U and σ_t versus P_U for a set of simulations with starting depth homogeneously distributed between 3 and 4 km and radius equal to 0 km.

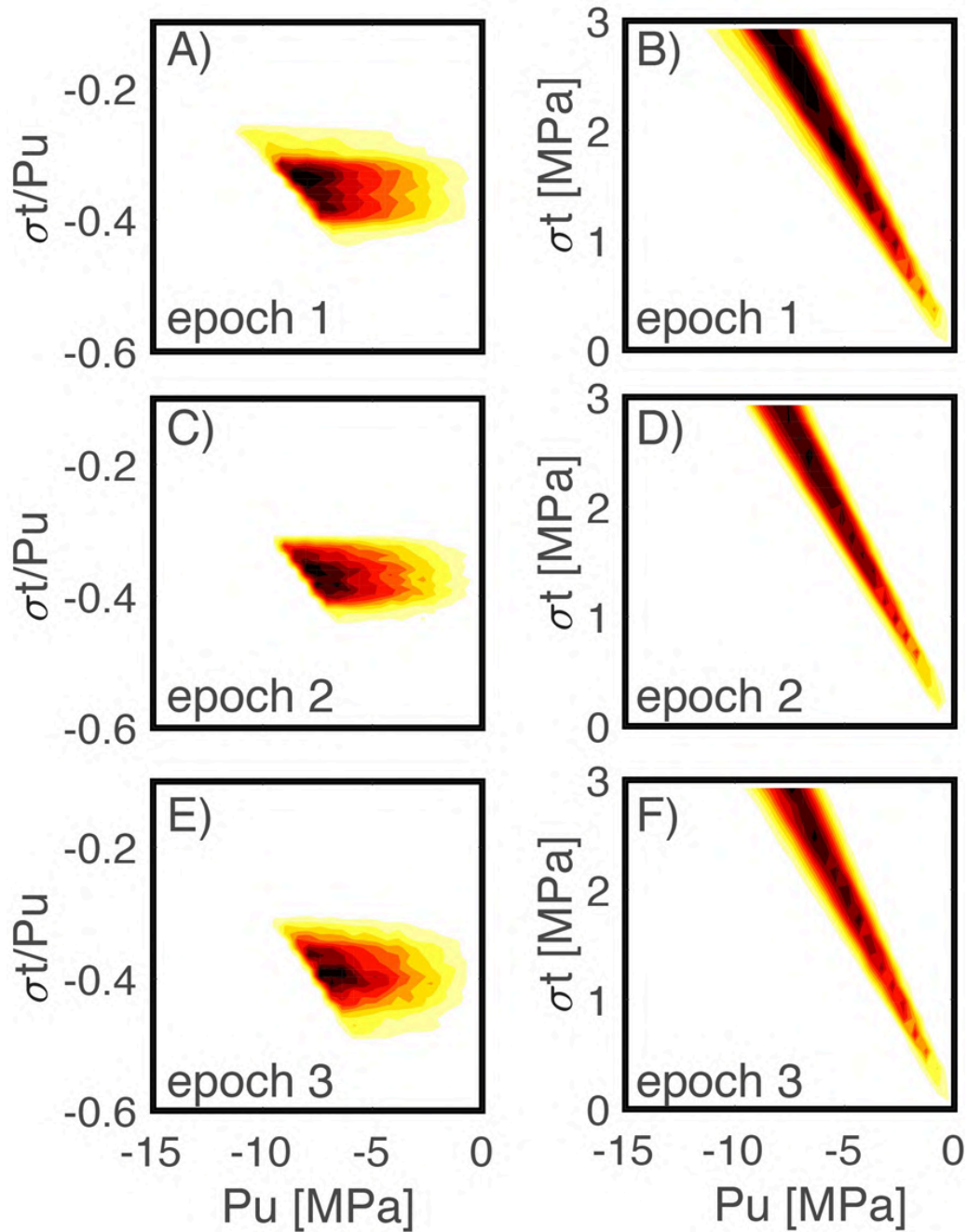


Figure S9: Impact of variability of starting depth. Effect on P_U and σ_t/P_U distributions (panels B, E, H, K, and C, F, I, L, respectively) and forecasted arrival radii (cyan stairs of panels A, D, G, J). The thin cyan lines of panels A, D, G, J highlight forecasted magma trajectories while the magenta bar high-lights the distance of Monte Nuovo from the caldera center. Each row represent simulations with a depth interval of 0.5 km from 2.5 to 4.5 km.

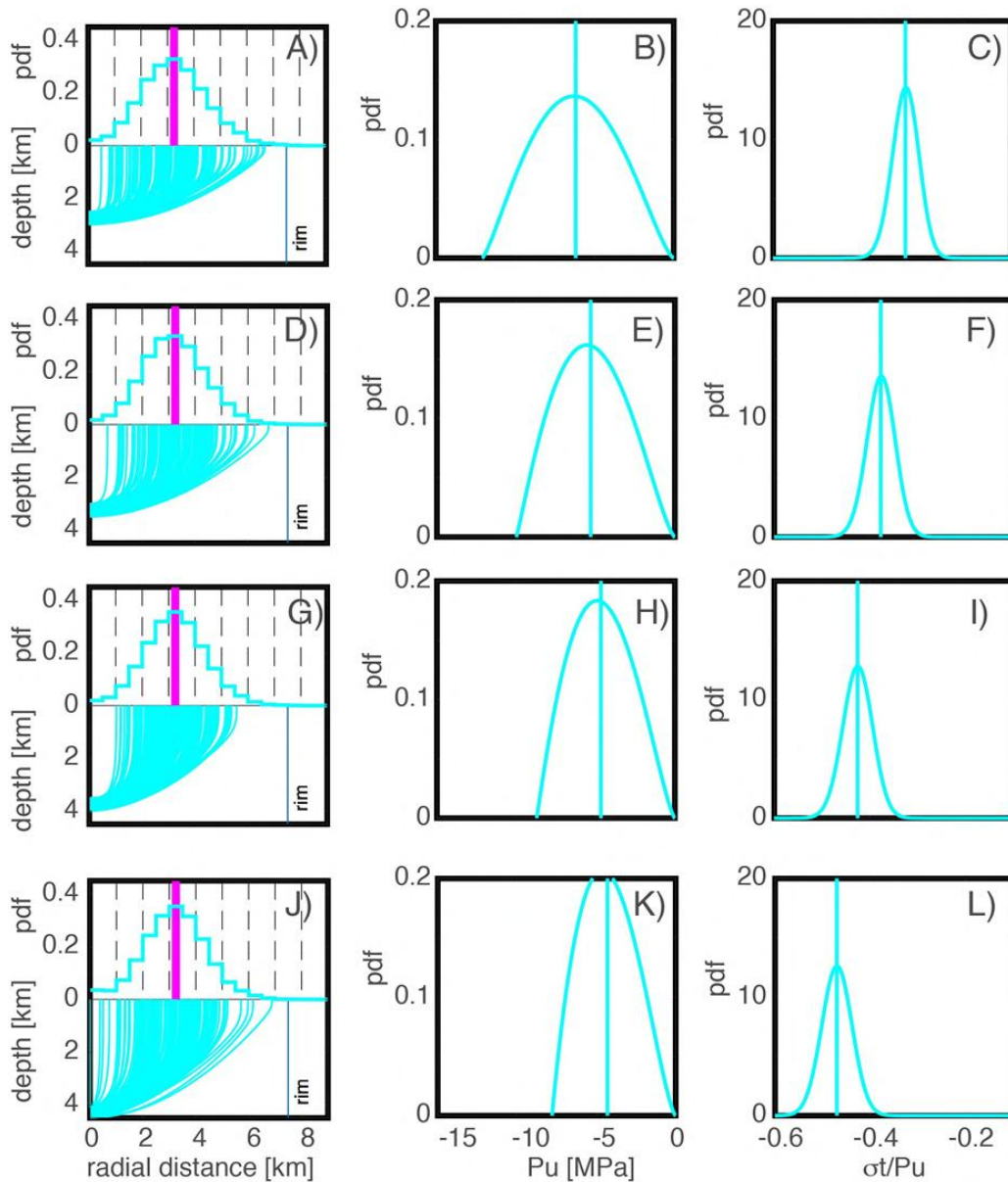
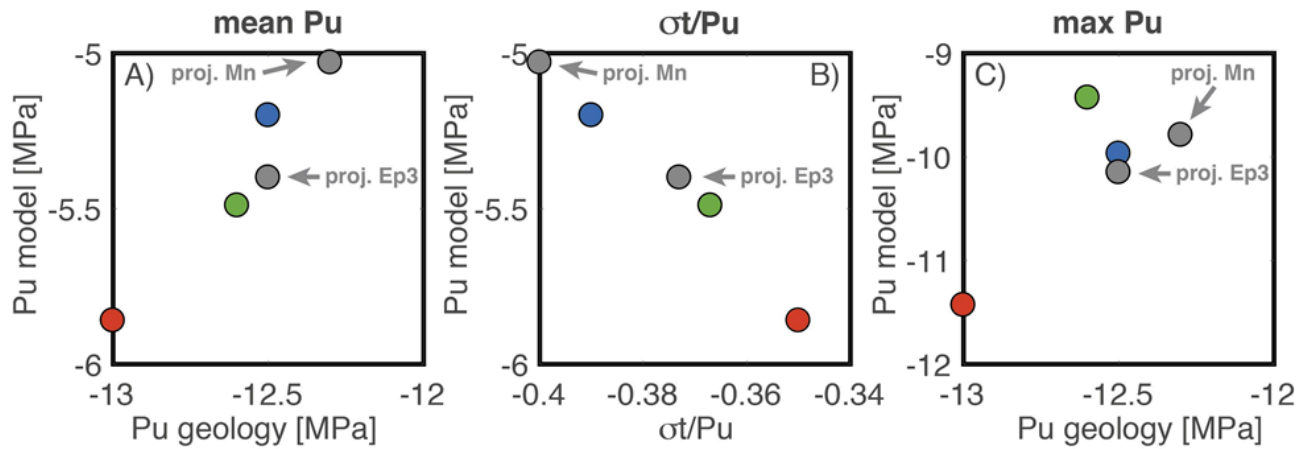


Figure S10: Parameters projection for the time-varying stress forecast. Plot of model derived mean unloading versus geology derived unloading (panel A), model derived unloading versus σ_t/P_U (panel B) and model derived maximum unloading versus geology derived unloading (panel C). The colorcoding red, green and blue is for epochs 1, 2 and 3, respectively. The gray dots represent the projections for epoch 3 and MN.



Supplementary information for Chapter 5: Analog stress inversion

The present Supplement includes information on scaling factors and measured parameters of the experiments we considered in the main text (tables S3 and S4) and the data sets we employed for inversions and forecasts (tables S5 and S6), as well as further results from the inversions (table S7).

We also show larger versions of the pictures of the experiments displayed in the main text (fig. S11 and S12), together with pictures of three discarded compressional experiments (fig. S13). Additional results of two tests we performed are shown in fig. S14.

The data displayed in the tables were either collected or evaluated between September 17, 2019 and May 25, 2020. Surface arrival points in table S5 were measured with a ruler directly on the surface of the gelatin blocks as soon as the experiments were over. w in table S4 was measured likewise. Imposed values of parameters d and h were measured with a digital caliber (in the case of h the measure was repeated 3 times on different points of the excavation floor), and T_{surf} was measured with a digital thermometer.

Information on possible discarded crack trajectories in the experiments are reported in the captions of fig. S11 and S12.

Figure S11: Detailed pictures of experiments with fixed imposed parameters d, h . The blue arrows point to the surface arrivals we considered for the forecasts ($x_i^{obs, F}$). **a)** 2DLA-1 (extension). **b)** 2DLA-2 (compression). The crack in the middle of the box became stuck beneath the unload as a sill-like intrusion; it eventually hit the back wall and reached the surface by further air injection. The leftmost crack was likely affected by a stress concentration due to a slight misplacement of the left side plate. Both were discarded (table S3). **c)** 2DLA-3 and **d)** 2DLA-4 (extension + layering).

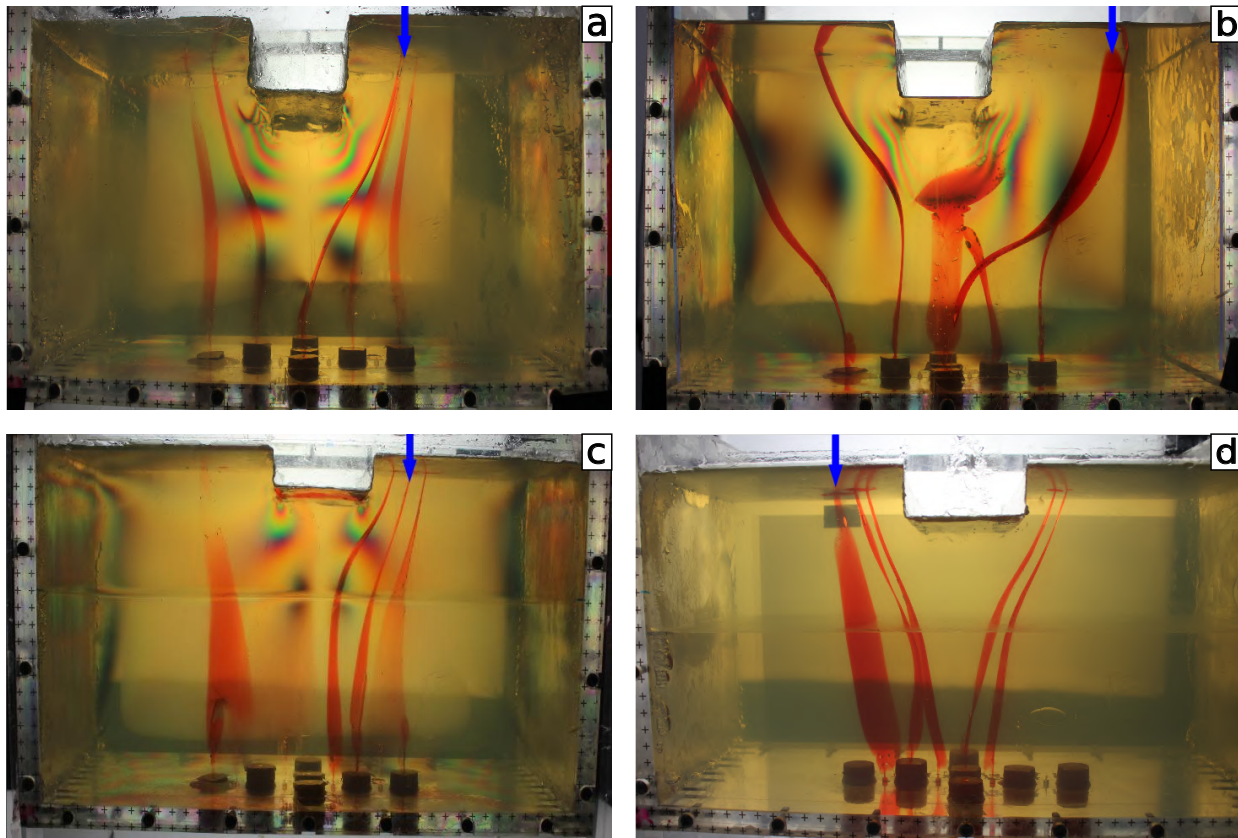


Figure S12: Detailed pictures of experiments with imposed parameters updated midway through their execution (either d or h). **a)** 2DLA-5 (extension induced in the second half of the experiment). **b)** 2DLA-6 and **c)** 2DLA-7: the surface excavations were refilled with water up to $\sim 55\%$ of their original depth after the injection of the crack sets on the left and on the right, respectively, while extension was imposed in both cases. The blue arrows point to the surface arrivals we considered for the forecasts ($x_i^{obs,F}$). The difference in the color of the post-injection ink in **a)** and **c)** corresponds to the sets injected before and after the stress update (from green to red in **a)** and reverse in **c)**). The first red crack from left to right in **c)** merged with the next one before reaching the surface.

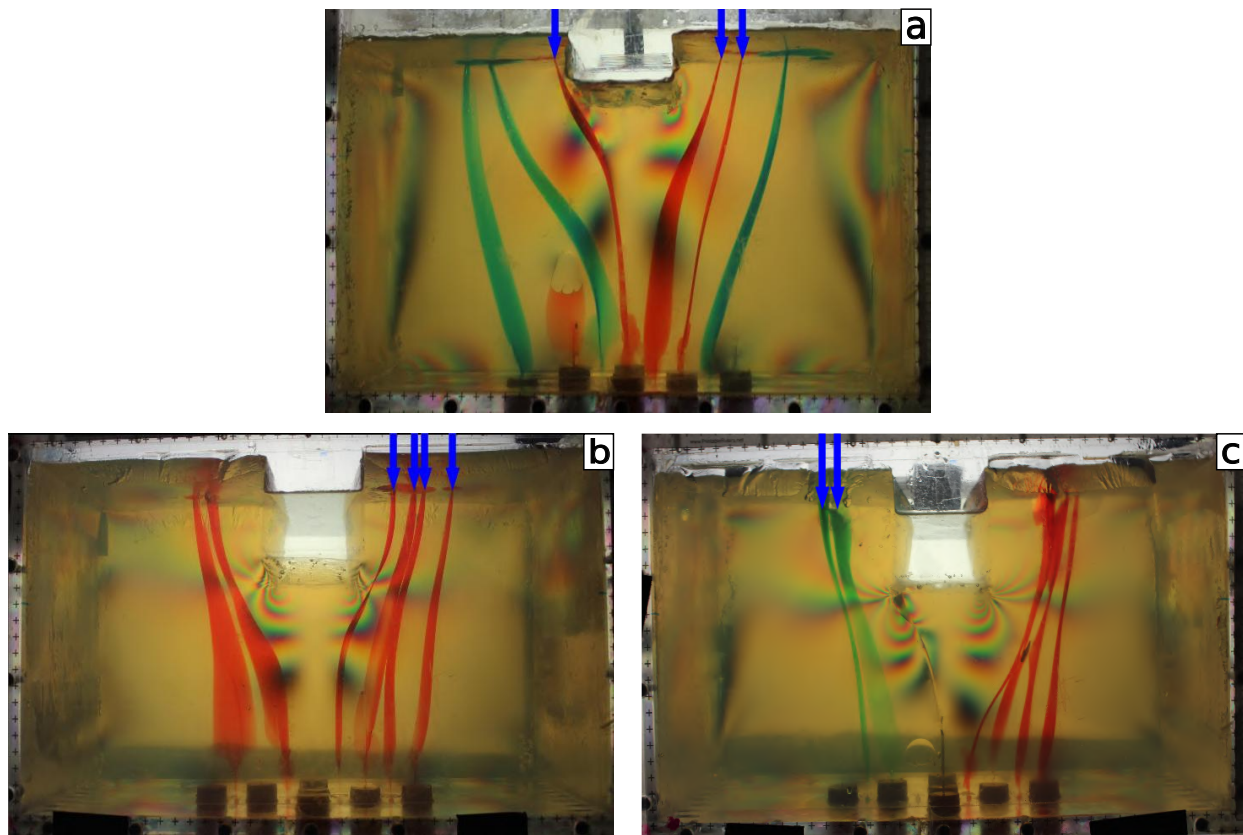


Table S3: Scaling factors between reference cases in nature (rift-like or caldera-like settings) and our experimental setup. The parameters L^* and σ^* are defined in the main text.

	Parameter (units) or equation	Nature (k=r)	Experiments (k=gel)	Scaling ratio
Medium and fluid properties				
Host medium density	$\rho_k \left(\frac{kg}{m^3}\right)$	2500	1020	
Fluid density	$\rho_f \left(\frac{kg}{m^3}\right)$	2400	1	
Density contrast	$\Delta\rho_k = \rho_k - \rho_f \left(\frac{kg}{m^3}\right)$	100	1019	
Poisson's ratio	ν	0.25	0.49	
Fracture toughness	$K_c^k \left(Pa \cdot m^{\frac{1}{2}}\right)$	$0.2-1 \cdot 10^9$	60-80	
Gravitational acceleration	$g \left(\frac{m}{s^2}\right)$	9.81	9.81	
Geometry				
Rift/Caldera diameter	w (m)	$5-25 \cdot 10^3$	$60-70 \cdot 10^{-3}$	$2.4 \cdot 10^{-6}-1.4 \cdot 10^{-5}$
Rift/Caldera depth	h (m)	$0.3-1 \cdot 10^3$	$21-72 \cdot 10^{-3}$	$2.1 \cdot 10^{-5}-2.4 \cdot 10^{-4}$
Depth of intrusion	z^{start} (m)	$1-5 \cdot 10^4$	$1-1.5 \cdot 10^{-1}$	$2 \cdot 10^{-6}-7.5 \cdot 10^{-6}$
Scaling expressions				
Lengths				
Buoyancy length	$L_b = \left(\frac{K_c}{\pi^{\frac{1}{2}} \Delta\rho g}\right)^{\frac{2}{3}}$	$2.37-6.92 \cdot 10^3$	$2.3-2.8 \cdot 10^{-2}$	$L^* = 3.3 \cdot 10^{-5}-1.2 \cdot 10^{-6}$
Stress				
Young's modulus	E (Pa)	$1-10 \cdot 10^9$	$2.3-5.25 \cdot 10^3$	$2.3 \cdot 10^{-10}-5.25 \cdot 10^{-9}$
Tectonic stress	$\sigma_x = \frac{4}{3} E e$ (Pa)	$1 \cdot 10^6-1 \cdot 10^7$	$5 \cdot 10^1$	$5 \cdot 10^{-6}-5 \cdot 10^{-5}$
Unloading	$\sigma_U = \rho_k g h$ (Pa)	$7.36 \cdot 10^6-2.45 \cdot 10^7$	$2.1 \cdot 10^2-7.2 \cdot 10^2$	$\sigma^* = 8.6 \cdot 10^{-6}-9.8 \cdot 10^{-5}$

Table S4: Additional measured parameters for the experiments. The last row refers to the mean values assumed in the pooling of data from experiments 2DLA-6 and 2DLA-7. Column 2,3 & 5: "t" = top; "b" = bottom layers. Column 5: values of Young's modulus E in parentheses are estimates for the top layers assuming average values from the measured E of the homogeneous experiments at 2.0 wt% (2DLA-3) and on an independent set of gelatin samples at 2.5 wt% (2DLA-4). Column 6: temperature measured at the surface of the gelatin blocks immediately after their removal from the fridge. The nominal fridge temperature is $T = 8^\circ \text{C}$.

# Exp.	wt %	H	w	E	T_{surf}
		± 1	± 1		± 0.1
		mm	mm	Pa	$^\circ \text{C}$
2DLA-1	2.0	190	70	2930 ± 120	10.5
2DLA-2	2.0	210	60	2740 ± 130	9.6
2DLA-3	t: 2.0	t: 120	70	t: 3150 ± 110 (2730 ± 240)	9.6
	b: 2.5	b: 110		b: 5250 ± 460	
2DLA-4	t: 2.5	t: 88	70	t: 2300 ± 70 (3800 ± 560)	9.8
	b: 2.0	b: 107		b: 1390 ± 50	
2DLA-5	2.0	196	70	2800 ± 70	8
2DLA-6	2.0	219	60	2480 ± 50	11
2DLA-7	2.0	219	60	2800 ± 60	9.8
2DLA-6&7	2.0	219	60	2640 ± 50	10.4

Table S5: Measured x-coordinate of arrival points of observed cracks for the experiments considered in the main text: x_i^{obs} and $x_i^{obs,F}$ were used for inversions and forecasts, respectively. All quantities are measured according to the reference system shown in fig. 5.1.

# Exp.	N^I (Inversion)				N^F (Forecast)			
	x_1^{obs}	x_2^{obs}	x_3^{obs}	x_4^{obs}	$x_1^{obs,F}$	$x_2^{obs,F}$	$x_3^{obs,F}$	$x_4^{obs,F}$
	± 1 mm							
2DLA-1	-86	-67	72	81	69			
2DLA-2	-118	139			126			
2DLA-3	-90	63	88		76			
2DLA-4	-70	-63	51	57	-84			
2DLA-5	-114	-95	105		-55	72	87	
2DLA-6	-90	-79			60	75	82	103
2DLA-7	82	94	102		-80	-73		

Table S6: Assumed depth (z^{start}) and measured x-coordinate (x_i^{start}) of the tips of observed cracks at $z = z^{start}$ for the experiments considered in the main text (see 5.1): x_i^{start} and $x_i^{start,F}$ were used for inversions and forecasts, respectively. All quantities are measured according to the reference system shown in fig. 5.1.

# Exp.	N^I (Inversion)				N^F (Forecast)				
	z^{start}	x_1^{start}	x_2^{start}	x_3^{start}	x_4^{start}	$x_1^{start,F}$	$x_2^{start,F}$	$x_3^{start,F}$	$x_4^{start,F}$
	± 1 mm								
2DLA-1	-100	-75	-40	51	74	5			
2DLA-2	-100	-40	85			40			
2DLA-3	-150	-70	20	70		40			
2DLA-4	-150	-40	-35	10	25	-70			
2DLA-5	-150	-90	-30	80		-1	30	50	
2DLA-6	-150	-60	-30			20	45	60	85
2DLA-7	-150	20	60	80		-40	-60		

Table S7: Comparison between imposed and retrieved parameters. Column 2, 5 and 8: imposed parameters. Column 3, 6 and 9: medians of the respective retrieved posterior distributions. Column 4, 7 and 10: standard deviation of the respective posterior distributions.

# Exp.	d	d^{med}	δx_d	h	h^{med}	δx_h	R	R^{med}	δx_R
	± 0.1			± 1			$(\times 10^{-3})$	$(\times 10^{-3})$	
	mm	mm	mm	mm	mm	mm			
2DLA-1	2.5	4.9	2.7	50	51	24	63 ± 4	100	124
2DLA-2	-2.5	-3.5	2.7	44	73	20	-57 ± 4	-55	33
2DLA-3	2.5	3.9	2.4	21	63	25	120 ± 10	63	90
2DLA-4	2.5	5.8	2.4	24	59	26	104 ± 8	102	72
2DLA-5	0	0.4	3.6	24	64	23	0 ± 10^{-2}	81×10^{-3}	78
2DLA-6&7	2.5	2.5	2.0	65	64	22	43 ± 2	39	37

Figure S13: Detailed pictures of discarded experiments with imposed compression. **a)** 2DLA-8. **b)** 2DLA-9. **c)** 2DLA-10.

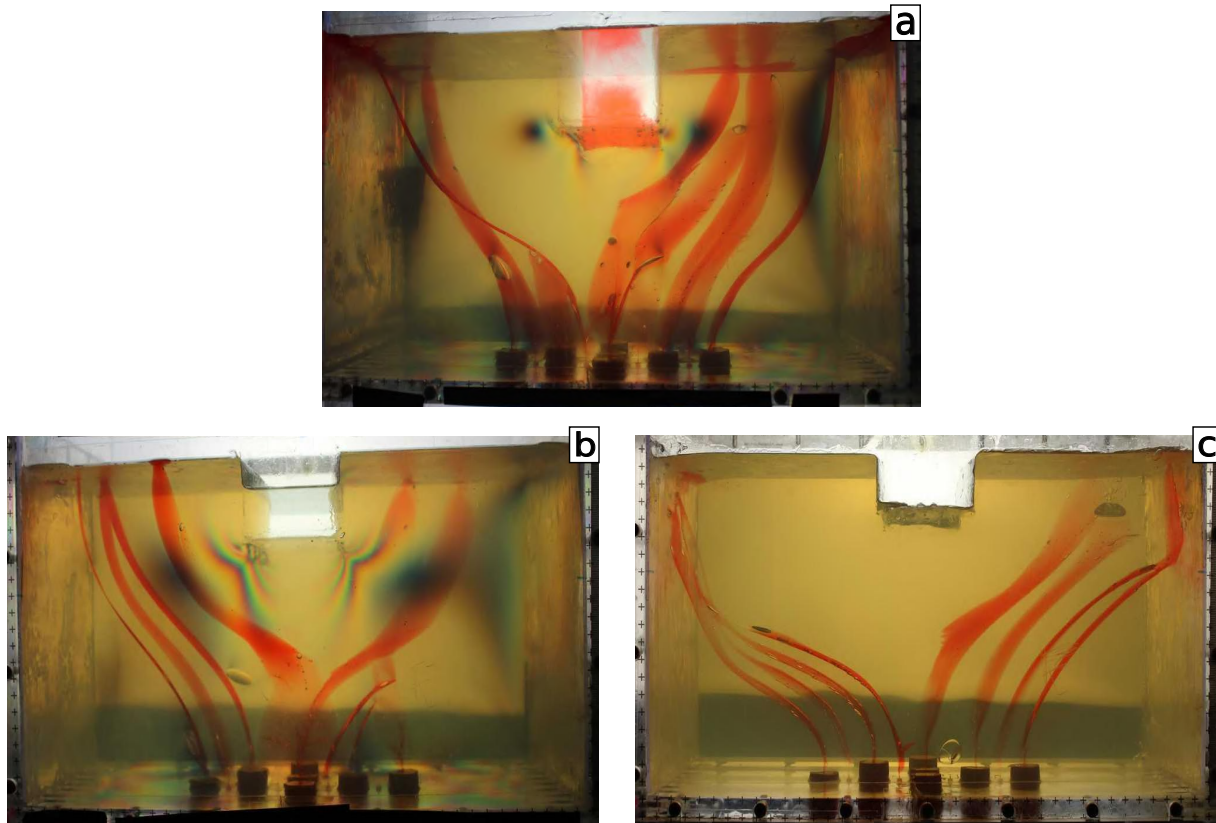


Figure S14: (Continued on the following page.)

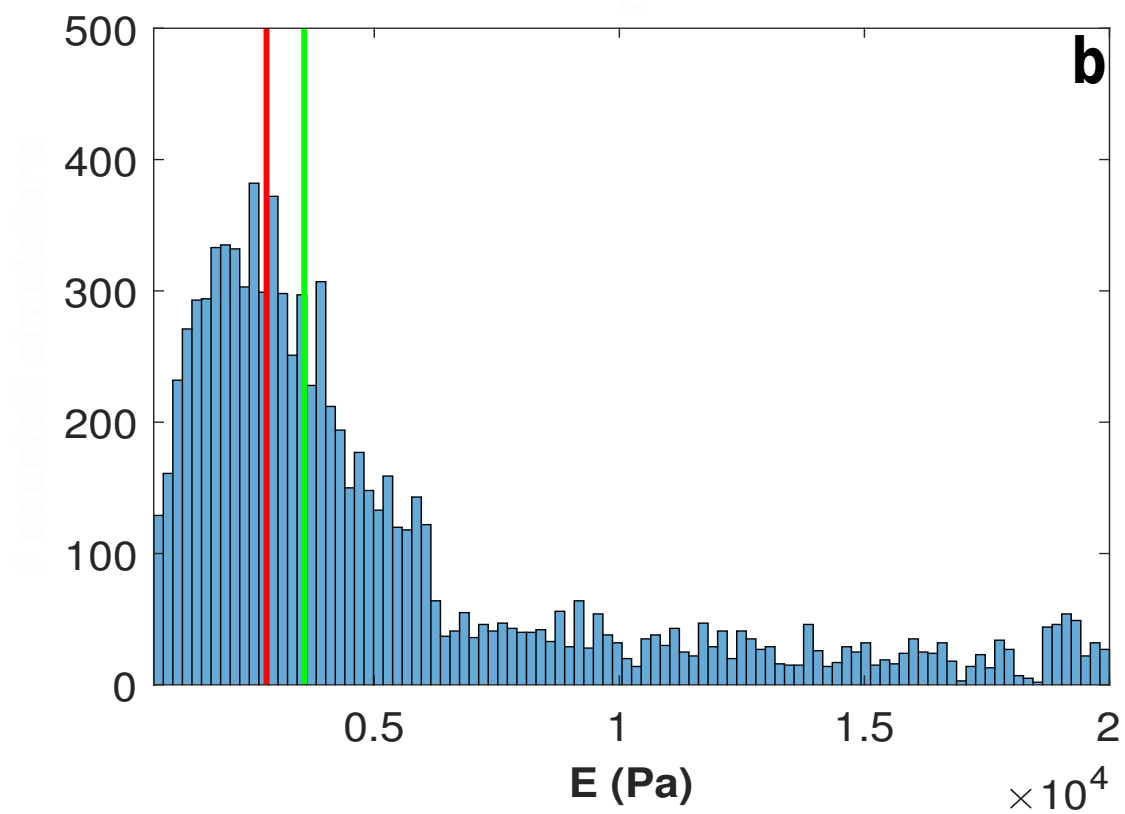
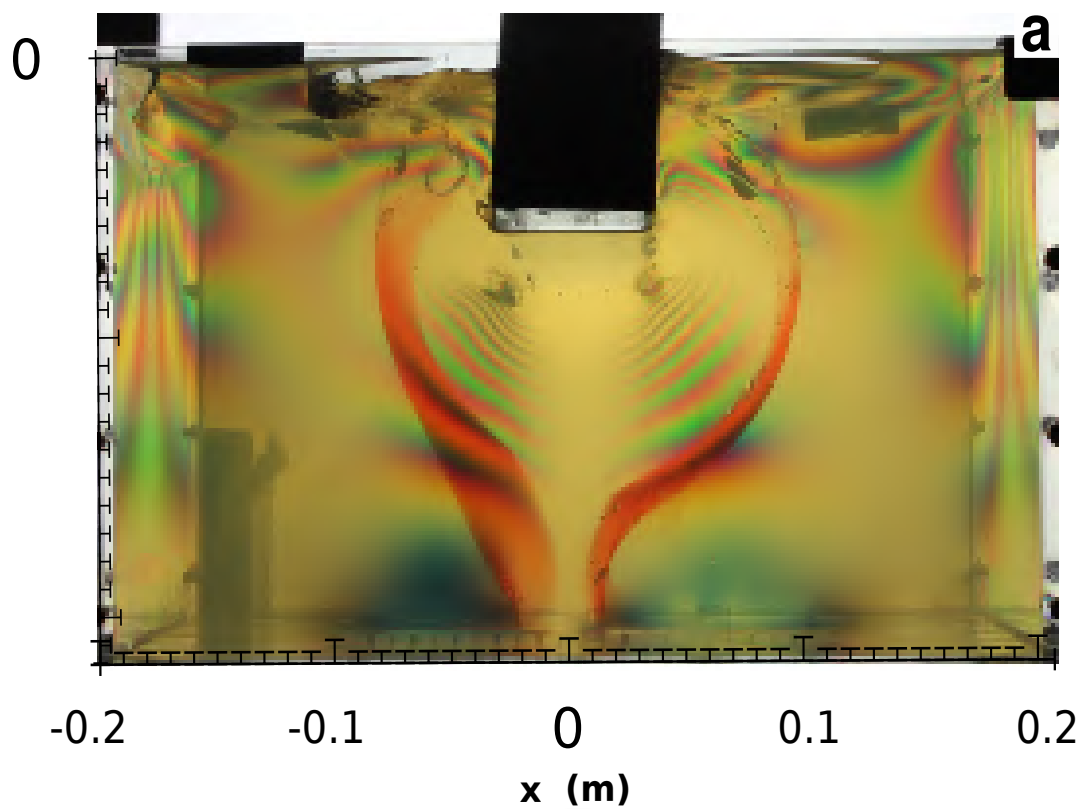


Figure S14: Additional tests for our MCMC strategy. **a)** Experiment 2DLA-11 (not reported in tables 5.1 and S4) with $h = 10$ cm and $w = 7$ cm. The purpose of the experiment was to verify the re-focusing of crack trajectories towards the center of the surface unload once, after having been deflected by the unloading, they approach the surface. This effect was observed in numerical simulations for surface excavations with $\frac{h}{w} \gg 1$ (see section 4.2). **b)** Posterior probability density of the Young's modulus E performed on the N^F data set of experiment 2DLA-5 (tables 5.1 and S4). Here we fixed d and h as known parameters. The measured value of E is represented by a red line; the median E^{med} by a green line. E falls at the 37th percentile of the sampled PPD (see section 4).

Supplementary information for Chapter 6: Unstable sill trajectories

Approximating the sill geometry as a penny

Here we estimate the error associated with approximating a 3D propagating crack as penny-shaped. We compare analytical formulas that describe K around the tip-line of penny-shaped cracks under uniform pressure and linear stress gradients, equation (6.1 & Fig. 6.2) to those of a more realistic 3D shape (Fig. S22a). We apply boundary conditions so that the opening of lengthened-tail crack matches that of the penny-shaped crack, at the location where the penny's opening is maximal. For penny-shaped cracks with constant internal pressure this is the crack centre. For a penny-shaped crack under a linear stress gradient the maximal opening is located along the direction of the stress gradient at $\sin(\pi/4)c$. We find the analytical formulas capture the scale and shape of the problem with some deviations (Fig. S22b, c and d). Note the accuracy of the numerical boundary element method to approximate K can have errors of up to 10% and the mesh used in Fig. S22 has ~ 2000 triangles (Davis, Healy, and Rivalta, 2019; Davis, Rivalta, and Dahm, 2020).

Reproducing Bárðarbunga's track

Here we test our analytical approach of approximating the crack as a series of isolated pennies on the case of the Bárðarbunga 2018 dyke track. The aim is to test how well the assumptions of our method perform in comparison to methods that take into account the entire dyke surface (Sigmundsson et al., 2015).

We use a series of vertical pennies with $c=2000$ m, $d=4000$ m, $V=3\pi c^2$ m³ (i.e. opening of 3 m if constant), $\nu=0.25$, $\mu=2\cdot 10^9$ Pa. All stresses are evaluated at the crack centre. We define the tectonic stress as that due to a vertical semi-infinite buried dislocation (Sigmundsson et al., 2015) of 4 m opening with an upper tip depth of 10 km, centred at Askja volcano and striking at 12° . As before, we use an analytical solution describing stresses beneath topographic slopes using a state of perfect confinement (Savage, Powers, and Swolfs, 1984), applied along the straight dashed line shown in Fig. S23. K_I around the tip-line is defined by the internal volume through equation (6.1), and by the gradient in normal traction taken from the slope stress solution, equation (6.2). Shear stresses due to the tectonic and gravitational stresses are resolved as shear traction (t_s) on the plane of the dyke at its centre and K_{II} is computed with:

$$K_{II} = \frac{4t_s \sqrt{c/\pi}}{2 - \nu} \quad (\text{S.16})$$

We compute K at the leading tip of the penny (black dots in Fig. S23). Free surface effects on values of K_I and K_{II} are below 10%, even with c/d ratios of 0.99. Turning of the leading tip is then computed using:

$$K_I \sin \theta + K_{II}(3 \cos \theta - 1) \quad (\text{S.17})$$

where the minimum value corresponds to the direction of the greatest circumferential stress ($\theta_0=0$) close to the tip, and as such the potential propagation direction (Pollard and Fletcher, 2005). We find our analytical approach predicts the dyke's pathway in a computationally efficient way (Fig. S23).

Table S8: Bayesian inversion results for profiles shown in Fig. S20, using rectangular dislocations (Okada, 1985). The 2.5 percentile value, the maximum a posteriori probability solution, and the 97.5 percentile value are shown for each parameter. The results for P7 are not shown, due to unsatisfactory fits to the data.

Profile	Opening [m]	Dip°	Dip Direction°	Depth [m]	Down-dip width [m]	Along-strike width [m]
P1	0.7 / 0.7 / 0.8	0.6 / 1.6 / 2.7	19 / 21 / 23	861 / 899 / 958	2907 / 2949 / 2986	2554 / 3175 / 4503
P2	1.0 / 1.0 / 1.0	11.0 / 12.8 / 15.4	136 / 140 / 142	998 / 1058 / 1335	2527 / 2637 / 3787	2356 / 2387 / 2421
P3	1.2 / 1.2 / 1.2	3.0 / 5.5 / 7.5	138 / 140 / 142	939 / 992 / 1040	3541 / 3891 / 13903	2119 / 2140 / 2172
P4	1.7 / 1.8 / 1.8	16.7 / 17.4 / 18.1	199 / 199 / 200	1053 / 1084 / 1115	3296 / 3604 / 3653	1754 / 1771 / 1789
P5	2.8 / 2.8 / 2.8	14.0 / 14.5 / 15.0	210 / 210 / 210	994 / 1010 / 1026	2196 / 2210 / 2224	2838 / 2850 / 2859
P6	2.80 / 2.83 / 2.85	14.1 / 14.6 / 14.9	352 / 353 / 353	976 / 993 / 1007	2322 / 2340 / 2353	2826 / 2840 / 2851

Figure S15: Vertical GPS movement's from continuous GPS stations GV01, 02 and 04 situated on Sierra Negra's summit. See Fig. 6.1 for station location.

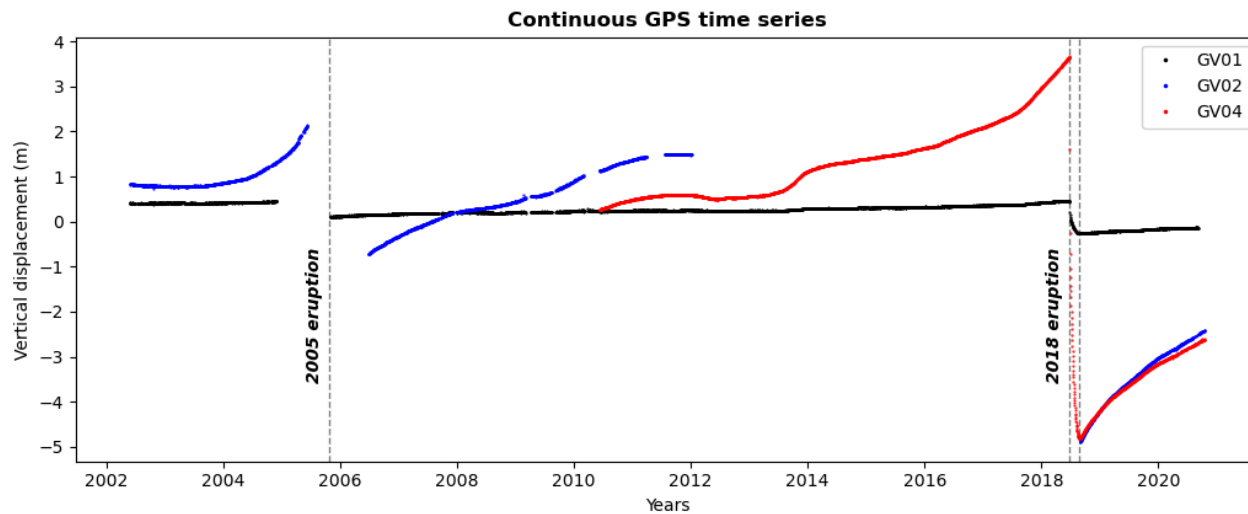


Figure S16: (Continued on the following page.)

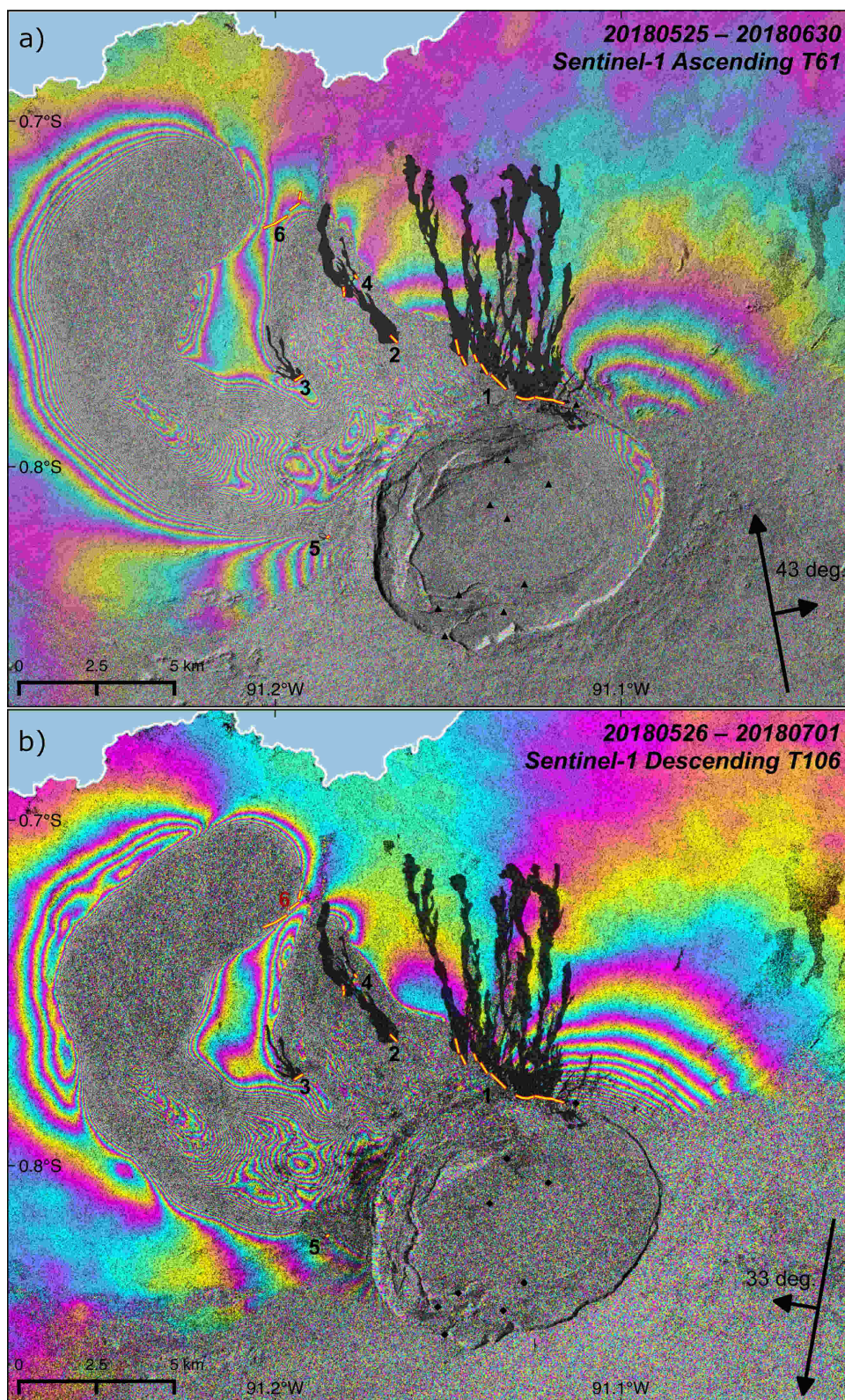


Figure S16: SAR data are from the Sentinel-1 satellite. Same colourbar as Fig. 6.1, with each colour cycle as 2.8 cm of LOS ground displacement. Black arrows show the satellite orbit direction, a) \sim S-N b) \sim N-S, look direction a) \sim W-E b) \sim E-W, and the incidence angle in degrees. a) Ascending pass, Track 61 TOPS mode. b) Descending pass, Track 106, TOPS mode. Symbols as in Fig. 6.1 in the main text.

Figure S17: (Continued on the following page.)

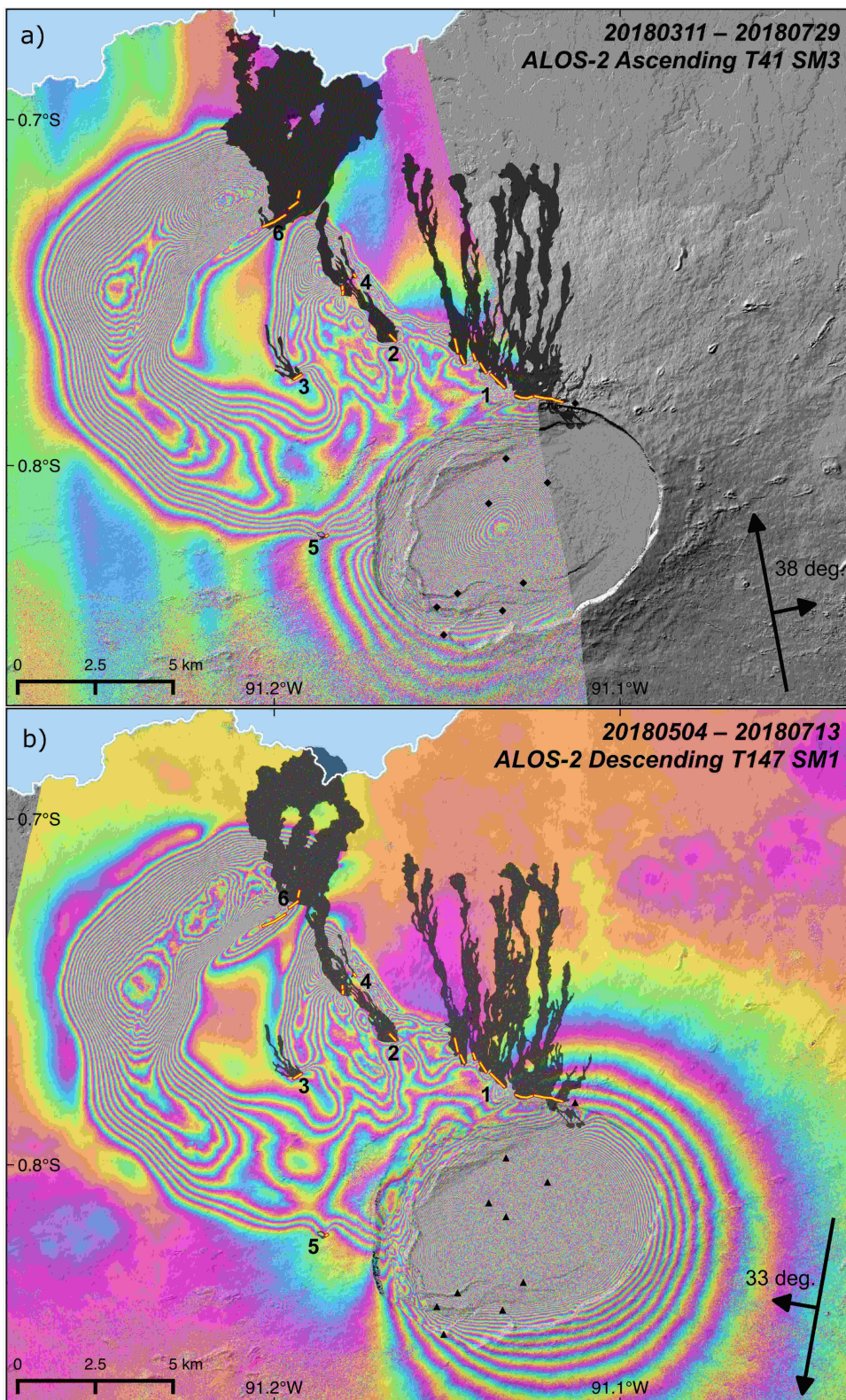


Figure S17: SAR data are from the ALOS-2 satellite. Colourbar as Fig. 6.1, with each colour cycle as 11.45 cm LOS ground displacement. Black arrows show the satellite orbit direction, a) \sim S-N b) \sim N-S, look direction a) \sim W-E b) \sim E-W, and the incidence angle in degrees. a) Ascending pass, Track 41, Fine Stripmap mode (SM3; pixel resolution 9.1x5.3 m). b) Descending pass, Track 147, Ultra-fine Stripmap mode (SM1; pixel resolution 3.0x3.0 m). Symbols as in Fig. 6.1 in the main text.

Figure S18: Magnitude of stress gradients, topographic vs buoyancy. Top panel shows in black the topographic profile of the volcano (profile A-A' in Fig. 6.2) and in blue an approximation of this profile used to calculate the analytical solution (Savage, Powers, and Swolfs, 1984). Bottom panel shows the required crack dip β such that the two competing gradients match, according to $(\rho_r - \rho_f)g \sin(\beta) = \delta\sigma_v/\delta h$. Plane strain boundary element method result due to the topography is shown in black, the result of the analytical solution (Savage, Powers, and Swolfs, 1984) due to the approximate slope shown is shown in blue.

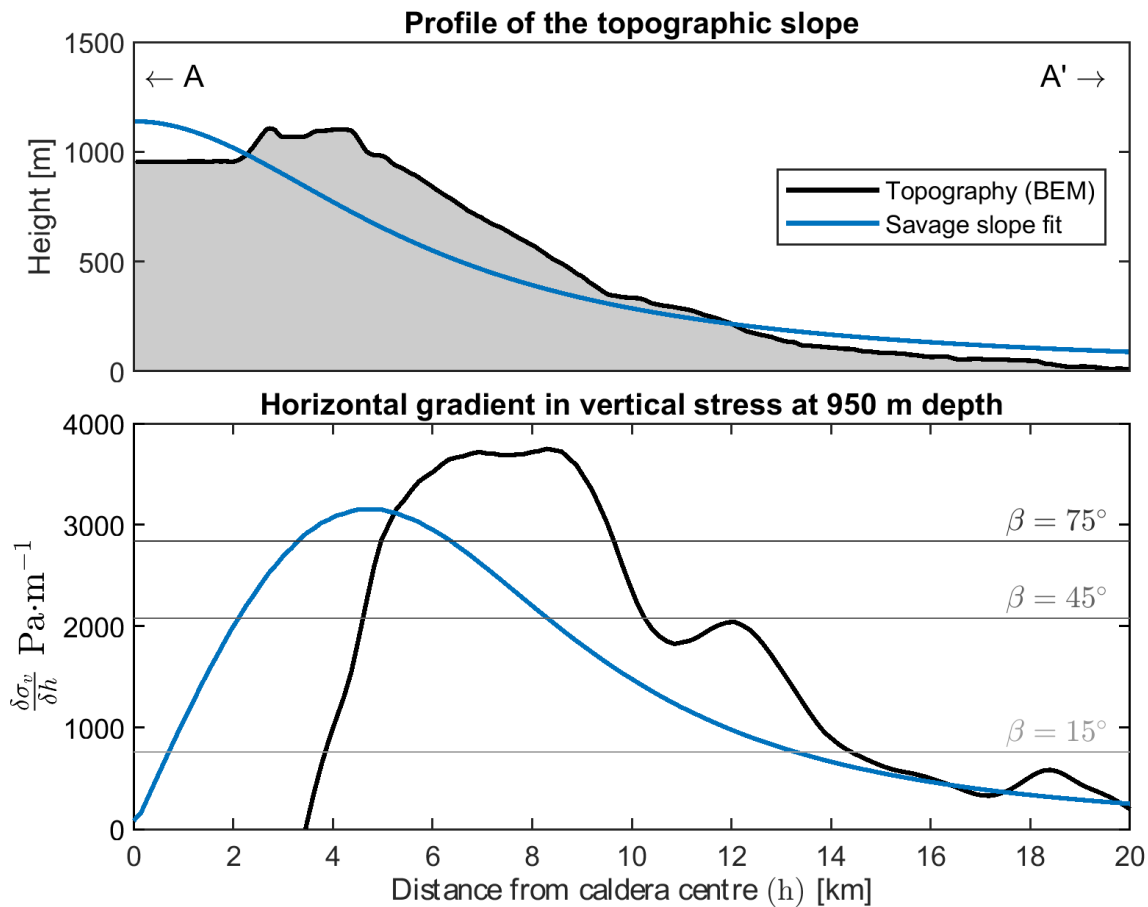


Figure S19: Half-space effects on K_I at the upper and lower tips of a dipping penny-shaped crack. Maximum and minimum K_I values (solid and dashed) for constant volume cracks, depth d below a half-space, with radius c . Values relative to K_∞ , equation (6.1)). Note the offset from 1 when $c/d=0$, indicates the size of the numerical error.

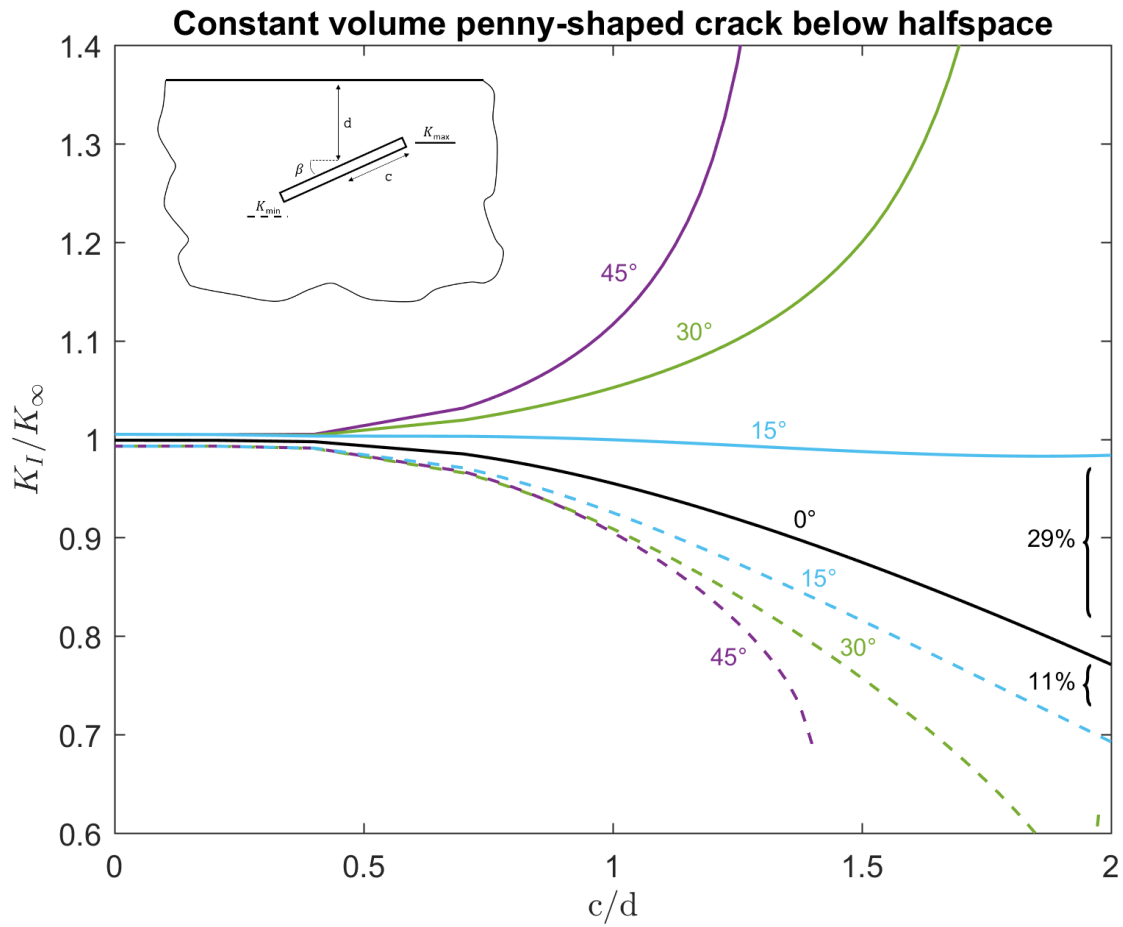


Figure S20: Profiles used to estimate intrusion geometry. a) InSAR as in Fig. S17 with the location of the profiles (P1 - P7) marked by blue shading. Gray polygons show the extent of the lava flows emplaced during the time period spanned by the interferogram. Yellow lines mark the location and extent of all eruptive fissures. b) Each plot shows the line-of-sight ground displacement for each data point included in profiles 1-7. Vertical scale is not constant. c) All profiles shown on one plot, (~ W-E).

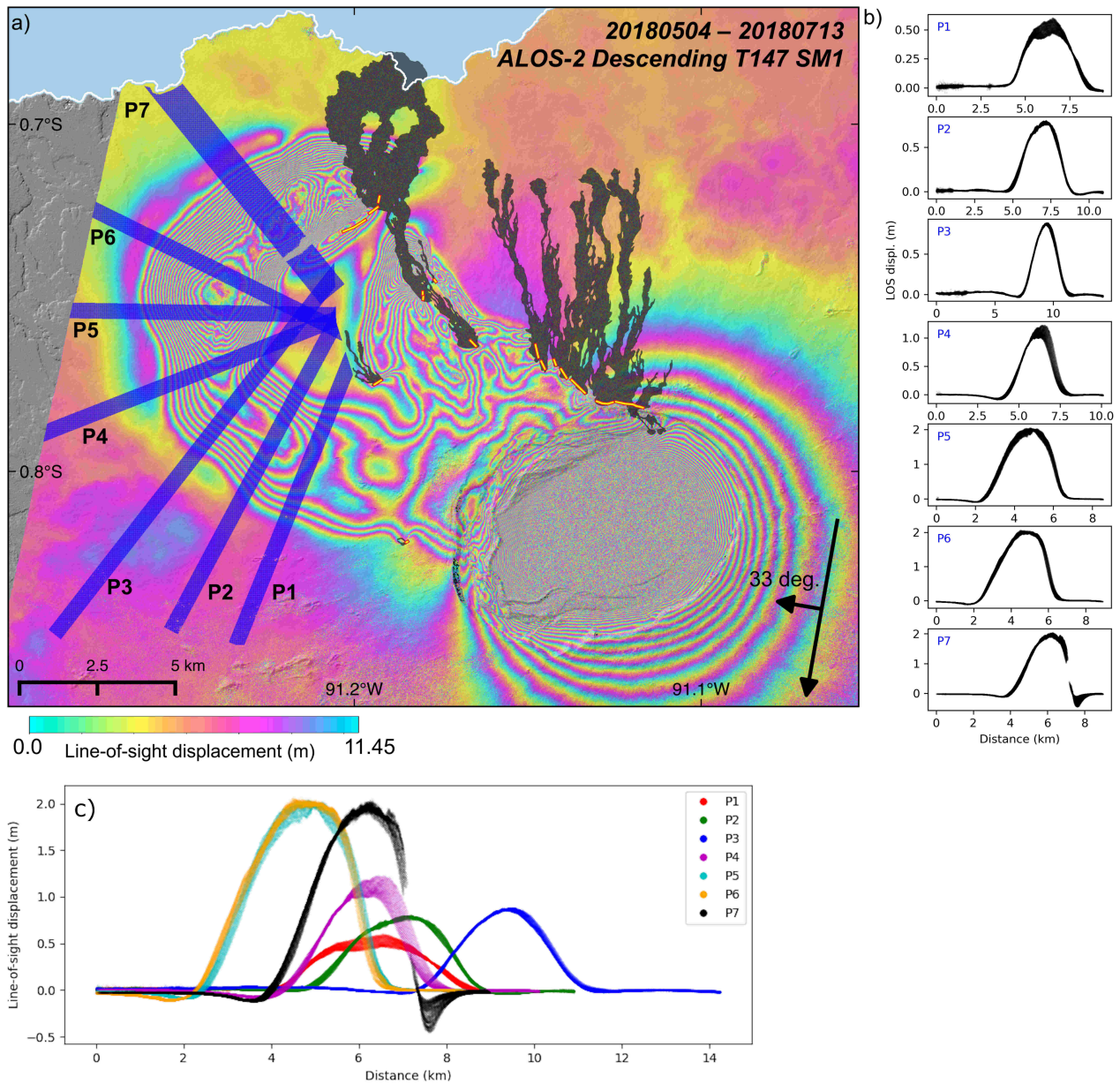
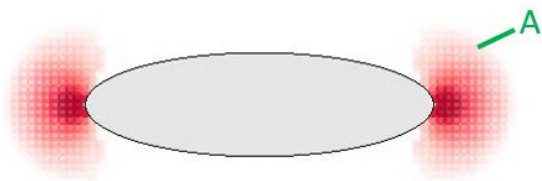
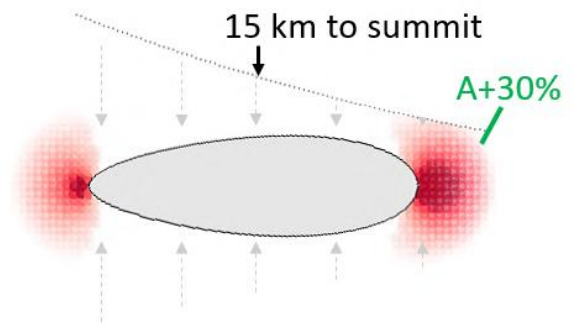


Figure S21: Summary of changes in K due to different effects on the sill at Sierra Negra. Cross sections of cracks showing changes in stress intensity, K_I , at the crack tip due to different processes. Crack opening exaggerated by 300, red patches show the 2nd invariant of stress computed from K at the tip. a) crack in a full space, b) crack under topographic stress gradient, topography exaggerated, c) crack with 15° dip, buoyancy as defined in text, d) interacting cracks with separation defined in text, e) flat crack close to the free surface, f) crack close to free surface with dip, only internal pressure.

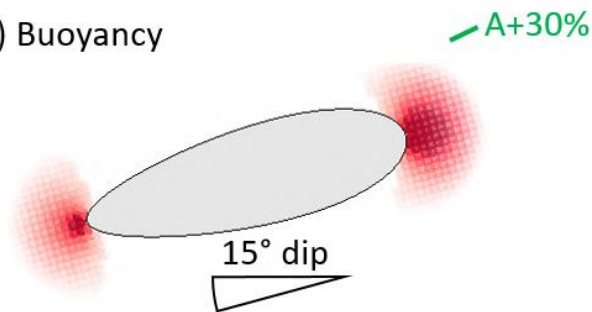
a) Isolated crack full-space



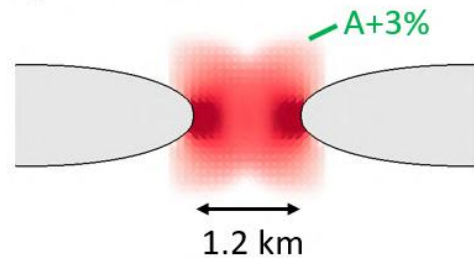
b) Topographic weight



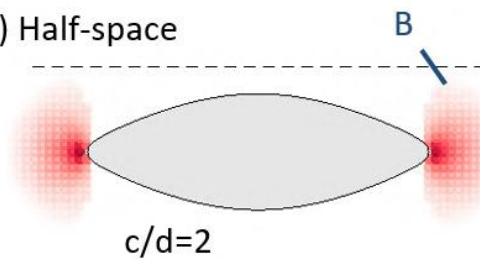
c) Buoyancy



d) Interaction



e) Half-space



f) Half-space

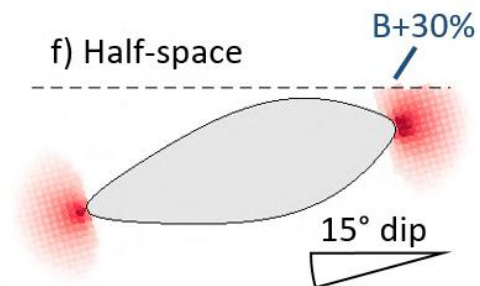


Figure S22: Comparison of K_I around a penny-shaped and elongated penny-shaped crack. a) The mesh used for this analysis. θ is defined in degrees away from the tip ($y = 1$). Comparison of K_I from equation (6.2) to that for an elongated penny-shaped crack as in a), assuming b) a stress gradient along the x -axis; c) a stress gradient along the y -axis. d) Comparison of K_I from equation (6.1) to that for an elongated penny-shaped crack with uniform pressure. Note some slight numerical inaccuracies are present.

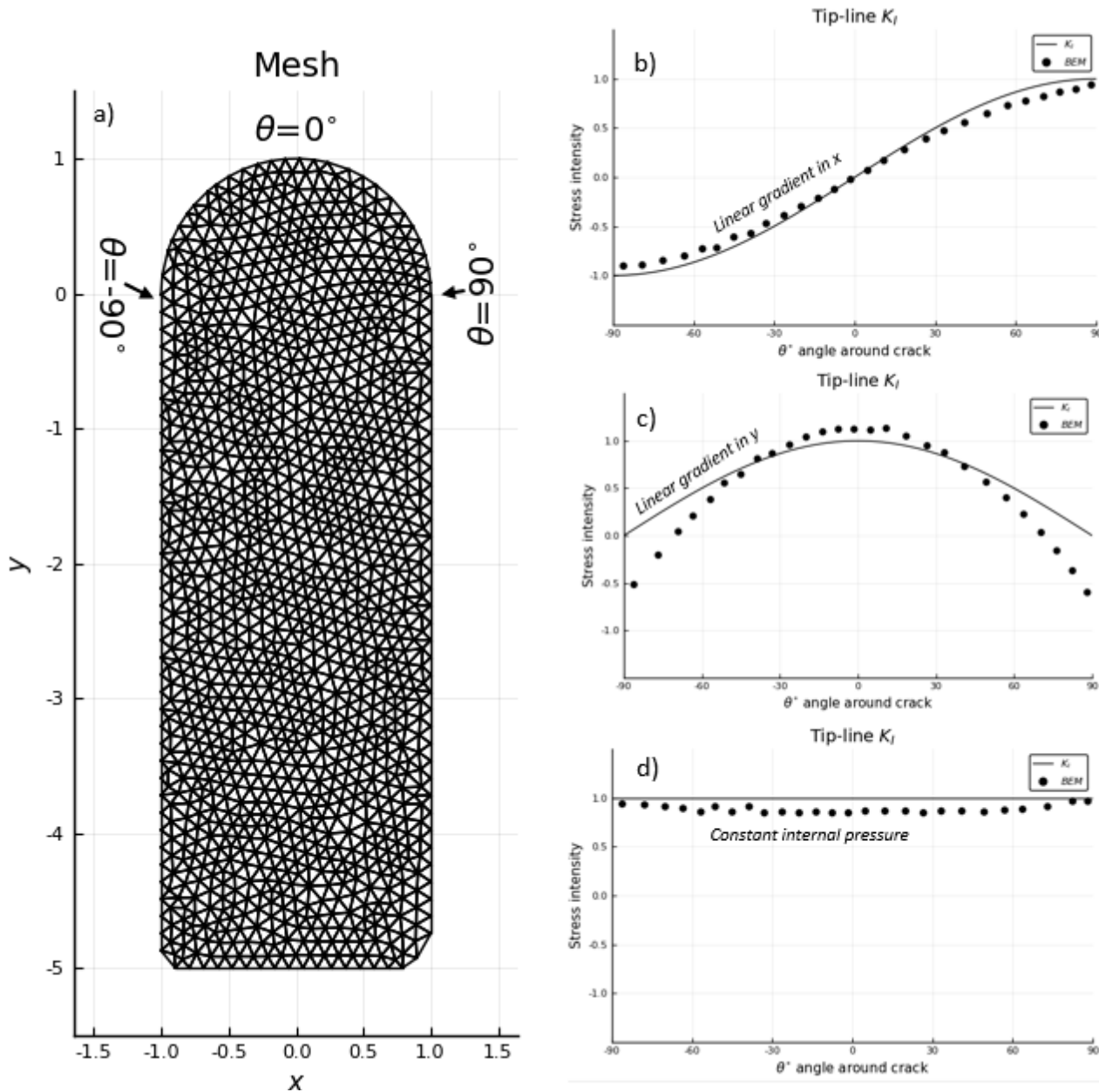
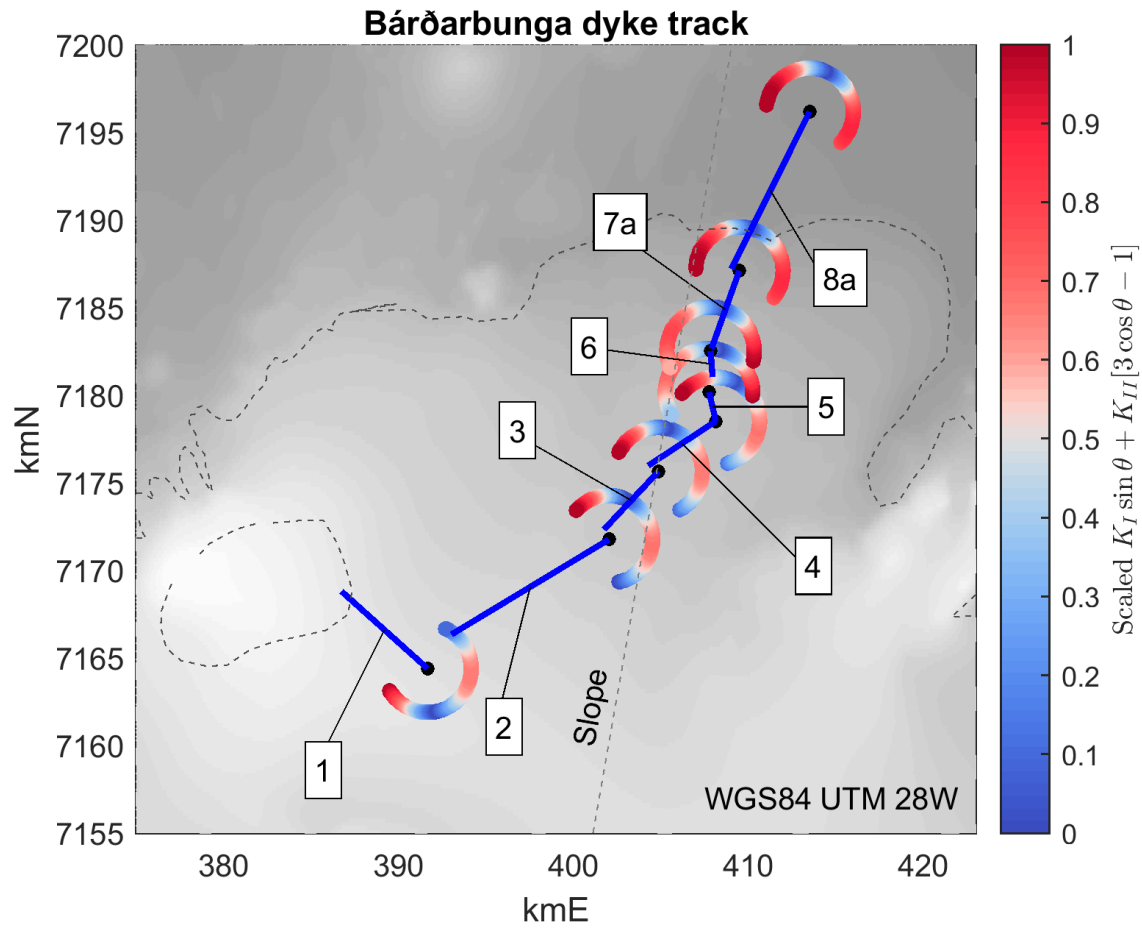


Figure S23: Forecasting propagation directions along the Bárðarbunga dyke track. Numbered labels indicate the position of the penny at test locations (Sigmundsson et al., 2015). Preferred directions of propagation, according to equation (S.17), where the maximum circumferential (hoop) stress is shown in blue.



Bibliography

- Acocella, V. (2010). “Evaluating fracture patterns within a resurgent caldera: Campi Flegrei, Italy”. In: *Bulletin of Volcanology* 72.5, pp. 623–638. doi: [10.1007/s00445-010-0347-x](https://doi.org/10.1007/s00445-010-0347-x).
- Acocella, V. and A. Tibaldi (2005). “Dike propagation driven by volcano collapse: a general model tested at Stromboli, Italy”. In: *Geophysical Research Letters* 32.8. doi: [10.1029/2004GL022248](https://doi.org/10.1029/2004GL022248).
- Alberico, I., L. Lirer, P. Petrosino, and R. Scandone (2002). “A methodology for the evaluation of long-term volcanic risk from pyroclastic flows in Campi Flegrei (Italy)”. In: *Journal of Volcanology and Geothermal Research* 116.1-2, pp. 63–78. doi: [10.1016/S0377-0273\(02\)00211-1](https://doi.org/10.1016/S0377-0273(02)00211-1).
- Amoruso, A, L Crescentini, A. Linde, I. Sacks, R Scarpa, and P Romano (2007). “A horizontal crack in a layered structure satisfies deformation for the 2004–2006 uplift of Campi Flegrei”. In: *Geophysical research letters* 34.22. doi: [10.1029/2007GL031644](https://doi.org/10.1029/2007GL031644).
- Amoruso, A., L. Crescentini, and I. Sabetta (2014). “Paired deformation sources of the Campi Flegrei caldera (Italy) required by recent (1980–2010) deformation history”. In: *Journal of Geophysical Research: Solid Earth* 119.2, pp. 858–879. doi: [10.1002/2013JB010392](https://doi.org/10.1002/2013JB010392).
- Anderson, E. M. (1937). “IX.—the dynamics of the formation of cone-sheets, ring-dykes, and caldron-subsidences”. In: *Proceedings of the Royal Society of Edinburgh* 56, pp. 128–157. doi: [10.1017/S0370164600014954](https://doi.org/10.1017/S0370164600014954).
- (1939). “XVII.—The Dynamics of Sheet Intrusion”. In: *Proceedings of the Royal Society of Edinburgh* 58, pp. 242–251. doi: [10.1017/S0370164600011159](https://doi.org/10.1017/S0370164600011159).
- (1951). *The dynamics of faulting and dyke formation with applications to Britain*. Hafner Pub. Co.
- Atkinson, B. K. and P. G. Meredith (1987a). “Experimental fracture mechanics data for rocks and minerals”. In: *Fracture mechanics of rock*. Ed. by B. K. Atkinson. Academic Press, London. Chap. 11, pp. 477–525. doi: [10.1016/C2009-0-21691-6](https://doi.org/10.1016/C2009-0-21691-6).
- (1987b). “The theory of subcritical crack growth with applications to minerals and rocks”. In: *Fracture mechanics of rock*. Ed. by B. K. Atkinson. Academic Press, London. Chap. 4, pp. 111–166. doi: [10.1016/C2009-0-21691-6](https://doi.org/10.1016/C2009-0-21691-6).
- Atroshchenko, E, S Potapenko, and G Glinka (2009). “Stress intensity factor for an embedded elliptical crack under arbitrary normal loading”. In: *International Journal of Fatigue* 31.11-12, pp. 1907–1910. doi: [10.1016/0013-7944\(71\)90052-X](https://doi.org/10.1016/0013-7944(71)90052-X).

Bibliography

- Bagnardi, M., F. Amelung, and M. P. Poland (2013). “A new model for the growth of basaltic shields based on deformation of Fernandina volcano, Galápagos Islands”. In: *Earth and Planetary Science Letters* 377, pp. 358–366. doi: [10.1016/j.epsl.2013.07.016](https://doi.org/10.1016/j.epsl.2013.07.016).
- Bagnardi, M. and A. Hooper (2018). “Inversion of surface deformation data for rapid estimates of source parameters and uncertainties: A Bayesian approach”. In: *Geochemistry, Geophysics, Geosystems* 19.7, pp. 2194–2211. doi: [10.1029/2018GC007585](https://doi.org/10.1029/2018GC007585).
- Barberi, F, E Cassano, P La Torre, and A Sbrana (1991). “Structural evolution of Campi Flegrei caldera in light of volcanological and geophysical data”. In: *Journal of volcanology and geothermal research* 48.1-2, pp. 33–49. doi: [10.1016/0377-0273\(91\)90031-T](https://doi.org/10.1016/0377-0273(91)90031-T).
- Baydoun, M and T. Fries (2012). “Crack propagation criteria in three dimensions using the XFEM and an explicit–implicit crack description”. In: *International journal of fracture* 178.1-2, pp. 51–70. doi: [10.1007/s10704-012-9762-7](https://doi.org/10.1007/s10704-012-9762-7).
- Bell, J., P. Price, and P. McLellan (1990). “In-situ stress in the western Canada Sedimentary Basin”. In: *Geological Atlas of the Western Canada Sedimentary Basin*. Vol. 38. 1. Canadian Society of Petroleum Geologists, Alberta Research Council. Chap. 29, pp. 439–446.
- Bevilacqua, A. et al. (2015). “Quantifying volcanic hazard at Campi Flegrei caldera (Italy) with uncertainty assessment: 1. Vent opening maps”. In: *Journal of Geophysical Research: Solid Earth* 120.4, pp. 2309–2329. doi: [10.1002/2014JB011775](https://doi.org/10.1002/2014JB011775).
- Bons, P. D. (2001). “The formation of large quartz veins by rapid ascent of fluids in mobile hydrofractures”. In: *Tectonophysics* 336.1-4, pp. 1–17. doi: [10.1016/S0040-1951\(01\)00090-7](https://doi.org/10.1016/S0040-1951(01)00090-7).
- Brandsdóttir, B. and P. Einarsson (1979). “Seismic activity associated with the September 1977 deflation of the Krafla central volcano in northeastern Iceland”. In: *Journal of Volcanology and Geothermal Research* 6.3-4, pp. 197–212. doi: [https://doi.org/10.1016/0377-0273\(79\)90001-5](https://doi.org/10.1016/0377-0273(79)90001-5).
- Brodsky, E. E., J. D. Kirkpatrick, and T. Candela (2016). “Constraints from fault roughness on the scale-dependent strength of rocks”. In: *Geology* 44.1, pp. 19–22. doi: [10.1130/G37206.1](https://doi.org/10.1130/G37206.1).
- Brown, E. T. and E Hoek (1978). Trends in relationships between measured in-situ stresses and depth. Tech. rep. 4, pp. 211–215. doi: [10.1016/0148-9062\(78\)91227-5](https://doi.org/10.1016/0148-9062(78)91227-5).
- Bunger, A. and E. Detournay (2007). “Early-time solution for a radial hydraulic fracture”. In: *Journal of engineering mechanics* 133.5, pp. 534–540. doi: [10.1061/\(ASCE\)0733-9399\(2007\)133:5\(534\)](https://doi.org/10.1061/(ASCE)0733-9399(2007)133:5(534)).
- Bunger, A. and B. Lecampion (2017). “Four critical issues for successful hydraulic fracturing applications”. In: *Rock Mechanics and Engineering*. Ed. by X.-T. Feng. Vol. 5. CRC Press. Chap. 16.
- Bürgmann, R., D. D. Pollard, and S. J. Martel (1994). “Slip distributions on faults: effects of stress gradients, inelastic deformation, heterogeneous host-rock stiffness, and fault interaction”. In: *Journal of Structural Geology* 16.12, pp. 1675–1690. doi: [10.1016/0191-8141\(94\)90134-1](https://doi.org/10.1016/0191-8141(94)90134-1).

Bibliography

- Byerlee, J. (1978). “Friction of rocks”. In: Rock friction and earthquake prediction. Springer, pp. 615–626. doi: [10.1007/978-3-0348-7182-2_4](https://doi.org/10.1007/978-3-0348-7182-2_4).
- Candela, T., F. Renard, J. Schmittbuhl, M. Bouchon, and E. E. Brodsky (2011). “Fault slip distribution and fault roughness”. In: *Geophysical Journal International* 187.2, pp. 959–968. doi: [10.1111/j.1365-246X.2011.05189.x](https://doi.org/10.1111/j.1365-246X.2011.05189.x).
- Cann, J. et al. (1997). “Corrugated slip surfaces formed at ridge–transform intersections on the Mid-Atlantic Ridge”. In: *Nature* 385.6614, pp. 329–332. doi: [10.1038/385329a0](https://doi.org/10.1038/385329a0).
- Cappello, A, M Neri, V Acocella, G Gallo, A Vicari, and C Del Negro (2012). “Spatial vent opening probability map of Etna volcano (Sicily, Italy)”. In: *Bulletin of Volcanology* 74.9, pp. 2083–2094. doi: [10.1007/s00445-012-0647-4](https://doi.org/10.1007/s00445-012-0647-4).
- Cayol, V. et al. (2014). “Sheared sheet intrusions as mechanism for lateral flank displacement on basaltic volcanoes: Applications to Réunion Island volcanoes”. In: *Journal of Geophysical Research: Solid Earth* 119.10, pp. 7607–7635. doi: [10.1002/2014JB011139](https://doi.org/10.1002/2014JB011139).
- Chadwick Jr, W. and J. Dieterich (1995). “Mechanical modeling of circumferential and radial dike intrusion on Galapagos volcanoes”. In: *Journal of Volcanology and Geothermal Research* 66.1-4, pp. 37–52. doi: [10.1016/0377-0273\(94\)00060-T](https://doi.org/10.1016/0377-0273(94)00060-T).
- Chen, C. W. and H. A. Zebker (2001). “Two-dimensional phase unwrapping with use of statistical models for cost functions in nonlinear optimization”. In: *JOSA A* 18.2, pp. 338–351. doi: [10.1364/JOSAA.18.000338](https://doi.org/10.1364/JOSAA.18.000338).
- Choi, M.-K., A. Bobet, and L. J. Pyrak-Nolte (2014). “The effect of surface roughness and mixed-mode loading on the stiffness ratio κ_x/κ_z for fractures”. In: *Geophysics* 79.5, pp. D319–D331. doi: [10.1190/geo2013-0438.1](https://doi.org/10.1190/geo2013-0438.1).
- Clair, J. S. et al. (2015). “Geophysical imaging reveals topographic stress control of bedrock weathering”. In: *Science* 350.6260, pp. 534–538. doi: [10.1126/science.aab2210](https://doi.org/10.1126/science.aab2210).
- Connor, C. B. and B. E. Hill (1995). “Three nonhomogeneous Poisson models for the probability of basaltic volcanism: application to the Yucca Mountain region, Nevada”. In: *Journal of Geophysical Research: Solid Earth* 100.B6, pp. 10107–10125. doi: [10.1029/95JB01055](https://doi.org/10.1029/95JB01055).
- Cooke, M. L. and D. D. Pollard (1996). “Fracture propagation paths under mixed mode loading within rectangular blocks of polymethyl methacrylate”. In: *Journal of Geophysical Research: Solid Earth* 101.B2, pp. 3387–3400. doi: [10.1029/95JB02507](https://doi.org/10.1029/95JB02507).
- Corbi, F., E. Rivalta, V. Pinel, F. Maccaferri, and V. Acocella (2016). “Understanding the link between circumferential dikes and eruptive fissures around calderas based on numerical and analog models”. In: *Geophysical Research Letters* 43.12, pp. 6212–6219. doi: [10.1002/2016GL068721](https://doi.org/10.1002/2016GL068721).

Bibliography

- Corbi, F., E. Rivalta, V. Pinel, F. Maccaferri, M. Bagnardi, and V. Acocella (2015). “How caldera collapse shapes the shallow emplacement and transfer of magma in active volcanoes”. In: *Earth and Planetary Science Letters* 431, pp. 287–293. doi: [10.1016/j.epsl.2015.09.028](https://doi.org/10.1016/j.epsl.2015.09.028).
- Cowie, P. A. and C. H. Scholz (1992). “Physical explanation for displacement-length relationship of faults using a post-yield fracture mechanics model”. In: *Journal of Structural Geology* 14, pp. 1133–1133. doi: [10.1016/0191-8141\(92\)90065-5](https://doi.org/10.1016/0191-8141(92)90065-5).
- Crider, J. G. (2001). “Oblique slip and the geometry of normal-fault linkage: mechanics and a case study from the Basin and Range in Oregon”. In: *Journal of Structural Geology* 23.12, pp. 1997–2009. doi: [10.1016/S0191-8141\(01\)00047-5](https://doi.org/10.1016/S0191-8141(01)00047-5).
- Crouch, S. L. and A. Starfield (1982). *Boundary element methods in solid mechanics: with applications in rock mechanics and geological engineering*. Allen & Unwin.
- Czerner, M., L. A. Fasce, J. F. Martucci, R. Ruseckaitė, and P. M. Frontini (2016). “Deformation and fracture behavior of physical gelatin gel systems”. In: *Food Hydrocolloids* 60, pp. 299–307. doi: [10.1016/j.foodhyd.2016.04.007](https://doi.org/10.1016/j.foodhyd.2016.04.007).
- Da, T. K. F. and D. Cohen-Steiner (2019). *Advancing Front Surface Reconstruction: CGAL User and Reference Manual*. 4.14.1. The Computational Geometry Algorithms Library. url: <https://doc.cgal.org/4.14.1/Manual/packages.html#PkgAdvancingFrontSurfaceReconstruction>.
- Dahm, T. (2000a). “Numerical simulations of the propagation path and the arrest of fluid-filled fractures in the Earth”. In: *Geophysical Journal International* 141.3, pp. 623–638. doi: [10.1046/j.1365-246x.2000.00102.x](https://doi.org/10.1046/j.1365-246x.2000.00102.x).
- (2000b). “On the shape and velocity of fluid-filled fractures in the Earth”. In: *Geophysical Journal International* 142.1, pp. 181–192. doi: [10.1046/j.1365-246x.2000.00148.x](https://doi.org/10.1046/j.1365-246x.2000.00148.x).
- Das, S. B. et al. (2008). “Fracture propagation to the base of the Greenland Ice Sheet during supraglacial lake drainage”. In: *Science* 320.5877, pp. 778–781. doi: [10.1126/science.1153360](https://doi.org/10.1126/science.1153360).
- Davis, T., D. Healy, A. Bubeck, and R. Walker (2017). “Stress concentrations around voids in three dimensions: The roots of failure”. In: *Journal of Structural Geology* 102, pp. 193–207. doi: [10.1016/j.jsg.2017.07.013](https://doi.org/10.1016/j.jsg.2017.07.013).
- Davis, T., D. Healy, and E. Rivalta (2019). “Slip on wavy frictional faults: Is the 3rd dimension a sticking point?” In: *Journal of Structural Geology* 119, pp. 33–49. doi: [10.1016/j.jsg.2018.11.009](https://doi.org/10.1016/j.jsg.2018.11.009).
- Davis, T., E. Rivalta, and T. Dahm (2020). “Critical fluid injection volumes for uncontrolled fracture ascent”. In: *Geophysical Research Letters* 47.14, e2020GL087774. doi: [10.1029/2020GL087774](https://doi.org/10.1029/2020GL087774).
- Decriem, J et al. (2010). “The 2008 May 29 earthquake doublet in SW Iceland”. In: *Geophysical Journal International* 181.2, pp. 1128–1146. doi: [10.1111/j.1365-246X.2010.04565.x](https://doi.org/10.1111/j.1365-246X.2010.04565.x).

Bibliography

- Deino, A. L., G. Orsi, S. de Vita, and M. Piochi (2004). “The age of the Neapolitan Yellow Tuff caldera-forming eruption (Campi Flegrei caldera–Italy) assessed by $^{40}\text{Ar}/^{39}\text{Ar}$ dating method”. In: *Journal of Volcanology and Geothermal Research* 133.1-4, pp. 157–170.
- Delaney, P. T. and D. D. Pollard (1981). “Deformation of host rocks and flow of magma during growth of minette dikes and breccia-bearing intrusions near Ship Rock, New Mexico”. In: 1202. USGS Numbered Series, 61 p.; 1 plate in pocket. U.S. Geological Survey. U.S. G.P.O. doi: [10.3133/pp1202](https://doi.org/10.3133/pp1202).
- Di Giuseppe, E, F Funiciello, F Corbi, G. Ranalli, and G Mojoli (2009). “Gelatin as rock analogs: A systematic study of their rheological and physical properties”. In: *Tectonophysics* 473.3-4, pp. 391–403. doi: [10.1016/j.tecto.2009.03.012](https://doi.org/10.1016/j.tecto.2009.03.012).
- Di Vito, M. A. et al. (1999). “Volcanism and deformation since 12,000 years at the Campi Flegrei caldera (Italy)”. In: *Journal of Volcanology and Geothermal Research* 91.2-4, pp. 221–246. doi: [10.1016/S0377-0273\(99\)00037-2](https://doi.org/10.1016/S0377-0273(99)00037-2).
- Di Vito, M. A. et al. (2016). “Magma transfer at Campi Flegrei caldera (Italy) before the 1538 AD eruption”. In: *Scientific reports* 6.1, pp. 1–9. doi: [10.1038/srep32245](https://doi.org/10.1038/srep32245).
- Dieterich, J. H. and D. E. Smith (2009). “Nonplanar faults: Mechanics of slip and off-fault damage”. In: *Mechanics, structure and evolution of fault zones*. Springer, pp. 1799–1815. doi: [10.1007/978-3-0346-0138-2_12](https://doi.org/10.1007/978-3-0346-0138-2_12).
- Dyskin, A., E Sahouryeh, R. Jewell, H Joer, and K. Ustinov (2003). “Influence of shape and locations of initial 3-D cracks on their growth in uniaxial compression”. In: *Engineering Fracture Mechanics* 70.15, pp. 2115–2136. doi: [10.1016/S0013-7944\(02\)00240-0](https://doi.org/10.1016/S0013-7944(02)00240-0).
- EPA, U. (2016). “Hydraulic fracturing for oil and gas: Impacts from the hydraulic fracturing water cycle on drinking water resources in the United States”. In: Washington, DC: US Environmental Protection Agency, EPA/600/R-16/236F.
- Erdogan, F. and G. Sih (1963). “On the crack extension in plates under plane loading and transverse shear”. In: *Journal of Basic Engineering* 85.4, pp. 519–525. doi: [10.1115/1.3656897](https://doi.org/10.1115/1.3656897).
- Erickson, B. A. et al. (2020). “The community code verification exercise for simulating sequences of earthquakes and aseismic slip (seas)”. In: *Seismological Research Letters* 91.2A, pp. 874–890. doi: [10.1785/0220190248](https://doi.org/10.1785/0220190248).
- Eshelby, J. D. (1963). “The distribution of dislocations in an elliptical glide zone”. In: *physica status solidi (b)* 3.11, pp. 2057–2060. doi: [10.1002/pssb.19630031109](https://doi.org/10.1002/pssb.19630031109).
- (1966). “A simple derivation of the elastic field of an edge dislocation”. In: *British Journal of Applied Physics* 17.9, pp. 1131–1135. doi: [10.1088/0508-3443/17/9/303](https://doi.org/10.1088/0508-3443/17/9/303).
- Fabrikant, V. (1987). “Close interaction of coplanar circular cracks in an elastic medium”. In: *Acta Mechanica* 67.1-4, pp. 39–59. doi: [10.1007/BF01182121](https://doi.org/10.1007/BF01182121).

Bibliography

- Fialko, Y. (2001). “On origin of near-axis volcanism and faulting at fast spreading mid-ocean ridges”. In: *Earth and Planetary Science Letters* 190.1-2, pp. 31–39. doi: [10.1016/S0012-821X\(01\)00376-4](https://doi.org/10.1016/S0012-821X(01)00376-4).
- Fisher, M. K. and N. R. Warpinski (2012). “Hydraulic-fracture-height growth: Real data”. In: *SPE Production & Operations* 27.01, pp. 8–19. doi: [10.2118/145949-PA](https://doi.org/10.2118/145949-PA).
- Forster, M. and E. Sober (1994). “How to tell when simpler, more unified, or less ad hoc theories will provide more accurate predictions”. In: *The British Journal for the Philosophy of Science* 45.1, pp. 1–35. doi: [10.1093/bjps/45.1.1](https://doi.org/10.1093/bjps/45.1.1).
- Froger, J.-L., Y Fukushima, P Briole, T. Staudacher, T. Souriot, and N Villeneuve (2004). “The deformation field of the August 2003 eruption at Piton de la Fournaise, Reunion Island, mapped by ASAR interferometry”. In: *Geophysical research letters* 31.14. doi: [10.1029/2004GL020479](https://doi.org/10.1029/2004GL020479).
- Fukushima, Y., V. Cayol, and P Durand (2005). “Finding realistic dike models from interferometric synthetic aperture radar data: The February 2000 eruption at Piton de la Fournaise”. In: *Journal of Geophysical Research: Solid Earth* 110.B3. doi: [10.1029/2004JB003268](https://doi.org/10.1029/2004JB003268).
- Fukushima, Y., V. Cayol, P Durand, and D Massonnet (2010). “Evolution of magma conduits during the 1998–2000 eruptions of Piton de la Fournaise volcano, Réunion Island”. In: *Journal of Geophysical Research: Solid Earth* 115.B10. doi: [10.1029/2009JB007023](https://doi.org/10.1029/2009JB007023).
- Gaete, A., J. L. Kavanagh, E. Rivalta, S. H. Hazim, T. R. Walter, and D. J. Dennis (2019). “The impact of unloading stresses on post-caldera magma intrusions”. In: *Earth and Planetary Science Letters* 508, pp. 109–121. doi: [10.1016/j.epsl.2018.12.016](https://doi.org/10.1016/j.epsl.2018.12.016).
- Gehne, S, N. Forbes Inskip, P. Benson, P. Meredith, and N Koor (2020). “Fluid-driven tensile fracture and fracture toughness in Nash Point shale at elevated pressure”. In: *Journal of Geophysical Research: Solid Earth*, e2019JB018971. doi: [10.1029/2019JB018971](https://doi.org/10.1029/2019JB018971).
- Griffith, A. A. (1921). “VI. The phenomena of rupture and flow in solids”. In: *Philosophical transactions of the Royal Society of London. Series A, containing papers of a mathematical or physical character* 221.582-593, pp. 163–198. doi: [10.1098/rsta.1921.0006](https://doi.org/10.1098/rsta.1921.0006).
- (1924). “The theory of rupture”. In: *First International Congress Applied Mechanics*, pp. 55–63.
- Griffith, W. A., S. Nielsen, G. Di Toro, and S. A. Smith (2010). “Rough faults, distributed weakening, and off-fault deformation”. In: *Journal of Geophysical Research: Solid Earth* 115.B8. doi: [10.1029/2009JB006925](https://doi.org/10.1029/2009JB006925).
- Gudmundsson, A. (1995). “Infrastructure and mechanics of volcanic systems in Iceland”. In: *Journal of Volcanology and Geothermal Research* 64.1-2, pp. 1–22. doi: [10.1016/0377-0273\(95\)92782-Q](https://doi.org/10.1016/0377-0273(95)92782-Q).
- (2002). “Emplacement and arrest of sheets and dykes in central volcanoes”. In: *Journal of Volcanology and Geothermal Research* 116.3-4, pp. 279–298. doi: [10.1016/S0377-0273\(02\)00226-3](https://doi.org/10.1016/S0377-0273(02)00226-3).

Bibliography

- Gudmundsson, A. (2012). “Magma chambers: Formation, local stresses, excess pressures, and compartments”. In: *Journal of Volcanology and Geothermal Research* 237, pp. 19–41. doi: [10.1016/j.jvolgeores.2012.05.015](https://doi.org/10.1016/j.jvolgeores.2012.05.015).
- Haario, H., M. Laine, A. Mira, and E. Saksman (2006). “DRAM: efficient adaptive MCMC”. In: *Statistics and computing* 16.4, pp. 339–354. doi: [10.1007/s11222-006-9438-0](https://doi.org/10.1007/s11222-006-9438-0).
- Harbord, C. W., S. B. Nielsen, N. De Paola, and R. E. Holdsworth (2017). “Earthquake nucleation on rough faults”. In: *Geology* 45.10, pp. 931–934. doi: [10.1130/G39181.1](https://doi.org/10.1130/G39181.1).
- Healy, D., R. Rizzo, M. Duffy, N. J. Farrell, M. J. Hole, and D. Muirhead (2018). “Field evidence for the lateral emplacement of igneous dykes: Implications for 3D mechanical models and the plumbing beneath fissure eruptions”. In: *Volcanica*. doi: [10.30909/vol.01.02.85105](https://doi.org/10.30909/vol.01.02.85105).
- Hedayat, A., L. J. Pyrak-Nolte, and A. Bobet (2014). “Multi-modal monitoring of slip along frictional discontinuities”. In: *Rock mechanics and rock engineering* 47.5, pp. 1575–1587. doi: [10.1007/s00603-014-0588-7](https://doi.org/10.1007/s00603-014-0588-7).
- Heidbach, O., M. Rajabi, K. Reiter, M. Ziegler, W. Team, et al. (2016). “World stress map database release 2016”. In: *GFZ Data Services* 10. doi: [10.5880/WSM.2016.001](https://doi.org/10.5880/WSM.2016.001).
- Heidbach, O. et al. (2018). “The World Stress Map database release 2016: Crustal stress pattern across scales”. In: *Tectonophysics* 744, pp. 484–498. doi: [10.1016/j.tecto.2018.07.007](https://doi.org/10.1016/j.tecto.2018.07.007).
- Heimpel, M. and P. Olson (1994). “Buoyancy-driven fracture and magma transport through the lithosphere: models and experiments”. In: *International Geophysics*. Vol. 57. Elsevier. Chap. 10, pp. 223–240. doi: [10.1016/S0074-6142\(09\)60098-X](https://doi.org/10.1016/S0074-6142(09)60098-X).
- Hoek, J. D. (1994). *Mafic dykes of the Vestfold Hills, East Antarctica. An analysis of the emplacement mechanism of tholeiitic dyke swarms and of the role of dyke emplacement during crustal extension*. Utrecht University.
- Hooper, A. et al. (2011). “Increased capture of magma in the crust promoted by ice-cap retreat in Iceland”. In: *Nature Geoscience* 4.11, pp. 783–786. doi: [10.1038/ngeo1269](https://doi.org/10.1038/ngeo1269).
- Huang, Y., Z. Yang, W. Ren, G. Liu, and C. Zhang (2015). “3D meso-scale fracture modelling and validation of concrete based on in-situ X-ray Computed Tomography images using damage plasticity model”. In: *International Journal of Solids and Structures* 67, pp. 340–352. doi: [10.1016/j.ijsolstr.2015.05.002](https://doi.org/10.1016/j.ijsolstr.2015.05.002).
- Inglis, C. E. (1913). “Stresses in a plate due to the presence of cracks and sharp corners”. In: *Trans Inst Naval Archit* 55, pp. 219–241.
- Irwin, G. R. (1957). “Analysis of stresses and strains near the end of a crack transversing a plate”. In: *Trans. ASME, Ser. E, J. Appl. Mech.* 24, pp. 361–364.
- (1958). “Fracture”. In: *Elasticity and Plasticity / Elastizität und Plastizität. Handbuch der Physik / Encyclopedia of Physics*. Ed. by S. Flügge. Vol. 3. 6. Springer-Verlag, pp. 551–590. doi: [10.1007/978-3-642-45887-3_5](https://doi.org/10.1007/978-3-642-45887-3_5).

Bibliography

- Isaia, R., P. Marianelli, and A. Sbrana (2009). “Caldera unrest prior to intense volcanism in Campi Flegrei (Italy) at 4.0 ka BP: Implications for caldera dynamics and future eruptive scenarios”. In: *Geophysical Research Letters* 36.21. doi: [10.1029/2009GL040513](https://doi.org/10.1029/2009GL040513).
- Jackson, D. B., D. Swanson, R. Koyanagi, and W. T.L. (1975). “The August and October 1968 east rift eruptions of Kilauea Volcano, Hawaii”. In: 890. U.S. Geological Survey. U.S. G.P.O. doi: [10.3133/pp890](https://doi.org/10.3133/pp890).
- Janeiro, R. P. and H. H. Einstein (2010). “Experimental study of the cracking behavior of specimens containing inclusions (under uniaxial compression)”. In: *International Journal of Fracture* 164.1, pp. 83–102. doi: [10.1007/s10704-010-9457-x](https://doi.org/10.1007/s10704-010-9457-x).
- Jones, R., S Kokkalas, and K. McCaffrey (2009). “Quantitative analysis and visualization of nonplanar fault surfaces using terrestrial laser scanning (LIDAR)—The Arkitsa fault, central Greece, as a case study”. In: *Geosphere* 5.6, pp. 465–482. doi: [10.1130/GES00216.1](https://doi.org/10.1130/GES00216.1).
- Kattenhorn, S. A. and D. D. Pollard (2001). “Integrating 3-D seismic data, field analogs, and mechanical models in the analysis of segmented normal faults in the Wytch Farm oil field, southern England, United Kingdom”. In: *AAPG bulletin* 85.7, pp. 1183–1210. doi: [10.1306/8626CA91-173B-11D7-8645000102C1865D](https://doi.org/10.1306/8626CA91-173B-11D7-8645000102C1865D).
- Kavanagh, J., T. Menand, and K. A. Daniels (2013). “Gelatine as a crustal analogue: Determining elastic properties for modelling magmatic intrusions”. In: *Tectonophysics* 582, pp. 101–111. doi: [10.1016/j.tecto.2012.09.032](https://doi.org/10.1016/j.tecto.2012.09.032).
- Kavanagh, J., B. Rogers, D Boutelier, and A. Cruden (2017). “Controls on sill and dyke-sill hybrid geometry and propagation in the crust: The role of fracture toughness”. In: *Tectonophysics* 698, pp. 109–120. doi: [10.1016/j.tecto.2016.12.027](https://doi.org/10.1016/j.tecto.2016.12.027).
- Kaven, J. O., S. H. Hickman, N. C. Davatzes, and O. Mutlu (2012). “Linear complementarity formulation for 3D frictional sliding problems”. In: *Computational Geosciences* 16.3, pp. 613–624. doi: [10.1007/s10596-011-9272-0](https://doi.org/10.1007/s10596-011-9272-0).
- Kaya, A. and F Erdogan (1980). “Stress intensity factors and COD in an orthotropic strip”. In: *International Journal of Fracture* 16.2, pp. 171–190. doi: [10.1007/BF00012620](https://doi.org/10.1007/BF00012620).
- Kim, Y.-S. and D. J. Sanderson (2005). “The relationship between displacement and length of faults: a review”. In: *Earth-Science Reviews* 68.3-4, pp. 317–334. doi: [10.1016/j.earscirev.2004.06.003](https://doi.org/10.1016/j.earscirev.2004.06.003).
- Kirkpatrick, J. D. and E. E. Brodsky (2014). “Slickenline orientations as a record of fault rock rheology”. In: *Earth and Planetary Science Letters* 408, pp. 24–34. doi: [10.1016/j.epsl.2014.09.040](https://doi.org/10.1016/j.epsl.2014.09.040).
- Laine, M (2013). MCMC toolbox for Matlab. 2.1. Finnish Meteorological Institute. url: [10.5281/zenodo.4105825](https://doi.org/10.5281/zenodo.4105825).

Bibliography

- Lazarus, V., F.-G. Buchholz, M Fulland, and J Wiebesiek (2008). “Comparison of predictions by mode II or mode III criteria on crack front twisting in three or four point bending experiments”. In: *International journal of fracture* 153.2, pp. 141–151. doi: [10.1007/s10704-008-9307-2](https://doi.org/10.1007/s10704-008-9307-2).
- Lecampion, B., A. Bungler, J. Kear, and D. Quesada (2013). “Interface debonding driven by fluid injection in a cased and cemented wellbore: Modeling and experiments”. In: *International Journal of Greenhouse Gas Control* 18, pp. 208–223. doi: [10.1016/j.ijggc.2013.07.012](https://doi.org/10.1016/j.ijggc.2013.07.012).
- Lecampion, B., A. Bungler, and X. Zhang (2018). “Numerical methods for hydraulic fracture propagation: a review of recent trends”. In: *Journal of natural gas science and engineering* 49, pp. 66–83. doi: [10.1016/j.jngse.2017.10.012](https://doi.org/10.1016/j.jngse.2017.10.012).
- Lengliné, O., Z. Duputel, and P. Okubo (2021). “Tracking dike propagation leading to the 2018 Kīlauea eruption”. In: *Earth and Planetary Science Letters* 553, p. 116653. doi: [10.1016/j.epsl.2020.116653](https://doi.org/10.1016/j.epsl.2020.116653).
- Li, H, C. Liu, Y Mizuta, and M. Kayupov (2001). “Crack edge element of three-dimensional displacement discontinuity method with boundary division into triangular leaf elements”. In: *Communications in numerical methods in engineering* 17.6, pp. 365–378. doi: [10.1002/cnm.410](https://doi.org/10.1002/cnm.410).
- Li, K., X. Jiang, H. Ding, and X. Hu (2019). “Three-Dimensional Propagation Simulation and Parameter Analysis of Rock Joint with Displacement Discontinuity Method”. In: *Mathematical Problems in Engineering* 2019. doi: [10.1155/2019/3164817](https://doi.org/10.1155/2019/3164817).
- Li, S., A. Firoozabadi, and D. Zhang (2020). “Hydromechanical Modeling of Nonplanar Three-Dimensional Fracture Propagation Using an Iteratively Coupled Approach”. In: *Journal of Geophysical Research: Solid Earth* 125.8, e2020JB020115. doi: [10.1029/2020JB020115](https://doi.org/10.1029/2020JB020115).
- Lister, J. R. and R. C. Kerr (1991). “Fluid-mechanical models of crack propagation and their application to magma transport in dykes”. In: *Journal of Geophysical Research: Solid Earth* 96.B6, pp. 10049–10077. doi: [10.1029/91JB00600](https://doi.org/10.1029/91JB00600).
- Maccaferri, F., M Bonafede, and E. Rivalta (2010). “A numerical model of dyke propagation in layered elastic media”. In: *Geophysical Journal International* 180.3, pp. 1107–1123. doi: [10.1111/j.1365-246X.2009.04495.x](https://doi.org/10.1111/j.1365-246X.2009.04495.x).
- (2011). “A quantitative study of the mechanisms governing dike propagation, dike arrest and sill formation”. In: *Journal of Volcanology and Geothermal Research* 208.1-2, pp. 39–50. doi: [10.1016/j.jvolgeores.2011.09.001](https://doi.org/10.1016/j.jvolgeores.2011.09.001).
- Maccaferri, F., N. Richter, and T. R. Walter (2017). “The effect of giant lateral collapses on magma pathways and the location of volcanism”. In: *Nature communications* 8.1, pp. 1–11. doi: [10.1038/s41467-017-01256-2](https://doi.org/10.1038/s41467-017-01256-2).
- Maccaferri, F., E. Rivalta, D. Keir, and V. Acocella (2014). “Off-rift volcanism in rift zones determined by crustal unloading”. In: *Nature Geoscience* 7.4, pp. 297–300. doi: [10.1038/ngeo2110](https://doi.org/10.1038/ngeo2110).

Bibliography

- Maccaferri, F., E. Rivalta, L. Passarelli, and Y. Aoki (2016). “On the mechanisms governing dike arrest: Insight from the 2000 Miyakejima dike injection”. In: *Earth and Planetary Science Letters* 434, pp. 64–74. doi: [10.1016/j.epsl.2015.11.024](https://doi.org/10.1016/j.epsl.2015.11.024).
- Maccaferri, F., E. Rivalta, L. Passarelli, and S. Jónsson (2013). “The stress shadow induced by the 1975–1984 Krafla rifting episode”. In: *Journal of Geophysical Research: Solid Earth* 118.3, pp. 1109–1121. doi: [10.1002/jgrb.50134](https://doi.org/10.1002/jgrb.50134).
- Maccaferri, F., D. Smittarello, V. Pinel, and V. Cayol (2019). “On the propagation path of magma-filled dikes and hydrofractures: The competition between external stress, internal pressure, and crack length”. In: *Geochemistry, Geophysics, Geosystems* 20.4, pp. 2064–2081. doi: [10.1029/2018GC007915](https://doi.org/10.1029/2018GC007915).
- Mair, R et al. (2012). Shale gas extraction in the UK: a review of hydraulic fracturing. Tech. rep. Royal Society and Royal Academy of Engineering.
- Marshall, S. T. and A. C. Morris (2012). “Mechanics, slip behavior, and seismic potential of corrugated dip-slip faults”. In: *Journal of Geophysical Research: Solid Earth* 117.B3. doi: [10.1029/2011JB008642](https://doi.org/10.1029/2011JB008642).
- Martel, S. J. (2000). “Modeling elastic stresses in long ridges with the displacement discontinuity method”. In: *Pure and Applied Geophysics* 157.6-8, pp. 1039–1057. doi: [10.1007/s000240050016](https://doi.org/10.1007/s000240050016).
- Martel, S. J. and J. R. Muller (2000). “A two-dimensional boundary element method for calculating elastic gravitational stresses in slopes”. In: *Pure and Applied Geophysics* 157.6-8, pp. 989–1007. doi: [10.1007/s000240050014](https://doi.org/10.1007/s000240050014).
- Martin, A. J., K. Umeda, C. B. Connor, J. N. Weller, D. Zhao, and M. Takahashi (2004). “Modeling long-term volcanic hazards through Bayesian inference: An example from the Tohoku volcanic arc, Japan”. In: *Journal of Geophysical Research: Solid Earth* 109.B10. doi: [10.1029/2004JB003201](https://doi.org/10.1029/2004JB003201).
- Menand, T, K. Daniels, and P Benghiat (2010). “Dyke propagation and sill formation in a compressive tectonic environment”. In: *Journal of Geophysical Research: Solid Earth* 115.B8. doi: [10.1029/2009JB006791](https://doi.org/10.1029/2009JB006791).
- Meng, C., F. Maerten, and D. D. Pollard (2013). “Modeling mixed-mode fracture propagation in isotropic elastic three dimensional solid”. In: *International Journal of Fracture* 179.1-2, pp. 45–57. doi: [10.1007/s10704-012-9771-6](https://doi.org/10.1007/s10704-012-9771-6).
- Mériaux, C. and J. R. Lister (2002). “Calculation of dike trajectories from volcanic centers”. In: *Journal of Geophysical Research: Solid Earth* 107.B4, ETG 1–10. doi: [10.1029/2001JB000436](https://doi.org/10.1029/2001JB000436).
- Mildren, S., R. Hillis, and J Kaldi (2002). “Calibrating predictions of fault seal reactivation in the Timor Sea”. In: *The APPEA Journal* 42.1, pp. 187–202. doi: [10.1071/AJ01011](https://doi.org/10.1071/AJ01011).

Bibliography

- Moorkamp, M., P. G. Lelièvre, N. Linde, and A. Khan (2016). Integrated imaging of the earth: Theory and applications. Vol. 218. John Wiley & Sons. doi: [10.1002/9781118929063](https://doi.org/10.1002/9781118929063).
- Muller, J. R., G. Ito, and S. J. Martel (2001). “Effects of volcano loading on dike propagation in an elastic half-space”. In: *Journal of Geophysical Research: Solid Earth* 106.B6, pp. 11101–11113. doi: [10.1029/2000JB900461](https://doi.org/10.1029/2000JB900461).
- Muller, O. H. and D. D. Pollard (1977). “The stress state near Spanish Peaks, Colorado determined from a dike pattern”. In: *Pure and Applied Geophysics* 115.1-2, pp. 69–86. doi: [10.1007/BF01637098](https://doi.org/10.1007/BF01637098).
- Murakami, Y. et al. (1987). “Handbook of stress intensity factors”. In: Pergamon Press, Oxford (UK). The Society of Materials Science, Japan. doi: [10.1111/j.1747-1567.1994.tb00808.x](https://doi.org/10.1111/j.1747-1567.1994.tb00808.x).
- Nakashima, Y. (1993). “Buoyancy-driven propagation of an isolated fluid-filled crack in rock: implication for fluid transport in metamorphism”. In: *Contributions to Mineralogy and Petrology* 114.3, pp. 289–295. doi: [10.1007/BF01046532](https://doi.org/10.1007/BF01046532).
- Napier, J. and E. Detournay (2020). “An unstructured mesh algorithm for simulation of hydraulic fracture”. In: *Journal of Computational Physics* 419, p. 109691. doi: [10.1016/j.jcp.2020.109691](https://doi.org/10.1016/j.jcp.2020.109691).
- Nejati, M., A. Paluszny, and R. W. Zimmerman (2016). “A finite element framework for modeling internal frictional contact in three-dimensional fractured media using unstructured tetrahedral meshes”. In: *Computer Methods in Applied Mechanics and Engineering* 306, pp. 123–150. doi: [10.1016/j.cma.2016.03.028](https://doi.org/10.1016/j.cma.2016.03.028).
- Neri, A. et al. (2015). “Quantifying volcanic hazard at Campi Flegrei caldera (Italy) with uncertainty assessment: 2. Pyroclastic density current invasion maps”. In: *Journal of Geophysical Research: Solid Earth* 120.4, pp. 2330–2349. doi: [10.1002/2014JB011776](https://doi.org/10.1002/2014JB011776).
- Historical unrest at the large calderas of the world (1988). 1855. USGS Numbered Series, 2v. 1108 p.:ill., maps; 28 cm. U.S. Geological Survey. U.S. G.P.O. doi: [10.3133/b1855](https://doi.org/10.3133/b1855).
- Niebe, S. and K. Erleben (2015). “Numerical methods for linear complementarity problems in physics-based animation”. In: *Synthesis Lectures on Computer Graphics and Animation* 7.1, pp. 1–159. doi: [10.2200/S00621ED1V01Y201412CGR018](https://doi.org/10.2200/S00621ED1V01Y201412CGR018).
- Niebe, S. M. (Nov. 2009). “Pain and Agony using a Newton Based Method”. Master’s Thesis. Department of Computer Science, University of Copenhagen Denmark.
- Nikkhoo, M. and T. R. Walter (2015). “Triangular dislocation: an analytical, artefact-free solution”. In: *Geophysical Journal International* 201.2, pp. 1119–1141. doi: [10.1093/gji/ggv035](https://doi.org/10.1093/gji/ggv035).
- Nunn, J. A. (1996). “Buoyancy-driven propagation of isolated fluid-filled fractures: Implications for fluid transport in Gulf of Mexico geopressured sediments”. In: *Journal of Geophysical Research: Solid Earth* 101.B2, pp. 2963–2970. doi: [10.1029/95JB03210](https://doi.org/10.1029/95JB03210).
- Okada, Y. (1985). “Surface deformation due to shear and tensile faults in a half-space”. In: *Bulletin of the seismological society of America* 75.4, pp. 1135–1154.

Bibliography

- Okada, Y. (1992). “Internal deformation due to shear and tensile faults in a half-space”. In: *Bulletin of the seismological society of America* 82.2, pp. 1018–1040.
- Okamoto, A. and N. Tsuchiya (2009). “Velocity of vertical fluid ascent within vein-forming fractures”. In: *Geology* 37.6, pp. 563–566. doi: [10.1130/G25680A.1](https://doi.org/10.1130/G25680A.1).
- Olson, J. E. (1991). “Fracture mechanics analysis of joints and veins”. PhD thesis. Stanford University.
- (2003). “Sublinear scaling of fracture aperture versus length: an exception or the rule?” In: *Journal of Geophysical Research: Solid Earth* 108.B9. doi: [10.1029/2001JB000419](https://doi.org/10.1029/2001JB000419).
- Olson, J. E. and D. D. Pollard (1989). “Inferring paleostresses from natural fracture patterns: A new method”. In: *Geology* 17.4, pp. 345–348. doi: [10.1130/0091-7613\(1989\)017<0345:IPFNFP>2.3.CO;2](https://doi.org/10.1130/0091-7613(1989)017<0345:IPFNFP>2.3.CO;2).
- Orsi, G, S De Vita, and M Di Vito (1996). “The restless, resurgent Campi Flegrei nested caldera (Italy): constraints on its evolution and configuration”. In: *Journal of Volcanology and Geothermal Research* 74.3-4, pp. 179–214. doi: [10.1016/S0377-0273\(96\)00063-7](https://doi.org/10.1016/S0377-0273(96)00063-7).
- Orsi, G., M. A. Di Vito, and R. Isaia (2004). “Volcanic hazard assessment at the restless Campi Flegrei caldera”. In: *Bulletin of Volcanology* 66.6, pp. 514–530. doi: [10.1007/s00445-003-0336-4](https://doi.org/10.1007/s00445-003-0336-4).
- Otterloo, J. van and A. R. Cruden (2016). “Rheology of pig skin gelatine: Defining the elastic domain and its thermal and mechanical properties for geological analogue experiment applications”. In: *Tectonophysics* 683, pp. 86–97. doi: [10.1016/j.tecto.2016.06.019](https://doi.org/10.1016/j.tecto.2016.06.019).
- Pandurangan, V., Z. Chen, and R. G. Jeffrey (2016). “Mapping hydraulic fractures from tiltmeter data using the ensemble Kalman filter”. In: *International Journal for Numerical and Analytical Methods in Geomechanics* 40.4, pp. 546–567. doi: [10.1002/nag.2415](https://doi.org/10.1002/nag.2415).
- Paris, P. and F. Erdogan (1963). “A critical analysis of crack propagation laws”. In: *Journal of Basic Engineering* 85.4, pp. 528–533. doi: [10.1115/1.3656900](https://doi.org/10.1115/1.3656900).
- Passarelli, L, B Sansò, L Sandri, and W Marzocchi (2010). “Testing forecasts of a new Bayesian time-predictable model of eruption occurrence”. In: *Journal of volcanology and geothermal research* 198.1-2, pp. 57–75. doi: [10.1016/j.jvolgeores.2010.08.011](https://doi.org/10.1016/j.jvolgeores.2010.08.011).
- Peng, X., E. Atroshchenko, P. Kerfriden, and S. P. A. Bordas (2017). “Isogeometric boundary element methods for three dimensional static fracture and fatigue crack growth”. In: *Computer Methods in Applied Mechanics and Engineering* 316, pp. 151–185. doi: [10.1016/j.cma.2016.05.038](https://doi.org/10.1016/j.cma.2016.05.038).
- Persson, B. N. (2006). “Contact mechanics for randomly rough surfaces”. In: *Surface science reports* 61.4, pp. 201–227. doi: [10.1016/j.surfrep.2006.04.001](https://doi.org/10.1016/j.surfrep.2006.04.001).
- Persson, P.-O. and G. Strang (2004). “A simple mesh generator in MATLAB”. In: *SIAM review* 46.2, pp. 329–345. doi: [10.1137/S0036144503429121](https://doi.org/10.1137/S0036144503429121).

Bibliography

- Pinel, V. and C. Jaupart (2000). “The effect of edifice load on magma ascent beneath a volcano”. In: *Philosophical Transactions of the Royal Society of London. Series A: Mathematical, Physical and Engineering Sciences* 358.1770, pp. 1515–1532. doi: [10.1098/rsta.2000.0601](https://doi.org/10.1098/rsta.2000.0601).
- Pinel, V., D. Smittarello, F. Maccaferri, E. Rivalta, and V. Cayol (2019). “Stress field control on magma path and velocity”. In: *AGUFM 2019*, V12A–01.
- Pollard, D. D. (1973). “Derivation and evaluation of a mechanical model for sheet intrusions”. In: *Tectonophysics* 19.3, pp. 233–269. doi: [10.1016/0040-1951\(73\)90021-8](https://doi.org/10.1016/0040-1951(73)90021-8).
- (1987). “Elementary fracture mechanics applied to the structural interpretation of dykes”. In: *Mafic dyke swarms*. Ed. by H. Halls and W. Fahrig. Vol. 34. Geological Association of Canada, pp. 112–128.
- Pollard, D. D., S Bergbauer, and I Mynatt (2004). “Using differential geometry to characterize and analyse the morphology of joints”. In: *Geological Society, London, Special Publications* 231.1, pp. 153–182. doi: [10.1144/GSL.SP.2004.231.01.10](https://doi.org/10.1144/GSL.SP.2004.231.01.10).
- Pollard, D. D. and R. C. Fletcher (2005). *Fundamentals of structural geology*. Cambridge University Press.
- Pollard, D. D. and O. H. Muller (1976). “The effect of gradients in regional stress and magma pressure on the form of sheet intrusions in cross section”. In: *Journal of Geophysical Research* 81.5, pp. 975–984. doi: [10.1029/JB081i005p00975](https://doi.org/10.1029/JB081i005p00975).
- Pollard, D. D., O. H. Muller, and D. R. Dockstader (1975). “The form and growth of fingered sheet intrusions”. In: *Geological Society of America Bulletin* 86.3, pp. 351–363. doi: [10.1130/0016-7606\(1975\)86<351:TFAGOF>2.0.CO;2](https://doi.org/10.1130/0016-7606(1975)86<351:TFAGOF>2.0.CO;2).
- Pollard, D. D. and P Segall (1987). “Theoretical displacements and stresses near fractures in rock: with applications to faults, joints, veins, dikes, and solution surfaces”. In: *Fracture mechanics of rock*. Ed. by B. K. Atkinson. Academic press, London. Chap. 8, pp. 277–374. doi: [10.1016/C2009-0-21691-6](https://doi.org/10.1016/C2009-0-21691-6).
- Pollard, D. D. and M. R. Townsend (2018). “Fluid-filled fractures in Earth’s lithosphere: Gravitational loading, interpenetration, and stable height of dikes and veins”. In: *Journal of Structural Geology* 109, pp. 38–54. doi: [10.1016/j.jsg.2017.11.007](https://doi.org/10.1016/j.jsg.2017.11.007).
- Polteau, S, E. Ferré, S Planke, E.-R. Neumann, and L Chevallier (2008). “How are saucer-shaped sills emplaced? Constraints from the Golden Valley Sill, South Africa”. In: *Journal of Geophysical Research: Solid Earth* 113.B12. doi: [10.1029/2008JB005620](https://doi.org/10.1029/2008JB005620).
- Poppe, S. et al. (2019). “An inside perspective on magma intrusion: Quantifying 3D displacement and strain in laboratory experiments by dynamic X-ray computed tomography”. In: *Frontiers in Earth Science* 7, p. 62. doi: [10.3389/feart.2019.00062](https://doi.org/10.3389/feart.2019.00062).

Bibliography

- Poppe, S. et al. (2020). “Structural and geochemical interactions between magma and sedimentary host rock: the Hovedøya case, Oslo Rift, Norway”. In: *Geochemistry, Geophysics, Geosystems* 21.3, e2019GC008685. doi: [10.1029/2019GC008685](https://doi.org/10.1029/2019GC008685).
- Power, W. and W. Durham (1997). “Topography of natural and artificial fractures in granitic rocks: Implications for studies of rock friction and fluid migration”. In: *International Journal of Rock Mechanics and Mining Sciences* 34.6, pp. 979–989. doi: [10.1016/S1365-1609\(97\)80007-X](https://doi.org/10.1016/S1365-1609(97)80007-X).
- Renard, F., K. Mair, and O. Gundersen (2012). “Surface roughness evolution on experimentally simulated faults”. In: *Journal of Structural Geology* 45, pp. 101–112. doi: [10.1016/j.jsg.2012.03.009](https://doi.org/10.1016/j.jsg.2012.03.009).
- Renshaw, C. and D. Pollard (1995). “An experimentally verified criterion for propagation across unbounded frictional interfaces in brittle, linear elastic materials”. In: *International journal of rock mechanics and mining sciences & geomechanics abstracts*. Vol. 32. 3. Elsevier, pp. 237–249. doi: [10.1016/0148-9062\(94\)00037-4](https://doi.org/10.1016/0148-9062(94)00037-4).
- Resor, P. G. and V. E. Meer (2009). “Slip heterogeneity on a corrugated fault”. In: *Earth and Planetary Science Letters* 288.3-4, pp. 483–491. doi: [10.1016/j.epsl.2009.10.010](https://doi.org/10.1016/j.epsl.2009.10.010).
- Reynolds, R. W., D. Geist, and M. D. Kurz (1995). “Physical volcanology and structural development of Sierra Negra volcano, Isabela island, Galápagos archipelago”. In: *Geological Society of America Bulletin* 107.12, pp. 1398–1410. doi: [10.1130/0016-7606\(1995\)107<1398:PVASDO>2.3.CO;2](https://doi.org/10.1130/0016-7606(1995)107<1398:PVASDO>2.3.CO;2).
- Ritz, E., O. Mutlu, and D. D. Pollard (2012). “Integrating complementarity into the 2D displacement discontinuity boundary element method to model faults and fractures with frictional contact properties”. In: *Computers & geosciences* 45, pp. 304–312. doi: [10.1016/j.cageo.2011.11.017](https://doi.org/10.1016/j.cageo.2011.11.017).
- Ritz, E. and D. D. Pollard (2012). “Stick, slip, and opening of wavy frictional faults: A numerical approach in two dimensions”. In: *Journal of Geophysical Research: Solid Earth* 117.B3. doi: [10.1029/2011JB008624](https://doi.org/10.1029/2011JB008624).
- Ritz, E., D. D. Pollard, and M. Ferris (2015). “The influence of fault geometry on small strike-slip fault mechanics”. In: *Journal of Structural Geology* 73, pp. 49–63.
- Rivalta, E., F. Corbi, L. Passarelli, V. Acocella, T. Davis, and M. A. Di Vito (2019). “Stress inversions to forecast magma pathways and eruptive vent location”. In: *Science advances* 5.7, eaau9784. doi: [10.1126/sciadv.aau9784](https://doi.org/10.1126/sciadv.aau9784).
- Rivalta, E., B. Taisne, A. Bungler, and R. Katz (2015). “A review of mechanical models of dike propagation: Schools of thought, results and future directions”. In: *Tectonophysics* 638, pp. 1–42. doi: [10.1016/j.tecto.2014.10.003](https://doi.org/10.1016/j.tecto.2014.10.003).
- Rivalta, E., M. Böttlinger, and T. Dahm (2005). “Buoyancy-driven fracture ascent: Experiments in layered gelatine”. In: *Journal of Volcanology and Geothermal Research* 144.1-4, pp. 273–285. doi: [10.1016/j.jvolgeores.2004.11.030](https://doi.org/10.1016/j.jvolgeores.2004.11.030).

Bibliography

- Rivalta, E. and T. Dahm (2006). “Acceleration of buoyancy-driven fractures and magmatic dikes beneath the free surface”. In: *Geophysical Journal International* 166.3, pp. 1424–1439. doi: [10.1111/j.1365-246X.2006.02962.x](https://doi.org/10.1111/j.1365-246X.2006.02962.x).
- Roberts, G. P. and A. Ganas (2000). “Fault-slip directions in central and southern Greece measured from striated and corrugated fault planes: Comparison with focal mechanism and geodetic data”. In: *Journal of Geophysical Research: Solid Earth* 105.B10, pp. 23443–23462. doi: [10.1029/1999JB900440](https://doi.org/10.1029/1999JB900440).
- Roman, A. and C. Jaupart (2014). “The impact of a volcanic edifice on intrusive and eruptive activity”. In: *Earth and Planetary Science Letters* 408, pp. 1–8. doi: [10.1016/j.epsl.2014.09.016](https://doi.org/10.1016/j.epsl.2014.09.016).
- Roper, S. and J. Lister (2007). “Buoyancy-driven crack propagation: the limit of large fracture toughness”. In: *Journal of Fluid Mechanics* 580, pp. 359–380. doi: [10.1017/S0022112007005472](https://doi.org/10.1017/S0022112007005472).
- Rosen, P., E. Gurrola, P. S. Agram, G. F. Sacco, and M. Lavalle (2015). “The InSAR Scientific Computing Environment (ISCE): A python framework for Earth science”. In: *AGUFM 2015*, IN11C–1789.
- Rosi, M. and A. Sbrana (1987). “Phlegrean fields”. In: *Quaderni De La Ricerca Scientifica* 9.114.
- Rubin, D. B. (1988). “Using the SIR algorithm to simulate posterior distributions”. In: *Bayesian statistics* 3, pp. 395–402.
- Sagy, A., E. E. Brodsky, and G. J. Axen (2007). “Evolution of fault-surface roughness with slip”. In: *Geology* 35.3, pp. 283–286. doi: [10.1130/G23235A.1](https://doi.org/10.1130/G23235A.1).
- Salimzadeh, S., R. W. Zimmerman, and N. Khalili (2020). “Gravity Hydraulic Fracturing: A Method to Create Self-driven Fractures”. In: *Geophysical Research Letters*, e2020GL087563. doi: [10.1029/2020GL087563](https://doi.org/10.1029/2020GL087563).
- In situ geomechanics of crystalline and sedimentary rocks; Part V, RVT, a Fortran program for an exact elastic solution for tectonics and gravity stresses in isolated symmetric ridges and valleys (1984). 84-827. USGS Numbered Series, 12 p. :ill.; 28 cm. U.S. Geological Survey. Denver, Colorado: U.S. G.P.O. doi: [10.3133/ofr84827](https://doi.org/10.3133/ofr84827).
- Schofield, N. J., D. J. Brown, C. Magee, and C. T. Stevenson (2012). “Sill morphology and comparison of brittle and non-brittle emplacement mechanisms”. In: *Journal of the Geological Society* 169.2, pp. 127–141. doi: [10.1144/0016-76492011-078](https://doi.org/10.1144/0016-76492011-078).
- Scholz, C. H. (2010). “A note on the scaling relations for opening mode fractures in rock”. In: *Journal of Structural Geology* 32.10, pp. 1485–1487. doi: [10.1016/j.jsg.2010.09.007](https://doi.org/10.1016/j.jsg.2010.09.007).
- Schultz, R. A. (2016). “Causes and mitigation strategies of surface hydrocarbon leaks at heavy-oil fields: examples from Alberta and California”. In: *Petroleum Geoscience* 23.2, pp. 231–237. doi: [10.1144/petgeo2016-070](https://doi.org/10.1144/petgeo2016-070).
- Schultz, R. A., U. Mutlu, and A. Bere (2016). “Critical issues in subsurface integrity”. In: *50th US Rock Mechanics/Geomechanics Symposium*. American Rock Mechanics Association.

Bibliography

- Secor, D. T. and D. D. Pollard (1975). “On the stability of open hydraulic fractures in the Earth’s crust”. In: *Geophysical Research Letters* 2.11, pp. 510–513. doi: [10.1029/GL002i011p00510](https://doi.org/10.1029/GL002i011p00510).
- Selva, J., G. Orsi, M. A. Di Vito, W. Marzocchi, and L. Sandri (2012). “Probability hazard map for future vent opening at the Campi Flegrei caldera, Italy”. In: *Bulletin of volcanology* 74.2, pp. 497–510. doi: [10.1007/s00445-011-0528-2](https://doi.org/10.1007/s00445-011-0528-2).
- Sheibani, F., J. E. Olson, et al. (2013). “Stress intensity factor determination for three-dimensional crack using the displacement discontinuity method with applications to hydraulic fracture height growth and non-planar propagation paths”. In: *ISRM International Conference for Effective and Sustainable Hydraulic Fracturing*. International Society for Rock Mechanics and Rock Engineering. doi: [10.5772/56308](https://doi.org/10.5772/56308).
- Shi, J., B. Shen, O. Stephansson, and M. Rinne (2014). “A three-dimensional crack growth simulator with displacement discontinuity method”. In: *Engineering Analysis with Boundary Elements* 48, pp. 73–86. doi: [10.1016/j.enganabound.2014.07.002](https://doi.org/10.1016/j.enganabound.2014.07.002).
- Sigmundsson, F. et al. (2015). “Segmented lateral dyke growth in a rifting event at Bárðarbunga volcanic system, Iceland”. In: *Nature* 517.7533, pp. 191–195. doi: [10.1038/nature14111](https://doi.org/10.1038/nature14111).
- Sih, G., P. Paris, and G. R. Irwin (1965). “On cracks in rectilinearly anisotropic bodies”. In: *International Journal of Fracture Mechanics* 1.3, pp. 189–203. doi: [10.1007/BF00186854](https://doi.org/10.1007/BF00186854).
- Smith, V., R. Isaia, and N. Pearce (2011). “Tephrostratigraphy and glass compositions of post-15 kyr Campi Flegrei eruptions: implications for eruption history and chronostratigraphic markers”. In: *Quaternary Science Reviews* 30.25-26, pp. 3638–3660. doi: [10.1016/j.quascirev.2011.07.012](https://doi.org/10.1016/j.quascirev.2011.07.012).
- Smittarello, D., V. Cayol, V. Pinel, A. Peltier, J.-L. Froger, and V. Ferrazzini (2019). “Magma Propagation at Piton de la Fournaise From Joint Inversion of InSAR and GNSS”. In: *Journal of Geophysical Research: Solid Earth* 124.2, pp. 1361–1387. doi: [10.1029/2018JB016856](https://doi.org/10.1029/2018JB016856).
- Smittarello, D. (Dec. 2019). “Propagation des intrusions basaltiques”. PhD thesis. Université Grenoble Alpes.
- Sneddon, I. N. (1946). “The distribution of stress in the neighbourhood of a crack in an elastic solid”. In: *Proceedings of the Royal Society of London. Series A. Mathematical and Physical Sciences* 187.1009, pp. 229–260. doi: [10.1098/rspa.1946.0077](https://doi.org/10.1098/rspa.1946.0077).
- Spacapan, J. B., O. Galland, H. A. Leanza, and S. Planke (2017). “Igneous sill and finger emplacement mechanism in shale-dominated formations: a field study at Cuesta del Chihuido, Neuquén Basin, Argentina”. In: *Journal of the Geological Society* 174.3, pp. 422–433. doi: [10.1144/jgs2016-056](https://doi.org/10.1144/jgs2016-056).
- Steinmann, L., V. Spiess, and M. Sacchi (2018). “Post-collapse evolution of a coastal caldera system: Insights from a 3D multichannel seismic survey from the Campi Flegrei caldera (Italy)”. In: *Journal of Volcanology and Geothermal Research* 349, pp. 83–98. doi: [10.1016/j.jvolgeores.2017.09.023](https://doi.org/10.1016/j.jvolgeores.2017.09.023).

Bibliography

- Sulistianto, B., T. Kido, and Y. Mizuta (1998). “Determination of far field stress from the point stress measurement, a numerical approach”. In: *Shigen-to-Sozai* 114.7, pp. 461–466. doi: [10.2473/shigentosozai.114.461](https://doi.org/10.2473/shigentosozai.114.461).
- Sun, R. J. (1969). “Theoretical size of hydraulically induced horizontal fractures and corresponding surface uplift in an idealized medium”. In: *Journal of Geophysical Research* 74.25, pp. 5995–6011. doi: [10.1029/JB074i025p05995](https://doi.org/10.1029/JB074i025p05995).
- Tada, H., P. Paris, and G. R. Irwin (2000). *The Stress Analysis of Cracks Handbook*; Third edition. Vol. 130. New York: ASME Press.
- Taisne, B and S Tait (2009). “Eruption versus intrusion? Arrest of propagation of constant volume, buoyant, liquid-filled cracks in an elastic, brittle host”. In: *Journal of Geophysical Research: Solid Earth* 114.B6. doi: [10.1029/2009JB006297](https://doi.org/10.1029/2009JB006297).
- Taisne, B., S. Tait, and C. Jaupart (2011). “Conditions for the arrest of a vertical propagating dyke”. In: *Bulletin of Volcanology* 73.2, pp. 191–204. doi: [10.1007/s00445-010-0440-1](https://doi.org/10.1007/s00445-010-0440-1).
- Takada, A. (1990). “Experimental study on propagation of liquid-filled crack in gelatin: Shape and velocity in hydrostatic stress condition”. In: *Journal of Geophysical Research: Solid Earth* 95.B6, pp. 8471–8481. doi: [10.1029/JB095iB06p08471](https://doi.org/10.1029/JB095iB06p08471).
- Thomas, A. L. and D. D. Pollard (1993). “The geometry of echelon fractures in rock: implications from laboratory and numerical experiments”. In: *Journal of Structural Geology* 15.3-5, pp. 323–334. doi: [10.1016/0191-8141\(93\)90129-X](https://doi.org/10.1016/0191-8141(93)90129-X).
- Thomas, A. L. (June 1993). “POLY3D: A three-dimensional, polygonal element, displacement discontinuity boundary element computer program with applications to fractures, faults, and cavities in the earth’s crust”. Master’s Thesis. Stanford University.
- Tolstoy, M et al. (2006). “A sea-floor spreading event captured by seismometers”. In: *Science* 314.5807, pp. 1920–1922. doi: [10.1126/science.1133950](https://doi.org/10.1126/science.1133950).
- Townsend, M. R., D. D. Pollard, and R. P. Smith (2017). “Mechanical models for dikes: a third school of thought”. In: *Tectonophysics* 703, pp. 98–118. doi: [10.1016/j.tecto.2017.03.008](https://doi.org/10.1016/j.tecto.2017.03.008).
- Urbani, S, V Acocella, and E Rivalta (2018). “What drives the lateral versus vertical propagation of dikes? Insights from analogue models”. In: *Journal of Geophysical Research: Solid Earth* 123.5, pp. 3680–3697. doi: [10.1029/2017JB015376](https://doi.org/10.1029/2017JB015376).
- Vasconez, F. J. et al. (2018). “The different characteristics of the recent eruptions of Fernandina and Sierra Negra volcanoes (Galápagos, Ecuador)”. In: *Volcanica* 1.2, pp. 127–133. doi: [10.30909/vol.01.02.127133](https://doi.org/10.30909/vol.01.02.127133).
- Veen, C. Van der (1998). “Fracture mechanics approach to penetration of bottom crevasses on glaciers”. In: *Cold Regions Science and Technology* 27.3, pp. 213–223. doi: [10.1016/S0165-232X\(98\)00006-8](https://doi.org/10.1016/S0165-232X(98)00006-8).

Bibliography

- Ventura, G., G. Vilaro, and P. P. Bruno (1999). “The role of flank failure in modifying the shallow plumbing system of volcanoes: an example from Somma-Vesuvius, Italy”. In: *Geophysical Research Letters* 26.24, pp. 3681–3684. doi: [10.1029/1999GL005404](https://doi.org/10.1029/1999GL005404).
- Vidic, R. D., S. L. Brantley, J. M. Vandenbossche, D. Yoxtheimer, and J. D. Abad (2013). “Impact of shale gas development on regional water quality”. In: *Science* 340.6134, p. 1235009. doi: [10.1126/science.1235009](https://doi.org/10.1126/science.1235009).
- Vigouroux, N., G. Williams-Jones, W. Chadwick, D. Geist, A. Ruiz, and D. Johnson (2008). “4D gravity changes associated with the 2005 eruption of Sierra Negra volcano, Galápagos”. In: *Geophysics* 73.6, WA29–WA35. doi: [10.1190/1.2987399](https://doi.org/10.1190/1.2987399).
- Vitale, S. and R. Isaia (2014). “Fractures and faults in volcanic rocks (Campi Flegrei, southern Italy): insight into volcano-tectonic processes”. In: *International Journal of Earth Sciences* 103.3, pp. 801–819. doi: [10.1007/s00531-013-0979-0](https://doi.org/10.1007/s00531-013-0979-0).
- Wadge, G., P. Young, and I. McKendrick (1994). “Mapping lava flow hazards using computer simulation”. In: *Journal of Geophysical Research: Solid Earth* 99.B1, pp. 489–504. doi: [10.1029/93JB01561](https://doi.org/10.1029/93JB01561).
- Warpinski, N. R., P. Branagan, and R. Wilmer (1985). “In-Situ Stress Measurements at US DOE’s Multiwell Experiment Site, Mesaverde Group, Rifle, Colorado”. In: *Journal of petroleum technology* 37.03, pp. 527–536. doi: [10.2118/12142-PA](https://doi.org/10.2118/12142-PA).
- Warpinski, N. R., R. A. Schmidt, and D. A. Northrop (1982). “In-situ stresses: the predominant influence on hydraulic fracture containment”. In: *Journal of Petroleum Technology* 34.03, pp. 653–664. doi: [10.2118/8932-PA](https://doi.org/10.2118/8932-PA).
- Watanabe, T., T. Masuyama, K. Nagaoka, and T. Tahara (2002). “Analog experiments on magma-filled cracks”. In: *Earth, planets and space* 54.12, pp. 1247–1261. doi: [10.1186/BF03352453](https://doi.org/10.1186/BF03352453).
- Weertman, J. (1971a). “Theory of water-filled crevasses in glaciers applied to vertical magma transport beneath oceanic ridges”. In: *Journal of Geophysical Research* 76.5, pp. 1171–1183. doi: [10.1029/JB076i005p01171](https://doi.org/10.1029/JB076i005p01171).
- (1971b). “Velocity at which liquid-filled cracks move in the Earth’s crust or in glaciers”. In: *Journal of Geophysical Research* 76.35, pp. 8544–8553. doi: [10.1029/JB076i035p08544](https://doi.org/10.1029/JB076i035p08544).
- (1973). “Can a water-filled crevasse reach the bottom surface of a glacier”. In: *IASH publ* 95, pp. 139–145.
- (1980). “The stopping of a rising, liquid-filled crack in the Earth’s crust by a freely slipping horizontal joint”. In: *Journal of Geophysical Research: Solid Earth* 85.B2, pp. 967–976. doi: [10.1029/JB085iB02p00967](https://doi.org/10.1029/JB085iB02p00967).
- Weertman, J. and J. R. Weertman (1964). *Elementary dislocation theory*. Macmillan.

Bibliography

- Weinlich, F. (2014). “Carbon dioxide controlled earthquake distribution pattern in the NW Bohemian swarm earthquake region, western Eger Rift, Czech Republic—gas migration in the crystalline basement”. In: *Geofluids* 14.2, pp. 143–159. doi: [10.1111/gfl.12058](https://doi.org/10.1111/gfl.12058).
- Wessel, B., M. Huber, C. Wohlfart, U. Marschalk, D. Kosmann, and A. Roth (2018). “Accuracy assessment of the global TanDEM-X Digital Elevation Model with GPS data”. In: *ISPRS Journal of Photogrammetry and Remote Sensing* 139, pp. 171–182. doi: [10.1016/j.isprsjprs.2018.02.017](https://doi.org/10.1016/j.isprsjprs.2018.02.017).
- Westergaard, H. M. (1939). “Bearing pressures and cracks”. In: *Trans AIME, J. Appl. Mech.* 6, pp. 49–53.
- Willemsse, E. J. (1997). “Segmented normal faults: Correspondence between three-dimensional mechanical models and field data”. In: *Journal of Geophysical Research: Solid Earth* 102.B1, pp. 675–692. doi: [10.1029/96JB01651](https://doi.org/10.1029/96JB01651).
- Williams, M (1957). “On the stress distribution at the base of a stationary crack”. In: *Journal of Applied Mechanics*. 1st ser. 24, pp. 109–114.
- Xu, W. and S. Jónsson (2014). “The 2007–8 volcanic eruption on Jebel at Tair island (Red Sea) observed by satellite radar and optical images”. In: *Bulletin of Volcanology* 76.2, p. 795. doi: [10.1007/s00445-014-0795-9](https://doi.org/10.1007/s00445-014-0795-9).
- Xu, W., R. Prioul, T. Berard, X. Weng, and O. Kresse (2019). “Barriers to hydraulic fracture height growth: A new model for sliding interfaces”. In: *SPE Hydraulic Fracturing Technology Conference and Exhibition*. Society of Petroleum Engineers. doi: [10.2118/194327-MS](https://doi.org/10.2118/194327-MS).
- Yang, S., Y. Jiang, W. Xu, and X. Chen (2008). “Experimental investigation on strength and failure behavior of pre-cracked marble under conventional triaxial compression”. In: *International Journal of Solids and Structures* 45.17, pp. 4796–4819. doi: [10.1016/j.ijstr.2008.04.023](https://doi.org/10.1016/j.ijstr.2008.04.023).
- Yue, K., J. E. Olson, and R. A. Schultz (2019). “The Effect of Layered Modulus on Hydraulic-Fracture Modeling and Fracture-Height Containment”. In: *SPE Drilling & Completion*. doi: [10.2118/195683-PA](https://doi.org/10.2118/195683-PA).
- Zia, H. and B. Lecampion (2020). “Pyfrac: A planar 3d hydraulic fracture simulator”. In: *Computer Physics Communications* 255.107368, pp. 1–11. doi: [10.1016/j.cpc.2020.107368](https://doi.org/10.1016/j.cpc.2020.107368).